

Diode Laser Cavity-based Techniques for Quantification of Trace Species in Laminar Sooting Flames

Precious O. Otti

Department of Chemical and Process Engineering
University of Strathclyde

A thesis submitted to the Department of Chemical and Process Engineering
University of Strathclyde in fulfilment of the requirements for the degree of
Doctor of Philosophy

September 2020

Declaration of Authenticity & Author's rights

This thesis is the result of the author's original research. It has been composed by the author and has not been previously submitted for examination which has led to the award of a degree.

The copyright of this thesis belongs to the author under the terms of the United Kingdom Copyright Acts as qualified by University of Strathclyde Regulation 3.50. Due acknowledgement must always be made of the use of any material contained in, or derived from, this thesis.

Signed:

Date:

Abstract

Cavity-enhanced absorption spectroscopy (CEAS) has been applied for the first time to *in situ* measurements of acetylene in sooting flames using a near-infrared diode laser. This is motivated by the role of acetylene as a major precursor in soot formation and the need for accurate measurements of acetylene to understand soot formation (with the eventual goal of reduced emissions). Vertical profiles of acetylene have been investigated in two flat-flame burners with some consideration of the effect of radial profiles on the results.

This thesis builds on the novel application of continuous-wave cavity ring-down spectroscopy (*cw*-CRDS) to *in situ* flame measurements of acetylene: in this work, refinements are made to the technique, which is developed to the point of generating reliable data in standard flames of interest in studies of soot formation. A key advantage of the *cw*-CRDS approach is that it is an absolute method, not requiring calibration. Nevertheless, the slow data acquisition led to the consideration of alternative approaches. This resulted in research on CEAS, which forms the bulk of this thesis. The advantages of the CEAS technique over *cw*-CRDS are highlighted, whilst noting the agreement between the two techniques. The CEAS approach allows spectra to be acquired much more rapidly and with better spectral resolution, as well as having a somewhat simpler experimental set-up. This has enabled the acquisition of a large dataset of broad scans over the full scanning range of the diode lasers employed. This thesis also goes on to explore the application of the CEAS technique to flame measurements of OH radical.

The recovered profiles of acetylene concentration show good agreement for both techniques and follow the expected trend of higher acetylene concentration with increasing equivalence ratio. They also show a trend of decreasing acetylene concentration with increasing height above the burner surface. This would be consistent with the consumption of acetylene, including in reactions forming polycyclic aromatic hydrocarbons and ultimately soot. However, this is contrary to model predictions also shown in the thesis.

Acknowledgement

I would like to say a big thank you to my supervisor, Dr Iain Burns for the great supervision throughout the duration of this project. My gratitude goes to my second supervisor, Dr Michael Lengden for his support and contributions towards the success of this project. I want to say a big thank you to Dr Gordon Humphries for putting me through the practical rudiments and tricks without which this project would have been more difficult. I extend my gratitude to Dr Robert Roy and Dr David Wilson for their help in the laboratory. I also do not forget the technical staff in the lab who were helpful with providing technical assistance and receiving deliveries. I appreciate the support from staff and PhD students in CMP who were always there to assist me whenever I used the labs at CMP.

My immense gratitude goes to my fellow PhD colleagues and members of staff in the Chemical and Process Engineering Department for the chats, laughs and memorable moments which have been a source of strength throughout this journey. Many thanks to Really Small Science Team and the Faculty of Engineering for the outreach programmes and the opportunity to be a student ambassador. I am grateful to the Strathclyde Nigerian Society for being my local family in Glasgow and for the opportunity to serve as the Welfare Officer.

Special thanks to my family, close friends and well-wishers for the support, encouragements, and kind words. From these I have drawn strength to complete this journey.

Finally, I give all thanks to God Almighty for the grace and strength to see this project through to completion.

Table of Contents

Abstract.....	ii
Acknowledgement	iii
List of Acronyms.....	ix
List of Figures	x
Chapter 1 : Introduction	1
1.1 Overview of Combustion.....	1
1.2 Societal Challenge	2
1.3 Soot Formation.....	4
1.3.1 Computational Studies of Soot Related Species in Combustion	6
1.4 Diagnostic Techniques for Soot Studies	9
1.4.1 Intrusive Techniques.....	9
1.4.2 Non-intrusive Techniques.....	10
1.4.3 Direct Absorption Spectroscopy	11
1.4.4 Wavelength Modulation Spectroscopy	11
1.4.5 Laser-Induced Fluorescence	13
1.4.6 Laser-Induced Incandescence.....	14
1.4.7 Spontaneous Raman Scattering	14
1.4.8 Coherent Anti-Stokes Raman Spectroscopy	16
1.4.9 Polarisation Spectroscopy	17
1.5 Motivation	18
1.6 Thesis Aims and Objectives	21
1.7 Thesis Outline	22
1.8 References	23
Chapter 2 : Diode Laser Spectroscopy for Combustion Diagnostics.....	29
2.1 Introduction.....	29

2.2 Atomic and Molecular Spectroscopy	29
2.2.1 Vibrational and Rotational Energy Levels.....	32
2.3 Characteristics and Modelling of Absorption Spectral Lines	36
2.3.1 Absorption Line Strength.....	37
2.3.2 Broadening of Absorption Spectral Lines	39
2.3.3 HITRAN and HITEMP Spectroscopic Databases.....	44
2.4 Determination of Concentration from Absorption Spectra.....	45
2.5 Theory of Optical Cavities	47
2.5.1 Fundamentals of Optical Cavities	47
2.5.2 Stability of Optical Cavities	52
2.6 Cavity-based Absorption Techniques.....	54
2.6.1 Theory of Cavity Ring-down Spectroscopy.....	55
2.6.2 Continuous-wave Cavity ring-down Spectroscopy.....	58
2.6.3 Phase-shift Cavity Ring-down Spectroscopy	59
2.6.4 Cavity-enhanced Absorption Spectroscopy.....	60
2.6.5 Off-axis Cavity Enhanced Absorption Spectroscopy	62
2.7 Application of Cavity-based Techniques to <i>in situ</i> Flame Measurements.....	63
2.8 Summary	66
2.9 References.....	66
Chapter 3 : Cavity-based Experimental Methodology for Flame Measurements.....	72
3.1 Introduction.....	72
3.2 Flame-Burner Configuration.....	72
3.2.1 McKenna Burner	74
3.2.2 Porous-plug Burner.....	78
3.2.3 Mass Flow controllers.....	82
3.3 Continuous-wave Cavity Ring-down Spectroscopy design	83
3.3.1 Semiconductor Optical Amplifier	84

3.3.2 Diode Laser	85
3.3.3 Optical Cavity	90
3.3.4 Configuration of Mode Matching Optics.....	91
3.3.5 Alignment of the Optical Cavity.....	92
3.3.6 Detection	93
3.3.7 Amplifier	94
3.3.8 Operation and Data Acquisition	95
3.3.9 Experimental Procedure for cw-CRDS Measurements of Acetylene	97
3.4 Cavity-Enhanced Absorption Spectroscopy Design	99
3.4.1 Challenges in implementing CEAS for flame measurements and approaches taken	99
3.4.2 Diode Laser	103
3.4.3 Optical Cavity	103
3.4.4 Cavity Alignment.....	104
3.4.5 Operation and Data Acquisition	104
3.4.6 Experimental Procedure for CEAS Measurements of Acetylene	108
3.4.7 Experimental Procedure for CEAS Measurements of OH Radical	109
3.5 Summary	110
3.6 References.....	110
Chapter 4 : Flame Measurements of Acetylene using cw-CRDS	113
4.1 Introduction.....	113
4.2 Model of Expected Flame Spectrum	113
4.3 Acetylene Absorption Spectra.....	115
4.4 Determination of Acetylene Concentration from cw-CRDS Measured Absorption Spectra.....	121
4.4.1 Fitting of Spectral Model	122
4.5 Acetylene Concentration Profiles.....	127

4.6 Uncertainty Analysis.....	128
4.7 Extinction Measurements	129
4.8 Summary	131
4.9 References.....	132
Chapter 5 : Development of Cavity-Enhanced Absorption Spectroscopy for measurement of Acetylene Concentration in Flames	135
5.1 Introduction.....	135
5.2 Acetylene Absorption Spectra.....	136
5.3 Determination of Acetylene Concentration from CEAS Measured Absorption Spectra.....	143
5.3.1 Extraction of Acetylene Spectrum	143
5.3.2 Fitting of Model Spectrum.....	149
5.4 Acetylene Concentration Profiles.....	151
5.4.1 Comparison of Acetylene Concentration Profiles with Model Predictions	153
5.4.2 Radial Profiles of Acetylene Concentration	159
5.5 Extinction Measurements	166
5.6 CEAS vs cw-CRDS	168
5.6.1 Comparison of Extinction Measurements for cw-CRDS and CEAS.....	173
5.7 Uncertainty Analysis.....	174
5.8 Summary	176
5.9 References.....	177
Chapter 6 : Cavity-Enhanced Absorption Spectroscopy of OH Radical in Flames. ..	180
6.1 Introduction.....	180
6.2 Broad Spectral Scans	181
6.3 OH Species in Combustion	190
6.4 OH Spectra.....	191

6.5 Uncertainty Analysis.....	198
6.6 Summary	198
6.7 References.....	199
Chapter 7 : Conclusions and Further Work.....	202
7.1 Conclusions.....	202
7.1.1 Continuous-wave Cavity Ring-down Measurements of Acetylene.....	203
7.1.2 Cavity-enhanced Absorption Measurements of Acetylene	204
7.1.3 Cavity-enhanced Absorption Measurements of OH	205
7.2 Further Work	206
7.3 References.....	207
Appendices.....	209
Appendix A: Conferences/meetings attended.....	209
Appendix B: Matlab code for calculating acetylene concentration.....	210
Appendix C: Matlab code for CEAS spectra calibration	215
Appendix D: Matlab code for the iterative extraction technique.....	218
Appendix E: Cantera code for a stagnation flame with a fixed temperature profile	220

List of Acronyms

ABF: Appel-Bockhorn-Frenklach

CARS: Coherent anti-Stokes Raman Spectroscopy

CEAS: Cavity-enhanced Absorption Spectroscopy

cw-CRDS: Continuous-wave Cavity ring-down Spectroscopy

DAS: Direct Absorption Spectroscopy

FWHM: Full Width at Half Maximum

HAB: Height Above Burner

HWHM: Half Width at Half Maximum

IR Card: Infrared Card

LIF: Laser Induced Fluorescence

LII: Laser Induced Incandescence

NI DAQ Card: National Instruments Data Acquisition Card

PAH: Polycyclic Aromatic Hydrocarbon

PC: Personal Computer

PS: Polarisation Spectroscopy

PZT: Piezo Transducer

SNR: Signal to Noise Ratio

SOA: Semi-conductor Optical Amplifier

SRS: Spontaneous Raman Spectroscopy

TDLAS: Tunable Diode Laser Absorption Spectroscopy

USC: University of Southern California

WMS: Wavelength Modulation spectroscopy

List of Figures

Figure 1.1: Overview of soot formation [20].	4
Figure 1.2: HACA mechanism (reproduced from Lu et al. [23]).	5
Figure 1.3: Schematic of a simple non-intrusive set-up.	10
Figure 1.4: Set-up for Direct Absorption Spectroscopy.	11
Figure 1.5: Set-up for Wavelength Modulation Spectroscopy.	12
Figure 1.6: Energy level diagram showing fluorescence emission.	13
Figure 1.7: LII set-up diagram.	14
Figure 1.8: a). Schematic of SRS process. b). Energy level diagram depicting various scattering processes.	15
Figure 1.9: Schematic of CARS process.	16
Figure 1.10: Polarisation Spectroscopy set-up diagram.	17
Figure 2.1: Absorption transition in a two-level energy system.	30
Figure 2.2: A least squares fit of a Voigt line shape to an absorption spectrum.	37
Figure 2.3: Comparison of Gaussian, Lorentzian and Voigt lineshapes with the same FWHM.	41
Figure 2.4: Schematic of a Fabry-Perot Interferometer.	48
Figure 2.5: Constructive interference resulting from two waves propagating in a cavity.	49
Figure 2.6: Ideal transmission function of a linear cavity for varying mirror reflectivity (image sourced from Humphries [16]).	50
Figure 2.7: 3-D representation of the spatial intensity profile of transverse electromagnetic modes (image sourced from OPI online courses [22]).	51
Figure 2.8: Schematic of a Gaussian beam in a symmetrical 2-spherical concave mirror cavity.	53
Figure 2.9: 2-mirror cavity stability diagram.	54
Figure 2.10: Schematic of phase-shift cavity ring-down spectroscopy.	60

Figure 3.1: Schematic of burner centre-line and HAB.	74
Figure 3.2: Cross-section of the McKenna burner (Image sourced from Prucker et al. [6]).	75
Figure 3.3: McKenna burner with stabilisation plate at 21 mm above the burner surface.	77
Figure 3.4: $\phi = 1.77$ ethylene-air flame on the McKenna burner. Figure 3.5: $\phi = 2.07$ ethylene-air flame on the McKenna burner.	78
Figure 3.6: 33 mm diameter porous-plug burner with a 38 mm diameter cylindrical stabilisation plate.	79
Figure 3.7: $\phi = 2.07$ ethylene-air flame on the porous-plug burner. Figure 3.8: $\phi = 2.37$ ethylene-air flame on the porous-plug burner.	81
Figure 3.9: Soot horizontal distribution profile across the burner surface at a height of 15 mm in a $\phi = 2.97$ flame (image reproduced from Dunn [1, 12]).	82
Figure 3.10: cw-CRDS set-up diagram: NI DAQ Card (National Instruments Data Acquisition Card), SOA (Semiconductor Optical Amplifier), LDC (Laser Diode Controller), TEC (Thermoelectric Controller).	84
Figure 3.11: cw-CRDS spectra for $\phi = 2.37$ flame recorded at 2 mm above the porous-plug burner surface.	86
Figure 3.12: Fibre-ring resonator.	88
Figure 3.13: Room temperature water absorption signal at 1536.29 nm plotted with a $\delta\nu_{FSR} = 0.4275$ GHz fibre ring resonator output.	89
Figure 3.14: Current-wavelength relationship for the 1535 nm laser at a TEC setting of 14.024 k Ω (image taken from Humphries [1]).	89
Figure 3.15: Relative positions of the optical cavity and mode-matching optics in a Keplerian telescope format.	91
Figure 3.16: Schematic of the cw-CRDS cavity configuration.	92
Figure 3.17: Flow chart for the function of the LabView program.	96
Figure 3.18: A single scan of the cavity transmission.	100

Figure 3.19: Acetylene spectra recorded with frequencies of 1 kHz and 10 Hz in a $\phi = 1.92$ flame at 3 mm above the porous-plug burner surface.....	101
Figure 3.20: CEAS set-up diagram: SOA (Semiconductor Optical Amplifier), LDC (Laser Diode Controller), TEC (Thermoelectric Controller).....	102
Figure 3.21: Ring-down trace from a nitrogen-purged cavity plotted with a fit.	106
Figure 4.1: Acetylene spectrum simulated from HITRAN using the parameters in Table 4.1.....	114
Figure 4.2: Measured acetylene spectrum plotted together with simulated spectra of acetylene (HITRAN) and water vapour (HITEMP) at experimental flame conditions.....	114
Figure 4.3: On-resonance ring-down time spectrum of acetylene and off-resonance ring-down time (normalisation point) with the laser held constant at 115 mA, recorded in a $\phi = 2.37$ flame at 2 mm height above the burner surface.....	116
Figure 4.4: Ring-down time recorded at the normalisation point for different heights above the burner surface in a $\phi = 1.77$ flame.	118
Figure 4.5: Ring-down time recorded at the normalisation point for different heights above the burner surface in a $\phi = 2.37$ flame.	118
Figure 4.6: cw-CRDS spectra for a range of different equivalence ratio flames recorded at 2 mm above the burner surface.	119
Figure 4.7: cw-CRDS spectra for a range of different equivalence ratio flames recorded at 4 mm above the burner surface.	119
Figure 4.8: cw-CRDS spectra for a range of different equivalence ratio flames recorded 7 mm above the burner surface.	120
Figure 4.9: cw-CRDS spectra for a range of different equivalence ratio flames recorded at the height of 2 mm above the burner surface following subtraction of the $\phi = 1.0$ spectrum plotted with an acetylene spectrum simulated from HITRAN.	122
Figure 4.10: Spectral model (HITRAN) fit over a broad range of the extracted $\phi = 2.37$ acetylene spectrum at 2 mm above the burner surface.	124

Figure 4.11: Fit of the spectral model calculated from HITRAN over a broad range of the subtracted $\phi = 2.37$ acetylene spectrum at 2 mm above the burner surface, shown together with the Voigt profiles of the individual acetylene lines.	125
Figure 4.12: Subtracted spectra of P17e acetylene line for a range of different flames at 2 mm above the burner surface, shown with a fit to model spectra calculated from HITRAN.....	126
Figure 4.13: (Upper plot) Recovered concentration profiles of acetylene as a function of height above the burner surface. (Lower plot) Previous OH-LIF temperature measurements in a $\phi = 2.37$ flame.	128
Figure 4.14: Extinction coefficients measured for various equivalence ratio flames at 1 mm increments of height above the burner surface. Error bars show the standard error in 3 measurements.	130
Figure 5.1: 512 averages of a raw CEAS spectrum of acetylene recorded in a $\phi = 2.37$ flame at 4 mm above the burner surface, with an acquisition time of 51.2 s and a scanning frequency of 10 Hz.	137
Figure 5.2: 512 averages of the cavity transmission, I_0 recorded in the absence of a flame in a nitrogen-flushed cavity with a scanning frequency of 10 Hz.....	137
Figure 5.3: 512 averages of the calibrated spectra of acetylene for a range of equivalence ratio flames in the porous-plug burner, recorded at 4 mm above the porous-plug burner surface before shifting the baseline to zero, with an acquisition time of 51.2 s.	138
Figure 5.4: 512 averages of the calibrated spectra of acetylene for a range of equivalence ratio flames in the McKenna burner, recorded at 4 mm above the burner surface before shifting the baseline to zero, with an acquisition time of 51.2 s.....	138
Figure 5.5: CEAS spectra for a range of different equivalence ratio flames recorded at 4 mm above the porous plug burner surface.....	140
Figure 5.6: CEAS spectra for a range of different equivalence ratio flames recorded at 4 mm above the McKenna burner surface.....	140

Figure 5.7: CEAS spectra of acetylene for $\phi = 1.0$ flame recorded at different heights above the McKenna burner surface.....	142
Figure 5.8: CEAS spectra for $\phi = 2.07$ and $\phi = 2.37$ recorded at 5 mm above the McKenna burner surface.....	142
Figure 5.9: CEAS spectra of acetylene for $\phi = 2.37$ flame recorded at different heights above the McKenna burner surface.....	143
Figure 5.10: Flow diagram for the iterative extraction technique.	144
Figure 5.11: Initial estimate of acetylene contribution from the extraction process for $\phi = 2.37$ and 1.77 spectra recorded at 4 mm above the porous-plug burner surface.....	146
Figure 5.12: Final estimate of water-background spectrum from the extraction process for $\phi = 2.37$ and 1.77 spectra both recorded at 4 mm above the porous-plug burner surface.....	147
Figure 5.13: Several estimates of acetylene contribution for the richer ($\phi = 2.37$) spectrum from the iterative extraction process using the $\phi = 1.77$ spectra. Both spectra were recorded at 4 mm above the porous-plug burner surface.	147
Figure 5.14: Extracted acetylene spectra for a range of different equivalence ratio flames recorded 4 mm above the porous-plug burner surface.....	148
Figure 5.15: Comparison of the extracted $\phi = 2.37$ spectra in Figure 5.14 to a model spectrum using parameters from HITRAN at a temperature and pressure of 1600 K and 1 atm respectively.	148
Figure 5.16: Extracted spectra of P17e acetylene line for a range of different flames at 4 mm above the porous-plug burner, shown with a fit to model spectra calculated from HITRAN.....	150
Figure 5.17: (Upper plot) Recovered concentration profiles of acetylene as a function of height above the McKenna and porous-plug burner surfaces. (Lower plot) Previous OH-LIF temperature measurements in the $\phi = 2.37$ flame on the porous-plug burner [5].....	152

Figure 5.18: Acetylene concentration profiles for the porous-plug burner (upper plot) and the McKenna burner (lower plot) calculated using the iterative extraction technique and by subtracting the $\phi = 1.0$ spectrum.	152
Figure 5.19: ABF temperature profile calculated for $\phi = 2.37$ flame.	154
Figure 5.20: ABF calculated temperature profile and scaled temperature profile for $\phi = 2.37$ flame. Inset: scaled temperature profile for $\phi = 2.37$ flame plotted together with OH-LIF temperature measurements in a $\phi = 2.37$ flame.	154
Figure 5.21: ABF concentration profiles of acetylene for $\phi = 2.37$ flame using ABF calculated and scaled temperature profiles.	156
Figure 5.22: Measured and calculated (ABF and USC) concentration of acetylene as a function of height above the burner surface.	156
Figure 5.23: Radial distribution of acetylene concentration for a range of equivalence ratio flames at 3 mm and 4 mm above the porous plug burner surface.	160
Figure 5.24: Radial distribution of acetylene concentration for a range of equivalence ratio flames at 3 mm and 4 mm above the McKenna burner surface.	160
Figure 5.25: Radial distribution of acetylene concentration for a range of equivalence ratio flames at 3 mm above the McKenna burner and porous-plug burner surfaces.	161
Figure 5.26: Fits of the flat distribution model to the radial concentration of acetylene at 3 mm and 4 mm above the McKenna burner surface.	161
Figure 5.27: Fits of the flat distribution model to the radial concentration of acetylene at 3 mm and 4 mm above the porous-plug burner surface.	162
Figure 5.28: Corrected concentration profiles of acetylene as a function of height above the McKenna and porous-plug burner surfaces.	165
Figure 5.29: Corrected profiles and calculated (ABF and USC) profiles of acetylene as a function of height above the burner surface.	166

Figure 5.30: Extinction coefficients measured for various equivalence ratio flames at 1 mm increments of height above the porous plug burner and McKenna burner surfaces.	167
Figure 5.31: Extinction measurements in Figure 5.30 shown on an expanded scale for 1 mm – 6 mm heights above the porous plug burner and McKenna burner surfaces.	167
Figure 5.32: CEAS and cw-CRDS spectra for a range of equivalence ratio flames recorded at 4 mm above the porous plug burner surface.	170
Figure 5.33: (Upper plot) CEAS and cw-CRDS recovered concentration profiles of acetylene as a function of height above the porous plug burner surface. (Lower plot) Previous OH-LIF temperature measurements in the $\phi = 2.37$ flame on the porous-plug burner.	170
Figure 5.34: CEAS spectra recorded for a range of equivalence ratio flames recorded at 1 mm above the porous-plug burner surface.	171
Figure 5.35: Extinction coefficients measured using CEAS and cw-CRDS techniques for various equivalence ratio flames at 1 mm increments of height above the burner surface.	174
Figure 6.1: Broad CEAS spectra for a range of different equivalence ratio flames recorded at 4 mm above the burner surface.	183
Figure 6.2: Broad CEAS spectra for a range of different equivalence ratio flames recorded at 4 mm above the burner surface.	183
Figure 6.3: Broad CEAS spectra for a range of different equivalence ratio flames recorded at 4 mm above the burner surface.	184
Figure 6.4: Broad CEAS spectra for a range of different equivalence ratio flames recorded at 4 mm above the burner surface.	184
Figure 6.5: Broad CEAS spectra for a range of different equivalence ratio flames recorded at 4 mm above the burner surface.	185
Figure 6.6: Broad CEAS spectra for a range of different equivalence ratio flames recorded at 4 mm above the burner surface.	185

Figure 6.7: Broad CEAS spectra for a range of different equivalence ratio flames recorded at 4 mm above the burner surface.	186
Figure 6.8: Broad CEAS spectra for a range of different equivalence ratio flames recorded at 4 mm above the burner surface.	186
Figure 6.9: Broad CEAS spectra for a range of different equivalence ratio flames recorded at 4 mm above the burner surface.	187
Figure 6.10: Broad CEAS spectra for a range of different equivalence ratio flames recorded at 4 mm above the burner surface.	187
Figure 6.11: HITRAN and HITEMP simulations of water vapour, OH and acetylene at 1600 K.	188
Figure 6.12: HITRAN and HITEMP simulations of water vapour, OH and acetylene at 1600 K.	188
Figure 6.13: HITEMP simulations of OH and water vapour spectra at 1600 K.	192
Figure 6.14: Cantera simulations of OH and water mole fractions at expected flame conditions using ABF mechanism.	192
Figure 6.15: Measured OH spectrum plotted with HITEMP simulations of OH and water vapour spectra.	193
Figure 6.16: Measured OH spectrum plotted with HITEMP simulations of OH and water vapour spectra.	193
Figure 6.17: CEAS spectra of OH recorded for a range of equivalence ratio flames at 2 mm above the burner surface.	195
Figure 6.18: CEAS spectra of OH recorded in the stoichiometric flame at different heights above the burner surface.	197

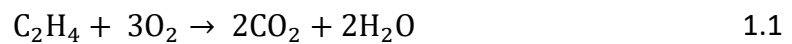
Chapter 1 : Introduction

1.1 Overview of Combustion

Combustion has been referred to as “the oldest technology of mankind” [1]. The combustion of hydrocarbon fuels, which are typically oil and gas, account for the greatest percentage of the world’s energy generation, with the alternatives being nuclear and renewable sources. The combustion of hydrocarbon fuels not only produces energy but results in the emission of substances, some of which pollute and impact the environment negatively. Climate change has been attributed greatly to CO₂ emissions resulting from combustion. It has been estimated that limiting global warming to 15 °C will require the removal of 100-1000 Gt of CO₂ over the 21st century [2]. Following this, policymakers and stakeholders are making effort to reduce atmospheric pollution while increasing combustion efficiency. Part of the effort includes intensifying research on combustion as well as funding research on renewables and other environmentally benign sources of energy [3]. Despite the increasing availability of alternative renewable sources of energy, some outlooks [4-6] have predicted the continued use of oil and gas for energy generation. Beyond energy generation, combustion is also useful in other applications such as transportation, heating, cooking and synthesis of materials like silica which are used in applications involving fibre optics [7]. This means that combustion processes will continue to form part of our everyday life. Therefore, investigative studies on various combustion processes will be very useful in developing efficient combustion devices and fuels, as well as enhance our daily living while reducing the emission of CO₂ and other pollutants [8].

1.2 Societal Challenge

A major motivation for this project stems from the societal challenge posed by combustion. Combustion of fossil fuels ideally should result in the production of CO₂ and H₂O, as shown in Equation 1.1 for the combustion of ethylene. However, in practice, incomplete combustion, and the presence of small amounts of sulphur and nitrogen result in the production of the oxides of carbon (CO_x), sulphur (SO_x) and nitrogen (NO_x) which pollute the environment.



Another product of incomplete combustion is soot which is also called black carbon. Soot has been reported to be carcinogenic as it contains polycyclic aromatic hydrocarbons (PAHs). PAHs have been reported to be carcinogenic and mutagenic and thus responsible for the carcinogenic properties of soot [9, 10]. Following the inhalation of fine soot particles from the atmosphere, these particles are deposited in the lungs, increasing the risk of lung cancer. The inhaled particle deposition rates and transport kinetics have been discussed in detail by M. Kennedy [11] and Darquenne et al. [12]. Other soot related health effects include chronic bronchitis, asthma, and cardiovascular issues. Many studies have correlated soot levels with the rate of occurrence of these health conditions and a summary of these studies have been reported by T. R. Barfknecht [10]. These conditions eventually result in death in some cases. In Asia, an estimated 400,000 deaths have been reported due to soot inhalation from smoke resulting from cooking indoors [13].

Soot also contributes to detrimental climatic effects as it has been recognised as “the second-largest man-made contributor to climate change” [14]. Soot being nearly a perfect black body absorbs radiation from the sun, thereby warming the atmosphere. This results in the melting of snow and glaciers which would naturally reflect some of the light from the sun to space. Soot could also act as a nucleus for the formation of ice and depending on the location of soot in the atmosphere, it could have a cooling

effect on the atmosphere. Ramanathan and Carmichael [13], as well as Bond et al. [14], have all discussed in detail the role of black carbon in climate change.

The effects of other pollutants such as CO₂ and SO₂ on the environment cannot be overemphasized. NO_x has been found to be involved in acid rain, and exposures to NO_x could result in breathing difficulties and other respiratory concerns [15]. Air quality safety standards stipulate maximum levels for these pollutants. However, high levels of pollutants beyond the limits are still being emitted, which violates air quality standards. For instance, an analysis by Friends of the Earth Scotland [16, 17] for NO₂ and particulate matter found NO₂ concentrations for Hope Street in Glasgow as well as some other locations in Scotland to be above the European stipulated limit. Environmental campaigners and ordinary citizens have expressed concerns, urging the government and relevant authorities to be more serious on the issue of pollution [16].

Following the detrimental effect of these pollutants, it is necessary to understand pollutant formation during the combustion process. Combustion in itself is a chemical reaction between a fuel and oxygen usually from air. This fuel-oxygen reaction is usually represented by an overall reaction equation, as shown in Equation 1.1. Information on the concentration of intermediate species during combustion is very important in understanding the various routes of formation of pollutant species. The detailed chemistry of combustion reveals the various pathways through which pollutant molecules such as soot are formed. This knowledge is crucial to the development of strategies aimed at reducing the emission of pollutants during combustion [18]. Basic knowledge of chemistry makes us understand that the concentration of reacting species is one of the factors that affect the rate of production of products in chemical reactions. Therefore, knowledge of the concentration of pollutant precursors is key to understanding the formation of pollutants during combustion.

1.3 Soot Formation

Soot forms following from the incomplete combustion of hydrocarbon-based fuels. The combustion of hydrocarbons is a complex process involving lots of intermediate species and hundreds of chemical reactions. While various chemical routes have been suggested to lead to the formation of PAHs and ultimately soot, these routes are dependent on the type of fuel used [19]. This section does not explore these individual chemical routes in detail as it is not within the scope of this project. This section instead highlights the important species and outlines the process of soot formation, which includes both chemical and physical steps summarized in Figure 1.1.

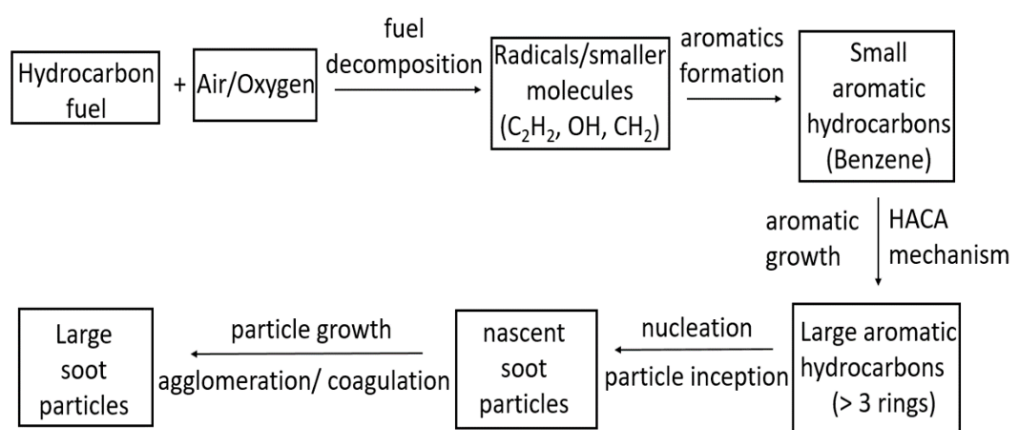
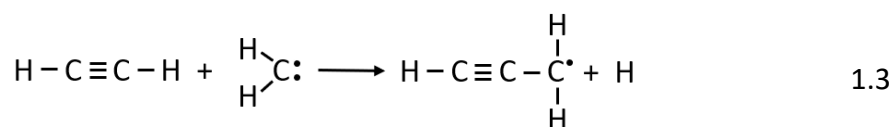
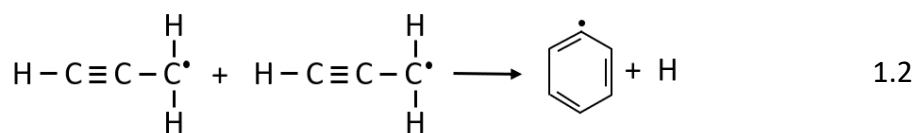


Figure 1.1: Overview of soot formation [20].

During combustion, hydrocarbon fuels are decomposed into radicals such as OH and ¹CH₂. An important specie produced from this decomposition is acetylene (C₂H₂) which plays a major role in soot formation. The radicals and smaller molecules (such as C₂H₂) react to produce larger hydrocarbon radicals and PAHs [21]. These larger radicals and PAH molecules react and together with other phenomena such as coagulation and agglomeration, grow to form soot.



The importance of acetylene comes to play in the formation of the first aromatic ring. This has been thought to happen through various pathways. One widely accepted pathway is through the combination of propargyl (C_3H_3) radicals as shown in Equation 1.2 [22].

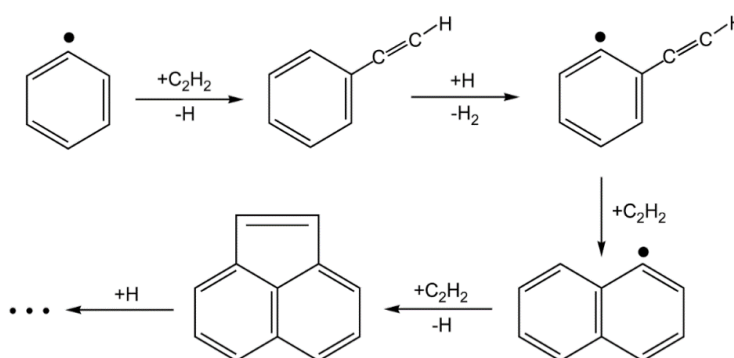


Figure 1.2: HACA mechanism (reproduced from Lu et al. [23]).

Acetylene contributes to the formation of propargyl through its reaction with singlet methylene in Equation 1.3. Also, the growth of PAH has been attributed by Frenklach and Wang [24] to the hydrogen abstraction- C_2H_2 addition (HACA) mechanism, which is shown in Figure 1.2 [23]. In the past two decades, some other pathways beyond HACA mechanism and propargyl recombination have been proposed and studying these pathways are essential for a robust understanding of soot formation process [7].

Through the HACA mechanism, PAH molecules grow from the smallest PAH molecule which is naphthalene (C_{10}H_8) to larger PAH molecules. The molecules grow further by

transiting from gas-phase species to particles in a nucleation step leading to the formation of nascent soot. This nucleation step is also referred to as particle inception and several mechanisms through which this occurs have been suggested [7].

The phase of PAH molecules transiting from gas to particulates during the formation of nascent soot is one of the significant areas of knowledge gap in the study of soot formation. During this phase, some properties of the incipient particles differ from those of mature soot, one of which is the optical properties. Studies in the nascent soot region of a premixed ethylene air flame report a “dark region” where the particles are “quasi-liquid” and “transparent”, and are not capable of fluorescence and incandescence [9, 25]. This presents a challenge of studying nascent soot using optical methods. Alternatively, extractive sampling diagnostic methods have been applied in some studies [9, 26].

Further soot growth to mature soot occurs through surface growth and coagulation. Surface growth reduces with the growth of soot particles [19]. The particles collide with one another, and as the particles age, they agglomerate forming a chain-like structure [19]. This is the eventual soot that is obtained as the by-product from combustion. In summary and as proposed by Lu et al. [23], the major steps involved in soot formation in ethylene flames can be broken down into pyrolysis yielding soot precursors, growth of soot, oxidation and coagulation of soot particles.

1.3.1 Computational Studies of Soot Related Species in Combustion

The process of soot formation is a complex one and not all aspects of the process are fully understood. There is a need for computational tools to make concentration predictions of PAHs and important precursor molecules such as acetylene to help advance knowledge on the process of soot formation. Various kinetic models have been developed previously that predict the concentration of PAH molecules up to 4-5 aromatic rings [27-29]. They include USC [30] and ABF [28] mechanisms which have been used in this project. These mechanisms require software packages such as

CHEMKIN and Cantera to run. CHEMKIN is a proprietary software package while Cantera is an open-source, object-oriented software package, and they are both used for modelling and solving problems involving chemically reacting flows [31].

The model predictions in this project were calculated using Cantera (version 1.7.1) and python (version 2.5) interface. These predictions are compared to the experimental results. The flame is a one-dimensional laminar premixed flat flame that is stabilized on a burner surface. Hence, the computational framework is reduced to a 1-D laminar flame model which is representative of the experimental model. This means that the properties of the flame vary only with height above the burner surface. Flames are governed by conservation equations for mass, energy and species which are given in Equations 1.4 - 1.6 respectively below.

$$\frac{\partial \rho}{\partial t} + \frac{\partial(\rho v)}{\partial z} = 0 \quad 1.4$$

$$\rho v \sum_i w_i \frac{\partial h_i}{\partial z} + \rho \sum_i w_i \frac{\partial h_i}{\partial t} + \sum_i h_i r_i + \sum_i j_i \frac{\partial h_i}{\partial z} + \frac{\partial j_q}{\partial z} = 0 \quad 1.5$$

$$\rho \frac{\partial w_i}{\partial t} + \rho v \frac{\partial w_i}{\partial z} + \frac{\partial j_i}{\partial z} - r_i = 0 \quad 1.6$$

Equation 1.4 is also referred to as the continuity equation. For the above conservation equations, v is velocity, ρ is species density, r_i is the chemical rate of production of species i , Z is the axial coordinate (burner-flame axis), j_q is heat flux, h_i , w_i , and j_i are the enthalpy, mass fraction and diffusion flux of species i respectively [1].

Cantera solves these equations simultaneously using numerical methods. Temperature and species mole fraction are solved for as a function of the vertical distance above the burner surface. The domain of the system is discretised into several units by generating a mesh (grid) with finite number of points, which are numbered from the cold (upstream) boundary to the hot (downstream) boundary. Initial values are specified at the cold boundary to begin the numerical solution, and

diminishing gradients are also specified at the hot boundary. The set-up employed in this work involves the case of a stabilisation plate suspended above the surface of the burner. This presents additional challenges as heat is transferred to the plate. The boundary condition at the plate surface assumes that the convective and diffusive velocities for the gaseous species vanish at the plate surface [32]. A value of about 900 K [33, 34] is inputted for the plate temperature in the computation.

Cantera allows the user to input a predetermined temperature profile and as such it does not solve the energy conservation equation (Equation 1.5). This can be exploited to obtain predictions of species concentration using experimental temperature profiles and then the predictions can be directly compared to experimental results. Often, the validity of predictions from reaction mechanisms are tested by comparing with experimental data. In this work we compare our experimental results to that predicted by the reaction mechanisms. It is important to note that the scope of this work is purely experimental and as such the mechanisms are not altered and the simulations are performed using the values of input parameters that match the experiments. Predictions from mechanisms may also play a role in the analysis of experimental data due to lack of some key data such as temperature or concentration for certain measurement heights and flame conditions. For instance, in an experimental study of OH radical measurements by Peeters et al. [35], the authors assume a temperature value obtained from numerical simulations which they used in their analysis to obtain concentration of OH. Previous temperature measurements in our research group were obtained at certain heights above the burner. This necessitated scaling the temperature profiles predicted by the models based on the experimental temperatures to obtain temperatures for other heights above the burner surface which was then used in analysing our experimental data. Thus, the models were only used in this work to scale temperature values used in analysing our experimental results.

1.4 Diagnostic Techniques for Soot Studies

Many techniques exist and have been used for soot studies. This stems from the complexities surrounding the studies on soot formation. Several intermediate species in a flame are relevant to soot studies and cannot all be quantified using a single technique. These techniques can generally be classified into intrusive and non-intrusive techniques. Some of the common non-intrusive techniques used in combustion studies are highlighted in this section. Cavity-based techniques which are also non-intrusive techniques form the subject of this thesis. The literature on cavity-based techniques is discussed in Chapter 2. Also, the principles of spectroscopy which underly the techniques are discussed.

1.4.1 Intrusive Techniques

Intrusive techniques require that the sample of interest be extracted from the measurement volume by use of probes. The extracted sample is then analysed *ex situ*. The extraction process involves physical insertion of a probe into the flame, and this accounts for the disadvantages that follow intrusive or invasive techniques. This is in addition to the fact that flames naturally present a hostile environment for making measurements.

Inserting a probe into a flame affects the concentration and temperature profiles of the flame [20]. A study by Hansen et al. [36] on probe perturbations show a significant reduction in flame temperature following the insertion of a sampling-probe. The flow field of the flame is also significantly perturbed. Thus, the probe generally disrupts the structure of the flame, making the extracted sample unrepresentative of the flame region of interest. As an object that has just been introduced into the combustion system, the probe introduces a new surface for reaction. Further reactions and catalysis could take place between when the sample is extracted and

analysed. All these would require that the resulting measurements be treated with a degree of caution.

1.4.2 Non-intrusive Techniques

The non-intrusive approach employs optical techniques to make *in situ* measurements. This approach which makes use of lasers as shown in Figure 1.3 eliminates the shortcomings of the intrusive approach as the sample is probed in the desired region of the flame, and the behaviour of the flame could be properly monitored. By so doing, more accurate information on the process is obtained. Optical techniques offer the further advantage of better spatial and temporal resolution, and even more with continuous-wave lasers. Owing to these advantages, the need for more *in situ* techniques has been reviewed by Michelsen [21].

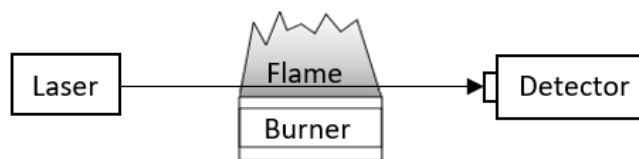


Figure 1.3: Schematic of a simple non-intrusive set-up.

However, flame perturbation by heat transfer from soot particles heated by laser radiation has been reported [37] in a sooting flame showing that some optical techniques are not fully non-intrusive. Also, some complex combustion systems may not allow proper optical access. This is to say that optical techniques are not without shortcomings. Therefore, depending on the priorities and sensitivities of the measurement, non-intrusive techniques could be favourable over intrusive techniques and vice versa. Owing to the delicate nature of combustion systems, many studies have favoured the use of non-intrusive techniques [38].

1.4.3 Direct Absorption Spectroscopy

Direct absorption spectroscopy (DAS) is a simple non-intrusive technique for obtaining spectroscopic information of target species. It is based on the measurement of light attenuation by a sample in line with the Beer-Lambert law. When the light from a laser is sent through a flame as depicted in Figure 1.4, the attenuated light is detected by a photodiode (detector). This simple technique generally suffers from low sensitivity which arises from the fact that a low change in intensity is being measured on a large background. Hence, the detection limit is about 1 part in 10^4 in the very most favourable conditions. Furthermore, DAS is susceptible to measurement instabilities, including the light source and detector instabilities, particle scattering and strong background from flame emission in combustion environments [39, 40]. Some studies employing this technique have had to account for the strong background on the photodiode signal using an extended Beer-Lambert equation [40-42]. Most DAS combustion soot studies employ tuneable diode lasers giving rise to the term tuneable diode laser absorption spectroscopy (TDLAS).

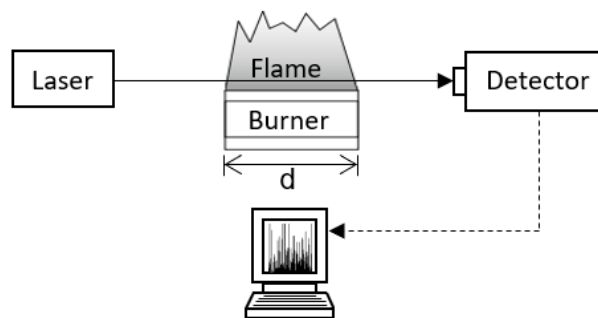


Figure 1.4: Set-up for Direct Absorption Spectroscopy.

1.4.4 Wavelength Modulation Spectroscopy

To increase the sensitivity of some optical techniques for combustion measurements, wavelength modulation spectroscopy (WMS) can be applied in combination. One of

the techniques that has commonly been combined with WMS is TDLAS. This is because of the low sensitivity of TDLAS technique and even lower sensitivity in harsh environments. The combination of WMS with TDLAS improves the sensitivity of DAS by 1-2 orders of magnitude [43-45]. WMS involves modulating the wavelength of a tuneable diode laser sinusoidally while scanning the wavelength across the target transition of the species of interest. This reduces noise and background effects of the measurement as the measured signal is detected at a higher frequency where the laser noise is reduced [43]. The modulation frequency, f_m and higher harmonics (usually $2f_m$) are detected using a lock-in amplifier which gives the WMS signal (Figure 1.5). A variant technique related to wavelength modulation spectroscopy (WMS) is frequency modulation spectroscopy (FMS). The difference between them is in the relationship between the modulation frequency and the half-width at half-maximum (γ) of the absorption line. While $f_m \approx \gamma$ for FMS, $f_m \ll \gamma$ for WMS [46]. Typical modulation frequencies are in the ranges of 10 kHz - 100 kHz and 50 MHz - 150 MHz for WMS and FMS respectively. To reduce noise and background effects, many studies [47-49] have applied WMS in measurements in combustion environments, leading to improved signal-to-noise ratio.

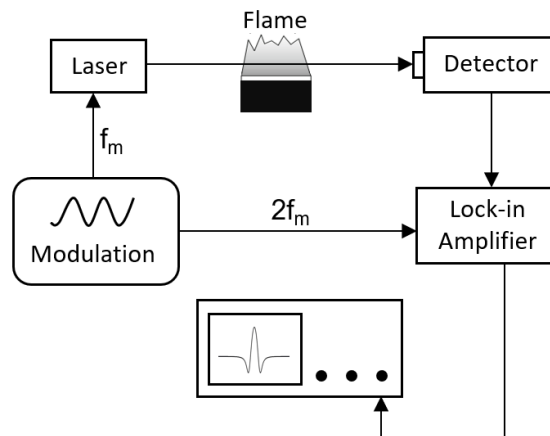


Figure 1.5: Set-up for Wavelength Modulation Spectroscopy.

1.4.5 Laser-Induced Fluorescence

Laser-Induced Fluorescence (LIF) is a non-invasive spectroscopic technique that follows on from the effect of absorption of electromagnetic radiation and hence is classified as an indirect absorption technique. When molecules absorb energy from laser radiation, they are excited to a higher electronic energy level. On relaxation to the ground state, the molecules can emit energy through fluorescence. This forms the detected LIF signal and provides information on the concentration of the fluorescing molecules. As seen in Figure 1.6, following excitation, the molecule first undergoes a non-radiative relaxation to lower ro-vibrational energy levels within the higher electronic [50] energy state which is then followed by fluorescence emission. The energy associated with this emission is typically lower than the energy absorbed by the molecule resulting in a longer wavelength emission (redshift). LIF is a background-free technique and has been widely used in combustion diagnostics for both quantitative and qualitative measurements of a variety of species including OH, CH, CH₂O and PAHs [9, 39, 51-54]. LIF offers an advantage of good spatial resolution and has been employed in imaging and thermometry measurements in flames [9, 55]. The challenges with LIF arise as the fluorescence emission competes with other simultaneously occurring processes such as quenching and pre-dissociation. Converting measured LIF signals to absolute concentration values can, therefore, be challenging as LIF is not ordinarily a self-calibrating technique.

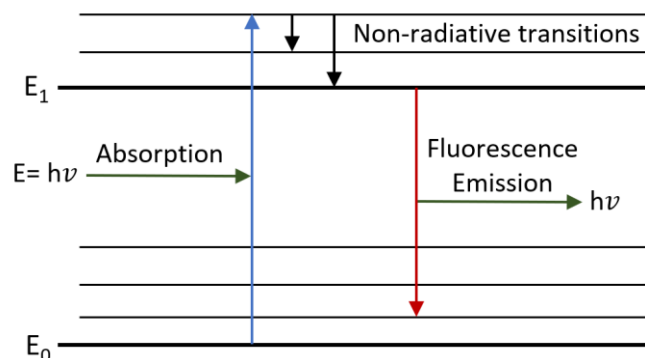


Figure 1.6: Energy level diagram showing fluorescence emission.

1.4.6 Laser-Induced Incandescence

Laser-Induced Incandescence (LII) is a technique well suited to studying particulates such as soot in flames, thus providing quantitative information on soot volume fraction and particle sizes. The standard methodology usually involves the use of a high-power pulsed laser producing very short pulses to heat up soot particles close to their sublimation temperatures of about 3500 K - 4000 K [56]. The heated particles emit light in the visible spectral range with an intensity that is proportional to the particle volume fraction. This emission is obtained as an LII signal using suitable optics. Information on the particle size can be inferred from the time-decay of the LII signal. In heating soot particles to temperatures of about 4000 K, it is important that the particles do not vaporise or decompose. LII is well suited to mature soot particles whose optical properties are fairly well known [21]. Studies involving incipient soot and soot precursors present a greater challenge. A typical LII set-up is shown below.

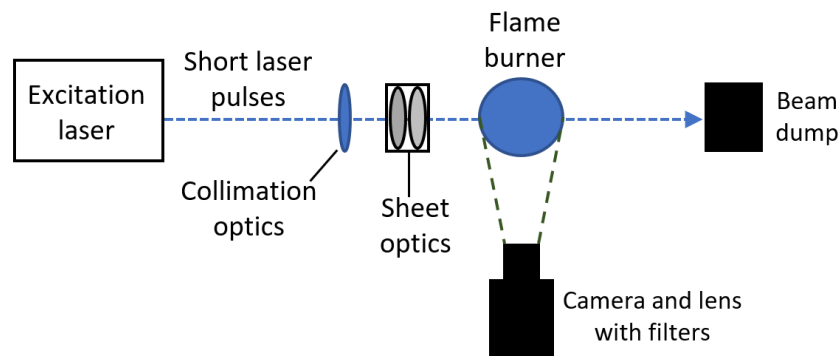


Figure 1.7: LII set-up diagram.

1.4.7 Spontaneous Raman Scattering

Raman spectroscopy is based on the phenomenon of Raman scattering. When light interacts with a molecule, some of the light is scattered in different directions. This results in frequency change in some of the scattered light following the exchange of energy between the photons of the scattered light and the molecule, while the

frequency of some scattered light remains the same as that of the light incident on the molecule. The scattering that results in a frequency change in the scattered light is an inelastic scattering and is referred to as Raman scattering. The frequency change provides chemical information. By contrast, Rayleigh scattering corresponds to the scattering where the frequency of the scattered light (f_i) remains unchanged. This is also referred to as elastic scattering. In Raman spectroscopy, Stokes and anti-Stokes lines shown in Figure 1.8b result when f_i is less than or greater than the frequency of the incident light. The scattered light is usually collected at right angles to the incident light with suitable optics as shown in Figure 1.8a. Several studies have usually combined spontaneous Raman scattering (SRS) with Rayleigh scattering in monitoring flames [57]. SRS is an inherently less sensitive technique. This is because Raman scattering is a very weak phenomenon as only a tiny fraction of the incident light undergoes inelastic scattering upon interaction with the molecule. Also, strong background emission from flames and fluorescence of target species from absorbing laser light could interfere with the signal.

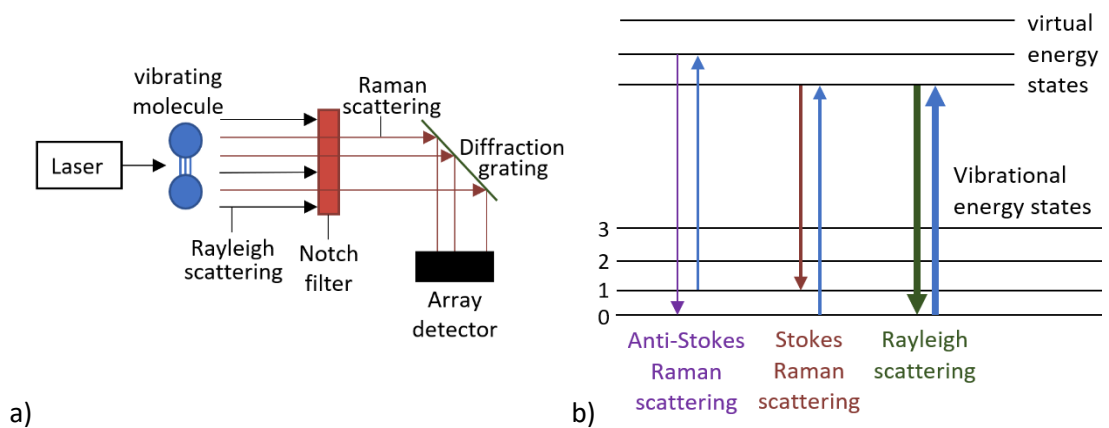


Figure 1.8: a). Schematic of SRS process. b). Energy level diagram depicting various scattering processes.

1.4.8 Coherent Anti-Stokes Raman Spectroscopy

Coherent Anti-Stokes Raman Spectroscopy (CARS) is a non-linear technique that requires the combination of a pump beam, a Stokes beam and a probe beam to generate a coherent CARS signal as shown in Figure 1.9. The pump beam which is usually of a higher frequency than the Stokes beam is combined to phase-match appropriately [58]. The frequency difference between the pump and Stokes beams is coincident with a ro-vibrational Raman active resonance of the species being interrogated. CARS is classified into vibrational CARS and rotational CARS when the frequency difference is coincident with either a vibrational or rotational mode respectively. In recent times, CARS is being improved with the use of picosecond and femtosecond lasers. These extremely short-pulsed lasers are opening up new dimensions to CARS [59]. CARS is mainly used in combustion diagnostics for thermometry in flames as it is limited to species concentration measurements on the order of 0.01 [58, 60]. CARS can be increasingly challenging in sooting flames as the presence of soot can result in light scattering and incandescence, which could interfere with the CARS signal [59, 61]. CARS is an extremely complex technique and even more with the introduction of costly picosecond and femtosecond lasers.

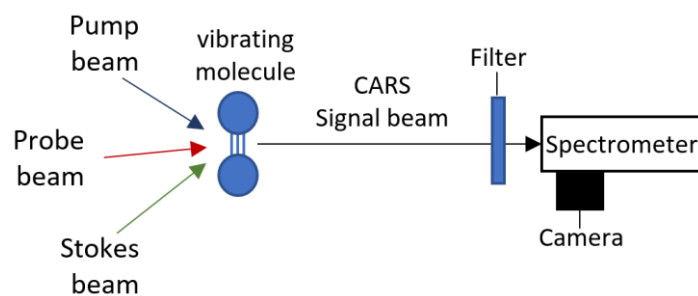


Figure 1.9: Schematic of CARS process.

1.4.9 Polarisation Spectroscopy

Polarisation Spectroscopy (PS) which was first developed by Wieman and Hänsch [62] is another non-linear optical technique. In this technique, a linearly polarised probe beam and a stronger pump beam, which is usually circularly polarised, are crossed in the measurement volume. The weak probe beam is tuned to resonate with a transition of the target species, and the pump beam produces birefringence (optical property of double refraction of light by a material due to the dependence of its refractive index on the polarization and direction of light propagation) in the target species. This causes a change in the polarisation of the probe beam giving rise to the PS signal. The signal is detected using suitable optics including a crossed polariser through which the probe beam is passed. PS is a sensitive technique with good spatial resolution and has been used in the study and detection of species in sooting flames [63, 64]. However, the sensitivity is affected by interference noise and random signal amplitude variations. These arise from the interaction between the generated PS signal and the pump beam, and changes in air density along the optical paths, respectively [65]. Also, PS involves complex set-up and alignment procedures like other non-linear techniques as can be seen in Figure 1.10.

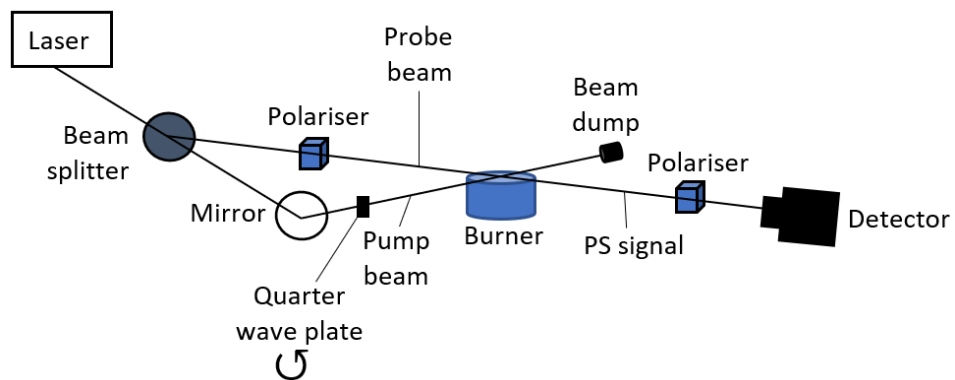


Figure 1.10: Polarisation Spectroscopy set-up diagram.

1.5 Motivation

Following the negative effects of soot on humans and the environment, strategies are being developed to reduce soot emissions from combustion. These strategies require that laboratory studies are performed to understand soot formation and to validate models for application to practical combustors. Also, measurement of important precursors to soot formation such as acetylene is required to better understand its role. It is, therefore, essential to measure acetylene in standard laboratory flames. In a review of *in situ* diagnostic techniques for soot measurement, Michelsen reports on the need for more *in situ* techniques to “enable reliable monitoring of molecular species and particles with high spatial and temporal resolution as well as reduce the disturbances to the combustion process” [21]. Optical diagnostic techniques present insignificant disturbance to combustion processes and are also of high sensitivity.

Over the years, several researchers have obtained measurements of acetylene using a variety of optical techniques, some of which have been discussed previously. Fuest et al. [57] and Mokhov et al. [61] performed Raman measurements of acetylene in laminar flames using high power pulsed lasers and reported detection limits of 3000 ppm at 840 K and 500 ppm at 1750 K respectively. The Raman measurements by Fuest et al. were affected by strong background interference from C_2 emissions and PAHs, as is the general case for rich hydrocarbon flames [66]. Mokhov et al. reports on the low intrinsic sensitivity of the Raman technique which they were able to overcome by using a high repetition rate (1 kHz) laser, and even upgrading to a higher repetition rate (5 kHz) laser in a subsequent measurement [67]. Tuneable diode laser absorption measurements of acetylene in laminar flames were performed by Wagner et al. [41, 42] where they achieved acetylene detection limits of 2.1 ppm and 2.6 ppm. Generally, TDLAS, which is a direct absorption technique, suffers from low sensitivity and even lower sensitivity in sooting flames because of the strong broadband losses. Extending the investigation on LIF detection

of acetylene by Raiche et al. [68], Williams and Fleming [69] obtained relative acetylene concentration in low-pressure methane and propane flames using LIF. Due to the lack of information on the quenching processes following interference from the fluorescence of nitric oxide and oxygen species at the excitation wavelength around 228 nm, the authors could not determine absolute concentration of acetylene.

Non-linear techniques such as CARS and PS have also been used for measurements and detection of acetylene in laminar flames [63, 64, 70, 71]. These non-linear techniques are quite complex to implement as they generally involve cumbersome set-ups requiring more than one laser system. Also, CARS suffers from low sensitivity for species measurements. The CARS measurement of acetylene in sooting ethylene flames by Farrow et al. [70] could not be quantified due to the strong non-resonant background. In a subsequent study [71], a detection limit of 2000 ppm was achieved at 1000 K. The authors report that improving the detection limit would result in reduced spatial resolution and increased measurement time.

Some other combustion studies for the detection of acetylene have rather employed extractive sampling techniques [72, 73]. Miller et al. [72] used a combination of continuous-wave cavity ring-down spectroscopy and extractive sampling for acetylene detection. Gersen et al. [73] obtained measurements of acetylene using direct laser absorption on a flame extracted acetylene sample. Extractive sampling techniques are intrusive and distort the flame's flow field, among other well-known disadvantages such as temperature distortion and catalysing reactions along the sampling path.

These techniques previously used for the measurement of acetylene suffer from common drawbacks of low spatial resolution, background interference, low sensitivity, complex set-up and need for calibration. Hence, there is no widely accepted technique for acetylene measurements in flames. Most of the techniques also required the use of high power pulsed lasers (Nd:YAG lasers) which are large,

bulky and relatively expensive. These lasers contain crystals for frequency doubling to the desired wavelength, typically resulting in pulses with large line-widths. Continuous-wave diode lasers are advantageous over these lasers since they are compact, rugged and inexpensive. They offer better spectral resolution and are therefore suitable for monitoring and acquiring measurements in flames.

Given the drawbacks of previous techniques, there is need for the development of a simple, sensitive and suitable technique for obtaining accurate measurements of acetylene in a flame. This is as accurate concentration measurements of acetylene in sooting flames will be a useful step in proceeding to understand the formation of soot. Various chemical kinetic models exist that predict soot precursors, including acetylene. Using the technique, a rich data-set of acetylene can be generated to validate and improve the various kinetic models. Owing to the advantages of diode lasers, a sensitive technique that employs the use of a diode laser will provide a simple and more sensitive approach for studying sooting flames.

Previous successes in laser diagnostics at Strathclyde have included the use of diode lasers in the first demonstration of continuous-wave cavity ring-down spectroscopy (cw-CRDS), to make combustion measurements *in situ* [74]. Cavity ring-down spectra of acetylene have been recorded in rich ethylene flames, showing the potential of cw-CRDS as a method to measure trace quantities of transient intermediates in such harsh environments. The design included the use of an optical switch and two diode lasers to interrogate the acetylene feature and normalise the measured signal. This set-up has been made simpler with the exclusion of some of these optical components, and the results presented in this thesis show that reliable and reproducible results can be obtained with the simpler set-up. Nevertheless, the first demonstration showed the 'proof of concept' and was used to obtain a limited data-set without repetitions. The demonstration leaves enough scope for further work and shows that opportunities exist with diode lasers. Therefore, this project has gone beyond this previous work by exploring further the application of diode lasers to a

sensitive and simpler technique based on cavity-enhanced absorption spectroscopy (CEAS) for acetylene measurement in sooting flames.

The technique of CEAS in itself is not novel. However, the novelty in this work resides in the application of this technique to *in situ* quantitative measurements of acetylene in a flame. This is as flames present a challenging environment to perform such measurements and the results contribute to enhancing our understanding of soot formation. The technique of cw-CRDS is also not novel and has now been applied for the first time to *in situ* quantitative measurements of acetylene in a flame by Humphries et al. [74]. This work refines the cw-CRDS set-up by Humphries et al. to improve the *in situ* quantitative measurements of acetylene in a flame and obtain more data-set as the work by Humphries et al. did not obtain repetitions of their measurements. The data-set including spectra for the stoichiometric flame were obtained with repeats. Also, extinction measurements (which was not done by Humphries et al.) were performed using the refined set-up. The extinction measurements are essential to account for the broadband optical losses. The refinement simplifies the set-up excluding the use of a second diode laser and an optical switch. Subsequently a comparison of both (CEAS and cw-CRDS) techniques for *in situ* laminar flame measurements was done. The literature and basic principles of the cw-CRDS and CEAS techniques are discussed in the next chapter.

1.6 Thesis Aims and Objectives

The overriding aim of this project is to develop a near infra-red diode laser sensor capable of *in situ* measurements of acetylene in a one-dimensional laminar premixed flame. The sensor is based on cavity-enhanced absorption spectroscopy. This follows on from building on the novel application of cw-CRDS to *in situ* flame measurements and exploring the potentials that exist with diode lasers. Therefore, the specific objectives of this project are:

Firstly, to refine the previous application (by Humphries et al.) of *in situ* quantitative cw-CRDS measurements of acetylene in a flame to obtain a larger data-set including extinction measurements. Secondly, to develop a cavity-enhanced absorption system that is capable of sensitive detection of acetylene in a laminar premixed flame. This CEAS technique will be used to obtain the absorption spectrum of acetylene across a range of sooting laminar flames of premixed ethylene-air and burners. Lastly, to explore the possibility of extending the CEAS system to detect other important flame species such as OH radical.

1.7 Thesis Outline

This chapter introduces the thesis with an overview of combustion, its importance and the societal challenge it presents in pollution. It outlines the process of soot formation and reviews the various optical techniques used in soot studies. The role of acetylene as an important chemical precursor in soot formation is discussed. Therefore, there is a need to measure acetylene. Previous studies on acetylene measurements and detection in flames are highlighted. The techniques used in these studies have been unsatisfactory; hence, the aim of this project.

Chapter 2 introduces some relevant principles of spectroscopy. It goes on to provide the background necessary to deduce concentration information from an absorption spectrum at high temperatures as in a flame environment. The underlying theories of various cavity-based techniques and optical cavities are discussed.

Chapter 3 discusses the methodology of this project. The design and set-up of the cavity ring-down technique and cavity-enhanced absorption technique are discussed. The modes of operation, control and data acquisition are also presented. The McKenna burner and other porous plug burner used as well as the premixed ethylene/air flame in which measurements were made are introduced.

In Chapter 4, *in situ* cw-CRDS spectra of acetylene and final concentration profiles are presented and interpreted. The methodology for analysing the acquired spectra to obtain final concentration is also presented.

In Chapter 5, *in situ* CEAS spectra of acetylene and final concentration profiles are presented. The acetylene concentration profiles are compared to those of cw-CRDS and model calculations. An overall comparison between both techniques is also shown.

Chapter 6 presents the application of the CEAS technique to obtain spectra of OH radical. The spectra of wide scans made over the spectral region of available diode lasers (1535 nm, 1547 nm, 1573 nm) are discussed. The challenges in obtaining quantitative concentration from the spectra of OH obtained are also discussed.

Chapter 7 concludes the thesis, highlighting the major points of this work and providing suggestions for further work.

1.8 References

1. Warnatz, J., U. Maas, and R.W. Dibble, *Combustion*. 4th ed. 2006, Berlin: Springer. 367.
2. Withey, P., C. Johnston, and J. Guo, *Quantifying the global warming potential of carbon dioxide emissions from bioenergy with carbon capture and storage*. *Renewable and Sustainable Energy Reviews*, 2019. **115**: p. 109408.
3. Owusu, P.A. and S. Asumadu-Sarkodie, *A review of renewable energy sources, sustainability issues and climate change mitigation*. *Cogent Engineering*, 2016. **3**(1).
4. Demirbas, A., *Global Renewable Energy Projections*. *Energy Sources, Part B: Economics, Planning, and Policy*, 2009. **4**(2): p. 212-224.
5. R. J. Johnston., R.B., R. Bell, *The role of oil and gas companies in the energy transition*. 2020, Atlantic Council. p. 36.
6. BP, *BP Energy Outlook*, in *BP Energy Economics*. 2018. p. 124.
7. Wang, H., *Formation of nascent soot and other condensed-phase materials in flames*. *Proceedings of the Combustion Institute*, 2011. **33**(1): p. 41-67.

8. Lindstedt, P., *Modeling of the chemical complexities of flames*. Symposium (International) on Combustion, 1998. **27**(1): p. 269-285.
9. R. L. Vander Wal, K. A. Jensen, and M.Y. Choi, *Simultaneous laser-induced emission of soot and polycyclic aromatic hydrocarbons within a gas-jet diffusion flame*. Combustion and Flame, 1997. **109**: p. 399-414.
10. Barfknecht, T.R., *Toxicology of soot*. Progress in Energy and Combustion Science, 1983. **9**(3): p. 199-237.
11. Kennedy, I.M., *The health effects of combustion-generated aerosols*. Proceedings of the Combustion Institute, 2007. **31**(2): p. 2757-2770.
12. Darquenne, C.J., O. Schmid, and G.K. Prisk, *Aerosols And The Human Lung: An Introduction*. 2020: World Scientific.
13. Ramanathan, V. and G. Carmichael, *Global and regional climate changes due to black carbon*. Nature Geoscience, 2008. **1**: p. 221 - 227.
14. Bond, T.C., et al., *Bounding the role of black carbon in the climate system: A scientific assessment*. Journal of Geophysical Research: Atmospheres, 2013. **118**(11): p. 5380-5552.
15. Boningari, T. and P.G. Smirniotis, *Impact of nitrogen oxides on the environment and human health: Mn-based materials for the NOx abatement*. Current Opinion in Chemical Engineering, 2016. **13**: p. 133-141.
16. Stephen, D., *No hope in sight over air pollution*, in *Metro*. 2017, Associated Newspapers Limited: Scotland. p. 8.
17. Thompson, G., *Scotland's most polluted streets*. 2020 [cited 2020 03/06]; Available from: <https://foe.scot/scotlands-most-polluted-streets-2019/>.
18. Humphries, G.S., et al., *A simple photoacoustic method for the in situ study of soot distribution in flames*. Applied Physics B, 2015. **119**(4): p. 709-715.
19. Frenklach, M., *Reaction mechanism of soot formation in flames*. Physical Chemistry Chemical Physics, 2002. **4**: p. 2028-2037.
20. McEnally, C.S., et al., *Studies of aromatic hydrocarbon formation mechanisms in flames: Progress towards closing the fuel gap*. Progress in Energy and Combustion Science, 2006. **32**(3): p. 247-294.
21. Michelsen, H.A., *Probing soot formation, chemical and physical evolution, and oxidation: A review of in situ diagnostic techniques and needs*. Proceedings of the Combustion Institute, 2017. **36**(1): p. 717-735.
22. Frenklach, M., *Reaction mechanism of soot formation in flames*. Physical Chemistry Chemical Physics, 2002. **4**(11): p. 2028-2037.
23. Lu, J., X. Ren, and L. Cao, *Studies on Characteristics and Formation of Soot Nanoparticles in an Ethylene/Air Inverse Diffusion Flame*. Journal of Energy Engineering, 2016. **142**(3): p. 04015041.
24. Frenklach, M. and H. Wang., *Detailed modelling of soot particle nucleation and growth*. Proc. Combust. Inst, 1991. **23**.

25. Dobbins, R.A. and H. Subramaniasivam, *Soot Precursor Particles in Flames*, in *Soot Formation in Combustion: Mechanisms and Models*, H. Bockhorn, Editor. 1994, Springer Berlin Heidelberg: Berlin, Heidelberg. p. 290-301.
26. Köylü, Ü.Ö., et al., *Simultaneous measurements of soot volume fraction and particle size / microstructure in flames using a thermophoretic sampling technique*. *Combustion and Flame*, 1997. **110**(4): p. 494-507.
27. Slavinskaya, N.A. and P. Frank, *A modelling study of aromatic soot precursors formation in laminar methane and ethene flames*. *Combustion and Flame*, 2009. **156**(9): p. 1705-1722.
28. Appel, J., H. Bockhorn, and M. Frenklach, *Kinetic Modeling of Soot Formation with Detailed Chemistry and Physics: Laminar Premixed Flames of C₂ Hydrocarbons*. *Combustion and Flame*, 2000. **121**(122).
29. Wang, H. and A. Laskin, *A Comprehensive Kinetic Model of Ethylene and Acetylene Oxidation at High Temperatures*. 1998: Newark. p. 1-82.
30. Wang, H. and M. Frenklach, *A Detailed Kinetic Modeling Study of Aromatics Formation in Laminar Premixed Acetylene and Ethylene Flames*. *Combustion and Flame*, 1997. **110**: p. 173-221.
31. Goodwin, D.G., *An Open-Source, Extensible Software Suit for CVD Process Simulation*. Proceedings of CVD XVI and EuroCVD Fourteen, Electrochemical Society, 2003: p. 155-162.
32. Abid, A.D., et al., *Quantitative measurement of soot particle size distribution in premixed flames – The burner-stabilized stagnation flame approach*. *Combustion and Flame*, 2009. **156**(10): p. 1862-1870.
33. Carbone, F., K. Gleason, and A. Gomez, *Probing gas-to-particle transition in a moderately sooting atmospheric pressure ethylene/air laminar premixed flame. Part I: gas phase and soot ensemble characterization*. *Combustion and Flame*, 2017. **181**: p. 315-328.
34. Pejpichestakul, W., et al., *Buoyancy effect in sooting laminar premixed ethylene flame*. *Combustion and Flame*, 2019. **205**: p. 135-146.
35. Peeters, R., G. Berden, and G. Meijer, *Near-Infrared Cavity Enhanced Absorption Spectroscopy of Hot Water and OH in an Oven and in Flames*. *Applied Physics B-Lasers and Optics*, 2001. **73**: p. 65-70.
36. Hansen, N., et al., *2D-imaging of sampling-probe perturbations in laminar premixed flames using Kr X-ray fluorescence*. *Combustion and Flame*, 2017. **181**: p. 214-224.
37. Nordström, E., et al., *Local gas heating in sooting flames by heat transfer from laser-heated particles investigated using rotational CARS and LII*. Proceedings of the Combustion Institute, 2015. **35**(3): p. 3707-3713.
38. Eckbreth, A.C., *Laser Diagnostics for Combustion Temperature and Species*. 2nd ed. Combustion Science & Technology. 1996, The Netherlands: Gordon and Breach Publishers.

39. Berden, G. and R. Engeln, *Cavity Ring-Down Spectroscopy: Techniques and Applications*. 2009, West Sussex: John Wiley. p. 313.
40. Schulz, C., et al., *Combustion Diagnostics*, in *Springer Handbook of Experimental Fluid Mechanics*, C. Tropea, A.L. Yarin, and J.F. Foss, Editors. 2007, Springer Berlin Heidelberg: Berlin, Heidelberg. p. 1241-1315.
41. Wagner, S., et al., *In situ TDLAS measurement of absolute acetylene concentration profiles in a non-premixed laminar counter-flow flame*. *Applied Physics B*, 2012. **107**(3): p. 585-589.
42. Wagner, S., et al., *TDLAS-based in situ measurement of absolute acetylene concentrations in laminar 2D diffusion flames*. *Proceedings of the Combustion Institute*, 2009. **32**(1): p. 839-846.
43. Silver, J.A., *Frequency-modulation spectroscopy for trace species detection: theory and comparison among experimental methods*. *Applied Optics*, 1992. **31**(6): p. 707-717.
44. Yang, C., et al., *Wavelength modulation spectroscopy by employing the first harmonic phase angle method*. *Optics Express*, 2019. **27**(9): p. 12137-12146.
45. Du, Y., Z. Peng, and Y. Ding, *Wavelength modulation spectroscopy for recovering absolute absorbance*. *Optics Express*, 2018. **26**(7): p. 9263-9272.
46. Bain, J.R.P., *Near infrared tunable diode laser spectroscopy for aero engine related applications*, in *Dept. of Electronic and Electrical Engineering*. 2012, Thesis [Eng. D] -- University of Strathclyde: Glasgow.
47. Rieker, G.B., J.B. Jeffries, and R.K. Hanson, *Calibration-free wavelength-modulation spectroscopy for measurements of gas temperature and concentration in harsh environments*. *Applied Optics*, 2009. **48**(29): p. 5546-5560.
48. Sun, K., et al., *TDL absorption sensors for gas temperature and concentrations in a high-pressure entrained-flow coal gasifier*. *Proceedings of the Combustion Institute*, 2013. **34**(2): p. 3593-3601.
49. Wright, P., et al. *Progress towards non-intrusive optical measurement of gas turbine exhaust species distributions*. in *2015 IEEE Aerospace Conference*. <https://doi.org/10.1109/AERO.2015.7119019>. 2015.
50. McIlroy, A., *Direct measurement of $^1\text{CH}_2$ in flames by cavity ringdown laser absorption spectroscopy*. *Chemical Physics Letters*, 1998. **296**(1): p. 151-158.
51. Kohse-Höinghaus, K., *Laser techniques for the quantitative detection of reactive intermediates in combustion systems*. *Progress in Energy and Combustion Science*, 1994. **20**(3): p. 203-279.
52. Vander Wal, R.L., *LIF-LII measurements in a turbulent gas-jet flame*. *Experiments in Fluids*, 1997. **23**(4): p. 281-287.
53. Brackmann, C., et al., *Laser-induced fluorescence of formaldehyde in combustion using third harmonic Nd:YAG laser excitation*. *Spectrochimica Acta Part A: Molecular and Biomolecular Spectroscopy*, 2003. **59**(14): p. 3347-3356.

54. Sappey, A.D., D.R. Crosley, and R.A. Copeland, *Laser-induced fluorescence detection of singlet CH₂ in low-pressure methane/oxygen flames*. Applied Physics B, 1990. **50**(6): p. 463-472.
55. Burns, I.S., et al., *A thermometry technique based on atomic lineshapes using diode laser LIF in flames*. Proceedings of the Combustion Institute, 2007. **31**(1): p. 775-782.
56. Olofsson, N.-E., et al., *Soot sublimation studies in a premixed flat flame using laser-induced incandescence (LII) and elastic light scattering (ELS)*. Applied Physics B, 2013. **112**(3): p. 333-342.
57. Fuest, F., et al., *Quantitative acetylene measurements in laminar and turbulent flames using 1D Raman/Rayleigh scattering*. Combustion and Flame, 2015. **162**(5): p. 2248-2255.
58. Eckbreth, A.C. and R.J. Hall, *CARS thermometry in a sooting flame*. Combustion and Flame, 1979. **36**: p. 87-98.
59. Ehn, A., et al., *Advanced Laser-Based Techniques for Gas-Phase Diagnostics in Combustion and Aerospace Engineering*. Applied Spectroscopy, 2017. **71**(3): p. 341-366.
60. Nordström, E., A. Bohlin, and P.-E. Bengtsson, *Pure rotational Coherent anti-Stokes Raman spectroscopy of water vapor and its relevance for combustion diagnostics*. Journal of Raman Spectroscopy, 2013. **44**(10): p. 1322-1325.
61. Mokhov, A.V., S. Gersen, and H.B. Levinsky, *Spontaneous Raman measurements of acetylene in atmospheric-pressure methane/air flames*. Chemical Physics Letters, 2005. **403**(4-6): p. 233-237.
62. Wieman, C. and T.W. Hänsch, *Doppler-Free Laser Polarization Spectroscopy*. Physical Review Letters, 1976. **36**(20): p. 1170-1173.
63. Li, Z.S., et al., *Mid-infrared polarization spectroscopy of C₂H₂: Non-intrusive spatial-resolved measurements of polyatomic hydrocarbon molecules for combustion diagnostics*. Proceedings of the Combustion Institute, 2007. **31**(1): p. 817-824.
64. Sun, Z.W., et al., *Quantitative C₂H₂ measurements in sooty flames using mid-infrared polarization spectroscopy*. Applied Physics B, 2010. **101**(1): p. 423-432.
65. Demtröder, W., *Laser Spectroscopy Vol 2: Experimental Techniques*. Fourth ed. 2008, Berlin: Springer-Verlag.
66. Meier, W. and O. Keck, *Laser Raman scattering in fuel-rich flames: background levels at different excitation wavelengths*. Measurement Science and Technology, 2002. **13**(5): p. 741.
67. Mokhov, A.V., et al., *Experimental and computational study of C₂H₂ and CO in a laminar axisymmetric methane-air diffusion flame*. Proceedings of the Combustion Institute, 2007. **31**(1): p. 997-1004.

68. Raiche, G.A., D.R. Crosley, and R.A. Copeland, *Laser-induced fluorescence and dissociation of acetylene in flames*. AIP Conference Proceedings, 1989. **191**(1): p. 758-760.
69. Williams, B.A. and J.W. Fleming, *Laser-induced fluorescence detection of acetylene in low-pressure propane and methane flames*. Applied Physics B, 2002. **75**(8): p. 883-890.
70. Farrow, R.L., et al., *Coherent anti-Stokes Raman spectroscopic measurements of temperature and acetylene spectra in a sooting diffusion flame: Colloquium on combustion diagnostics*. Symposium (International) on Combustion, 1985. **20**(1): p. 1307-1312.
71. Lucht, R.P., R.L. Farrow, and R.E. Palmer, *Acetylene Measurements in Flames by Coherent Anti-Stokes Raman Scattering*. Combustion Science and Technology, 1986. **45**(5-6): p. 261-274.
72. Miller, J.H., et al., *Measurements of Hydrogen Cyanide and its Chemical Production Rate in a Laminar Methane/Air, Non-Premixed Flame Using cw Cavity Ringdown Spectroscopy*. Proceedings of the Combustion Institute, 2002. **29**: p. 2203-2209.
73. Gersen, S., A.V. Mokhov, and H.B. Levinsky, *Extractive probe/TDLAS measurements of acetylene in atmospheric-pressure fuel-rich premixed methane/air flames*. Combustion and Flame, 2005. **143**(3): p. 333-336.
74. Humphries, G.S., I.S. Burns, and M. Lengden, *Application of Continuous-Wave Cavity Ring-Down Spectroscopy to Laminar Flames*. IEEE Photonics Journal, 2016. **8**(1).

Chapter 2 : Diode Laser Spectroscopy for Combustion Diagnostics

2.1 Introduction

The need for accurate concentration data of species in flames is driving the development of new techniques and modification of existing techniques. *In situ* techniques are preferred in combustion measurements because they provide insignificant or no disturbance to the combustion system. These techniques, some of which have been discussed in the previous chapter, employ optical sensing methods. Continuous improvements in optical diagnostics have influenced methods of obtaining concentration measurements in flames. These diagnostic techniques apply the principles of spectroscopy, and this chapter discusses the details of these principles as they apply to flame measurements.

2.2 Atomic and Molecular Spectroscopy

Spectroscopy describes the interaction of matter with electromagnetic radiation in a way that we can obtain useful information. This can either be by absorption or emission of light. This chapter is focused on the absorption of light as it is the basis for this project. Absorption spectroscopy is based on the Beer-Lambert law shown in Equation 2.1, where I & I_o are the intensities of the transmitted and incident light, respectively, $\alpha(\nu)$ is the sample absorption coefficient, x is the sample mole fraction and d is the path length of the sample.

$$I/I_o = \exp(-\alpha(\nu)xd) \quad 2.1$$

Atoms move across various energy levels when they interact with light. The atoms absorb energy that equals the difference between the energy levels given by ΔE

represented in Equation 2.2 and shown in Figure 2.1, where h is Planck's constant and ν is the frequency of the emitted or absorbed light. This can also be represented in terms of wavenumbers, $\tilde{\nu}$ and speed of light, c .

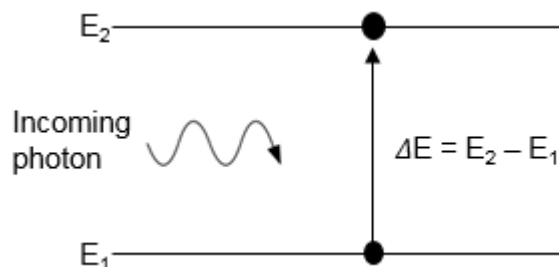


Figure 2.1: Absorption transition in a two-level energy system.

$$\Delta E = (E_2 - E_1) = h\nu = hc\tilde{\nu} \quad 2.2$$

In atomic spectroscopy, the atoms move from one energy level to another following the absorption of radiation. The atomic energy levels (E) are given by solving Schrödinger's wave equation below.

$$\frac{1}{\psi} \left[-\frac{h^2}{2m} \frac{d^2\psi}{dx^2} + V(x)\psi \right] = E \quad 2.3$$

where m is the electron mass, $V(x)$ is the potential, and E is the corresponding energy value for the wave function ψ .

The absorption of electromagnetic radiation by atoms results only in a change in their electronic configuration. However, with respect to molecules, vibrational and rotational movements occur, which makes molecular spectroscopy more complex than atomic spectroscopy. The absorption or emission of light by a molecule results in a change in the internal energy of the molecule. From the Born-Oppenheimer approximation in Equation 2.4, the total energy of a molecule is equal to the sum of its rotational, vibrational and electronic energies. Vibrational transitions are usually accompanied by rotational transitions. Therefore, the total frequency of the transition expressed in Equation 2.5 includes the contribution from the

accompanying rotational transition. Also, electronic transitions are accompanied by rotational and vibrational transitions, and the total frequency includes contributions from the accompanying vibrational and electronic transitions as expressed in Equation 2.6. Molecular spectroscopy defines these transitions as well as the corresponding configurations and associated energies [1].

$$E_{total} = E_{electronic} + E_{vibrational} + E_{rotational} \quad 2.4$$

$$\nu = \nu_v + \nu_r \quad 2.5$$

$$\nu = \nu_e + \nu_v + \nu_r \quad 2.6$$

The frequencies of pure rotational spectra are in the microwave region (wavelengths of 1 mm – 1 m) of the electromagnetic spectrum, which is of less interest in combustion diagnostics due to the high temperatures associated with combustion. In the UV-visible region of the electromagnetic spectrum, transitions usually occur from one electronic level to another. The transitions of interest to this project are those that occur in the infra-red region (700 nm – 1000 μ m) of the electromagnetic spectrum, which are due to molecular vibrations and rotations. The infra-red region is useful to combustion diagnostics as most gaseous species absorb in this region [2].

The distribution of atoms over the various energy levels of a molecule is essential in obtaining species concentration from recorded spectra. This distribution is given by the Boltzmann equation below (Equation 2.7) where N_j is the initial number density of molecules in the probed state j , N is the total number density, k is Boltzmann's constant, g_j is the state degeneracy and T is temperature. The denominator $\sum_i g_i e^{-\epsilon_i/kT}$ is referred to as the partition function, Q which is equal to $Q_{rot} + Q_{vib} + Q_{elec}$. Q_{rot} , Q_{vib} , and Q_{elec} are the partition functions for the rotational, vibrational and electronic energy levels respectively.

$$N_j = N \frac{g_j e^{-\epsilon_j/kT}}{\sum_i g_i e^{-\epsilon_i/kT}} \quad 2.7$$

From the Boltzmann equation, we can tell that temperature determines the population distribution over the electronic, rotational and vibrational states. Eckbreth [1] states that what spectroscopic techniques do is to “measure these population distributions and from them infer the temperature and concentration at the measurement location”.

2.2.1 Vibrational and Rotational Energy Levels

Energy levels are discrete, as dictated by quantum mechanics, and according to the selection rules, transitions do not occur between all energy levels. Although some transitions can occur which do not comply with these rules. These transitions, which are referred to as forbidden transitions, are usually weak, and as such are of less importance in diagnostics [1]. In the infrared region, allowed vibrational and rotational transitions occur following a change in the molecule’s dipole moment. The atoms making up a molecule vibrate and rotate around some mean position. The vibrating atoms in a diatomic molecule can be considered as anharmonic oscillators, and their resultant energy function can be approximated by the Morse function given below:

$$E = D_{eq}(1 - \exp[-a(r - r_{eq})])^2 \quad 2.8$$

D_{eq} represents the bond dissociation energy, a is a molecular constant and r_{eq} represents the bond length. Schrödinger’s equation, when solved with the Morse function gives discrete energy levels with eigenvalues [3]:

$$E_{vibrational} = \left(v + \frac{1}{2}\right)\omega_e - \left(v + \frac{1}{2}\right)^2 \omega_e x_e \quad 2.9$$

where v is the vibrational quantum number, ω_e is the vibration frequency, and x_e is the anharmonicity constant. The selection rules for allowable vibrational transitions are given by:

$$\Delta\nu = \pm 1, \pm 2, \pm 3, \dots \quad 2.10$$

The absorption coefficient for a given transition is proportional to the population in the initial state and is given by the Boltzmann distribution in Equation 2.7. Excitations that result in the fundamental transitions occur between $\nu = 0 \rightarrow \nu = 1$, while the first and second overtones which are weaker transitions occur between $\nu = 0 \rightarrow \nu = 2$ and between $\nu = 0 \rightarrow \nu = 3$ respectively. Transitions originating from $\nu \neq 0$ are usually inconsequential except at high temperatures where the Boltzmann distribution shows an increase in the population of $\nu = 1$ state; hence, they are referred to as “hot lines” [4].

The vibrational states become complex to model as we move from simple diatomic molecules to polyatomic molecules as the number of vibrational modes increases. The number of degrees of vibrational freedom is dependent on the molecular structure and number of atoms present in the molecule. Linear and non-linear molecules possess $3N - 5$ and $3N - 6$ degrees of freedom, respectively. N defines the number of atoms present in the molecule. Typical examples of linear and non-linear molecules are acetylene which is the species of interest in this project, and water respectively. The vibrational modes are characterised as a stretch or a bend and can be symmetrical or asymmetrical. Acetylene ($\text{H} - \text{C} \equiv \text{C} - \text{H}$) being a linear molecule should have seven normal modes; however, there are two degenerate bending modes with the same frequency. The five fundamental modes of acetylene can be seen in Table 2.1. High-temperature water which is also involved in this project has three normal modes, including the symmetric and asymmetric OH stretches shown in Table 2.2. Another relevant species in this project is the diatomic OH molecule which has a single normal mode.

The vibrating molecule simultaneously rotates about a mean axis with about 1000 vibrations per rotational cycle, giving rise to a rotational structure [3]. The slower rotational timescale allows the vibrational and rotational structures to be modelled separately, giving rise to: $E_{total} = E_{vibrational} + E_{rotational}$.

Mode	Description	Degeneracy	Structural Description
ν_1	Symmetric C-H stretch	1	$\overleftarrow{\text{H}} - \text{C} \equiv \text{C} - \overrightarrow{\text{H}}$
ν_2	Symmetric C-C stretch	1	$\overleftarrow{\text{H}} - \text{C} \equiv \overrightarrow{\text{C}} - \text{H}$
ν_3	Asymmetric C-H stretch	1	$\overleftarrow{\text{H}} - \text{C} \equiv \text{C} - \overleftarrow{\text{H}}$
ν_4	Symmetric bend	2	$\uparrow \text{H} - \downarrow \text{C} \equiv \text{C} \uparrow - \text{H} \downarrow$ $\text{H}^+ - \text{C}^- \equiv \text{C}^+ - \text{H}^-$
ν_5	Asymmetric bend	2	$\uparrow \text{H} - \downarrow \text{C} \equiv \text{C} \downarrow - \text{H} \uparrow$ $\text{H}^+ - \text{C}^- \equiv \text{C}^+ - \text{H}^-$

Table 2.1: Fundamental vibrational normal modes of acetylene (+ and -signs represent bending out of and into the page plane, respectively) [3].

$$E_{\text{rotational}} = B_e J(J + 1) \quad 2.11$$

If we consider the rotation of the molecule to be like that of a rigid rotor, then $E_{rotational}$ is given by Equation 2.11 where B_e and J are the rotational constant and rotational quantum number, respectively. B_e is defined below where I is the moment of inertia.

$$B_e = \frac{h^2}{8\pi^2 I} \quad 2.12$$

The selection rule for rotational transitions is $\Delta J = 0, \pm 1$, allowing transitions for $\Delta J = -1, 0, +1$ states which are designated P, Q and R branches respectively. This project probed the P17e acetylene line, precisely. The P17e acetylene line is the number 17 transition of the P-branch ($\Delta J = -1, -2, -3, \dots$) for acetylene spectrum. The 'e' designation refers to the parity of the levels of the transition and is related to a slight splitting of levels due to coupling between the rotational and vibrational angular momenta [5].

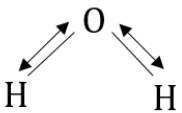
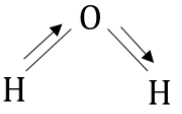
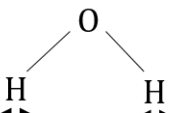
Mode	Description	Degeneracy	Structural Description
ν_1	Symmetric O-H stretch	1	
ν_2	Asymmetric O-H stretch	1	
ν_3	Symmetric bend	1	

Table 2.2: Fundamental vibrational normal modes of water [3].

2.3 Characteristics and Modelling of Absorption Spectral Lines

The absorption of light by a sample results in a spectrum that is characterised by absorption lines. Absorption lines are not infinitely sharp but are characterised by a narrow frequency range with a lineshape function ($\Phi(\nu)$). This is due to the broadening of the spectral line, which is discussed further in this section. The exponential part of the Beer-Lambert equation (Equation 2.1) can be expanded such that [4]:

$$\alpha(\nu)xd = PxdS(T)\Phi(\nu - \nu_0) \quad 2.13$$

where x is the sample mole fraction, P is the total pressure, $S(T)$ is the temperature-dependent line strength, $\Phi(\nu)$ is the absorption lineshape function, $\alpha(\nu)$ is the absorption coefficient and ν_0 is the frequency at the centre of the absorption line. Equation 2.13 gives the absolute transmission function for a single transition. If the value at the centre of the line and the full-width at half-maximum (FWHM) shown in Figure 2.2 is obtained, then properties such as concentration and pressure or temperature can be determined. An effective methodology to employ in extracting these parameters is to fit theoretical models to the experimental signal. A common approach is to perform a least-squares fit of a suitable lineshape function to the absolute transmission function recovered from the spectra. The fits performed in this thesis are based on the Voigt profile, which is appropriate for the conditions obtainable in flame measurements. The basic parameters in the fit are concentration, temperature and pressure. Other parameters are sourced from spectroscopic databases. Some of these parameters may be known while others will be determined from the fitting process. Fewer unknown parameters in the fit will result in a more accurate and faster fitting process.

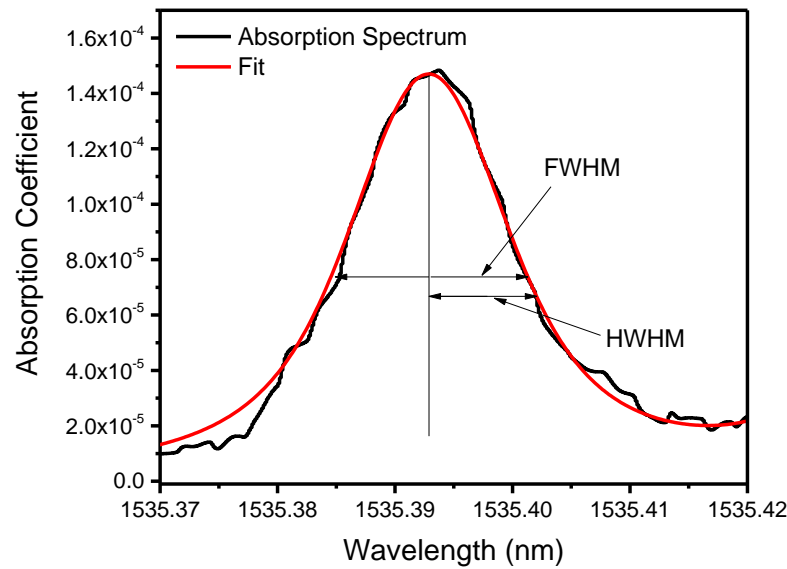


Figure 2.2: A least squares fit of a Voigt line shape to an absorption spectrum.

2.3.1 Absorption Line Strength

The intensity of an absorption transition depends on the transition probability, the fractional population of the originating transition state, the concentration of the absorbing species and the path length [3]. The transition probability, usually given by the Einstein coefficient A , is the probability that a given transition will absorb an incident photon. The transition probability between two energy levels is determined from the solutions of the quantum mechanical wave functions between the two levels. This is quite complex and can hardly be done accurately and is outside the scope of this thesis. Also, there are selection rules that define forbidden and allowed transitions which have been discussed earlier.

Given an upper energy level, 2 and a lower energy level, 1, the Einstein coefficients A_{21} , B_{12} and B_{21} are used to describe spontaneous emission, stimulated absorption and stimulated emission transitions respectively between the energy levels [6]. The relationship between the Einstein A and B coefficients is given by Equations 2.14 and

2.15 below [7], where g is the degeneracy of the energy level, h is Planck's constant and ν is transition frequency.

$$g_1 B_{12} = g_2 B_{21} \quad 2.14$$

$$A_{21} = 8\pi h \nu^3 B_{21} \quad 2.15$$

The absorption coefficient, α is related to B_{12} using the equation below, where N_1 is the number density of molecules in level 1. Thus, the relationship between α and the line strength, S of a transition follows as given in Equation 2.17, where $Q(T)$ is the partition function, k is Boltzmann constant, T is temperature, c is speed of light and I_a is the isotopic abundance (given in percentage) [7].

$$\alpha(\nu) = \frac{N_1 B_{12} \Phi(\nu)}{4\pi} h \quad 2.16$$

$$S = \frac{I_a A_{21}}{8\pi c \nu^2} \frac{g_2 e^{-\frac{hcE_1}{kT}} (1 - e^{-\frac{hc\nu}{kT}})}{Q(T)} \quad 2.17$$

If we consider two energy levels with equal probabilities of transition, A , to the same higher level, the level with the initial higher population will exhibit stronger spectral intensity; hence, stronger absorption. The relative population distribution among the different energy levels follows Boltzmann distribution. Consider two energy levels (a lower level and an upper level) with a population density N , at equilibrium, Boltzmann distribution shows that:

$$\frac{N_{upper}}{N_{lower}} = \exp(-\Delta E/kT) \quad 2.18$$

where $\Delta E = E_{upper} - E_{lower}$, T is temperature and is k Boltzmann constant.

Recall Equation 2.1, which shows the relationship between the transmitted intensity and the product of concentration and path-length. Absorption will increase with an

increase in the number of molecules for interaction along the path-length. Thus, Equation 2.1 can be rewritten as follows for a sample with unit number density in the ground state, 1 where $\sigma(\nu)$ is the absorption cross section:

$$\ln \frac{I}{I_0} = \alpha(\nu)xd = N_1\sigma(\nu)d \quad 2.19$$

2.3.2 Broadening of Absorption Spectral Lines

The absorption line is affected by line broadening effects which include the Doppler broadening effect, pressure broadening effect and natural broadening effect. They influence the measurements and spectra interpretation and as such are very important in spectroscopic measurements. This is because absorption lines are characterised by the line shape function $\Phi(\nu)$ shown in Equation 2.13 for absorption measurements.

2.3.2.1 Doppler Broadening

The Doppler broadening effect is due to the thermal motion of the absorbing molecules according to the molecular velocity distribution. This molecular velocity distribution is given by Maxwell-Boltzmann function for a given temperature. Therefore, where Doppler broadening is dominant, it is possible to determine the temperature from the width of the absorption line. This is usually obtainable at very low pressure. Monochromatic light can solely interact with specific molecular velocities, particularly those in the direction parallel to the incident beam, and this velocity component is characterised by a Gaussian distribution.

The Gaussian lineshape function is defined such that its integral over all frequencies equals one. The mathematical expression for the normalised Gaussian lineshape function, $\Phi_G(\nu)$ is given by [1]:

$$\Phi_G(\nu) = \frac{2}{\Gamma_G} \sqrt{\frac{\ln 2}{\pi}} \exp \left[-4 \ln 2 \left(\frac{\nu - \nu_0}{\Gamma_G} \right)^2 \right] \quad 2.20$$

where ν_0 is the line centre frequency and Γ_G is the FWHM of the Gaussian profile. Γ_G is determined using:

$$\Gamma_G = \nu_0 \sqrt{\frac{8kT \ln 2}{mc}} \quad 2.21$$

This can also be presented concisely as:

$$\Gamma_G = 7.162 \times 10^{-7} \nu_0 \sqrt{\frac{T}{m}} \quad 2.22$$

where c is the speed of light, m is the molecular weight of the absorbing species, T is temperature, and k is Boltzmann constant. The Γ_G for acetylene at 1535.39 nm is calculated as 0.036 cm^{-1} for a temperature of 1600 K. The relationship between the peak and the FWHM of the Gaussian profile is given by:

$$\Phi_G(\nu_0) = \frac{2}{\Gamma_G} \sqrt{\frac{\ln 2}{\pi}} \quad 2.23$$

The Doppler width (FWHM) at low pressures is dependent only on temperature for any given species and as such increases with increasing temperature enabling the determination of temperature according to Equation 2.22.

2.3.2.2 Natural and Pressure Broadening

Pressure broadening results from the collisional interaction of absorbing molecules as molecules are always in random motion. Hence, it is also referred to as collisional broadening. It is associated with a Lorentzian lineshape. Natural broadening is due to the finite lifetime of molecules in a particular energy level, also resulting in a

Lorentzian lineshape. Figure 2.3 shows a comparison between the Lorentzian and Gaussian lineshapes with the same FWHM. For a given FWHM, the wings of the Lorentzian lineshape are spread over a wider frequency range while the Gaussian lineshape has a larger peak height.

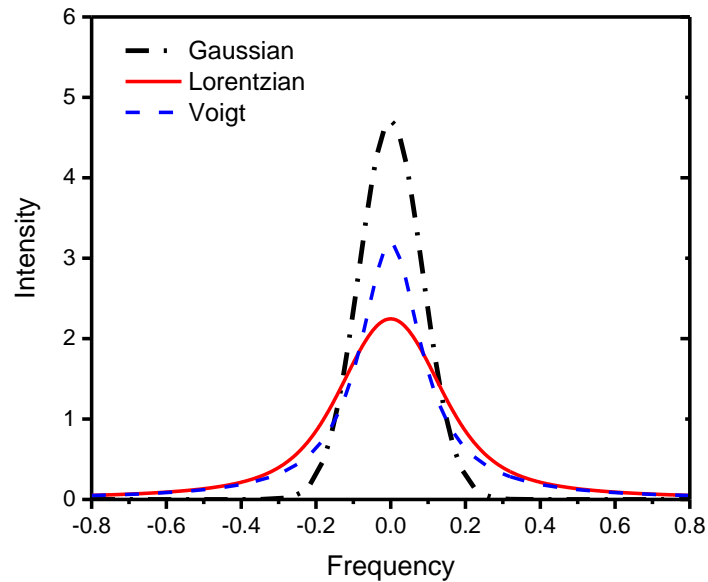


Figure 2.3: Comparison of Gaussian, Lorentzian and Voigt lineshapes with the same FWHM.

The Lorentzian profile is used to model natural and pressure broadened lineshapes. Just like the Gaussian lineshape function, the Lorentzian lineshape function (Φ_L) is defined such that $\int_{-\infty}^{\infty} \Phi_L(\Delta\nu) d\nu = 1$. The mathematical expression for Φ_L is given by [8]:

$$\Phi_L = \frac{1}{\pi} \frac{\Gamma_L/2}{(\nu - \nu_0)^2 + (\Gamma_L/2)^2} \quad 2.24$$

where the Lorentzian FWHM (Γ_L) which also represents the collisional width for any given component, say j is:

$$\Gamma_L = P \sum_j (x_j \Gamma_j) \quad 2.25$$

where x_j is the mole fraction of component j . The dependence of the collisional broadening coefficient Γ_j due to component j on temperature is expressed thus:

$$\Gamma_j(T) = \Gamma_j(T_0) \left(\frac{T_0}{T} \right)^{n_j} \quad 2.26$$

where T_0 is the reference temperature for which Γ_j is provided and n_j is the temperature dependence coefficient (usually assigned a value of 0.75 for acetylene [9]). The half-width at half-maximum (HWHM) γ_j , which is given by $\Gamma_j/2$, can be used in place of Γ_j . The peak height of the Lorentzian profile is expressed as:

$$\Phi_L(\nu_0) = \frac{2}{\Gamma_j \pi} \quad 2.27$$

The collisional broadening parameters for air and component species which contribute to Γ_L are provided in HITRAN at 298 K. The parameters have to be extrapolated to higher temperatures that are characteristic of combustion and as such, Γ_L is subject to some uncertainty.

2.3.2.3 The Voigt Lineshape Function

At conditions where neither Doppler nor pressure broadening is dominant, the Voigt lineshape function, which combines the contributions of Doppler and pressure broadening is employed to model the lineshape. The Voigt lineshape function (Φ_V) is expressed mathematically as:

$$\Phi_V = \int_{-\infty}^{\infty} \Phi_G(\nu') \Phi_L(\nu - \nu') d\nu' \quad 2.28$$

Φ_G and Φ_L represent the respective Gaussian and Lorentzian contributions to Φ_V . Several numerical approximations to the Voigt function exist as there is no simple analytical solution to Equation 2.28 [10, 11]. This project employs McLean's numerical approximation of the Voigt function, which is [12]:

$$\Phi_V = \frac{2\sqrt{\ln 2}}{\Gamma_G \sqrt{\pi}} V(X, Y) \quad 2.29$$

where:

$$V(X, Y) = \sum_{i=1}^4 \frac{C_i(Y - A_i) + D_i(X - B_i)}{(Y - A_i)^2 + (X - B_i)^2} \quad 2.30$$

X and Y are given below as:

$$X = \frac{2\sqrt{\ln 2}}{\Gamma_G} (\nu - \nu_0) \quad \text{and} \quad Y = \frac{\Gamma_L \sqrt{\ln 2}}{\Gamma_G} \quad 2.31$$

i	A_i	B_i	C_i	D_i
1	-1.215	1.2359	-0.3085	0.021
2	-1.3509	0.3786	0.5906	-1.1858
3	-1.215	-1.2359	-0.3085	-0.021
4	-1.3509	-0.3786	0.5906	1.1858

Table 2.3: Coefficients for McLean's numerical approximation.

The coefficients A_i , B_i , C_i , and D_i are presented in Table 2.3. An estimation of the FWHM of the Voigt profile by Olivero and Longbothum is expressed as [11]:

$$\Gamma_V = 0.5346\Gamma_L + \sqrt{0.2166\Gamma_L^2 + \Gamma_G^2} \quad 2.32$$

2.3.3 HITRAN and HITEMP Spectroscopic Databases

HITRAN (high-resolution transmission molecular absorption database) [13] and HITEMP (high-temperature molecular spectroscopic database) [14] are spectroscopic databases that provide spectroscopic parameters for several molecules. Some of these parameters, which include line strength, self and air broadening parameters, have been obtained and applied in calculating final concentration values in this thesis. A list of some important HITRAN parameters can be found in Table 2.4.

Parameter	Description
ν	Vacuum wave number [cm^{-1}]
S	Line strength (at 296 K) [$\text{cm}^{-1}/\text{molecule}\cdot\text{cm}^{-2}$]
A	Einstein A coefficient [s^{-1}]
Γ_{air}	Air-broadened FWHM (at 296 K) [$\text{cm}^{-1}/\text{atm}$]
Γ_{self}	Self-broadened FWHM (at 296 K) [$\text{cm}^{-1}/\text{atm}$]
E''	Energy of lower state [cm^{-1}]
n_{air}	Temperature-dependent coefficient
δ_{air}	Air pressure shift [$\text{cm}^{-1}/\text{atm}$]
g'	Degeneracy of higher energy state
g''	Degeneracy of lower energy state

Table 2.4: Spectroscopic parameters from HITRAN database [13, 15].

HITRAN contains information for transitions whose ground states have appreciable population at ambient temperature. The spectroscopic information required for flame measurements involves transitions that occur at high temperatures. Following

this insufficiency in the HITRAN database, HITEMP was established. HITEMP is an analogous database that contains information at elevated temperatures. These databases are useful for extracting concentration information from combustion measurements. In selecting a suitable spectral region for measurements, it is vital to carry out a diligent survey of the region and the relevant spectroscopic parameters to avoid interference from other species that may be present in the measurement volume. A major interfering species in combustion measurements is high-temperature water vapour which is known to have many absorption lines in the near-infrared (NIR) region. The predictions, especially of high-temperature water vapour absorption by these databases are not entirely accurate. However, they provide useful information on what to expect.

2.4 Determination of Concentration from Absorption Spectra

The primary objective of measurements in this project is to determine the concentration of species from measured absorption spectra. Following the Beer-Lambert law, the relationship between the absorption coefficient, α and concentration, C is given by Equation 2.33.

$$C = \frac{\alpha}{PS(T)d} \quad 2.33$$

The temperature-dependent line strength $S(T)$ in Equation 2.33 is defined below. Temperature is essential for calculating concentration and previous temperature measurements used in calculation concentration in this work are discussed later in this thesis.

$$S(T) = S(T_0) \frac{Q(T_0)}{Q(T)} \left(\frac{T_0}{T}\right) \exp\left[-\frac{hcE''}{k} \left(\frac{1}{T} - \frac{1}{T_0}\right)\right] x \left[1 - \exp\left(\frac{hcv_0}{kT}\right)\right] \left[1 - \exp\left(\frac{hcv_0}{kT_0}\right)\right]^{-1} \quad 2.34$$

In the above equation, T_0 is the HITRAN reference temperature of 296 K, $Q(T)$ is the molecular partition function defined in Equation 2.35, E'' is the energy of the

transition lower state which is obtained from HITRAN. For a given species in HITRAN, the coefficients (a, b, c, d) of $Q(T)$ are provided for a range of temperatures (70 K to 3000 K for acetylene).

$$Q(T) = a + bT + cT^2 + dT^3 \quad 2.35$$

The spectroscopic databases (HITRAN/HITEMP) present the values of the line strength S in $[\text{cm}^{-1}/(\text{molecule}\cdot\text{cm}^2)]$ units. Most applications such as Equation 2.13 use convenient units of $\text{cm}^{-2}/\text{atm}$ where the line strength in cm^{-2} units is normalised by pressure in atm [16]. It is, therefore, necessary to convert to units that are convenient to work with practically. The conversion follows the equation below [15]:

$$S[\text{cm}^{-2}\text{atm}^{-1}] = \frac{S[\text{cm}^{-1}/(\text{molecule}\cdot\text{cm}^2)]n_i[\text{molecule}\cdot\text{cm}^{-3}]}{P_i[\text{atm}]} \quad 2.36$$

The above equation can be simplified to recover S as a function of temperature. This is done by applying the ideal gas law to yield Equation 2.37.

$$S[\text{cm}^{-2}\text{atm}^{-1}] = \frac{7.339 \times 10^{21} [\text{molecule}\cdot\text{cm}^{-3}\text{K}] S[\text{cm}^{-1}/(\text{molecule}\cdot\text{cm}^2)]}{T[\text{K}]} \quad 2.37$$

The final transmission is given by Equation 2.38, which is a Voigt profile for a single transition line.

$$\frac{I}{I_0} = \exp \left[PCd\Gamma_G S(T) \sqrt{\frac{\ln 2}{\pi}} V(X, Y) \right] \quad 2.38$$

The absorption spectra resulting from most combustion measurements includes contributions from some close absorption lines. This is because a number of species have overlapping absorption lines at elevated temperatures and as such absorption by other species usually occurs on the wings of the absorption profile. It is important

to account for these lines by calculating and including them in the final transmission profile. An existing algorithm in Matlab previously used [15, 16] for simulating this process was adapted for use in this project. The algorithm uses an unconstrained non-linear fitting process to fit the final transmission in Equation 2.38 to the measured data based on the least-squared fitting function. Where temperature and pressure information is available, the final transmission function is calculated until the least-squares error is obtained between the fit and the measured data. The iteration is usually executed using the *fminsearch* function in Matlab.

2.5 Theory of Optical Cavities

To properly understand the operation of cavity-based techniques, it is necessary to describe the principles of optical cavities. Resonant optical cavities consist of highly reflective mirrors in a configuration that supports a standing wave. The most straightforward setup is a linear cavity comprised of two mirrors facing each other. The cw-CRDS and CEAS set-ups used in this work consist of a linear cavity, so the narrative in this section will be limited to linear cavities.

2.5.1 Fundamentals of Optical Cavities

The Fabry-Perot interferometer shown in Figure 2.4 exemplifies a simple linear optical resonator made up of two plane-parallel mirrors spaced at a suitable distance. The fundamental properties of optical cavities can be based on the theory of the Fabry-Perot interferometer. With the mirrors properly aligned, they reflect light multiple times causing constructive interference to occur within the cavity. The incoming light wave overlaps the light wave reflected from the second cavity mirror, and this is also referred to as resonance. Resonance builds the intensity of the light within the cavity.

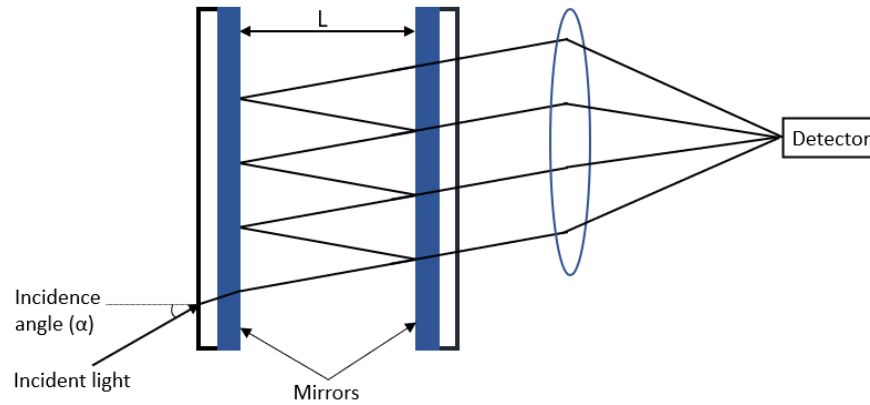


Figure 2.4: Schematic of a Fabry-Perot Interferometer.

The length of the cavity and the wavelength of the light determine the condition of constructive interference shown in Figure 2.5. The condition of constructive interference corresponds to the longitudinal modes of the cavity. The length of the cavity has to be equal to an integer number of half-wavelengths, $n\lambda/2$ as this will cause the waves to peak at the same point in the cavity [17, 18]. The longitudinal mode are the frequencies that are preferred to circulate in the cavity [19]. The resonance condition can be described mathematically as [20]:

$$L_c = q \left(\frac{\lambda}{2n} \right) \quad 2.39$$

L_c the distance between the mirrors, n is the refractive index of the intra-cavity medium, q is an integer describing the mode number, λ is the wavelength of the incident light.

Following the above condition, the frequencies of the longitudinal modes are separated by a constant frequency spacing called the free spectral range ($\delta\nu_{FSR}$) given by:

$$\delta\nu_{FSR} = c/2nL_c \quad 2.40$$

where c is the speed of light in the cavity.

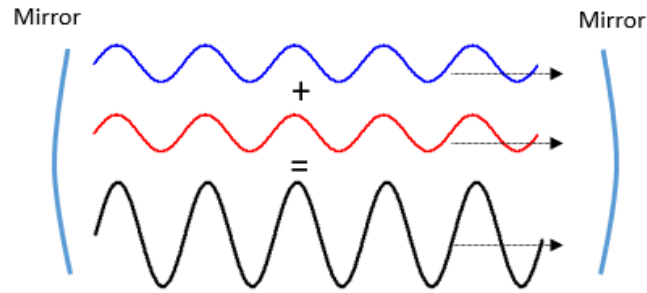


Figure 2.5: Constructive interference resulting from two waves propagating in a cavity.

For the purpose of continuous-wave cavity ring-down spectroscopy, and for some other purposes, one of the cavity mirrors is usually held on a piezoelectric mount. This allows slight variation of the cavity length resulting in a transmission function shown in Figure 2.6. Either this or the laser is scanned with the cavity length kept constant to obtain the cavity transmission function. The shape of the cavity transmission function is related to the ‘finesse’ of the cavity. Finesse refers to the extent which the cavity can sustain resonance over its effective path-length following a variation in the cavity length or frequency of the incident light wave [17]. The finesse of a cavity is dependent on the losses in the cavity, hence the reflectivity of the mirrors (R), and is represented mathematically as [17]:

$$\mathcal{F} = \frac{\pi\sqrt{R}}{1-R} \quad 2.41$$

The longitudinal modes which possess a Lorentzian shape have a FWHM also referred to as the cavity bandwidth given by:

$$\delta\nu_{FWHM} = \frac{\delta\nu_{FSR}}{\mathcal{F}} \quad 2.42$$

In the absence of an absorbing sample, optical cavities experience losses as the cavity and the mirrors will scatter and absorb some of the incident light. The linewidth of the laser may also exceed the width of the cavity transmission mode, which is

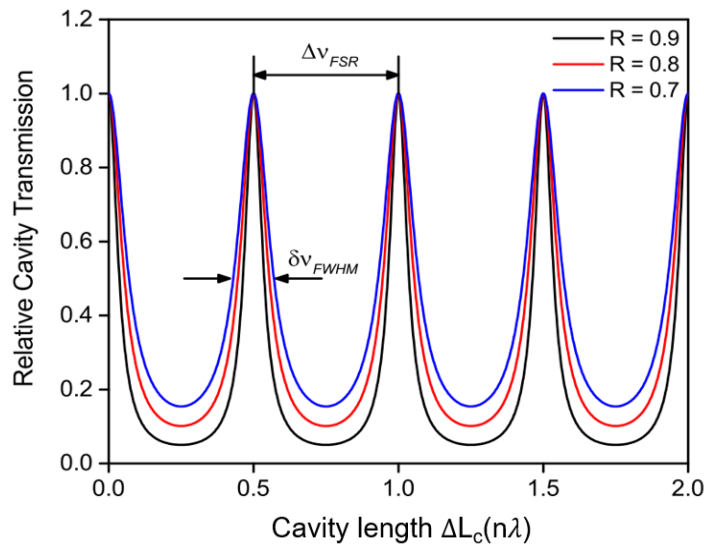


Figure 2.6: Ideal transmission function of a linear cavity for varying mirror reflectivity (image sourced from Humphries [16]).

generally the case for a high-finesse cavity and DFB lasers of the type used in this thesis. The remaining portion of the light is transmitted and reflected. The losses resulting from reduced mirror reflectivity lead to broadening of the cavity longitudinal modes, as seen in Figure 2.6. The term effective reflectivity is introduced to include all losses in the cavity and not only losses due to the mirrors alone. Increasing the reflectivity of the cavity will result in transmission of less light through the mirrors. Less transmission would mean more intensity of light circulating in the cavity. Usually mirrors with reflectivity far greater than 99.9% are used in constructing optical cavities for cavity-enhanced techniques [21]. This leads to an enhanced path-length and consequently, better sensitivity. However, the resulting cavity transmission will have an FWHM that is significantly narrower than the linewidth of few MHz for lasers commonly used in these techniques. Consequently, only a small proportion of the incident light will resonate with the modes of the cavity.

The cavity is also characterised by transverse modes which describe the transverse profile of beams within the cavity. The relationship between the transverse modes

and longitudinal modes is such that the geometry of the cavity and the number of transverse modes define the longitudinal mode structure. An increase in the number of transverse modes that are excited will reduce the FSR as the density of the longitudinal modes will increase.

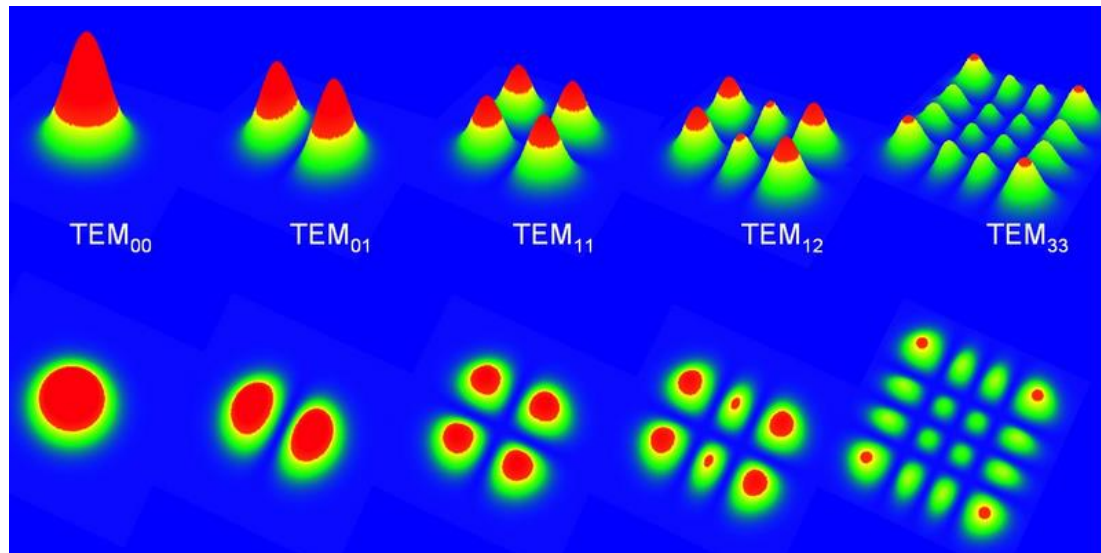


Figure 2.7: 3-D representation of the spatial intensity profile of transverse electromagnetic modes (image sourced from OPI online courses [22]).

Transverse modes represent the energy distribution across the beam axis in the cavity [17]. They are designated TEM_{mn} modes with the fundamental transverse mode of a stable optical cavity designated the TEM_{00} mode. This fundamental mode has a Gaussian intensity distribution. The subscripts m and n are integers representing the number of radial and angular nodes, respectively [17, 23]. Figure 2.7 shows the transverse intensity distribution of the fundamental transverse mode and higher-order transverse modes. As can be seen in the figure, increasing higher-order modes have wider spatial distribution compared to the TEM_{00} mode. This means that the beam impinges on a larger area of the mirror surface for the higher-order modes.

Several higher-order modes resonate at the same frequency leading to individual decay rates for each mode, and this is generally referred to as transverse mode

degeneracy [23]. The degeneracy of higher-order modes can result in a multi-exponential decay function output from the cavity; as such, it is preferable to obtain the cavity decay rate from the fundamental cavity mode [24]. For a technique that involves measuring the transmitted intensity from several higher-order modes of the cavity, the sensitivity would be limited by the degeneracy of the modes.

2.5.2 Stability of Optical Cavities

The stability of an optical cavity refers to the ability of the cavity to support resonating modes with low losses, mostly due to diffraction [25]. The incident and reflected light have to be spatially contained within the cavity volume. The stability of optical cavities largely depends on the radius of curvature of the mirrors and the length of the cavity. Usually, curved mirrors are employed in constructing optical cavities for cavity-enhanced techniques. The use of planar mirrors requires much care in aligning such cavities as even slight deviation from the normal alignment can result in light straying out of the cavity. It is also difficult in practice to achieve a very high finesse with planar mirrors because the mirror surfaces are not perfectly smooth.

Given an optical cavity with bi-concave mirrors, the condition for light to be confined within the cavity is such that $0 \leq \left[1 - \frac{L_c}{R_1}\right] \left[1 - \frac{L_c}{R_2}\right] \leq 1$, where R_1 and R_2 are the radii of curvature of the mirrors. The radius of curvature (ROC) is an important property of the mirrors which could ensure that the beam remains confined within the cavity. The propagation of light in the cavity using the curved mirrors results in a beam which can be modelled using the Gaussian profile [26-28]. The cavity configuration in Figure 2.8 (where the curved path is due to diffraction and grey lines are the wavefronts) represents the simple and typical configuration used for cavity-enhanced set-ups, where ω_0 is the beam waist, M_1 and M_2 are the mirrors, L_c is the cavity length and z is the beam axis. The Rayleigh range is defined as the distance along the beam propagation from the beam waist $\omega_0(z = 0)$ to the point where ω_0 increases by a

factor of 1.414, because at this point the cross-sectional area of the beam doubles. The Rayleigh range is defined mathematically as [29]:

$$z_R = \frac{\pi\omega_0^2}{\lambda} \quad 2.43$$

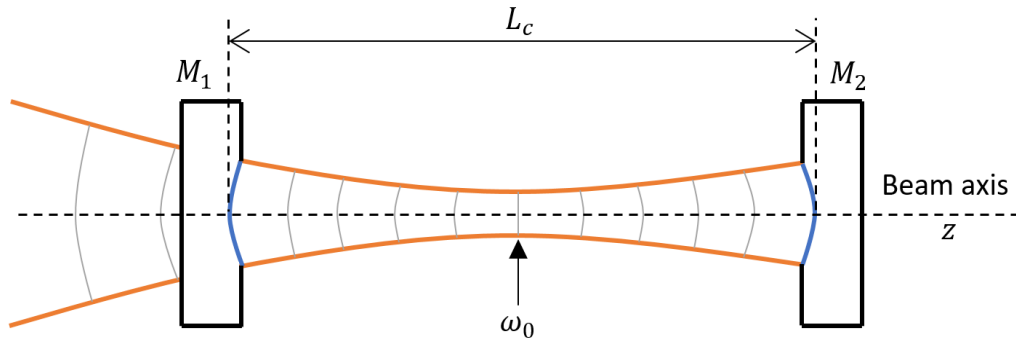


Figure 2.8: Schematic of a Gaussian beam in a symmetrical 2-spherical concave mirror cavity.

The g_n parameter for mirrors determine the stability of the cavity and is given by:

$$g_n = \left[1 - \left(\frac{L_c}{R_c} \right) \right] \quad 2.44$$

where R_c is the mirror radius of curvature. The g_n stability condition for a linear cavity with two mirrors is such that:

$$0 < g_1 g_2 < 1 \quad 2.45$$

The stable configurations for a two-mirror cavity are shown in Figure 2.9 (blue-highlighted areas). The possible symmetrical cavity configurations that exist for a two-mirror cavity include concentric, plane-parallel and confocal configurations. Within the cavity, the beam is reflected back and forth; it is, therefore, important to ensure the stability and confinement of the beam within the cavity through the selection of appropriate mirrors and cavity length. The cavity employed in this work is symmetrical and consists of two identical concave mirrors ($g_1 = g_2$) with $R_c =$

1 m. Applying Equation 2.44, g for the mirrors is determined as 0.5 and 0.25 respectively for the 0.5 m and 0.75 m cavity lengths used in this thesis, corresponding to g_1g_2 values of 0.25 and 0.0625 for the respective cavity lengths. This satisfies the stability condition in Equation 2.45.

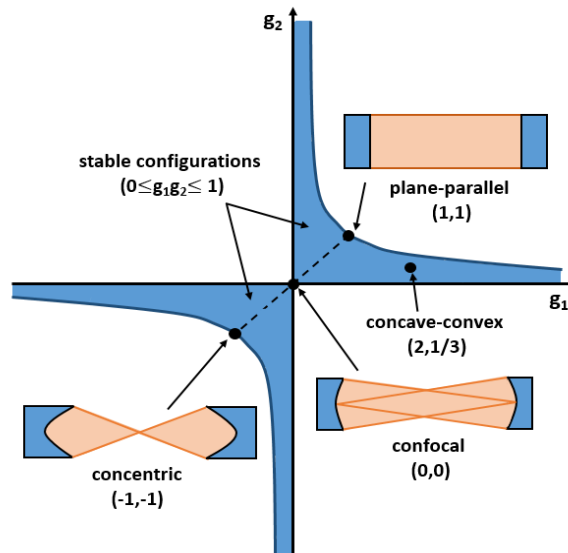


Figure 2.9: 2-mirror cavity stability diagram.

2.6 Cavity-based Absorption Techniques

Cavity-based techniques provide greater sensitivity which is derived from the enhanced path length provided by the highly reflective mirrors. Two cavity-based techniques, namely continuous-wave cavity ring-down spectroscopy (cw-CRDS) and cavity-enhanced absorption spectroscopy (CEAS) have been used for flame measurements in this project. These techniques derive their origin from cavity ring-down spectroscopy (CRDS). In this section, the theories of both techniques, as well as other variant cavity techniques, are discussed.

Cavity ring-down spectroscopy is a sensitive direct absorption technique, and its experimental set-up is relatively straightforward [30]. It derives its higher sensitivity from its increased path length and the fact that it is not affected by intensity

fluctuations from the laser, hence, noise reduction [31]. This makes it suitable for making measurements of weakly absorbing species and species occurring in trace amounts. It is unlike conventional absorption measurements which take into account the relative change in the intensity of light upon passing through the sample present along the optical path. The intensity change is usually infinitesimal relative to the large intensity of the light incident on the sample, limiting the minimum detectable change to an order of about 0.001.

2.6.1 Theory of Cavity Ring-down Spectroscopy

CRDS which is also called cavity ring-down laser absorption spectroscopy (CRLAS) in some texts, was first performed in 1988 by O'Keefe and Deacon [32]. It developed from the advancements in mirror reflectivity characterised by cavity attenuated phase shift (CAPS) technique in the 1980s [33]. As the reflectivity (R) of mirrors improved, i.e. $R \approx 1$, measuring R became difficult but transmission, T could easily be measured leading to the development of optical resonators using the mirrors; from which information on losses due to transmission can be obtained as the mirrors reflect light [17]. In other words, subsequent improvements of the CAPS technique were instrumental to the advancements that resulted in the development of CRDS [33]. One of these is the work of Anderson et al. also in the 1980s, in which mirror reflectivity measurements were obtained by injecting a laser beam into a cavity and obtaining the decay time. Over time, the limitations of conventional absorption spectroscopy have also encouraged the drive and need for a more sensitive approach. Some of the limitations include noise from intensity fluctuations of the light and the small absorption path length and the difficulty in measuring the small fractional difference in light intensity over a large intensity value, i.e. the ratio I/I_0 in the Beer-Lambert equation. The development of CRDS now spans over 3 decades and its use has become widespread over a range of applications.

The basic concept of CRDS involves coupling a laser pulse into a cavity containing two highly reflective concave mirrors which send the pulse back and forth through the sample in the cavity. The mirrors are highly reflective with reflectivity usually > 0.999 to ensure that the pulse travels a sufficient distance within the cavity. This distance is called the path length, which can run into several kilometres making CRDS to be considered somewhat as a multi-pass technique. On each pass, light is transmitted out of the cavity through the mirrors to produce a detectable ring-down signal on a detector from which the decay rate in the cavity is extracted and subsequently the absorption coefficient. This shows that CRDS is based on the rate of absorption rather than the amount of light absorbed.

The intensity of the light transmitted out of the cavity decays exponentially with time and the rate of this decay is dependent on the mirrors and the presence of an absorbing medium inside the cavity. The presence of an absorbing sample increases the loss of light in the cavity. This reduces the decay rate, which varies inversely with the losses in the cavity. In the absence of an absorbing sample, the losses and consequently the rate of decay are only determined by the mirror transmission and scattering losses. Ideally in the absence of an absorbing sample, Transmission, $T = 1 - R$, where R is mirror reflectivity. The decay time is the cavity ring-down time (τ) and is inversely proportional to the rate of decay, k given by:

$$k = (\text{losses}) c/L_c \quad 2.46$$

where c is the speed of light and L_c is the space between the mirrors. Ideally, in the absence of an absorbing sample, Equation 2.46 should be:

$$k = (1 - R) c/L_c \quad 2.47$$

However, in reality, with respect to all the losses in the cavity, Equation 2.47 becomes:

$$k = (1 - R + \mathcal{L} + \alpha_s d) c/L_c \quad 2.48$$

where \mathcal{L} and α_s are the scattering losses due to the sample and the absorption coefficient, respectively, and d is the length occupied by the sample. The scattering losses are usually lesser than the transmission, T by the mirror [34]. Over a narrow frequency range, the dependence of the scattering losses on frequency is negligible, and given the reciprocal relationship between τ and k , from Equation 2.48, the ring-down time is [17]:

$$\tau = L_c / (1 - R + \alpha_s d) c \quad 2.49$$

By plotting the cavity losses ($1/c\tau$) as a function of frequency, an absorption spectrum can be obtained. The above equation can be rearranged as below:

$$\frac{1}{c\tau} = \alpha_s \frac{d}{L_c} + \frac{1 - R}{L_c} \quad 2.50$$

Thus, the losses in the cavity are a sum of the absorption due to the sample and the loss due to the mirror. The accuracy of obtaining τ is dependent on factors such as data acquisition, cavity structure, mirror reflectivity and the detector used. These altogether determine the sensitivity of CRDS measurements.

CRDS spectra are obtained from the record of the decay rate as a function of the laser frequency. To ensure a complete spectrum is recovered, the spacing between the longitudinal modes should be small, in other words, the absorption linewidth of the species should be broader than the free spectral range [19]. By obtaining the exponential decay with and without an absorbing sample, τ and τ_0 are obtained respectively. The absorption due to the sample is obtained by subtracting the off-resonance losses ($1/c\tau_0 = (1 - R/L_c)$) from the on-resonance losses. Assuming the sample fills the cavity ($d = L_c$), the absorption coefficient α is obtained as [17]:

$$\alpha = \left(\frac{1}{c\tau} - \frac{1}{c\tau_0} \right) \quad 2.51$$

To extract τ from the experimental ring-down signal for use in the above equation, the ring-down trace is fitted to the exponential in Equation 2.53. This is because

following the termination of the laser light, the intensity built up in the cavity decays exponentially [17]:

$$I(t) = I_o \exp \left[-\frac{tc}{L_c} (1 - R + \alpha_s d) \right] \quad 2.52$$

where $I(t)$ is the intensity of light in the cavity at any time following the termination of the laser input to the cavity, I_o is the intensity of the incident light and t is the round-trip time of light in the cavity. Using Equation 2.49, the above equation can be simplified thus:

$$I(t) = I_o \exp \left(-\frac{t}{\tau} \right) \quad 2.53$$

2.6.2 Continuous-wave Cavity ring-down Spectroscopy

The CRDS concept described above is the standard CRDS operation involving a pulsed laser but gives a general idea of CRDS. The past two decades have seen the use of continuous-wave (cw) lasers to perform CRDS [35-38]. The use of a cw laser to carry out CRDS experiments presents some challenges which require modifications to the CRDS experimental set-up [21]. Since the light source is continuous, there is a challenge of properly determining a reference point or ring-down event so as to define when to measure the rate of decay in the cavity. This challenge is taken care of by a scheme devised to build up the intensity of light in the cavity, after which the laser radiation is switched off so that the rate of decay of this intensity built up in the cavity can be measured.

Coupling a laser beam may excite several cavity transverse modes resulting in different decay rates as each excited mode will have its characteristic decay rate. This effect can be reduced by mode-matching which shapes the incident beam from the laser so that it suits the fundamental cavity mode (TEM_{00}). This is because it is easier to match the incident beam to the Gaussian intensity distribution of the TEM_{00} mode. In essence, both the waist and the angle of convergence of the incident beam

is matched with the fundamental transverse mode of the cavity by means of a Keplerian telescope (i.e. two convex lenses). The beam waist, $\omega(z)$ at the focus and mirror surface can be calculated for the TEM₀₀ mode using the equation below [39]:

$$\omega(z) = \omega_0 \left[1 + \left(\frac{\lambda z_R}{\pi \omega_0^2} \right)^2 \right]^{1/2} \quad 2.54$$

ω_0 is the beam waist at the centre of the cavity ($z = 0$), λ is wavelength and z_R is the Rayleigh range given in Equation 2.43.

Mode-matching builds the intensity of light within the cavity. When the intensity reaches a pre-set threshold and the laser is switched off fast enough (in the range of ns), the intensity built up within the cavity decays (“rings-down”) and this is observed using a fast detector [34]. Different schemes have been identified, which can be used to achieve a fast switching of the laser radiation. One method involves the use of an acousto-optic modulator (AOM) which acts as a fast switch to extinguish the laser radiation, and it is triggered when the intensity in the cavity builds up to a predefined threshold value. In this work, a semiconductor optical amplifier (SOA) was used in place of an AOM as the SOA is also able to amplify the laser output [40]. Another method involves mounting the cavity mirrors on a piezoelectric transducer. When a certain threshold level is reached just like in the first method, a voltage is applied to the piezoelectric transducer, which moves the mirrors to alter the resonance condition in the cavity.

2.6.3 Phase-shift Cavity Ring-down Spectroscopy

Phase shift cavity ring-down spectroscopy (PS-CRDS) is a variant cw-CRDS scheme that is based on the CAPS technique introduced by Herbelin et al. [41, 42]. PS-CRDS which to the best of our knowledge has not been applied to *in situ* flame measurements provides an alternative way of obtaining ring-down times. Thus, it can be used to calibrate cavity-based measurements [43]. The technique involves

applying a sinusoidal modulation to the intensity of the beam from a cw-laser source. As the beam propagates through the stable cavity, the intensity modulation is phase-shifted relative to that of the incident beam as seen in Figure 2.10, and this is detected using a lock-in amplifier. The absorption spectrum is obtained from the magnitude of the phase-shift [17]. The relationship between the phase-shift angle, $\phi(\nu)$ and the ring-down time of the cavity $\tau(\nu)$ is given by the equation below where ω is the angular modulation frequency of the incident beam [16].

$$\tan[\phi(\nu)] = -\omega\tau(\nu) \quad 2.55$$

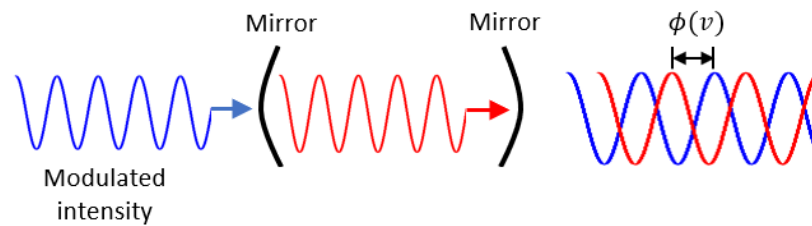


Figure 2.10: Schematic of phase-shift cavity ring-down spectroscopy.

This phase shift angle, $\phi(\nu)$ is the component being detected by the phase-sensitive detector, and from Equation 2.55, we can relate $\phi(\nu)$ to the absorption coefficient by [17]:

$$\alpha(\nu) = \frac{\omega}{c} \left(\frac{1}{\tan\phi(\nu)} - \frac{1}{\tan\phi_0(\nu)} \right) \quad 2.56$$

2.6.4 Cavity-enhanced Absorption Spectroscopy

CEAS which is a variant cavity technique that also employs continuous-wave lasers presents a less challenging process as we do not have to bother about switching off the continuous wave laser beam at any point during the process. Thus, the difficult mode-matching process encountered in cw-CRDS is avoided. Although all the

techniques discussed in this section are ‘cavity-enhanced’ techniques, CEAS could also be referred to as integrated cavity output spectroscopy (ICOS).

Just like cw-CRDS, a laser beam is coupled to an optical cavity. The process excites the higher-order cavity modes and the time-integrated intensity that leaks out of the cavity is measured with the help of a detector [44]. The laser is scanned continuously in such a way that it equally excites each cavity mode as the cavity length is varied slowly. Alternatively, the cavity modes could be scanned rapidly while the laser is scanned slowly, and the resonance time would depend on the rate of scan of the cavity modes [21, 45, 46]. The latter approach is experimentally more involved [44]. In a study by Bakowski et al. where both the cavity modes and the laser frequency were both scanned rapidly, the authors report that this was of no benefit to the quality of the measurements [47].

The length of the cavity in the CEAS set-up is very important to the sensitivity of the CEAS technique. The CEAS technique is based on the simultaneous excitation of several higher-order transverse modes of the cavity. At certain cavity configurations, these modes can be degenerate, which means that they are resonant at the same frequency [48]. This reduces the mode density distribution and limits the transmission from the cavity modes, resulting in limited sensitivity (reduced SNR) of the technique. The cavity length and the mirror ROCs determine the cavity configuration. Where the ROCs are equal (symmetric cavity), and at certain ratios of cavity length to the ROC, certain higher-order modes become degenerate [48]. It is therefore essential to utilise a cavity length that will result in a configuration that ensures the non-degeneracy of the higher-order modes of the cavity.

For a CEAS spectrum to be obtained, the cavity must be aligned to increase the mode density. The transmission from the cavity would ordinarily be dominated by the cavity mode structure. Increasing the mode density washes out the effects of the cavity mode structure by smoothing out the mode structure to a near-continuum. Common approaches to achieve this include: modulating the cavity length as the laser is

scanned, partial misalignment of the cavity, and mechanical vibrations that change the cavity length randomly [21, 46, 47]. Another approach used to reduce the effect of the mode structure on cavity transmission is to employ off-axis alignment of the incident beam relative to the cavity axis. This technique is discussed in the next section.

In comparison to cw-CRDS, CEAS is not a self-calibrating technique and is not totally immune to intensity fluctuations. However, CEAS utilises a simpler set-up and provides greater flexibility in that species can be monitored in about “real-time”, as a CEAS spectrum can be obtained in about a few seconds on the oscilloscope [45].

The absorption coefficient α from CEAS measurements is given by [17, 49]:

$$\alpha = \frac{I_0 - I}{I} \left(\frac{1 - R}{L_c} \right) \quad 2.57$$

where is L_c the length of the cavity, R is the effective mirror reflectivity, I and I_0 are the intensities of light with and without an absorber in the cavity, respectively. The origin of this equation has been explored by Fiedler et al. [49]. Calibrating the eventual absorption spectrum from CEAS will require calculating the effective mirror reflectivity, R in the above equation. This can be done by a number of ways which include: a CRDS measurement of the ring-down time, τ of the empty cavity [50, 51], a reference measurement using an absorber with a known concentration [52], and phase-sensitive detection [53]. The use of phase-detection makes the CEAS set-up complex and relatively expensive, which erodes a major advantage of CEAS.

2.6.5 Off-axis Cavity Enhanced Absorption Spectroscopy

This variant ICOS technique is based on introducing the cw-beam into the stable cavity at an angle slightly off the axis of the beam path in the cavity. The beam then undergoes several reflections that are spatially separate until it retraces the original beam path within the cavity [54, 55]. The number of reflections leads to longer round-

trips that cancel out noise from the resonance structure of the cavity. However, the spatial resolution of the technique is significantly reduced from the off-axis introduction of the beam [16]. This makes it unsuitable for flame measurements. For an empty optical cavity, the transmitted intensity, I is related to the ring-down time, τ by the equation below [55] where I_L is the incident laser intensity, τ is the ring-down time, C_p is a cavity coupling parameter, R and T are the mirror intensity reflection and transmission coefficients.

$$I = \frac{I_L C_p T}{2(1 - R)} [1 - \exp(-t/\tau)] \quad 2.58$$

2.7 Application of Cavity-based Techniques to *in situ* Flame Measurements

The application of diode lasers to *in situ* cavity-based absorption measurements in flames has before now received very little attention by researchers, probably because of the perceived challenges of implementing this set up in a hostile environment. Most focus and reportage have been on the pulsed CRDS regime for flame measurements. The pulsed regime is easier to implement as it does not require the resonant build-up of intensity intracavity, and subsequent attenuation of the incident laser light; as such, it is more robust in a flame environment. Meijer et al. [56] reported the first application of CRDS to flames for the detection of OH radical in a Bunsen flame. Since then, flame measurements of various species using this technique have been performed by several studies, including the first extension to the infrared region by Scherer et al. [31, 57-63]. Xie et al. [64] subsequently performed CRDS in the near-infrared region to obtain flame measurements of water vapour. Studies in the pulsed regime have largely involved the use of dye lasers which are bulky and more expensive than diode lasers. Dye lasers have broad linewidths that are usually larger than the cavity $\delta\nu_{FSR}$, which can result in decreased sensitivity.

Diode lasers are now increasingly being used as light sources in the near-infrared region for CRDS [21]. However, up until the previous success of the application of cw-CRDS to *in situ* flame measurements recorded at Strathclyde, there has been no known reported application [40]. An earlier study by Miller et al. [65] mentioned in the previous chapter has preferably used a combination of extractive sampling and cw-CRDS. Peeters et al. [45] performed CEAS flame measurements of OH radical in the near-infrared region. This is similar to the OH measurements in this project as they employed the use of a diode laser source. However, they show semi-quantitative measurements of OH as they calibrate the measurements using an effective mirror reflectivity obtained from a measurement of ambient water absorption. The authors also assume temperature from measurements in an oven and from simulations in the calculation of OH concentration from spectra recorded in a flame.

Cavity-based techniques are generally sensitive techniques and even more sensitive with the use of diode lasers. However, the hostile environment of flames presents a challenge. Challenges such as thermal lensing alongside scattering fluctuations in the flame affect their sensitivity [17]. For cw-CRDS, the flame perturbs the difficult mode matching as it steers the laser beam away, thereby reducing light intensity in the cavity. This makes the broadband losses (off-resonance) more significant, leading to a reduction in the ring-down time, τ . Flame emissions which include soot and water vapour can be challenging to deal with in the course of cavity-enhanced experiments. Over time the mirrors can become blurred, and soot can distort the optical path, especially with very rich flames. This will ultimately reduce the sensitivity of these techniques. A flow of nitrogen gas can be used to purge the mirrors during operation and soot can be cleaned off intermittently as the experiment proceeds [66]. Filters can be used to reduce these background effects on the detector [45]. Also, the product gases from the flame should be conveyed out using an extractor or through any other method that will not perturb the experiment. The presence of soot particles in the flame limits the application of CEAS and cw-CRDS techniques at heights downstream in the flame. So far, both techniques have mostly been discussed

with respect to laminar flames. This is as turbulent flames present a more difficult environment, and also concentration varies greatly in turbulent flames [17]. Also, cavity-based techniques are ‘line-of-sight techniques’ and as such are well-suited to homogenous flames.

The first application of cw-CRDS to *in situ* flame measurements demonstrates significant potential for use in detecting trace species in stable flames [16, 40]. The initial design faced a challenge in which the alignment degraded over time as the mirrors become fouled with soot and ambient dust particles following from the long data acquisition time of the technique, especially in richer flames. As such, it was difficult to accurately normalise the measured signal. The design was refined to include a second diode laser to normalise the measured signal and to also account for the broadband losses. This required the use of an optical switch to switch between the interrogation laser and the second laser for each data point. The design has been further refined for the work in this thesis by excluding the second laser and the optical switch; thus, a simpler design. With this design, a robust data-set has been obtained to complement the limited data-set obtained with the previous design. This thesis goes further to explore the CEAS technique using diode lasers for *in situ* flame measurements.

Making quantitative measurements of flame species using both techniques of cw-CRDS and CEAS ultimately require that the measured signals obtained at a given location (HAB) in the flame are converted into absolute concentration. Generally, the accuracy with which quantitative measurements are made in cavity-based techniques is subject to the accurate determination of ring-down times [30]. In CRDS technique, concentration determination generally involves calibrating the profile of the net losses per pass [67]. The net loss per pass is the difference between the on-resonance and off-resonance ring-down times. In CEAS, the ring-down time of the empty cavity is used to obtain the effective reflectivity for use in calibrating the measured intensity. Since CEAS measures the time-integrated intensity leaking from the cavity, it is essential to subtract the flame radiation that gets to the detector from

the raw absorption spectrum. The methodology for modelling the recovered absorption spectra to determine concentration has been described in Section 2.4.

2.8 Summary

In this chapter, the principles of spectroscopy and optical cavities upon which this project is based have been established. The Beer-Lambert law, as well as an overview of molecular spectroscopy, with emphasis on rotational and vibrational transitions, were introduced in Section 2.2. In Section 2.3, the characteristics of absorption spectra were discussed, highlighting the various spectral broadening mechanisms and consequent lineshape functions. This section also discusses the application of lineshape functions and parameters from HITRAN to mathematical models used in modelling absorption spectra. Following this, the determination of concentration is described in Section 2.4. The underlying principles of optical cavities, cavity-based techniques and their application to flame measurements are presented in Sections 2.5, 2.6 and 2.7 respectively.

2.9 References

1. Eckbreth, A.C., *Laser Diagnostics for Combustion Temperature and Species*. 2nd ed. Combustion Science & Technology. 1996, The Netherlands: Gordon and Breach Publishers.
2. Carey, S., *Chemical species tomography by near infra-red absorption*. Chemical Engineering Journal, 2000. **77**(1-2): p. 111-118.
3. Banwell, C.N.M., E. M. , *Fundamentals of Molecular Spectroscopy*. Fourth ed. 1994: McGraw-Hill.
4. Hollas, J.M., *Modern spectroscopy*. 4th ed. 2004, Chichester, Hoboken, NJ: J. Wiley.
5. Brown, J., et al., *The labeling of parity doublet levels in linear molecules*. Journal of Molecular Spectroscopy, 1975. **55**(1-3): p. 500-503.
6. Hilborn, R.C., *Einstein coefficients, cross sections, f values, dipole moments, and all that*. American Journal of Physics, 1982. **50**(11): p. 982-986.

7. Šimečková, M., et al., *Einstein A-coefficients and statistical weights for molecular absorption transitions in the HITRAN database*. Journal of Quantitative Spectroscopy and Radiative Transfer, 2006. **98**(1): p. 130-155.
8. Xhou, X., *Diode-laser absorption sensors for combustion control in Mechanical Engineering Department*. 2005, Stanford University: Stanford, California.
9. Gordon, I.E., et al., *The HITRAN2016 molecular spectroscopic database*. Journal of Quantitative Spectroscopy and Radiative Transfer, 2017. **203**: p. 3-69.
10. Whiting, E.E., *An empirical approximation to the Voigt profile*. Journal of Quantitative Spectroscopy and Radiative Transfer, 1968. **8**(6): p. 1379-1384.
11. Olivero, J.J. and R.L. Longbothum, *Empirical fits to the Voigt line width: A brief review*. Journal of Quantitative Spectroscopy and Radiative Transfer, 1977. **17**(2): p. 233-236.
12. McLean, A., C. Mitchell, and D. Swanston, *Implementation of an efficient analytical approximation to the Voigt function for photoemission lineshape analysis*. Journal of Electron Spectroscopy and Related Phenomena, 1994. **69**(2): p. 125-132.
13. Rothman, L.S., et al., *The HITRAN 2008 molecular spectroscopic database*. Journal of Quantitative Spectroscopy and Radiative Transfer, 2009. **110**(9): p. 533-572.
14. Rothman, L.S., et al., *HITEMP, the high-temperature molecular spectroscopic database*. Journal of Quantitative Spectroscopy and Radiative Transfer, 2010. **111**(15): p. 2139-2150.
15. Bain, J.R.P., *Near infrared tunable diode laser spectroscopy for aero engine related applications*, in *Dept. of Electronic and Electrical Engineering*. 2012, Thesis [Eng. D] -- University of Strathclyde: Glasgow.
16. Humphries, G., *Novel diode laser absorption techniques for combustion diagnostics*, in *Department of Electronic and Electrical Engineering*. 2017, University of Strathclyde: Glasgow. p. 144.
17. Berden, G. and R. Engeln, *Cavity Ring-Down Spectroscopy: Techniques and Applications*. 2009, West Sussex: John Wiley. p. 313.
18. Hertzog, M., et al., *Strong light-matter interactions: a new direction within chemistry*. Chemical Society Reviews, 2019. **48**(3): p. 937-961.
19. Zalicki, P.a.Z., R. N., *Cavity ring-down spectroscopy for quantitative absorption measurements*. J. Chem. Phy, 1995. **102**(7): p. 10.
20. Saleh, B.E.A., *Fundamentals of photonics*, ed. M.C. Teich. 1991, New York: Wiley.
21. Mazurenka, M., et al., *Cavity ring-down and cavity enhanced spectroscopy using diode lasers*. Annual Reports Section "C" (Physical Chemistry), 2005. **101**: p. 100.

22. OPI. *Optical resonators and Gaussian beams*. 09/2/2020 [cited 2020 03-02]; Available from: http://www.optique-ingenieur.org/en/courses/OPI_ang_M01_C03/co/Grain_OPI_ang_M01_C03_7.html.
23. Lee, D.H., et al., *Optimization of the mode matching in pulsed cavity ringdown spectroscopy by monitoring non-degenerate transverse mode beating*. Applied Physics B, 2002. **74**(4): p. 435-440.
24. Huang, H. and K.K. Lehmann, *Noise in cavity ring-down spectroscopy caused by transverse mode coupling*. Optics Express, 2007. **15**(14): p. 8745-8759.
25. Yariv, A., *Photonics: optical electronics in modern communications*. 6th ed, ed. P. Yeh and A. Yariv. 2007, New York: Oxford University Press.
26. Porras, M.A., J. Alda, and E. Bernabeu, *Complex beam parameter and ABCD law for non-Gaussian and nonspherical light beams*. Applied Optics, 1992. **31**(30): p. 6389-6402.
27. Taché, J., *Derivation of ABCD law for Laguerre-Gaussian beams*. Applied optics, 1987. **26**(14): p. 2698-2700.
28. Kogelnik, H., *Imaging of optical modes—resonators with internal lenses*. Bell System Technical Journal, 1965. **44**(3): p. 455-494.
29. Svelto, O. and D.C. Hanna, *Principles of Lasers*. Fifth ed. 2010, Boston, MA: Boston, MA: Springer US.
30. Berden, G., R. Peeters, and G. Meijer, *Cavity ring-down spectroscopy: Experimental schemes and applications*. International Reviews in Physical Chemistry, 2000. **19**(4): p. 565-607.
31. Evertsen, R., R.L. Stolk, and J.J. Ter Meulen, *Investigations of Cavity Ring Down Spectroscopy applied to the detection of CH in Atmospheric Flames*. Combustion Science and Technology, 1999. **149**(1-6): p. 19-34.
32. O'Keefe, A. and D.A.G. Deacon, *Cavity ring-down optical spectrometer for absorption measurements using pulsed laser sources*. Review of Scientific Instruments, 1988. **59**(2544).
33. Scherer, J.J., et al., *Cavity Ringdown Laser Absorption Spectroscopy: History, Development, and Application to Pulsed Molecular Beams*. Chemical Reviews, 1997. **97**(1): p. 25-52.
34. Romanini, D., Kachanov, A. A., Sadeghi, N., Stoeckel, F., *CW cavity ring down spectroscopy*. Chemical Physics Letters, 1997. **264**: p. 316-322.
35. Simpson, W.R., *Continuous-wave cavity ring-down spectroscopy applied to in situ detection of dinitrogen pentoxide (N₂O₅)*. Review of scientific instruments, 2003. **74**(7): p. 3442-3452.
36. Fawcett, B., et al., *Trace detection of methane using continuous wave cavity ring-down spectroscopy at 1.65 μm*. Physical Chemistry Chemical Physics, 2002. **4**(24): p. 5960-5965.

37. Mazurenka, M.I., et al., *410-nm diode laser cavity ring-down spectroscopy for trace detection of NO₂*. Chemical Physics Letters, 2003. **367**(1): p. 1-9.
38. Starikova, E., et al., *CW-Cavity Ring Down Spectroscopy of ¹⁸O₃. Part 3: Analysis of the 6490–6900 cm⁻¹ region and overview comparison with the ¹⁶O₃ main isotopologue*. Journal of Molecular Spectroscopy, 2009. **257**(1): p. 40-56.
39. Demtröder, W., *Laser spectroscopy: Basic Principles*. Vol. 5. 2014: Springer.
40. Humphries, G.S., I.S. Burns, and M. Lengden, *Application of Continuous-Wave Cavity Ring-Down Spectroscopy to Laminar Flames*. IEEE Photonics Journal, 2016. **8**(1).
41. Herbelin, J., et al., *Sensitive measurement of photon lifetime and true reflectances in an optical cavity by a phase-shift method*. Applied Optics, 1980. **19**(1): p. 144-147.
42. Herbelin, J.M. and J.A. McKay, *Development of laser mirrors of very high reflectivity using the cavity-attenuated phase-shift method*. Applied Optics, 1981. **20**(19): p. 3341-3344.
43. Laurila, T., et al., *A calibration method for broad-bandwidth cavity enhanced absorption spectroscopy performed with supercontinuum radiation*. Applied Physics B, 2011. **102**(2): p. 271-278.
44. Engeln, R., et al., *Cavity enhanced absorption and cavity enhanced magnetic rotation spectroscopy*. Review of scientific instruments, 1998. **69**(11): p. 3763-3769.
45. Peeters, R., G. Berden, and G. Meijer, *Near-Infrared Cavity Enhanced Absorption Spectroscopy of Hot Water and OH in an Oven and in Flames*. Applied Physics B-Lasers and Optics, 2001. **73**: p. 65-70.
46. Cheung, A.-C., T. Ma, and H. Chen, *High-resolution cavity enhanced absorption spectroscopy using an optical cavity with ultra-high reflectivity mirrors*. Chemical physics letters, 2002. **353**(3-4): p. 275-280.
47. Bakowski, B., et al., *Cavity-enhanced absorption spectroscopy with a rapidly swept diode laser*. Applied Physics B, 2002. **75**(6-7): p. 745-750.
48. Papageorge, A.T., A.J. Kollár, and B.L. Lev, *Coupling to modes of a near-confocal optical resonator using a digital light modulator*. Optics Express, 2016. **24**(11): p. 11447-11457.
49. Fiedler, S.E., A. Hese, and A.A. Ruth, *Incoherent broad-band cavity-enhanced absorption spectroscopy*. Chemical physics letters, 2003. **371**(3-4): p. 284-294.
50. Watt, R.S., et al., *Cavity enhanced spectroscopy of high-temperature H₂O in the near-infrared using a supercontinuum light source*. Applied Spectroscopy, 2009. **63**(12): p. 1389-1395.
51. Johnston, P.S. and K.K. Lehmann, *Cavity enhanced absorption spectroscopy using a broadband prism cavity and a supercontinuum source*. Optics express, 2008. **16**(19): p. 15013-15023.

52. Langridge, J., et al., *Cavity enhanced absorption spectroscopy of multiple trace gas species using a supercontinuum radiation source*. Optics Express, 2008. **16**(14): p. 10178-10188.
53. Chan, M.-C. and S.-H. Yeung, *High-resolution cavity enhanced absorption spectroscopy using phase-sensitive detection*. Chemical Physics Letters, 2003. **373**(1): p. 100-108.
54. Baer, D.S., et al., *Sensitive absorption measurements in the near-infrared region using off-axis integrated-cavity-output spectroscopy*. Applied Physics B, 2002. **75**(2-3): p. 261-265.
55. Paul, J.B., L. Lapson, and J.G. Anderson, *Ultrasensitive absorption spectroscopy with a high-finesse optical cavity and off-axis alignment*. Applied optics, 2001. **40**(27): p. 4904-4910.
56. Meijer, G., et al., *Coherent cavity ring down spectroscopy*. Chemical Physics Letters, 1994. **217**(1): p. 112-116.
57. Scherer, J.J. and D.J. Rakestraw, *Cavity ringdown laser absorption spectroscopy detection of formyl (HCO) radical in a low pressure flame*. Chemical Physics Letters, 1997. **265**(1): p. 169-176.
58. Scherer, J.J., D. Voelkel, and D.J. Rakestraw, *Infrared cavity ringdown laser absorption spectroscopy (IR-CRLAS) in low pressure flames*. Applied Physics B, 1997. **64**(6): p. 699-705.
59. Scherer, J.J., et al., *Determination of methyl radical concentrations in a methane/air flame by infrared cavity ringdown laser absorption spectroscopy*. The Journal of Chemical Physics, 1997. **107**(16): p. 6196-6203.
60. Mercier, X., et al., *Cavity ring-down measurements of OH radical in atmospheric premixed and diffusion flames.: A comparison with laser-induced fluorescence and direct laser absorption*. Chemical Physics Letters, 1999. **299**(1): p. 75-83.
61. Spaanjaars, J.J.L., J.J. ter Meulen, and G. Meijer, *Relative predissociation rates of OH ($A\ 2\Sigma^+$, $v'=3$) from combined cavity ring down—Laser-induced fluorescence measurements*. The Journal of Chemical Physics, 1997. **107**(7): p. 2242-2248.
62. Derzy, I., V.A. Lozovsky, and S. Cheskis, *Absolute CH concentration in flames measured by cavity ring-down spectroscopy*. Chemical Physics Letters, 1999. **306**(5): p. 319-324.
63. Cheskis, S., et al., *Cavity ring-down spectroscopy of OH radicals in low pressure flame*. Applied Physics B, 1998. **66**(3): p. 377-381.
64. Xie, J., et al., *Near-infrared cavity ringdown spectroscopy of water vapor in an atmospheric flame*. Chemical Physics Letters, 1998. **284**(5): p. 387-395.
65. Miller, J.H., et al., *Measurements of Hydrogen Cyanide and its Chemical Production Rate in a Laminar Methane/Air, Non-Premixed Flame Using cw Cavity Ringdown Spectroscopy*. Proceedings of the Combustion Institute, 2002. **29**: p. 2203-2209.

66. Xie, J., et al., *Near-infrared cavity ringdown spectroscopy of water vapour in an atmospheric flame*. Chemical Physics Letters, 1998. **284**(5-6): p. 387-395.
67. Mercier, X. and P. Desgroux, *Cavity Ring-Down Spectroscopy for Combustion Studies*, in *Cavity Ring-Down Spectroscopy: Techniques and Applications*. 2009, John Wiley: West Sussex. p. 273-311.

Chapter 3 : Cavity-based Experimental Methodology for Flame Measurements

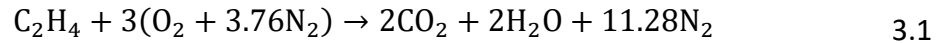
3.1 Introduction

This chapter presents the methodology for the cavity-based techniques employed to make the repeatable measurements in this project. The combustion system, which is a flame stabilised on a burner, is described in detail. The methodology for the continuous-wave cavity ring-down spectroscopy (cw-CRDS) technique described here builds on the first demonstration of *in situ* cw-CRDS flame measurements of acetylene in this research group [1]. The initial design by Humphries [1] has been modified, excluding the use of some optical components from the cw-CRDS set-up. The results presented in the next chapter show that sensitive measurements can be obtained using the modified set-up. The development of the cavity-enhanced absorption spectroscopy (CEAS) technique employed for the flame measurements of acetylene and hydroxyl radical is described as well as the various components included in the set-up.

The structure of this chapter begins with a description of the flame-burner system and the burners used. This is followed by the presentation of the cw-CRDS methodology. Next is the presentation of the CEAS methodology for acetylene and hydroxyl radical measurements.

3.2 Flame-Burner Configuration

The flames employed for the measurements in this project are laminar premixed flat flames of ethylene and air, stabilised on flat burners at atmospheric pressure. The overall reaction equation for ethylene-air combustion is given as:



The target flames were of different compositions characterised by equivalent ratios, ϕ according to Equation 3.2. A range of flames from lean to highly sooting conditions ($\phi = 0.8$ to 2.59) were employed in this project.

$$\phi = \frac{\left[\frac{x_{air}}{x_{\text{C}_2\text{H}_4}} \right]_{\text{stoichiometric}}}{x_{air}/x_{\text{C}_2\text{H}_4}} \quad 3.2$$

where x is mole fraction and $\left[\frac{x_{air}}{x_{\text{C}_2\text{H}_4}} \right]_{\text{stoichiometric}}$ refers to the stoichiometric air-to-fuel ratio.

The design of a burner is known to impact the flame structure, and it is ideal that conditions such as concentration, temperature and flow patterns in the flame are stable at the measurement volume [2]. In this project we have chosen to work with laminar flat-flames as they have the advantage that these conditions are well-defined, and the path-integrated techniques (cw-CRDS and CEAS) wouldn't be readily applicable in other flame configurations [3]. This emphasises the need for well characterised burner-flame configurations to be employed for standard measurements to ensure reproducibility of results.

Owing to the need to synergise research efforts and the associated benefits as discussed in the 'International Workshop on Laser Induced Incandescence' meeting of 2005 in Germany [4], a set of burners and flame conditions were identified. The identified burners include McKenna burner, Gülder burner and Santoro burner. The International Sooting Flame (ISF) workshop recommends flame conditions for these burners [5]. This enables comparable data-sets to be generated which can be used to validate models. Two burners have been used in this project. One is a water-cooled porous-plug burner sharing some features with the standard McKenna burner but of narrower diameter, which will after now be referred to as porous-plug burner in this thesis. The other is the standard McKenna burner (Holthuis & Associates). These

burners are flat flame burners which have been commonly used for studying pollutant formation [2]. Flat-flame burners are assumed to be one-dimensional at the centre-line which means that flame parameters such as temperature and concentration change only with respect to the height above the surface of the burner (HAB) near to the centre-line of the flow shown in Figure 3.1. This ensures consistent conditions which are suitable for line-of-sight absorption techniques such as cavity-enhanced techniques. In a study by Prucker et al. [6] of a hydrogen-air flame supported on a McKenna burner, they observed no temporal fluctuation of temperature in the measurements. Also, there was no observation of spatial variation at the centre-line of the burner in the measurements.

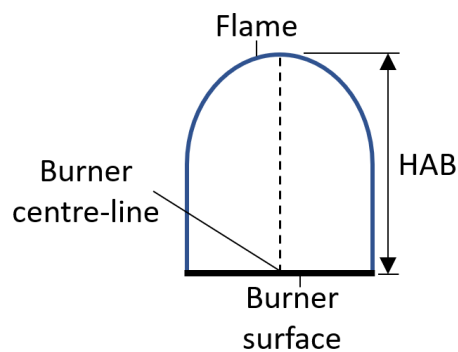


Figure 3.1: Schematic of burner centre-line and HAB.

3.2.1 McKenna Burner

The standard McKenna burner is made of a 60 mm diameter stainless-steel or bronze sintered porous plug within which a cooling circuit for water is housed. The cooling circuit serves to maintain a well-defined burner-plate temperature. The premixed mixture of fuel and oxidiser flows into a hollow chamber below the matrix from which it passes evenly through the porous plug. The hollow chamber also serves to reduce the impact of any irregular flow of the premixed gas. Around the 60 mm burner plate is a co-annular porous plug for co-flow of a shroud gas. The shroud gas shields the flame from external disturbances such as air currents [7]. The choice of shroud gas

influences the characteristics of the flame [8]. This project utilised air as the shroud gas which promotes the formation of a diffusion flame at the edges of the burner, giving rise to a more homogeneous temperature profile across the burner surface [8, 9]. However, this might result in non-uniform soot characteristics radially. This is in contrast to using nitrogen as a shroud gas which promotes radially homogeneous soot characteristics and as such is well suited to line-of-sight measurements in studies of soot [9]. However, this results in cooling of the flame at the burner edges and as such non-uniform radial distribution of temperature. The air flow rate for the air co-flow was set at a rotameter reading of 15 litres per minute. This value is higher than the velocity (10.4 litres per minute) of the premixed gases to enhance the flame stability as employed in previous studies [9, 10]. A cross-section of the McKenna burner highlighting some of the details described in this section is shown in Figure 3.2 [6].

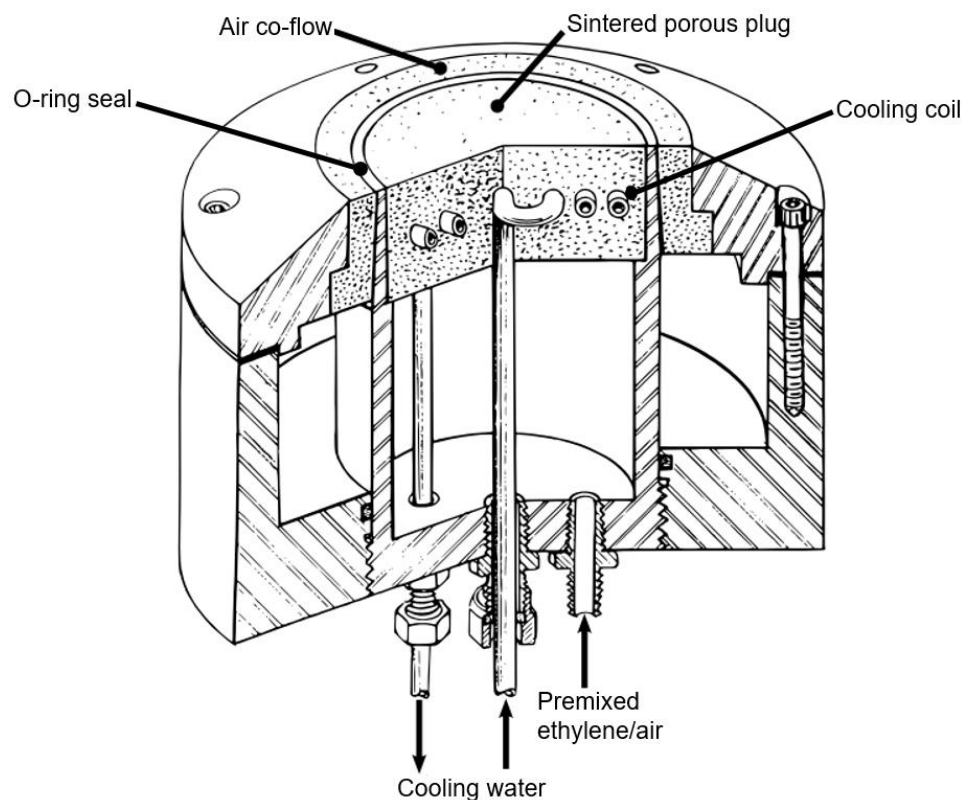


Figure 3.2: Cross-section of the McKenna burner (Image sourced from Prucker et al. [6]).

A bronze sintered porous plug is used in the manufacture of the McKenna burner used in this project. A difference between a stainless-steel porous plug and a bronze porous plug was reported by Migliorini et al. based on soot profile measurements using LII and other techniques [10]. They observed a soot radial distribution for the bronze burner that is considered flat as expected. However, their stainless-steel burner produced a hollow soot radial distribution at the centre. Since the centre of the flame is the region of interest, measurements performed using the stainless-steel porous plug could be questionable.

In keeping with many previous soot studies elsewhere, and some within this research group, and as recommended by ISF workshop [4, 11-13], a 20 mm thick cylindrical plate of 60 mm in diameter, made from stainless-steel, is placed 21 mm above the burner surface. This helps further to stabilise the flame against currents of ambient air as well as preventing a tapering of the sooting region with increasing height above the burner surface. The McKenna burner with the stabilisation plate used in this project is shown in Figure 3.3. The flow rates for the flame conditions run with the McKenna burner in this project are shown in Table 3.1. The flow rates are based on the standard temperature and pressure of 20 °C and 1 atm respectively. The total gas flow rate is 10.4 litres per minute which achieved a total mass flux of $0.065 \text{ kgs}^{-1}\text{m}^{-2}$.

A procedure was established to ensure the reproducibility of flame conditions. This includes allowing the flame to run for about 15 minutes before taking measurements to ensure the thermal stability of the stabilisation plate. Over the course of running the rich flames ($\phi = 2.07$ and 2.37), soot builds up on the surface of the stabilisation plate. However, care is taken to ensure that a sequence of experiments is not run for more than 1 hour to avoid the large accumulation of soot on the plate. This is because soot risks falling off the plate into the flame, which influences the measurements and risks damage to the burner. The burner is mounted on a vertical translation stage to enable measurements at different vertical positions.

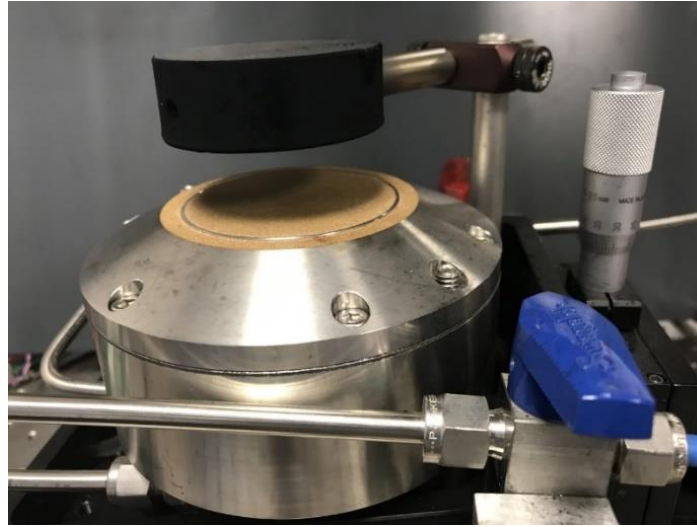


Figure 3.3: McKenna burner with stabilisation plate at 21 mm above the burner surface.

ϕ	Flow rates (sL min ⁻¹)		$x_{C_2H_4}$	x_{air}
	C ₂ H ₄	air		
0.8	0.55	9.85	0.053	0.95
1.0	0.68	9.72	0.065	0.93
1.77	1.14	9.25	0.11	0.89
2.07	1.31	9.08	0.13	0.87
2.37	1.48	8.94	0.14	0.86

Table 3.1: Summary of the flame conditions supported on the McKenna burner at standard temperature and pressure of 20 °C and 1 atm respectively.



Figure 3.4: $\phi = 1.77$ ethylene-air flame on the McKenna burner.



Figure 3.5: $\phi = 2.07$ ethylene-air flame on the McKenna burner.

Visually examining the flames supported on the McKenna burner in Figure 3.4 and Figure 3.5, the sooting characteristics of the flames can be seen. The flames produce orange radiation of varying intensities. This radiation is an indication of the presence of soot in the flames. By eye, it is seen that the $\phi = 2.07$ flame exhibits far more intense radiation than the $\phi = 1.77$ flame. Also, clearly seen is a blue-transparent region up to about 7 mm, which is the non-sooting part of the flame. These observations are also the case for the flames supported on the porous plug burner, which are shown in Figure 3.7 and Figure 3.8.

3.2.2 Porous-plug Burner

The porous-plug burner is a 33 mm diameter porous-plug burner made from sintered stainless-steel. The burner is also water-cooled, and a 38 mm diameter cylindrical plate that is 30 mm thick is mounted 21 mm above the burner surface. The plate was suspended using a right-angled clamp to ensure its surface is parallel to the burner. Following this, the sides are checked using a right-angled ruler to also ensure that the plate is horizontal to the burner surface. As stated earlier, the use of a stabilisation

plate is typical in soot studies as the plate serves to stabilise the flame by acting as a heat sink [12]. The plate also plays a role in avoiding tapering (narrowing) of the flame with increasing height above the burner surface. In addition to the reduced burner plate diameter, a distinction from the standard McKenna burner is the absence of a co-flow of shielding gas. This makes the flame susceptible to draughts of ambient air. As a result, careful efforts were made to stabilise the flame, including the use of temporary shields carefully placed around the flame with respect to the window in the laboratory which was the major source of draught (despite the light-tight window blind in place for laser safety). Careful positioning of the extraction system installed in the laboratory was adopted as well. As a vital practical check to ensure the stability of the flame, experiments were thoroughly repeated (three times), leading to results that are highly reproducible as seen in Chapters 4, 5 and 6. The results of some earlier measurement sequences, for which reproducible data were not obtained, were discarded; the effect of draughts on the flame was also observed during these preliminary measurements, and the configuration of the shielding was adjusted until reproducible results were obtained. Previous studies using this burner have also recorded reproducible data sets [1, 12-14].



Figure 3.6: 33 mm diameter porous-plug burner with a 38 mm diameter cylindrical stabilisation plate.

The accumulation of soot is also a challenge with this burner, especially with highly sooting flames over an extended period of time. Sometimes, soot accumulates unevenly on the plate surface as can be seen in Figure 3.6 for the porous-plug burner. The flame $\phi = 2.59$ is highly sooting and to avoid the uneven accumulation of soot on the stabilisation plate, a procedure was established not to run the $\phi = 2.59$ flame for more than 30 minutes (in fact this flame condition was largely avoided due to the heavily sooting conditions, as discussed elsewhere), and the other sooting flames for not more than 120 minutes. The flame is extinguished, and the plate is allowed to cool for 20 minutes, following which it is carefully cleaned. The burner is also installed on a translation stage to facilitate measurements at different vertical positions in the flame.

ϕ	Flow rates (sLmin ⁻¹)		$x_{C_2H_4}$	x_{air}
	C ₂ H ₄	air		
0.80	0.167	2.98	0.0531	0.947
1.00	0.206	2.94	0.0655	0.934
1.40	0.281	2.87	0.0892	0.911
1.77	0.346	2.80	0.110	0.890
1.92	0.372	2.77	0.118	0.882
2.07	0.397	2.75	0.126	0.874
2.37	0.447	2.70	0.142	0.858
2.59	0.480	2.65	0.153	0.846

Table 3.2: Summary of the flame conditions supported on the porous-plug burner at standard temperature and pressure of 20 °C and 1 atm respectively.

The flame conditions for the porous-plug burner were varied using the flow rates for ethylene and air shown in Table 3.2. A total flow rate of 3.1 litres per minute was used. These flow rates shown in Table 3.2 are determined to achieve the same mass flux ($0.065 \text{ kgs}^{-1}\text{m}^{-2}$) for the premixed gases as in the McKenna burner and to match the standard flame conditions as well as previous measurements in this group [1, 12, 13]. The flow rates listed in Table 3.2 are based on the standard temperature and pressure of 20°C and 1 atm respectively.



Figure 3.7: $\phi = 2.07$ ethylene-air flame on the porous-plug burner.



Figure 3.8: $\phi = 2.37$ ethylene-air flame on the porous-plug burner.

Following the work by Migliorini et al. it is important to test individual burners for the “flat-flame” assumption. The porous matrix of the porous-plug burner is manufactured from stainless-steel. Given the “non-flat” radial distribution reported by Migliorini et al. for a burner with a porous plug manufactured from stainless-steel, it is important to know how the “flat-flame” assumption holds for the porous-plug burner used in this work. Similar measurements of soot radial distribution for the McKenna burner was performed by Dunn [12], and Roy [13] for the porous-plug burner at 15 mm HAB using LII in a $\phi = 2.97$ ethylene-air flame.

The result from Dunn [12] shown in Figure 3.9 gives the soot radial distribution for the porous-plug burner. The profile is constant across most part of the diameter while varying at the edges. The reduction at the edges is insignificant to imaging measurements (LII and LIF) performed at the centre of the burner. The radial uniformity observed at the centre-line in the porous-plug burner tends to confirm the flat-flame assumption. Whilst we should be cautious about extrapolating this conclusion to the lower part of the flame where soot is absent, it may lead us to expect similar vertical concentration profiles in the porous-plug burner to those obtained in the McKenna burner. A comparison of acetylene concentration profiles obtained in the two burners is shown in Chapter 5.

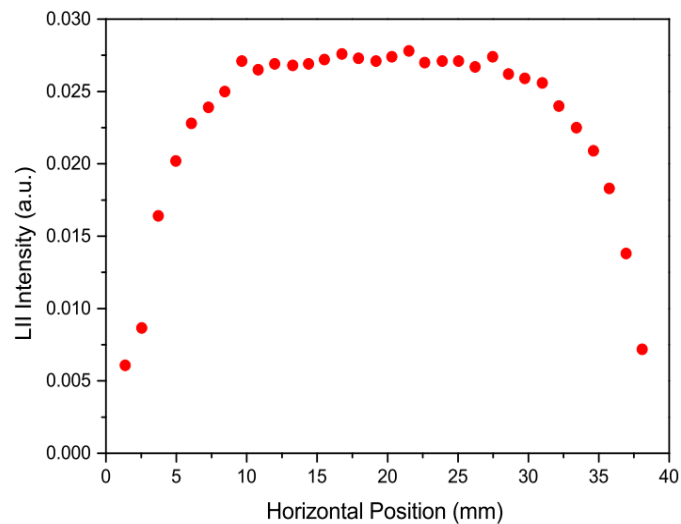


Figure 3.9: Soot horizontal distribution profile across the burner surface at a height of 15 mm in a $\phi = 2.97$ flame (image reproduced from Dunn [1, 12]).

3.2.3 Mass Flow controllers

The laboratory-grade ethylene used in this project is supplied in a pressurised gas cylinder (Supplier: BOC, CP grade N3.0), and the flow is regulated using a suitable regulator. The air is compressed and piped into the laboratory. The piped air is filtered to remove oil droplets and water vapour. The flow rates of ethylene and air

supplied to the burners were regulated using mass-flow controllers (manufacturer: Cole-Palmer). The flow rates are given in units of standard litres per minute at 1 atm and 20 °C. To ensure the correctness of the output from the mass-flow controllers, they have previously been checked against bubble flow-meters, and the results were in agreement within the expected error limits [13]. The manufacturer [15] gives the accuracy of each of the mass flow controllers as $\pm(0.8\% \text{ of reading} + 0.2\%)$ of the full scale.

3.3 Continuous-wave Cavity Ring-down Spectroscopy design

Let us now turn our attention from the burner systems to the cavity-based measurement approaches developed during this project. The basis of the methodology for the cw-CRDS measurements was established in a previous thesis in this research group by Humphries [1]. Further work in this thesis has been undertaken to make certain refinements to the methodology and to establish a comprehensive data-set for acetylene in laminar flat-flames. This then served as a basis for the novel application of cavity-enhanced absorption spectroscopy (CEAS) to sooting flames.

The cw-CRDS methodology previously established by Humphries included the use of two diode lasers and an optical switch to switch between the two lasers. The first laser was used to interrogate the acetylene feature, and the second laser was used to provide a baseline for the measurements. This required tuning the second laser to a region of negligible absorption. In this work, the set-up has been modified to use a single laser which excludes the use of the optical switch. This requires assessing the spectral tuning range of the interrogation laser for a region of negligible narrow-band absorption.

The cw-CRDS design employed in this project is schematically presented in Figure 3.10, showing the various components and connections. Some of the underlying

theory of this approach has been described in Section 2.6.2. The mode of operation, the various components and their functions are described in detail in this section.

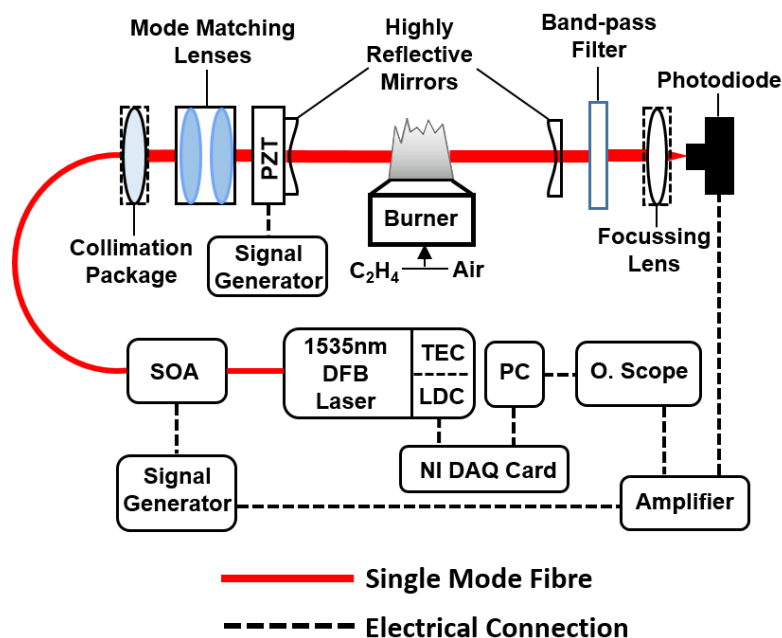


Figure 3.10: cw-CRDS set-up diagram: NI DAQ Card (National Instruments Data Acquisition Card), SOA (Semiconductor Optical Amplifier), LDC (Laser Diode Controller), TEC (Thermoelectric Controller).

3.3.1 Semiconductor Optical Amplifier

A semiconductor optical amplifier (SOA) is used to initiate the ring-down event by interrupting the laser. It also has the important purpose of amplifying the laser so that the intensity of light transmitted through the cavity will be greater than without amplification. This is a significant advantage over the use of an acousto-optic modulator (AOM), which is how cw-CRDS is more typically performed. The light from the laser is fibre-coupled into the SOA (manufactured by Kamelian, OPB-09-15-C-FA) which amplifies the output from the laser. The output from the SOA exits via a fibre-collimator. The maximum output power of the light leaving the SOA is ≈ 20 mW. A DC voltage (10 V which corresponds to a drive current of ≈ 200 mA) at a suitable

frequency of about 300 Hz from a function generator (Agilent Technologies: 33250A) is sent to the SOA. The drive current supplied to the SOA is externally controlled via a voltage signal to the power supply unit. During operation, the intensity of light within the cavity is monitored and compared to the trigger threshold. When this trigger level is reached, the function generator outputs 0 V for a sufficient time (40 ms) to allow the cavity ring-down completely.

3.3.2 Diode Laser

The light source for the cavity ring-down set up is a telecommunication type distributed feedback (DFB) diode laser. Generally, DFB lasers contain a diffraction grating which selectively allows a single wavelength of light to resonate in the laser cavity, making it a single-mode laser. The DFB laser, which is fibre-coupled and housed in a butterfly package, emits light through an SMF-28 single-mode fibre (Thorlabs) [16]. The package includes an optical isolator and a thermoelectric cooler (also known as a Peltier element). The optical isolator prevents optical feedback to the gain medium of the laser, which could potentially damage the laser. The laser (Bookham, LC25W3504CA-J28, mounted on a laser mount from OptoSci Ltd [16]) which has a maximum power output of 15 mW and a centre wavelength of 1535 nm was used to interrogate the P17e acetylene feature at 1535.39 nm. This wavelength choice was employed by Humphries [1] following from modelling of the high-temperature absorption feature of acetylene at 1535.39 nm, which was previously used for the interrogation of acetylene by Wagner et al. [17, 18].

To acquire an absorption spectrum, the laser wavelength has to be tuned over the region of the absorption feature by imposing a modulation on the current supplied to the laser diode via the Thorlabs laser current controller (LDC 210C). The Thorlabs temperature controller (TED 200C) maintains the diode laser at a constant temperature by applying a voltage to the laser TEC, which drives heat transfer to or from the heat sink on which the laser is mounted. The voltage is applied by setting

the temperature controller to a resistance value. For the cw-CRDS measurements, the laser wavelength is tuned sequentially in discrete steps and 32 individual ring-down traces are averaged for each point in the spectrum. An exponential decay is fitted to each averaged ring-down trace to obtain the ring-down time (typically about 10 μ s) which is used to calculate the absorption coefficient via Equation 3.3. Refer to Equation 2.51 for calculating the absorption coefficient where the sample occupies the entire cavity length. Here the flame (with diameter, d) does not occupy the entire cavity length L_c , as such Equation 2.51 becomes Equation 3.3. To allow correction for any drifts in mirror reflectivity or cavity alignment, the wavelength of the laser is tuned in-between measurements to a region (1535.34 nm) where there is insignificant absorption (shown in Figure 3.11) to determine the off-resonance ring-down time, τ_0 . This revised approach allows a simplification of the methodology through the use of a single laser and obviates the need for a fibre-optical switch.

$$\alpha = \frac{L_c}{d} \left(\frac{1}{c\tau} - \frac{1}{c\tau_0} \right) \quad 3.3$$

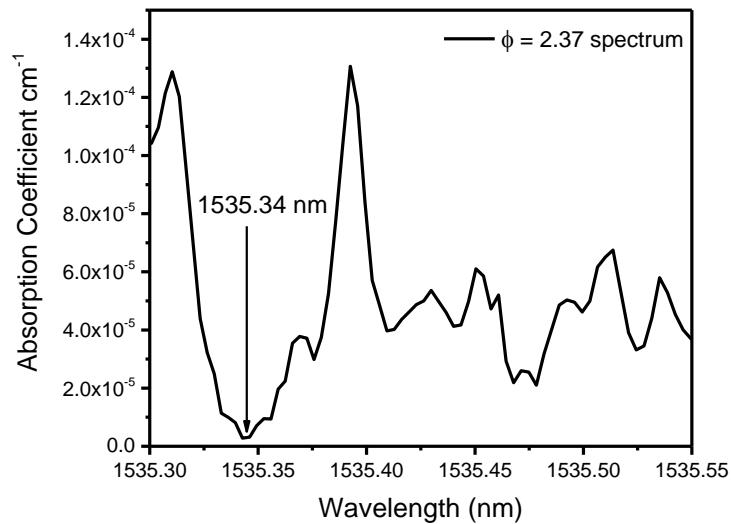


Figure 3.11: cw-CRDS spectra for $\phi = 2.37$ flame recorded at 2 mm above the porous-plug burner surface.

3.3.2.1 Laser Wavelength Characterisation

The spectrum from the measurement shown in Figure 3.11 is obtained as the laser is scanned sequentially and the averaged ring-down trace is recorded at each discrete wavelength in the scan. The duration of this process is about 20 minutes (for spectra recorded in a stoichiometric flame and $\phi = 1.77$ flame) and largely depends on the flame condition, and measurement height as the strong broad-band losses in richer flames slow down the data acquisition rate of the cw-CRDS technique.

To obtain information on concentration from the line strength of the measured absorption feature, it is necessary to map an accurate wavelength scale to the scan. A simple method is to assume a linear current-wavelength tuning rate over the absorption feature. However, the assumption of linearity between current and wavelength is not exactly the case for diode lasers as can be seen in Figure 3.14 which shows the current-wavelength relationship for the 1535 nm diode laser used in this project. This is due to the finite thermal relaxation of the heat deposited in the semiconductor crystal [19]. Also, it is widely known that the output wavelength from diode lasers drifts very slightly with time due to ageing [20]. This casts doubts on the repeatability of wavelength scans.

Options exist such as an optical spectrum analyser, an open optical cavity, and an optical fibre ring resonator for assigning relative wavelength scales to the measured spectrum. The wavelength resolution for optical spectrum analysers may not be quite sufficient, especially when tuning over an extensive wavelength range. An open cavity is susceptible to instabilities. The fibre-ring resonator, which is similar to an open linear cavity in function is preferable because of its higher stability. In this work, we utilised an optical fibre-ring resonator to assign relative wavelength scales to the measured spectrum. The optical fibre-ring resonator is made from two couplers in such a way that a ring cavity is formed, as shown in Figure 3.12. This follows the configuration reported by Urquhart [21] and more details about the optical fibre-ring resonator have been fully described by Duffin [22] and others [23, 24]. The frequency

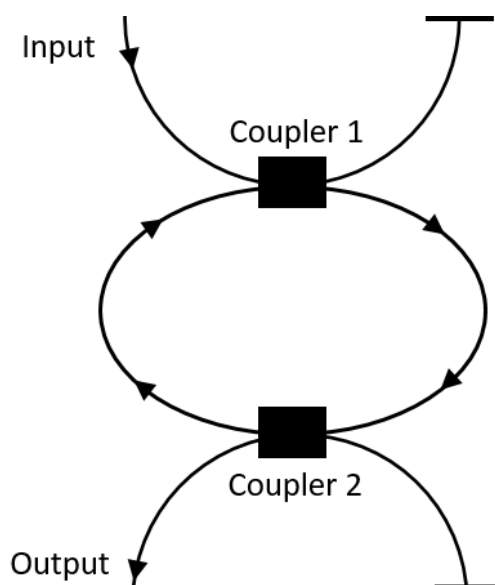


Figure 3.12: Fibre-ring resonator.

response of the fibre-ring resonator is similar to that of the Fabry-Perot etalon (Figure 2.4) and the mode spacing (125.31 MHz) of the fibre-ring resonator was previously characterised by comparing its transmission with the absorption spectrum of a known gas. When light from the laser is fed into the first coupler, a portion of this incident light is coupled into the ring, which is then transmitted through the second coupler.

The second coupler decouples some portion of the light which is detected by a photodiode. The couplers are like partially reflecting mirrors in the case of a linear cavity and as such when the resonance condition given by Equation 2.39 is satisfied, resonant transmission peaks are recorded from the output using a photodiode as seen in Figure 3.13 alongside the related absorption spectrum. The transmission peaks were recorded for both techniques presented in this chapter. The transmission peaks in Figure 3.13 were recorded using the CEAS technique described later for a water vapour spectrum at 1536.29 nm. A similar one had to be taken for cw-CRDS as the spacing between the peaks depend on the rate at which the laser is scanned, and this varies for both techniques. From Figure 3.13, it can be seen that the spacing

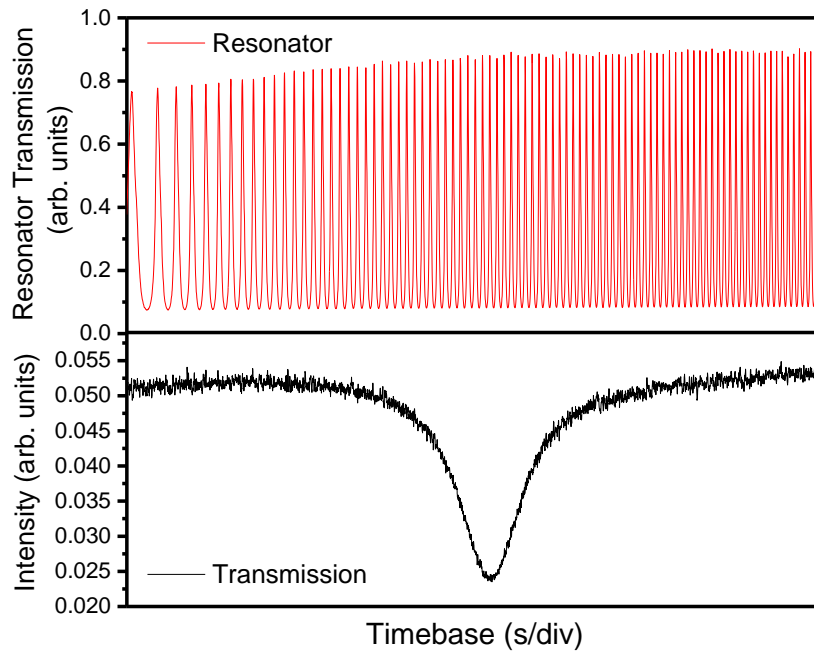


Figure 3.13: Room temperature water absorption signal at 1536.29 nm plotted with a $\delta\nu_{FSR} = 0.4275$ GHz fibre ring resonator output.

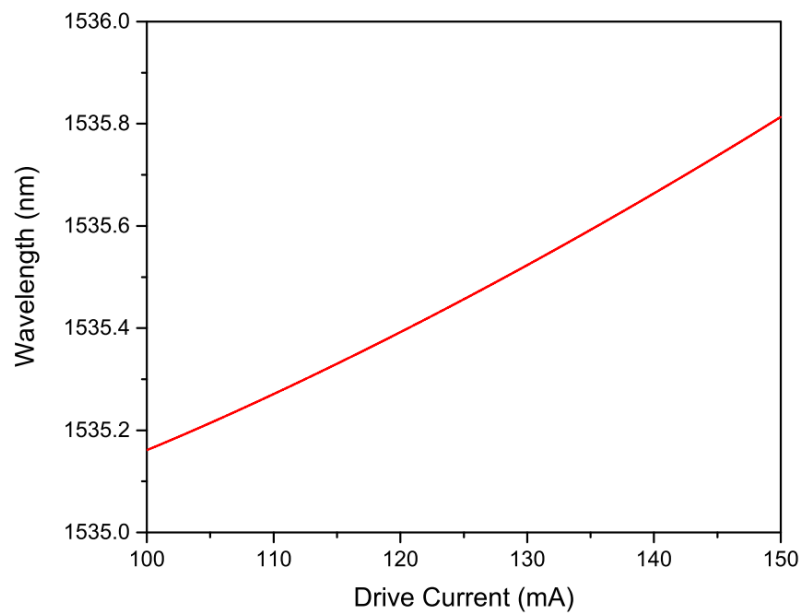


Figure 3.14: Current-wavelength relationship for the 1535 nm laser at a TEC setting of 14.024 k Ω (image taken from Humphries [1]).

in the time axis between successive transmission peaks is not equal due to the nonlinearity in the current-wavelength relationship, as mentioned earlier. The frequency spacing between successive peaks is given by the free spectral range (FSR) which was used to establish a relative frequency scale based on the line centre of the absorption feature. The peak which corresponds to the line centre of the absorption feature is assigned a zero value and a polynomial fit to the peaks based on the time domain gives the relative frequency scale. To obtain an absolute wavelength scale, the centre wavelength value of the absorption feature obtained from HITRAN is assigned to the peak, which corresponds to the line centre of the measured absorption feature. A relationship can then be derived for the absolute wavelength scale and drive current shown in Figure 3.14 for a particular diode temperature.

3.3.3 Optical Cavity

The optical cavity which houses the burner is of 500 mm in length and consists of two mirrors that are 1 inch in diameter with a radius of curvature of 1 m. The stability parameter, g_n calculated from Equation 2.44 is 0.5 for each of the mirrors. This corresponds to a g_1g_2 value of 0.25 which satisfies the stability condition in Equation 2.45. The mirrors have a specification of 99.995% reflectivity at 1550 nm by the manufacturers (CRD Optics). The cavity configuration results in a frequency spacing of 300 MHz for the cavity longitudinal modes. In the cavity, the mirrors are prone to contamination by dust, soot and ambient particles. This increases the mirror losses and affects the sensitivity of the concentration measurements. The mirrors are covered with plates with 4 mm aperture to allow passage of the beam. The plates also help to eliminate coupling into higher-order TEM modes. The waist of a symmetrical cavity is located at the centre of the cavity, as shown in Figure 2.8. The beam corresponding to the TEM_{00} cavity mode has a waist size of 0.465 mm at the centre of the cavity and a Rayleigh distance of 434.5 mm. The waist refers to the $1/e^2$ radius of the beam.

The entry mirror is displaced continuously during operation using a sine-wave signal at an amplitude of 1 V and a frequency of 50 Hz. This varies the cavity length by $3\ \mu\text{m}$ to excite a single longitudinal mode of the cavity into resonance with the laser. To achieve this, the mirror is mounted on a piezoelectric mount from Thorlabs (model: KC1-PZ/M).

3.3.4 Configuration of Mode Matching Optics

To achieve the coupling of the laser light to the TEM_{00} mode of the cavity, two biconvex spherical lenses with focal lengths of 60 mm and 30 mm are used. The lenses are arranged in a Keplerian telescope format [1, 25] (i.e. two convex lenses) as shown in Figure 3.15. This configuration which is shown in Figure 3.15 reduces the beam size to match the waist position of the TEM_{00} mode. The lenses have to be positioned at the right distances relative to the cavity. The distances for the various optics have been calculated, and the beam diameter measured using a knife-edge profiler in previous work by Humphries [1]. Optimisation of the alignment is needed in practice, despite the distances having been calculated. The mode matching brings about a beam diameter of 0.93 mm (which corresponds to the waist size of 0.465 mm) at the centre of the cavity.

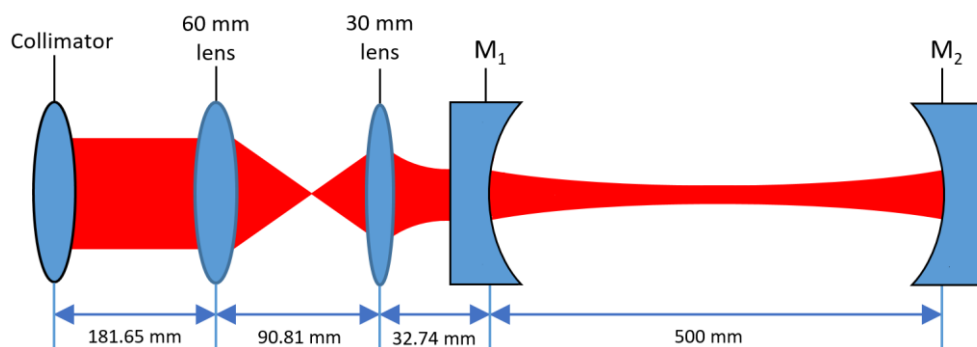


Figure 3.15: Relative positions of the optical cavity and mode-matching optics in a Keplerian telescope format.

3.3.5 Alignment of the Optical Cavity

The aim of the alignment procedure is to couple as much light as possible into the TEM_{00} mode of the cavity. This required very fine adjustments of the mirror positions, and it required a lot of time to develop an aptitude for the best way to do this. The detailed steps below first describe the process of installing the cavity and subsequently describes aligning the installed cavity.

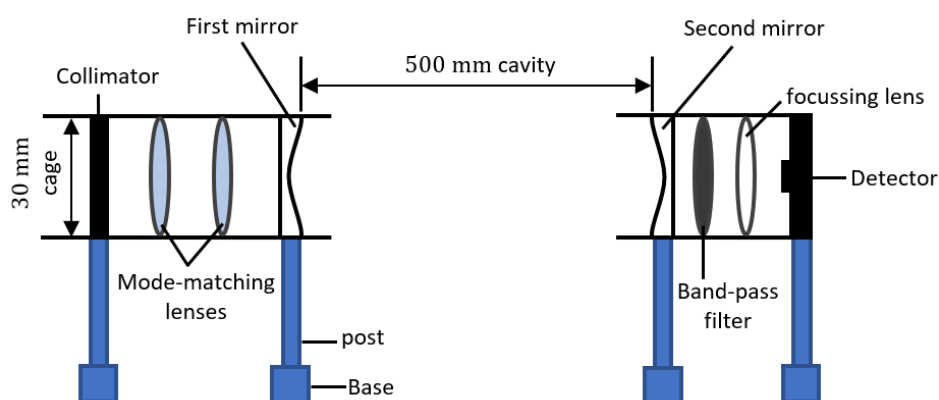


Figure 3.16: Schematic of the cw-CRDS cavity configuration.

The two posts holding the cavity mirror mounts are installed 500 mm apart. The mode-matching optics and collimator are also mounted at the correct distances from the cavity. The optics including the collimator, mode-matching lenses and first cavity mirror are mounted within a 30 mm cage system as shown in Figure 3.16. The second cavity mirror, band-pass filter, focussing lens and the detector are also mounted within a 30 mm cage system (that is 500 mm from the first cavity mirror). The beam exits the fibre through an in-built collimation lens, which is aligned to centre the beam within the cage system. There are two turning mirrors on kinematic mounts, which provides four degrees of freedom required to centre the beam on the two-cavity mirrors.

In aligning the cavity, two infrared (IR) circular cards with a 1 mm hole in the middle are placed on the cavity mirror mounts. The beam is aligned to go through the centre

of the IR card on the first cavity mirror mount by adjusting the knobs on the kinematic mounts of the two turning mirrors. Following this, the beam is aligned to go through the centre of the IR card on the second cavity mirror mount by adjusting the knobs on the mount of the first cavity mirror. The photodetector and focusing lens behind the second mirror are aligned. The second cavity mirror is cleaned and installed, and with the help of a fibre-optic component known as a circulator, the back reflection from the second cavity mirror is aligned so that it is superimposed on the incoming beam by adjusting the knobs on the mount of the second cavity mirror. The circulator is analogous in air-spaced optics to an electronic circulator. It allows you to maximise the collection of retro-reflected light by a single-mode fibre and thus to very precisely overlap the back-reflection with the incident beam. This ensures that the beam from the back reflection goes through the centre of the IR card on the mount of the first mirror. The first cavity mirror is cleaned and installed on a piezoelectric mount, and the back reflection from the second cavity mirror is further optimised.

The piezo mount is translated using a sine wave signal (50 Hz) to excite the modes of the cavity. Upon doing so, a characteristic Airy function pattern (shown in Figure 2.6) is observed on the oscilloscope for the transmitted light detected by the photodiode. Following this, the cavity mirrors and the mode-matching optics are slightly adjusted with the flame *in-situ* to optimise the amplitude of the TEM_{00} modes of the cavity (and to suppress higher-order transverse modes, which appear as additional, lower-amplitude peaks between the fundamental modes).

3.3.6 Detection

The detection of ring-down signals was achieved using an InGaAs amplified photodiode (Thorlabs model: PDA10CS-EC, bandwidth: 17 MHz) placed behind the second mirror. Just before the detector is a bandpass filter (Thorlabs FB1550-40, FWHM of 40 nm at a centre wavelength of 1550 nm) that serves to block radiation from the flame. This filter is critical to the ring-down event as slight disturbances to

the flame could result in varying voltage responses from the detector, leading to false triggers and consequently, false ring-down events. The flame radiation would otherwise dwarf the transmitted laser light, and so very slight fluctuations in the flame would perturb the measurement. For this reason, the trigger level was set at 2.5 V which is high enough to prevent false triggers and low enough for the intensity in the cavity to achieve a true trigger. The wide bandwidth of the mirrors (1490 nm – 1615 nm) can only prevent a narrow range of the radiant flame emission that falls within the bandwidth (700 nm – 1800 nm) of the detector from going through. With the filter in place, the remaining emission is blocked. A one-inch diameter focusing lens is placed after the filter to focus the light onto the detector.

3.3.7 Amplifier

The peculiar challenge with cw-CRDS in comparison to other cavity-enhanced techniques is the triggering of a ring-down event, as discussed in Chapter 2. Transmission fringes can be readily seen on the oscilloscope by eye, but a signal is required in the right form to cease output from the SOA. A variable gain high-speed amplifier (Femto: DHCPA-100) is used to amplify the output of the photodiode above the threshold value of 2.5 V. As described previously, a voltage output from a function generator is used to set the SOA drive current. The output from the high-speed amplifier is fed to the function generator, which has the capacity to accept an external trigger signal. The function generator triggers when a short rise time (few nanoseconds) pulse above 2.5 V is received. Upon receiving this trigger, the function generator cuts the voltage output to zero, thus terminating amplification by the SOA and causing a ring-down event. The trigger threshold is set using the gain settings on the amplifier. It should be noted that the technique is reliant on the bandwidth of all the sub-systems described (detector, amplifier, function generator and SOA power supply) here being high enough to extinguish the incident beam on the timescale required (which is in nanoseconds).

3.3.8 Operation and Data Acquisition

An existing LabView program was used to control the process and establish communication using a GPIB interface between the PC and the oscilloscope (Tektronix: TDS3014B) [1]. LabView is a product of National Instruments used in measurement and control applications. It is a graphical programming language that integrates drivers for measurement hardware from manufacturers. A schematic of the function of the LabView program is shown in Figure 3.17. The program incrementally tunes the laser wavelength by increasing the current applied from the NI DAQ card (National Instruments: PCI 6120) to the laser diode controller and averages 32 ring-down traces for each increment. It is important not to average for too long as long term drifts in the cavity alignment can result in slightly varying ring-down times included in the average [26]. The averaged trace is recorded by the oscilloscope and transferred to the PC. The tuning range was set from 110 mA to 130 mA at 0.2 mA increments (which correspond to the range of 1535.30 nm to 1535.55 nm at ≈ 0.25 nm increments). The amount of time taken to obtain a spectrum varies depending on the set increment value, flame equivalence ratio and the measurement position in the flame. The data acquisition is slower for richer flames due to the strong broad-band losses in those flames. The broadband losses make it difficult for the intensity of light circulating in the cavity to achieve the trigger threshold.

Between each wavelength increment, the laser is tuned to a reference wavelength of 1535.34 nm (corresponding to an LDC setting of 115 mA) corresponding to where absorption is taken to be negligible and 32 ring-down traces are also recorded. This serves to correct any drifts in the effective reflectivity of the mirrors by continuously monitoring the off-resonance ring-down time, τ_0 . The process continues until the full spectrum is acquired. The process is graphically summarised in the flow chart below. The obtained ring-down traces are fitted to the exponential in Equation 2.53 to extract the ring-down times.

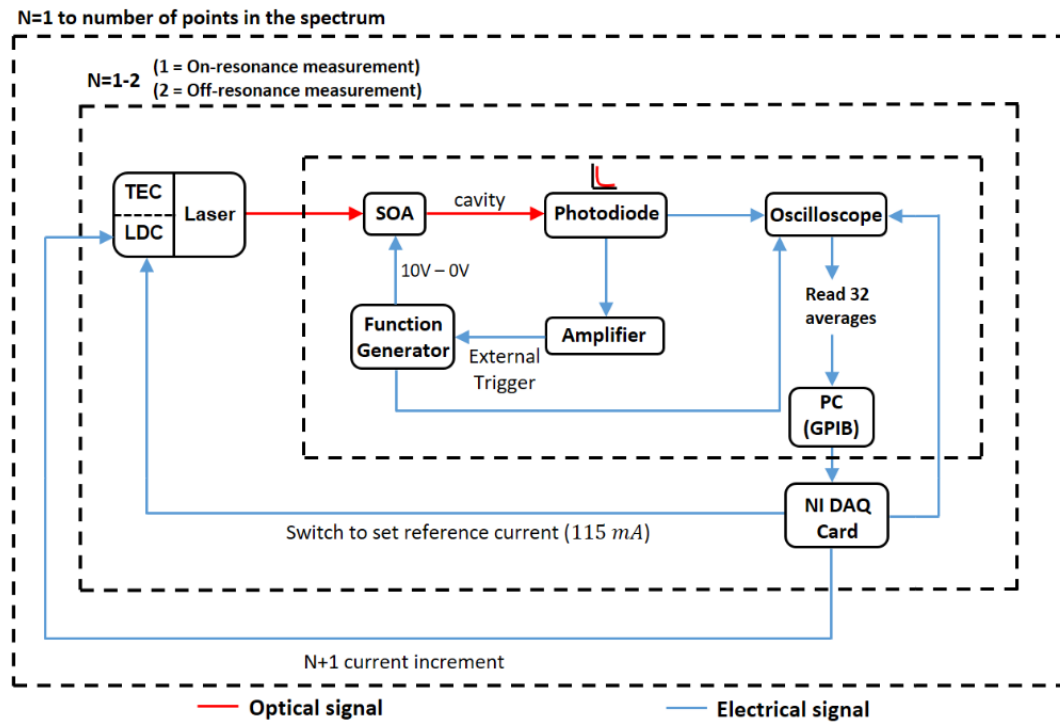


Figure 3.17: Flow chart for the function of the LabView program.

The process described above is an improvement to the previous design by Humphries which included the use of an additional 20 mW diode laser (Anritsu GB5A016, mounted on a laser mount from OptoSci Ltd) with centre wavelength around 1547 nm to correct the measured spectrum against any effects of gradual deposition on the mirrors or degrading alignment during the scan. The laser was tuned to an identified region assumed to have insignificant absorption (which corresponds to a constant drive current ≈ 195 mA). This approach required the use of a fibre-optic component (optical switch) to switch between the lasers, thus complicating the set-up. The lasers were connected to the optical switch preceding the SOA. With the optical switch, only one laser can seed the SOA at a particular time. The current approach in this work obviates the need for this additional laser and fibre-optic component as it allows the laser to switch between the probe and reference wavelengths.

A major advantage of the cw-CRDS technique is that it is self-calibrating and possesses good spatial resolution. However, its sensitivity when applied to flame measurements can be significantly degraded as the flame disturbs the delicate mode-matching process. Also, the broad-band losses, especially in the richer flames, result in slow data acquisition for the cw-CRDS technique. Despite its success in generating *in situ* concentration profiles of acetylene in flames (to be presented in Chapter 4), these shortcomings of cw-CRDS when applied to flames led us to consider whether another cavity-based approach may be suitable for measurement of trace species in high-temperature reacting flows. Therefore, the bulk of the work presented in this thesis concerns the development of the variant method of cavity-enhanced absorption spectroscopy for this purpose.

3.3.9 Experimental Procedure for cw-CRDS Measurements of Acetylene

The experimental procedure for the cw-CRDS measurements of acetylene in Chapter 4 is presented in this section. Although some elements of the procedure have been alluded to previously, the detailed steps which would allow for these measurements to be repeated even by another researcher is presented here. The optical and electronic components of the experimental set-up which have been mentioned in Section 3.3.1-Section 3.3.7 will be referenced here.

The cavity is installed on the optical table with the mirrors mounted on posts that are 500 mm apart. Other optical components (collimator, mode-matching lenses, detector, etc.) are installed following the description in Section 3.3.5. The output of the laser is coupled to the input of the SOA, and the output of the SOA is coupled to the collimator. This couples the laser beam into the cavity. The laser diode controller is connected to the NI DAQ card housed in the PC. Other components are connected as shown in the set-up diagram in Figure 3.10. The porous-plug burner described in Section 3.2.2 (with the stabilization plate affixed) is placed at the centre of the cavity. The supply of air and ethylene is piped to mass flow controllers and the output of the

mass flow controllers is connected to the burner. The flow rates for the equivalence ratios are shown in Table 3.2.

With the cavity set up and the electronic components connected, the power supply to all electronic components (PC, PZT, signal generators, amplifier, detector, oscilloscope, SOA, laser diode and temperature controllers) is switched on. The laser diode and temperature controllers are activated so that the beam propagates through the cavity. The cavity is then aligned following the description in Section 3.3.5. Ethylene and air are properly piped to the burner from the mass flow controllers and the flame is turned on following which the alignment is maximised. The flame stability is improved using temporary shields placed around the burner.

The 1535 nm laser is set to the desired wavelength region by inputting the setting of 14.42 k Ω to the laser temperature controller. The signal generator that drives the PZT is set to 1 V at 50 Hz, and the signal generator that drives the SOA is set to 10 V at 300 Hz. The LabView program described in Section 3.3.8 is activated and the spectral tuning range (110 mA to 130 mA), the off-resonance current (115 mA) as well as the laser current increment value (0.2 mA) for the measurement is set in the program. The program scans the laser incrementally and the intensity within the cavity builds up. When the intensity reaches a pre-set threshold of 2 V, the signal generator that drives the SOA outputs 0 V, switching off the SOA and 32 ring-down traces are recorded and averaged by the LabView programme. In between the laser current increment, the LabView program records the off-resonance ring-down time (τ_0) by switching the current applied to the laser diode to 115 mA. The process is repeated for each HAB.

The extinction measurements are also performed in the same manner as described above with the laser tuned to the reference wavelength of 1535.34 nm. The measurement background is obtained before the flame is turned on following which the flame is turned on and switched off, and the laser is immediately scanned to obtain the ring-down trace.

3.4 Cavity-Enhanced Absorption Spectroscopy Design

The CEAS technique has a set-up that is similar to the cw-CRDS set-up in Figure 3.10 as it utilises similar components such as the laser, SOA and detection set-up. The technique is less demanding than cw-CRDS with regards to the experimental set-up and methodology. The major distinction between cw-CRDS and CEAS, simply put, is that the resonance condition established between the laser and the modes of the cavity is never broken and this obviates the need for optical switch electronics [27]. The development of the current CEAS approach required that some modification be made to the cw-CRDS set-up, and some of the challenges encountered in doing this as well as the approaches taken are discussed next.

3.4.1 Challenges in implementing CEAS for flame measurements and approaches taken

In developing the CEAS approach, much attention had to be paid to the challenging aspects which are actually the areas of distinction between the CEAS and cw-CRDS techniques. These include the length of the cavity (cavity configuration), cavity alignment (mode density), mode of operation and calibration as the CEAS technique is not self-calibrating. The cavity length is very important to the CEAS technique as together with the mirrors, it determines the cavity mode structure. In choosing the length for the cavity, the goal is to prevent the degeneracy of the higher-order transverse modes. At certain ratios of cavity length to the radius of curvature of the mirrors, the cavity modes can be degenerate [28]. To determine a suitable cavity length, several lengths were tested, including the 500 mm length used for the previous cw-CRDS measurements. The configuration provided by these cavity lengths did not support a near-continuum mode structure for the cavity. Following the iterative approach, a cavity length of 750 mm was adopted.

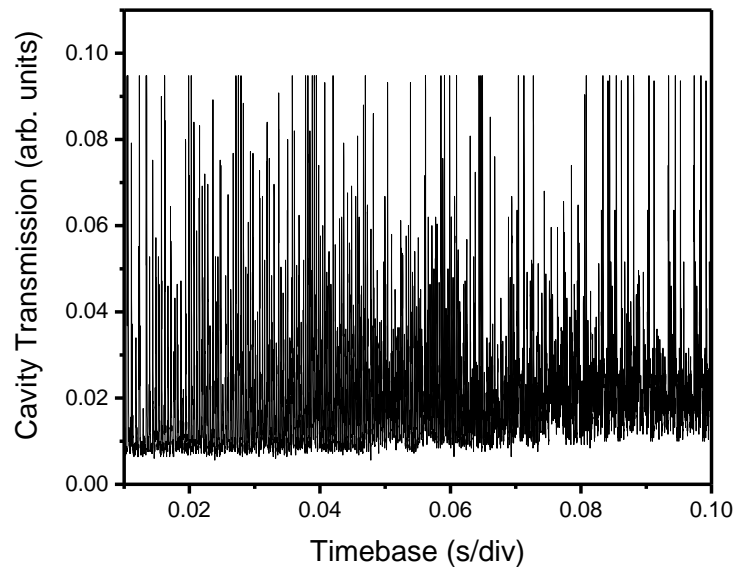


Figure 3.18: A single scan of the cavity transmission.

The higher-order transverse modes are very important to the CEAS technique, and in keeping with this, it is important that the cavity is aligned in a way that increases the density of these modes. In contrast, the cw-CRDS approach matched the frequency of the laser beam to the TEM_{00} mode of the cavity and this was achieved using mode-matching lenses. In aligning the CEAS cavity, these lenses were initially displaced to excite several higher-order transverse modes of the cavity. This was challenging because the lenses suppressed the excitation of these modes. The lenses had to be taken out, resulting in a dense mode cavity structure, as seen in Figure 3.18. The excitation of several modes of the CEAS cavity results in a larger beam waist which was not measured. However, being able to obtain a spectrum at 1 mm as shown in Chapter 5 helps us place an upper bound of 1 mm for the beam waist at the centre of the cavity, which gives an idea of the spatial resolution.

During operation, a ramp signal is applied to scan the laser at a frequency of 10 Hz and the cavity length is slowly modulated to randomly sample the cavity transverse modes. The laser frequency could be scanned rapidly while slowly modulating the cavity length or vice versa [29-31]. To determine a suitable laser scan frequency,

several frequencies were tested. The higher frequencies were seen to distort the spectrum, as seen in Figure 3.19 for spectra recorded with laser scan frequencies of 10 Hz and 1 kHz. The 10 Hz frequency which is typical for CEAS measurements allows for sufficient interaction-time between the cavity modes and the laser frequency as observed by Mazurenka et al. in a comparison between 10 Hz, 100 Hz and 500 Hz scanning frequencies [26]. This increases the intensity in the cavity and consequently improves the SNR. A much lower frequency of 0.5 Hz was chosen to modulate the cavity length. However, varying the cavity modulation frequency was insignificant to the measurements. The spectra shown in Figure 3.19 were obtained by applying an amplitude of 150 mV to the ramp signal used to scan the laser. To obtain a broader spectrum which extends over the spectral region covered with the cw-CRDS technique, a higher amplitude of 400 mV was adopted.

The raw measurements obtained using the CEAS approach show relative absorption and would need to be calibrated. The challenge of calibration is inherent to CEAS and is a major distinction between the CEAS and cw-CRDS techniques. Several schemes

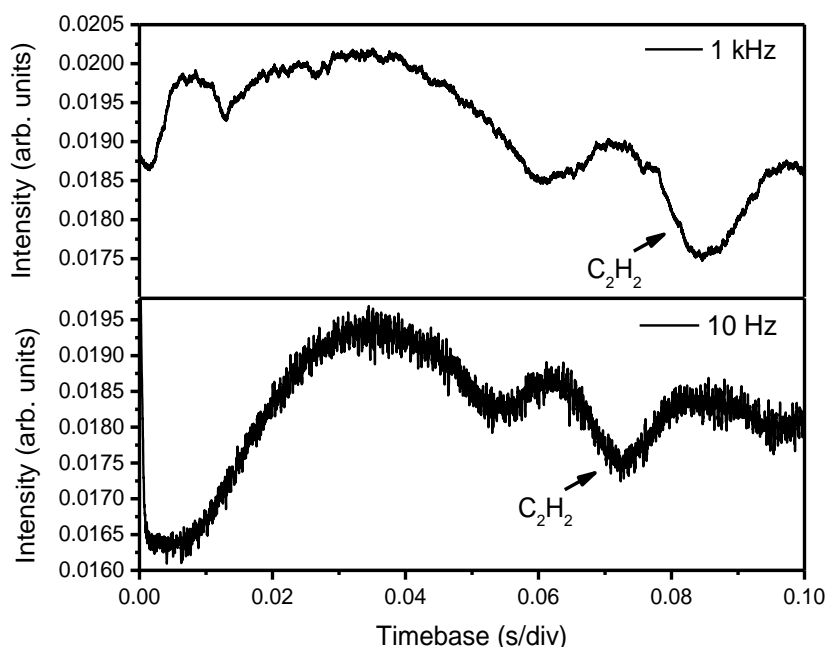


Figure 3.19: Acetylene spectra recorded with frequencies of 1 kHz and 10 Hz in a $\phi = 1.92$ flame at 3 mm above the porous-plug burner surface.

were stated in the literature (Section 2.6.4) for calibrating CEAS measurements, some of which erode the CEAS advantage of a relatively simple set-up when compared to cw-CRDS. Keeping in line with this advantage, a procedure to calibrate the measurements was developed. This procedure is a cavity ring-down technique different from the one discussed earlier in this chapter for obtaining acetylene measurements as no mode-matching is required. It is essential to state that the alignment is not altered. This is necessary since the calibration must be based on the specific cavity alignment used for CEAS. The calibration procedure involves sending a square-wave signal of 2 kHz (was arrived at iteratively) frequency to the SOA driver, resulting in an on-off modulation of the light entering the nitrogen-purged cavity. To the best of the author's knowledge, this is the first known application of this technique to calibrate CEAS flame measurements.

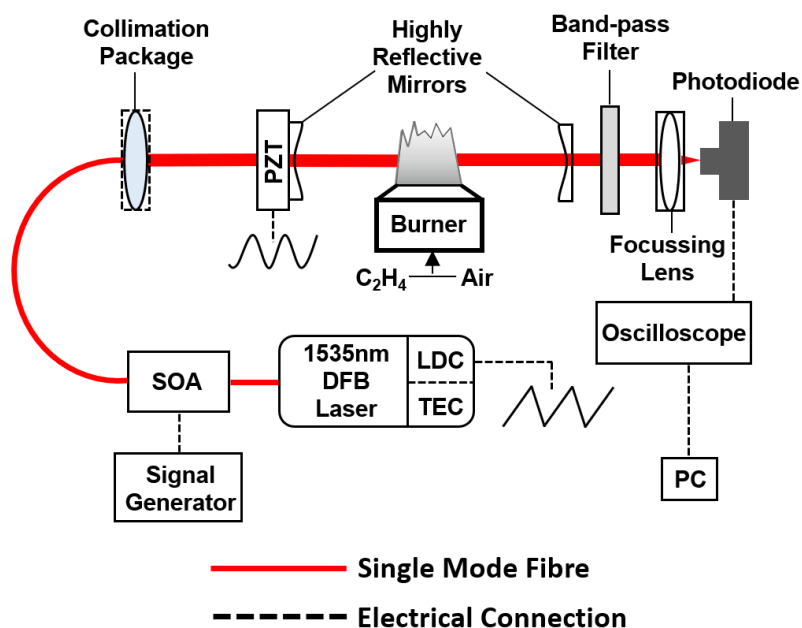


Figure 3.20: CEAS set-up diagram: SOA (Semiconductor Optical Amplifier), LDC (Laser Diode Controller), TEC (Thermoelectric Controller).

Following this description of the challenges and approaches taken, the specific components of the CEAS set-up shown in Figure 3.20, and their functions are described next.

3.4.2 Diode Laser

The laser source for acetylene measurements is as described in Section 3.3.2 for measurements of acetylene. In the CEAS experiments, the SOA is only being used to amplify the laser output. A 1573 nm laser (JDS Uniphase CQF915/208-19060, mounted on a laser mount from OptoSci Ltd) with a maximum power output of 20 mW was employed for measurements of OH species. The 1535 nm and 1547 nm lasers were used to obtain wide spectral scans using the CEAS set-up. During operation, a ramp signal of 10 Hz frequency from a function generator is sent through the laser diode controller to the laser as seen in the set-up diagram. This scans the wavelength over the desired range determined by the amplitude of the ramp signal. The wavelength of the lasers is characterised according to Section 3.3.2.1.

3.4.3 Optical Cavity

The cavity just like in the cw-CRDS set-up consists of two highly reflective mirrors. The spacing between the mirrors is very crucial in CEAS as it determines the frequency spacing of cavity modes (both longitudinal and transverse). As stated earlier, the goal in setting up the cavity was to adopt a configuration which enabled the cavity to reduce the degeneracy of the higher-order transverse modes. This would allow for a dense mode spectrum, and thus a near continuum of transmission as the laser wavelength is scanned as shown in Figure 3.18. A 750 mm spacing was adopted (resulting in a cavity FSR of 200 MHz) and the stability parameter, g_n calculated from Equation 2.44 is 0.25 for each of the mirrors. This gives a g_1g_2 value of 0.0625 which satisfies the stability condition in Equation 2.45.

During the course of the experiments, the mirrors are covered with plates to reduce fouling. The plates have adjustable apertures which are opened wide enough to allow passage of the beam and coupling of light into higher-order transverse cavity modes. This is in contrast to cw-CRDS where the plates serve to prevent coupling of light to these modes. The entry cavity mirror is held on a piezoelectric mount which is modulated using a sine-wave signal of 150 mV at 0.5 Hz.

3.4.4 Cavity Alignment

Just like cw-CRDS, the alignment of the cavity is very critical to the quality of the output signal from the cavity as a good alignment ensures that enough light resonates within the cavity. The mode-matching lenses utilised for the cw-CRDS measurements were removed to allow a dense mode transmission from the cavity. To begin the alignment, the posts holding the mirror mounts are adjusted to be 750 mm apart. The preliminary alignment steps are similar to that of cw-CRDS described in Section 3.3.5. Following the maximisation of the back reflection after mounting the first cavity mirror, the mirrors are carefully adjusted to maximise transmission from a near-continuum of higher-order modes of the cavity. In this way, the transmitted spectrum (especially with averaging) has the appearance of a direct absorption spectrum, since light can be transmitted through the cavity at all wavelengths due to the dense mode spectrum. This is monitored using the oscilloscope. The flame is introduced, and the cavity alignment is further optimised.

3.4.5 Operation and Data Acquisition

During operation, the laser is scanned over the set wavelength range by applying a ramp signal of 400 mV at a frequency of 10 Hz using a function generator to the laser diode controller. This scanned over a broader range (0.5 nm) and with better spectral resolution (5×10^{-5} nm) than the cw-CRDS (0.25 nm) measurements which were acquired with a resolution of (2.5×10^{-3} nm). A second function generator sends a

sine-wave signal of 0.5 Hz to the entry cavity mirror mount which moves the entry mirror. The transmitted intensity during a scan is averaged (over 512 wavelength sweeps) by the oscilloscope. Averaging so many scans improves the SNR of the measurements. The absorption spectrum acquired on the oscilloscope is transferred to the PC using a LabView programme. The Cavity-enhanced absorption experiments were performed under a range of flame conditions.

From the above data, the transmitted intensity I , in Equation 3.4 is obtained directly. After the laser is switched off, a flame background measurement is taken, and this value is subtracted from the transmitted intensities. This is done for each measurement location. It should be noted that this is only relevant to the measurement of broad-band extinction: the acetylene spectra are referenced to an "off-resonance" point in the spectrum as described above.

Calibration is a vital feature of cavity-enhanced measurements, since the flame measurements already described provide us with what looks like a direct absorption spectrum but with no knowledge of the effective path-length. Note that the intention is to make quantitative CEAS measurements that are entirely independent of the cw-CRDS measurements described previously (CRDS having the advantage of being an inherently calibration-free approach). To quantify the absorption coefficient from CEAS data, it was necessary to measure both the cavity transmission, I_0 , and the effective mirror reflectivity, R , in the absence of absorption. These quantities can then be used to determine the absorption coefficient via Equation 3.4, shown again below. We take the diameter of the flame to be that of the burner and this is used in Equation 3.4 for calibrating the absorption spectrum where the diameter of the flame d is used in place of the cavity length, L_c (refer to Equation 2.57). This is because the flame (sample) does not occupy the entire length of the cavity.

$$\alpha = \frac{I_0 - I}{I} \left(\frac{1 - R}{d} \right) \quad 3.4$$

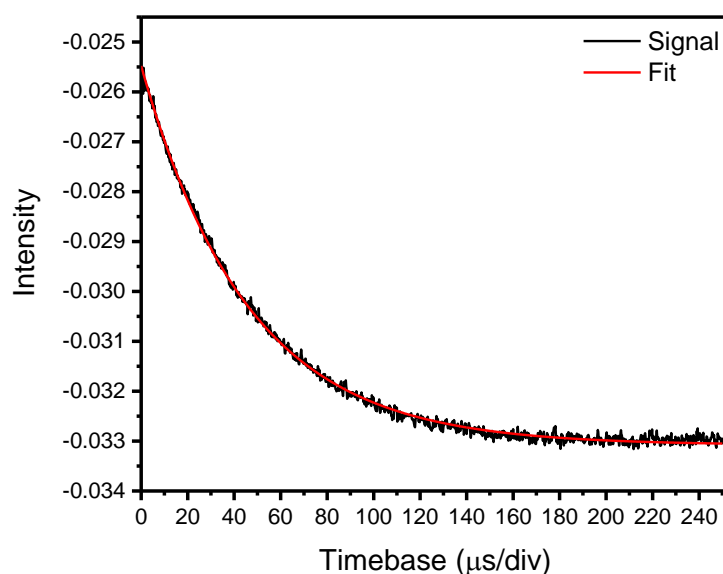


Figure 3.21: Ring-down trace from a nitrogen-purged cavity plotted with a fit.

I_o was measured with the purged cavity, with all other experimental settings held constant from the flame measurements. The cavity was purged by flowing nitrogen through a tube placed in the cavity. This is to prevent absorption by ambient water and effects of ambient particles such as dust. Comparing I_o to I , gives an I_o/I value of ~ 18 . The effective mirror reflectivity, R is calculated from the ring-down time of the nitrogen-purged cavity obtained using the developed cavity ring-down technique wherein the CEAS alignment is not altered. The light entering the cavity is modulated using a square-wave signal of 2 kHz frequency. Averages of 512 individual ring down traces were recorded. Figure 3.21 shows a ring-down trace from the nitrogen-purged cavity plotted with a fit to extract the ring-down time. The effective mirror reflectivity, R is calculated from the ring-down time, τ according to Equation 3.5 (refer to the derivation of Equation 2.51). The ring-down times ($\sim 50 \mu\text{s}$) measured before and after measurements were in good agreement given that a sequence of the experiments was always performed within an hour. This is also the case for I_o obtained before and after the measurements.

$$R = 1 - \left(\frac{L_c}{\tau c} \right) \quad 3.5$$

Experiment	Flame (ϕ)	Burner
Acetylene measurements	1.0, 1.77, 2.07, 2.37	McKenna, porous-plug
Extinction measurements	1.0, 1.4, 1.77, 2.07, 2.37, 2.59	McKenna, porous-plug
Radial measurements of acetylene	1.77, 2.07, 2.37	McKenna, porous-plug
Broad spectral scans	1.0, 1.77, 2.07, 2.37	porous-plug
Hydroxyl radical measurements	0.8, 1.0, 2.07	porous-plug

Table 3.3: Summary of CEAS experiments.

The above CEAS experimental procedure developed for flame measurements was used to obtain the results shown in Chapter 5. Following the success of the technique in generating *in situ* concentration profiles of acetylene in flames, the technique was extended to obtain flame measurements of OH radical which are presented in Chapter 6. The wavelength choices for the OH radical measurements were chosen based on the availability of a suitable diode laser (1573 nm) and careful examination of the spectral region. Before the consideration of OH radical, the wide spectral scans were obtained using the 1535 nm and 1547 nm lasers. This was done to look out for absorption by any other flame species. The spectra obtained using both lasers are also shown in Chapter 6. The CEAS technique was also applied to obtain radial measurements of acetylene in both burners used in this work. This would not be possible with the cw-CRDS technique as radial translation of the flame would adversely degrade the mode-matching process. The cw-CRDS technique was used to

acquire acetylene concentration measurements and extinction measurements. Table 3.3 presents a summary of the CEAS experiments performed in this work.

3.4.6 Experimental Procedure for CEAS Measurements of Acetylene

The steps in the experimental procedure for the CEAS measurements of acetylene is presented here. Just like the cw-CRDS technique, the cavity is first installed on the optical board with the cavity mirrors placed 750 mm apart. The other optical components (collimator, filter, focusing lens, detector, etc) are also installed in a 30 mm cage system from Thorlabs as described in Section 3.3.5. The burner is placed at the centre of the cavity and is connected to the mass flow controllers. The electronic components which have been previously discussed are connected as shown in the set-up diagram (Figure 3.20) and the power supply is switched on. The cavity is aligned following the description in section 3.4.4 during which the flame is introduced. The flow rates of air and ethylene for the McKenna and porous-plug burners are shown in Table 3.1 and Table 3.2 respectively. The shroud gas (air) is piped to a rotameter and then to the McKenna burner at a setting of 15 litres per minute as mentioned in Section 3.2.1. For the porous-plug burner, temporary shields are put in place to enhance the flame stability.

The 1535 nm laser is set to the desired wavelength by inputting the setting of 14.42 k Ω to the laser temperature controller and 122 mA to the laser diode controller. The signal generator that drives the PZT is set to 150 mV at 0.5 Hz, and the signal generator that drives the SOA is set to a DC voltage of 10 V. A ramp signal of 400 mV at a frequency of 10 Hz is sent to the laser diode using a signal generator. This scans the laser over the desired wavelength range and the transmitted intensity, I is averaged by the oscilloscope over 512 wavelength sweeps yielding an acetylene spectrum. The laser is switched off and the flame background measurement is recorded. After this, the flame is extinguished, and the cavity is purged using

nitrogen. The above process for obtaining the spectrum is repeated to obtain the cavity transmission, I_o in the purged cavity (absence of an absorber).

To calibrate the measurements, a measurement of the ring-down time of the nitrogen-purged cavity is obtained with the alignment of the cavity unaltered by sending a square wave signal of 2 kHz to the SOA. This modulates the light entering the cavity and 512 traces of the ring-down signal are averaged by the oscilloscope.

The extinction measurements are obtained using the process described above with the laser tuned to the reference wavelength. This is done immediately the flame is switched off, and the intensity, I (512 averages) is recorded. The ring-down trace and transmitted intensity, I_o in a purged cavity for calibrating the measurements are obtained as described above.

3.4.7 Experimental Procedure for CEAS Measurements of OH Radical

The CEAS measurements of OH radical presented in Chapter 6 largely follows the same procedure as that presented for the acetylene measurements. The initial steps of installing and aligning the cavity follow as described above. The measurements of OH radical were only performed in the porous-plug burner as such the procedure excludes the use of the shroud gas used in the McKenna burner. A 1573 nm diode laser was employed to access the desired wavelength regions (1572.4 nm and 1572.14 nm). The laser diode controller is set at 90 mA and the laser temperature controller is set at 12.7 k Ω for the 1572.4 nm OH line. To probe the 1572.14 nm OH line, the laser temperature controller and laser diode controller are set at 14.5 k Ω and 90 mA respectively. At the end of all measurements described in this chapter, the wavelength tuning rate of the lasers used were characterised using an optical fibre-ring resonator as described in Section 3.3.2.1.

3.5 Summary

The methodology and design of the cavity-enhanced set-ups used for the combustion measurements in the project have been described in this chapter. The various components of the design and their functions were discussed as well as the mode of operation. The flame-burner configuration was discussed with respect to the “flatness” of the burners employed in this project. A range of flames from fuel lean to fuel-rich conditions was investigated using the described set-ups allowing for proper monitoring of soot.

3.6 References

1. Humphries, G., *Novel diode laser absorption techniques for combustion diagnostics*, in *Department of Electronic and Electrical Engineering*. 2017, University of Strathclyde: Glasgow. p. 144.
2. Efthimos, K.N.a.Z. *Analysis of flat burners used to study gaseous pollutants emitted from combustion of hydrocarbons* in *2nd International Conference on Waste Management, Water Pollution, Air Pollution, Indoor Climate (WWAI'08)* 2008. Corfu, Greece.
3. Weigand, P., R. Lückerath, and W. Meier, *Documentation of flat premixed laminar CH₄/air standard flames: Temperatures and species concentrations*. URL <http://www.dlr.de/vt/datenarchiv>, 2003.
4. Schulz, C., et al., *Laser-induced incandescence: recent trends and current questions*. *Applied Physics B*, 2006. **83**(3): p. 333.
5. Adelaide, U.o. *Laminar Flames: International Sooting Flame (ISF) Workshop*. [cited 2020 26-02-2020]; Available from: <https://www.adelaide.edu.au/cet/isfworkshop/data-sets/laminar-flames#isf-4-linked-premixed-flames-mckenna-burner-stabilised-flames-slightly-lifted-flames>.
6. Prucker, S., W. Meier, and W. Stricker, *A flat flame burner as calibration source for combustion research: Temperatures and species concentrations of premixed H₂/air flames*. *Review of scientific instruments*, 1994. **65**(9): p. 2908-2911.
7. Gregor, M.A. and A. Dreizler, *A quasi-adiabatic laminar flat flame burner for high temperature calibration*. *Measurement Science and Technology*, 2009. **20**(6): p. 065402.

8. Olofsson, N.-E., et al., *Are sooting premixed porous-plug burner flames one-dimensional? A laser-based experimental investigation*. Combustion science and technology, 2013. **185**(2): p. 293-309.
9. Campbell, M.F., et al., *A small porous-plug burner for studies of combustion chemistry and soot formation*. Review of Scientific Instruments, 2017. **88**(12): p. 125106.
10. Migliorini, F., et al., *How "flat" is the rich premixed flame produced by your McKenna burner?* Combustion and Flame, 2008. **153**(3): p. 384-393.
11. Axelsson, B., R. Collin, and P.-E. Bengtsson, *Laser-induced incandescence for soot particle size measurements in premixed flat flames*. Applied Optics, 2000. **39**(21): p. 3683-3690.
12. Dunn, J., *Investigation of premixed sooting flames by combined laser induced incandescence and laser induced fluorescence*, University of Strathclyde. Dept. of Chemical and Process Engineering, Thesis [Ph. D] -- University of Strathclyde, 2013.
13. Roy, R.G., *Laser induced incandescence imaging for the investigation of soot formation in laminar flames*, University of Strathclyde. Department of Chemical and Process Engineering, Thesis [Ph. D.] -- University of Strathclyde, 2019.
14. Hu, Y., *Radical concentration and temperature measurements in sooting flames by cavity ringdown spectroscopy and laser-induced fluorescence*, in *Chemical and Process Engineering*. 2015, University of Strathclyde: Glasgow, United Kingdom.
15. ColeParmer, *Precision gas flow meter operating manual*. 2014.
16. Li, L., et al., *Absorption line profile recovery based on residual amplitude modulation and first harmonic integration methods in photoacoustic gas sensing*. Optics communications, 2011. **284**(1): p. 312-316.
17. Wagner, S., et al., *In situ TDLAS measurement of absolute acetylene concentration profiles in a non-premixed laminar counter-flow flame*. Applied Physics B, 2012. **107**(3): p. 585-589.
18. Wagner, S., et al., *TDLAS-based in situ measurement of absolute acetylene concentrations in laminar 2D diffusion flames*. Proceedings of the Combustion Institute, 2009. **32**(1): p. 839-846.
19. Teichert, H., T. Fernholz, and V. Ebert, *Simultaneous in situ measurement of CO, H₂O, and gas temperatures in a full-sized coal-fired power plant by near-infrared diode lasers*. Applied optics, 2003. **42**(12): p. 2043-2051.
20. Chung, Y.C., J. Jeong, and L. Cheng, *Aging-induced wavelength shifts in 1.5- μ m DFB lasers*. IEEE photonics technology letters, 1994. **6**(7): p. 792-795.
21. Urquhart, P., *Compound optical-fiber-based resonators*. JOSA A, 1988. **5**(6): p. 803-812.
22. Duffin, K., *Wavelength modulation spectroscopy with tunable diode lasers : a calibration-free approach to the recovery of absolute gas absorption line-*

-
- shapes*, University of Strathclyde. Dept. of Electronic and Electrical Engineering, Thesis [Ph. D] -- University of Strathclyde, 2007.
23. Johnstone, W., et al., *Tunable Diode Laser Spectroscopy for Industrial Process Applications: System Characterization in Conventional and New Approaches*. IEEE Sensors Journal, 2008. **8**(7): p. 1079-1088.
 24. Bain, J.R.P., *Near infrared tunable diode laser spectroscopy for aero engine related applications*, in *Dept. of Electronic and Electrical Engineering*. 2012, Thesis [Eng. D] -- University of Strathclyde: Glasgow.
 25. Humphries, G.S., I.S. Burns, and M. Lengden, *Application of Continuous-Wave Cavity Ring-Down Spectroscopy to Laminar Flames*. IEEE Photonics Journal, 2016. **8**(1).
 26. Mazurenka, M., et al., *Cavity ring-down and cavity enhanced spectroscopy using diode lasers*. Annual Reports Section "C" (Physical Chemistry), 2005. **101**: p. 100.
 27. Berden, G., R. Peeters, and G. Meijer, *Cavity ring-down spectroscopy: Experimental schemes and applications*. International Reviews in Physical Chemistry, 2000. **19**(4): p. 565-607.
 28. Papageorge, A.T., A.J. Kollár, and B.L. Lev, *Coupling to modes of a near-confocal optical resonator using a digital light modulator*. Optics Express, 2016. **24**(11): p. 11447-11457.
 29. Engeln, R., et al., *Cavity enhanced absorption and cavity enhanced magnetic rotation spectroscopy*. Review of scientific instruments, 1998. **69**(11): p. 3763-3769.
 30. Bakowski, B., et al., *Cavity-enhanced absorption spectroscopy with a rapidly swept diode laser*. Applied Physics B, 2002. **75**(6-7): p. 745-750.
 31. Peeters, R., G. Berden, and G. Meijer, *Near-Infrared Cavity Enhanced Absorption Spectroscopy of Hot Water and OH in an Oven and in Flames*. Applied Physics B-Lasers and Optics, 2001. **73**: p. 65-70.

Chapter 4 : Flame Measurements of Acetylene using cw-CRDS

4.1 Introduction

The cw-CRDS methodology employed in this project, as well as the importance of acetylene in soot formation, have been discussed in Chapter 3 and Chapter 1, respectively. Previous techniques employed in flame measurements of acetylene have also been presented in Chapter 1. This chapter presents the measurements of acetylene obtained using the already described cw-CRDS methodology in the porous-plug burner and the analysis of the results. The measurements build on the first demonstration of *in situ* cw-CRDS flame measurements of acetylene [1]. This first demonstration utilised a set-up which has been modified to perform the current measurements. The current approach eliminates some components in the previous set-up, which include an optical switch and an extra diode laser for normalising the spectra. The spectra obtained with the current approach have been repeated and are reproducible. Also, the spectra are largely consistent with the spectra from the previous demonstration. These show that sensitive measurements can be obtained without the components excluded from the previous set-up. A limited data-set without repetitions were obtained in the previous measurement, hence the need for more measurements which are presented in this chapter.

4.2 Model of Expected Flame Spectrum

A simulation from HITRAN of the P17e acetylene feature, which was interrogated in this measurement is shown in Figure 4.1. It was also necessary to simulate high-temperature water vapour spectrum because at elevated temperatures as obtained in flames, there is a significant presence of high-temperature water vapour which

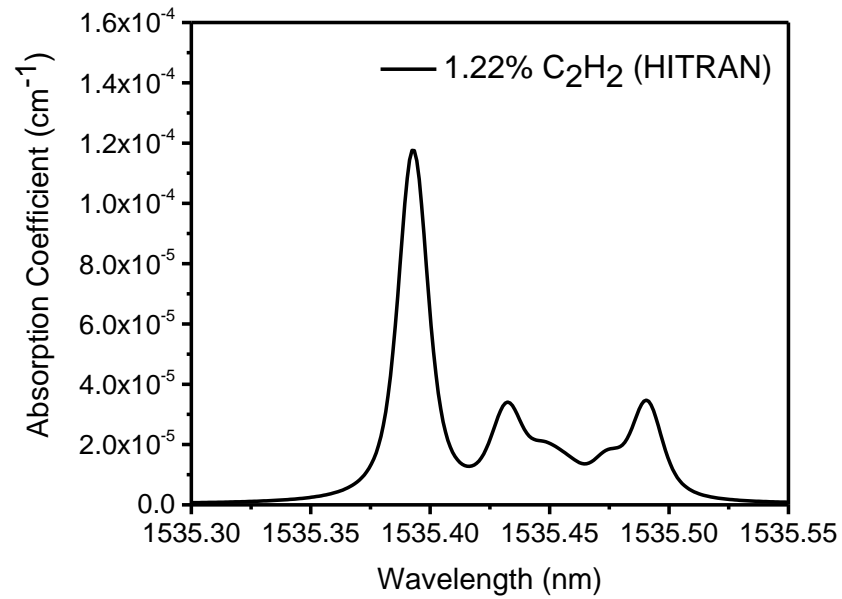


Figure 4.1: Acetylene spectrum simulated from HITRAN using the parameters in Table 4.1.

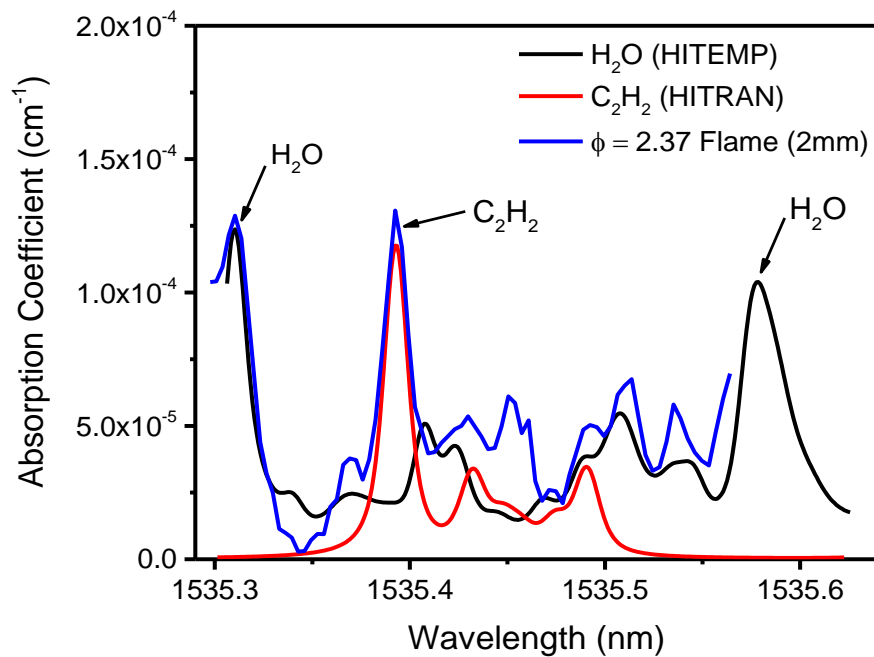


Figure 4.2: Measured acetylene spectrum plotted together with simulated spectra of acetylene (HITRAN) and water vapour (HITEMP) at experimental flame conditions.

absorbs in the near-infrared region. It is vital to put this into consideration in analysing the measured spectrum. A similar simulation, including a combined model spectrum of acetylene and water was performed and shown by Humphries [1, 2], to give an idea of what to expect from the measurements. This is with regards to the shape of the acetylene spectrum, and to aid in the identification of non-acetylene features. The parameters for the simulations are shown in Table 4.1. The simulations are shown in Figure 4.2, together with a measured spectrum of acetylene. The P17e acetylene feature is seen to be sufficiently isolated from neighbouring features, some of which have been identified as water vapour.

Parameter	Value
Path-length	1 cm
Temperature	1600 K
Pressure	1 atm
Water concentration	7 %
Acetylene Concentration	1.22 %

Table 4.1: Parameters for HITRAN and HITEMP simulations.

4.3 Acetylene Absorption Spectra

The cw-CRDS design has a measurement repetition rate averaged as 4.2 Hz with the flame *in situ*. The rate is affected by the trigger threshold which is intentionally set to a high level to ensure triggering occurs from the resonance build-up in the TEM₀₀ mode. This will maintain a good signal-to-noise ratio (SNR) for the measurements. The broad-band losses in the flame limit the ability of the on-resonance signal to

attain the trigger threshold. Setting the trigger threshold to a lower level will improve the measurement repetition rate but reduce the SNR. A suitable trigger level would, therefore, be a good compromise between the SNR and the ability to achieve a ring-down from the resonance build-up in the TEM_{00} mode. The actual time taken to acquire a ring-down time spectrum of acetylene over the measurement wavelength range (1535.30 nm – 1535.55 nm) was relatively slow and was affected by the flame composition and measurement position. The acquisition time was even slower for richer flames at higher measurement positions above the burner surface due to the strong broad-band losses. For instance, it took 20 minutes and 80 minutes to acquire ring-down time spectra in a $\phi = 2.37$ flame at measurement positions of 2 mm and 7 mm respectively. Due to the even longer time required to acquire a spectrum in the $\phi = 2.59$ flame and its highly sooting nature, a complete data-set could not be obtained for the $\phi = 2.59$ flame.

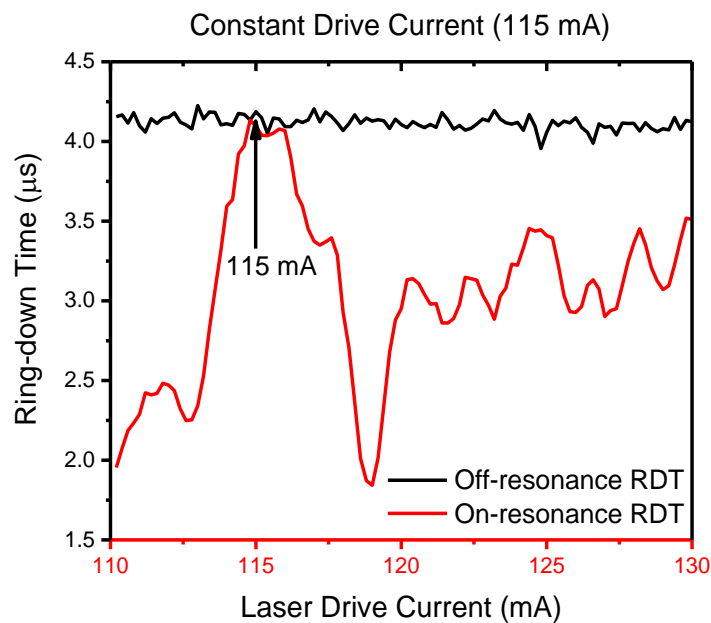


Figure 4.3: On-resonance ring-down time spectrum of acetylene and off-resonance ring-down time (normalisation point) with the laser held constant at 115 mA, recorded in a $\phi = 2.37$ flame at 2 mm height above the burner surface.

The measured ring-down time spectrum of acetylene is converted into an absorption spectrum using Equation 4.1 to calculate the absorption coefficient. The cw-CRDS technique is self-calibrating, and the off-resonance ring-down time, τ_0 obtained from the measurements is used in the calculation. As mentioned in the methodology chapter, the laser is tuned to a reference wavelength of 1535.34 nm in between the recording of each data-point in the spectrum. This mitigates against the possible drift in the off-resonance ring-down time due, for example, to the slight accumulation of deposits on the surface of the mirrors. Figure 4.3 shows a ring-down time spectrum of acetylene and the reference wavelength, which corresponds to a drive current of 115 mA. For the purpose of data analysis, the assumption is that the absorption not due to acetylene at this reference wavelength is equal to that at the line centre of the main peak. This seems justifiable based on the simulated water spectrum in Figure 4.2.

$$\alpha = \left(\frac{1}{c\tau} - \frac{1}{c\tau_0} \right) \quad 4.1$$

Monitoring the reference point for different heights above the burner surface and two equivalence ratio flames, the broad-band losses can be observed. This can be seen in Figure 4.4 and Figure 4.5, where the broad-band losses are greater for the $\phi = 2.37$ flame than for the $\phi = 1.77$ flame. Figure 4.5 also shows an increase in broad-band absorption beginning from 5 mm upwards to 7 mm above the burner surface, which is due to the presence of polycyclic aromatic hydrocarbon species (PAHs). The onset of soot formation has been reported [3-5] to be about 8 mm above the burner surface, which is later than the onset of PAHs formation in the flame. The presence of PAHs limits the sensitivity of the measurements of acetylene concentration at these heights above the burner surface as PAHs contribute to the broadband losses. This observation is in contrast to what is observed in the $\phi = 1.77$ flame, which is in the region of a nucleation flame, characterised by conditions that are just above the threshold for the onset of soot formation [6]. Such nucleation

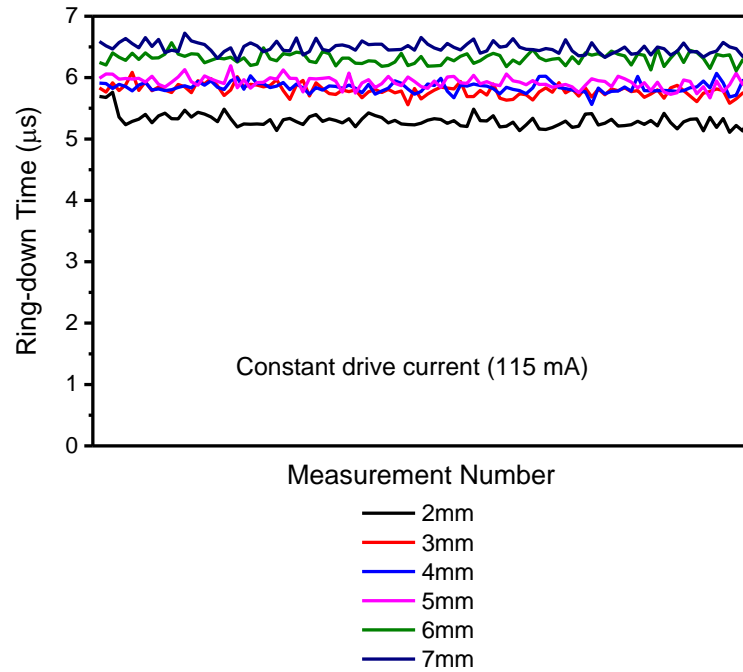


Figure 4.4: Ring-down time recorded at the normalisation point for different heights above the burner surface in a $\phi = 1.77$ flame.

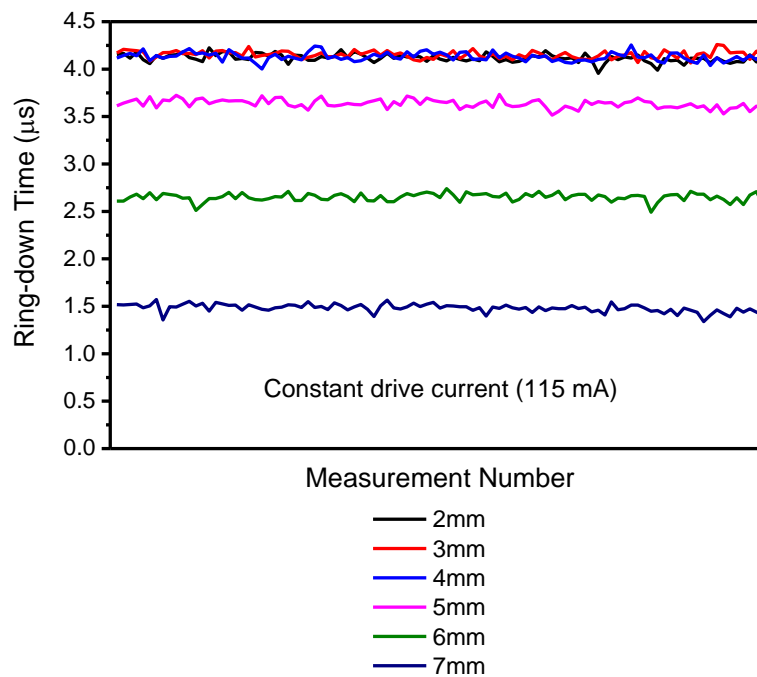


Figure 4.5: Ring-down time recorded at the normalisation point for different heights above the burner surface in a $\phi = 2.37$ flame.

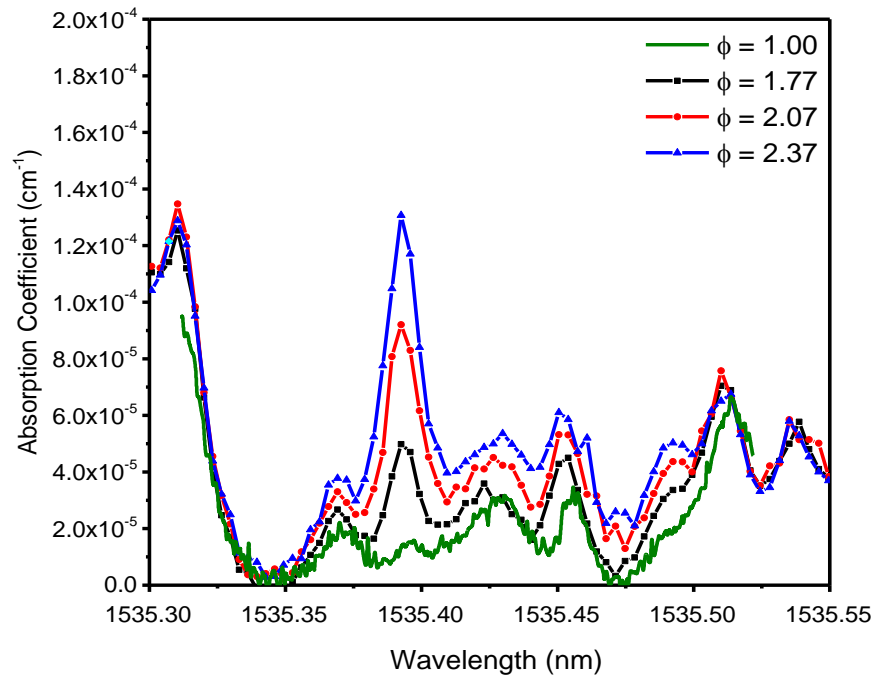


Figure 4.6: cw-CRDS spectra for a range of different equivalence ratio flames recorded at 2 mm above the burner surface.

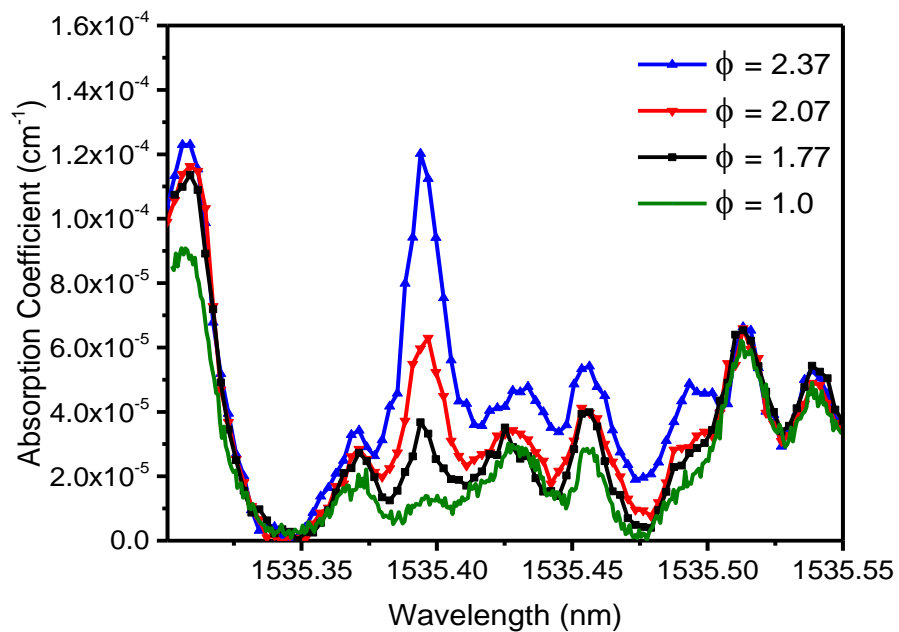


Figure 4.7: cw-CRDS spectra for a range of different equivalence ratio flames recorded at 4 mm above the burner surface.

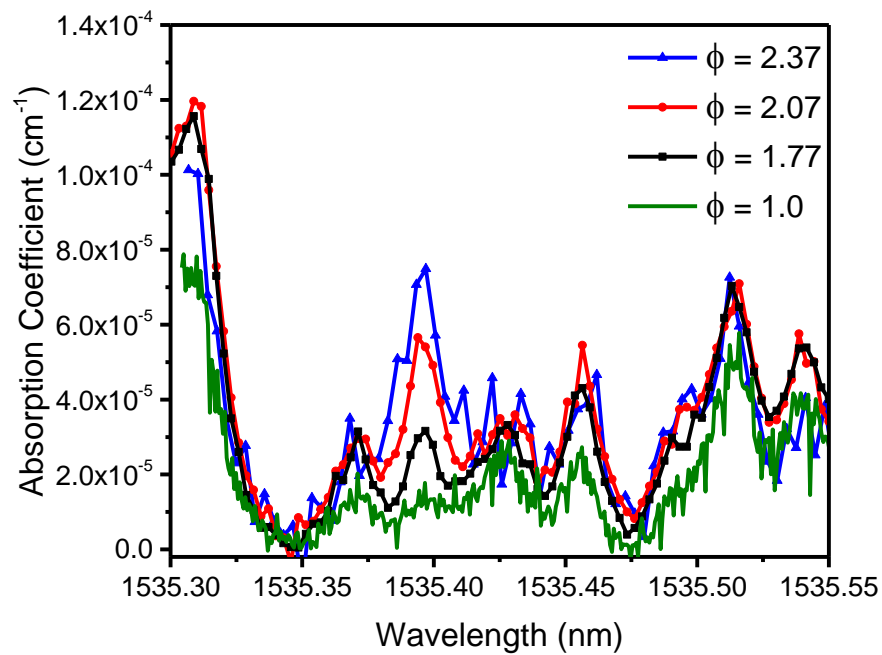


Figure 4.8: cw-CRDS spectra for a range of different equivalence ratio flames recorded 7 mm above the burner surface.

flames have been the subject of recent interests by various other research groups [6-8], and the availability of acetylene measurements complements the existing data in the literature. In the $\phi = 1.77$ flame, there is no progressive increase in PAH concentration with HAB as evidenced by the extinction results presented later in this chapter. As such, the slightly increased broad-band losses in Figure 4.4 at lower HAB are due to the modest presence of PAHs compared to higher HAB, together with thermal gradients low down in the flame.

The recovered spectra of acetylene are shown in Figure 4.6 for a range of rich flames and a stoichiometric flame recorded at 2 mm above the burner surface. For the rich flames, the shape of the measured spectra is somewhat similar to the model spectrum of acetylene in areas where there is the contribution from the strong P17e acetylene feature and other weak acetylene features (refer to Figure 4.2). In other areas, especially towards the right-hand side of the spectrum, good agreement is observed for all the flame conditions. This tends to suggest that where there is no

acetylene feature, the spectra tend to converge, i.e. that the contribution of water vapour to the spectra is rather similar in all cases. The peak acetylene absorption is observed near 1535.39 nm. The height of the peak acetylene feature increases with equivalence ratios as higher equivalence ratios possess greater acetylene concentration. The magnitude of this peak feature is almost negligible for the stoichiometric flame ($\phi = 1.0$). This observation is similar for equivalent spectra recorded at 4 mm and 7 mm above the burner surface and shown in Figure 4.7 and Figure 4.8 respectively, and at other heights for which spectra were recorded.

The measurements generally achieved good SNR. An SNR of over 17 was calculated for the main acetylene feature of the $\phi = 2.37$ spectrum recorded at 2 mm above the burner surface (Figure 4.6). The SNR was calculated by dividing the peak absorption value of $1.31 \times 10^{-4} \text{ cm}^{-1}$ by the standard deviation (σ) of the residual from a fit to the main acetylene feature of a model calculated from HITRAN. This leads to a detection limit of $2.2 \times 10^{-5} \text{ cm}^{-1}$ (three times the standard deviation (3σ)). The limit of detection is calculated for a given flame condition and measurement position in the flame. The spectra recorded at 4 mm and 7 mm possess lower SNR. The SNR for the spectra recorded in the $\phi = 2.37$ flame at 4 mm and 7 mm was calculated to be 16 and 7, respectively. This significant reduction in SNR for the spectra recorded at 7 mm is congruous with the increase in broad-band losses from 5 mm, as shown in Figure 4.5.

4.4 Determination of Acetylene Concentration from cw-CRDS Measured Absorption Spectra

The purpose of the measurements, as mentioned in Section 2.4, is to determine concentration of acetylene from the measured spectra. The methodology employed to do this is largely the same used by Humphries [1]. To determine absolute concentration profiles of acetylene, it is necessary to obtain, for each flame condition and at each vertical location, a spectrum that is due to acetylene alone. Owing to the

extra data-set recorded in the stoichiometric flame ($\phi = 1.0$), the approach employed to do this is more straightforward than that by Humphries [1] where a method of iteratively subtracting the spectrum of a less rich flame from a richer flame was adopted. Here, the spectrum obtained for each vertical position in the stoichiometric flame, where there is a negligible contribution from acetylene, is subtracted from the corresponding rich spectrum to give a spectrum due to acetylene alone. This is shown in Figure 4.9 for spectra recorded at 2 mm above the burner surface. The spectra bear a resemblance to the model acetylene spectrum simulated based on parameters from HITRAN and shown in Figure 4.1.

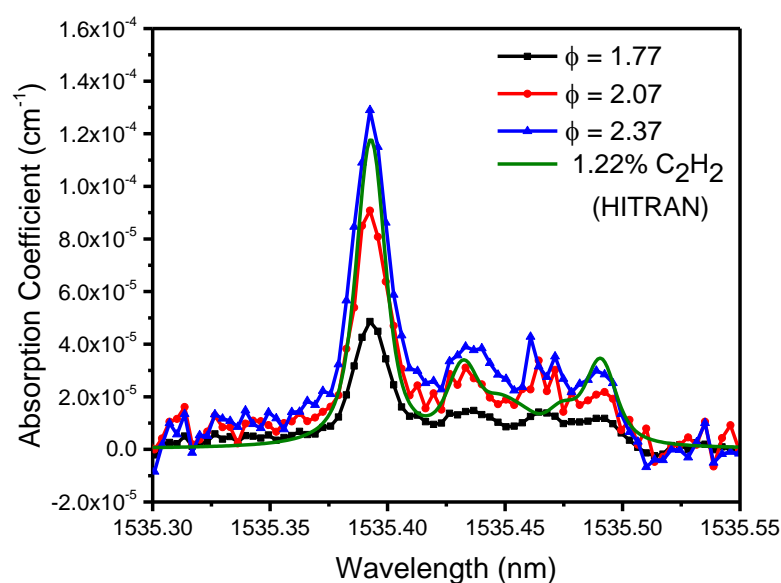


Figure 4.9: cw-CRDS spectra for a range of different equivalence ratio flames recorded at the height of 2 mm above the burner surface following subtraction of the $\phi = 1.0$ spectrum plotted with an acetylene spectrum simulated from HITRAN.

4.4.1 Fitting of Spectral Model

To obtain final concentration, the resulting spectrum is fitted using a non-linear least-squares fit to a model spectrum calculated based on parameters such as line strength

and partition function from the HITRAN database [9]. The fitting process is constrained to the region of the peak acetylene feature to improve the fit and thus obtain a better estimation of acetylene concentration as discussed later in this section. Fitting the model to the experimental data was achieved using a fitting algorithm in Matlab adopted from previous work by Bains [10] and Humphries [1] and shown in Appendix B. The algorithm uses a least-squares fitting process to quantify the absolute wavelength scale, collisional broadening parameter and concentration of acetylene. The temperature values inputted in the algorithm for each measurement position is listed in Table 4.2; also, the pressure and path-length are shown in Table 4.1.

As stated in Section 2.3.3, the HITRAN database is not perfect, especially at high temperatures. At high temperatures, the dependence of the collisional broadening parameter on temperature given by HITRAN is thought to be incorrect [1, 11]. Applying this to the fit would result in a lower concentration of acetylene.

Height above the burner surface	$\phi = 2.37$	$\phi = 2.07$	$\phi = 1.77$
1.5 mm	1537 K	1584 K	1623 K
2 mm	1559 K	1607 K	1646 K
3 mm	1572 K	1620 K	1660 K
4 mm	1575 K	1623 K	1663 K
5 mm	1575 K	1623 K	1663 K
6 mm	1575 K	1623 K	1663 K
7 mm	1575 K	1623 K	1663 K

Table 4.2: Temperature values for each of the flames at various heights above the burner surface.

The exponent tabulated in HITRAN reflects the temperature-dependence near to ambient conditions and extrapolation to much higher temperature is therefore problematic [12, 13]. The collisional broadening parameter, Γ_L was floated in the algorithm exclusively for the calculation of acetylene concentration in the $\phi = 2.37$ spectrum at 2 mm above the burner surface. This spectrum possesses a better signal to noise ratio than a spectrum acquired for $\phi = 2.59$ at 2 mm, which contains a higher concentration of acetylene. The purpose of this was to use the collisional width thus evaluated as a fixed parameter in the analysis of the spectra recorded at all the other flame conditions and locations. By performing the fit for three repeated runs of the experiment, the collisional broadening parameter was averaged as 0.0551 cm^{-1} , which is greater than the value predicted based on the n exponent (Equation 2.26) from HITRAN. This value was fixed in the algorithm for subsequent calculations of acetylene concentration for all other flame compositions and measurement locations. This avoided spurious results for collisional width in spectra with less good SNR.

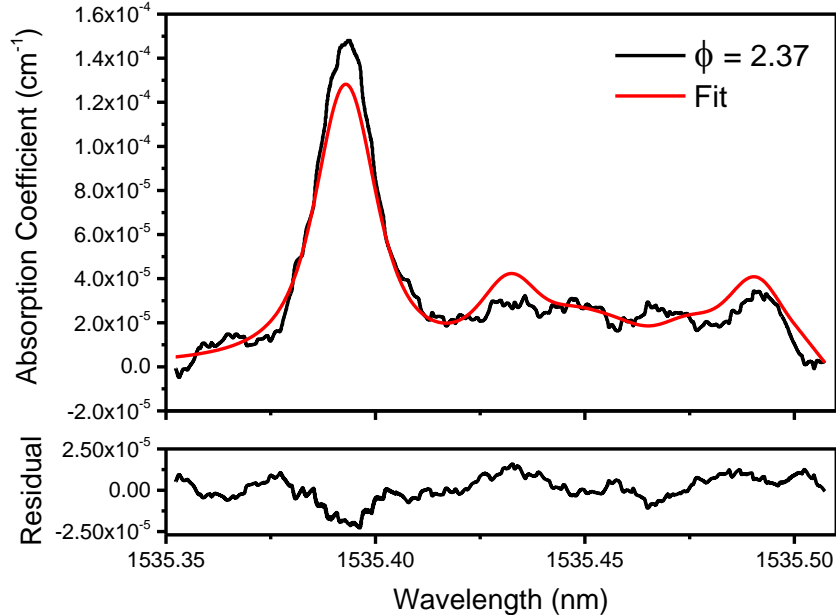


Figure 4.10: Spectral model (HITRAN) fit over a broad range of the extracted $\phi = 2.37$ acetylene spectrum at 2 mm above the burner surface.

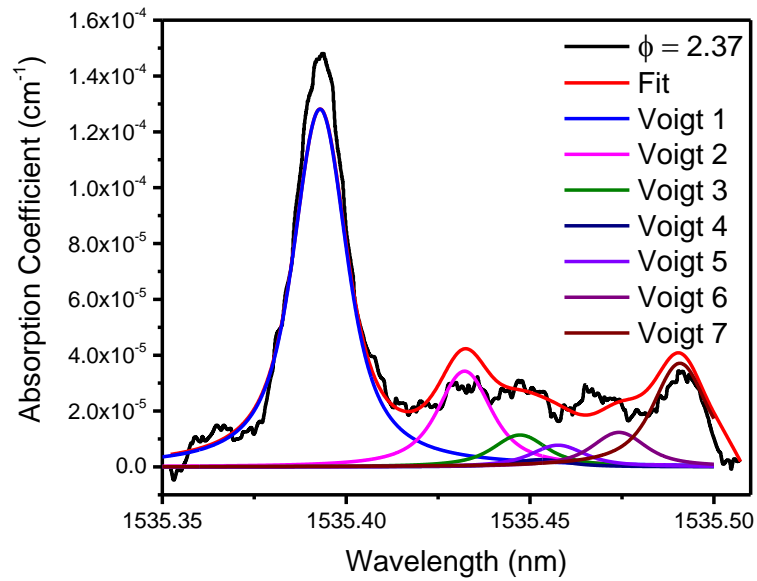


Figure 4.11: Fit of the spectral model calculated from HITRAN over a broad range of the subtracted $\phi = 2.37$ acetylene spectrum at 2 mm above the burner surface, shown together with the Voigt profiles of the individual acetylene lines.

Acetylene Line	Line Centre (nm)	$S(T)$ at 1600 K (cm^2/atm)
Voigt 1	1535.39265	4.01e-23
Voigt 2	1535.43219	1.07e-23
Voigt 3	1535.44703	3.58e-24
Voigt 4	1535.45276	8.12e-25
Voigt 5	1535.45738	2.44e-24
Voigt 6	1535.47396	3.87e-24
Voigt 7	1535.49053	1.16e-23

Table 4.3: Values of line centre and temperature-dependent line strength for acetylene lines within the measurement wavelength range obtained from HITRAN.

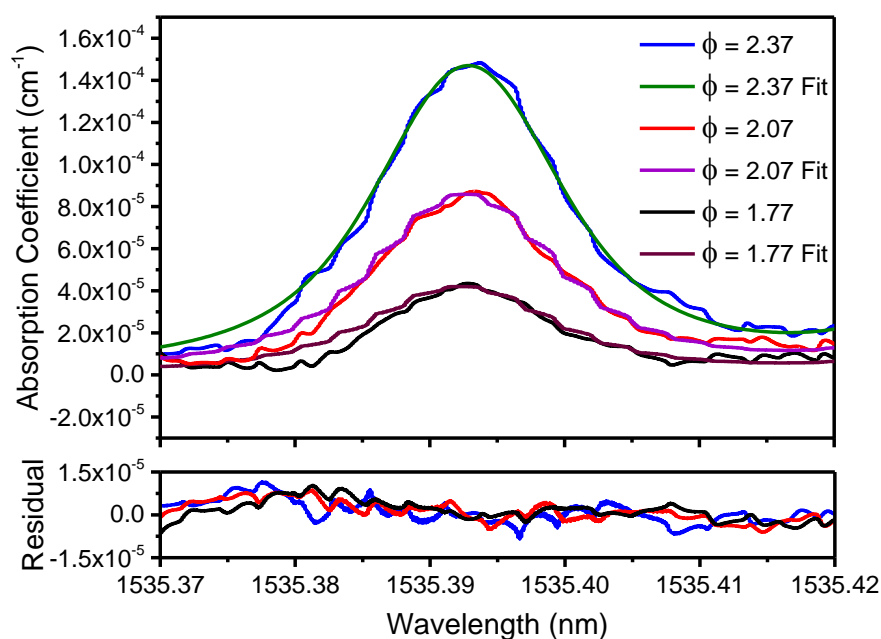


Figure 4.12: Subtracted spectra of P17e acetylene line for a range of different flames at 2 mm above the burner surface, shown with a fit to model spectra calculated from HITRAN.

The fit was initially done to include the main acetylene feature and other acetylene features in the spectrum. There are a number of acetylene lines within the wavelength range of the measurement which were included in this initial fit. The individual Voigt profiles for the acetylene lines, including the main acetylene feature, are shown in Figure 4.11. The individual acetylene lines are listed in Table 4.3 together with their line centre wavelengths and temperature-dependent line strengths ($S(T)$) evaluated at 1600 K. This initial fit was poor as seen in Figure 4.10, especially at the peak acetylene feature, and consequently gave a somewhat poorer estimate of the acetylene concentration.

For instance, the fit, including other features of acetylene shown in Figure 4.10 gave a concentration of 1.34%. Truncating the fit to the peak acetylene feature for the same spectrum gave a better fit and concentration of 1.38%. Limiting the fit to the main feature is more reliable owing to the strong acetylene absorption and low water

absorption. The fit is therefore limited to the peak acetylene feature (1535.37 nm – 1535.42 nm), taking into account only the FWHM range of the peak acetylene feature. Figure 4.12 shows an example fit over the main acetylene feature for spectra recorded at 2 mm above the burner surface in a $\phi = 2.37$ flame. Thus, the fit only includes the 1535.39265 nm acetylene line

4.5 Acetylene Concentration Profiles

The concentration profiles obtained from the fitting process described above are shown in Figure 4.13 for a range of different equivalence ratio flames recorded at 1 mm height increments above the surface of the burner. The profiles for higher equivalence ratios possess greater concentration of acetylene. Beyond 2 mm above the burner surface, acetylene concentration is seen to reduce with increasing height above the burner surface. This suggests that acetylene is being consumed in the formation of PAH and soot downstream in the flame, which is in agreement with the role of acetylene in HACA mechanism. Previous flame studies [14-17] have also reported the decaying trend of acetylene with increasing height above the burner surface, albeit in premixed flames of somewhat different composition.

At flame temperatures, the line-strength of the P17e transition significantly depends on temperature. The temperature values used in calculating the absolute concentration values of acetylene and shown in Table 4.2 were obtained in a previous measurement using OH-LIF scanning in a $\phi = 2.37$ flame [18]. The temperature measurements were performed for a range of positions between 0.6 mm and 4 mm heights above the burner surface, as shown in Figure 4.13 (lower plot). The temperature was scaled for the other heights above the burner surface, as explained elsewhere [18]. The temperature values for other equivalence ratio flames were scaled based on the difference in maximum temperature between the flame conditions calculated using ABF mechanism. The resulting temperature values contribute to the uncertainty in the measurements which was evaluated by varying

the temperature by ± 80 K, which is about 5%. This was done using a spectrum recorded in a $\phi = 2.37$ flame at 2 mm, and the fitting process repeated, resulting in an uncertainty of +29% and -25% in the absolute concentration of acetylene.

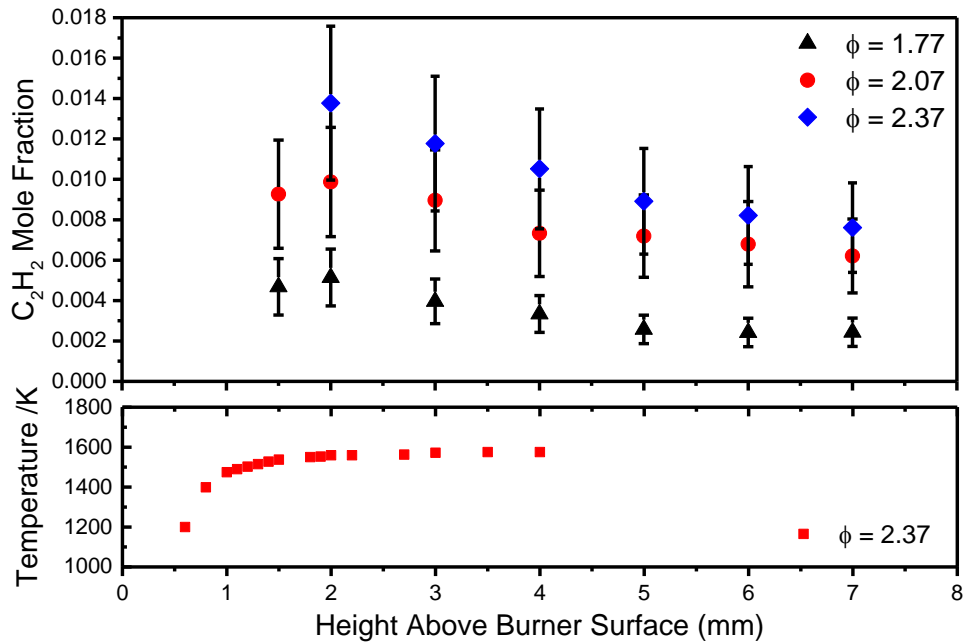


Figure 4.13: (Upper plot) Recovered concentration profiles of acetylene as a function of height above the burner surface. (Lower plot) Previous OH-LIF temperature measurements in a $\phi = 2.37$ flame.

4.6 Uncertainty Analysis

Several sources of uncertainty contribute to determining the concentration values of acetylene. The temperature values formed the major source of uncertainty in recovering the absolute concentration of acetylene. As mentioned earlier, the uncertainty of +29% and -25% in the absolute concentration of acetylene resulting from temperature was evaluated by varying the temperature for the $\phi = 2.37$ spectrum recorded at 2 mm, by ± 80 K. The uncertainty in the reading of the mass flow controllers is $\pm(0.8\%$ of reading + 0.2%). This puts error bounds on the resulting equivalence ratio (ϕ) flames and propagate into the measurements, although this pales in comparison to the uncertainty resulting from temperature.

Also, the uncertainty in obtaining the ring-down times pales in comparison to that from temperature. The random errors in obtaining the ring-down times affect the measurement precision and propagate into the standard errors for the measurements. The standard errors are of different magnitudes depending on the flame location and composition. The standard error averages less than 10% for the measurements. Another uncertainty in the measurements results from the line strength $S(T_0)$ of the P17e acetylene feature obtained from HITRAN database which is given as $\pm 2\%$ [19]. The line strength is used in calculating the temperature dependent line strength at the flame temperature using Equation 2.34.

A further uncertainty in the measurements arises from the value of the collisional broadening parameter which was averaged with an uncertainty of $\pm 0.8\%$. These uncertainties propagate into the measurements and the estimated uncertainty in the recovered concentration of acetylene at various heights is obtained as the square root of the sum of the squares of the individual uncertainties.

4.7 Extinction Measurements

We now look at extinction measurements obtained at 1 mm increments for the various equivalence ratio flames considered in the measurements. The extinction measurements are necessary as they provide a measure of the broad-band optical losses in the flame. The measurements were obtained by measuring the ring-down time of the flames at the normalisation wavelength of 1535.34 nm. Thus, this is a reference wavelength at which narrow-band absorption is considered to be low and invariant with the flame location. The extinction coefficients are shown in Figure 4.14 and exhibit a trend where there are higher broad-band losses for flames with higher equivalence ratios. This can be attributed to the increased presence of species which may include larger aromatic species in the higher equivalence ratio flames. In the rich flames, considerable additional broad-band losses can be seen with increasing distance downstream in the flame.

It should be noted that for the $\phi = 2.37$ and especially the $\phi = 2.59$ flames, this increase occurs far upstream of the onset of soot (which is at about 8 mm above the burner [3]). This would tend to indicate strongly increasing concentration of PAH in these flames upstream of the onset of soot, consistent with a large reservoir of PAHs that are not yet in a form that allows nucleation to form incipient particles. By contrast, for the $\phi = 2.07$ flame, the rise in extinction corresponds with the appearance of soot beyond 8 mm without an apparent increase in PAH absorption upstream of that location (indeed, extinction reduces slightly from 3 mm to 7 mm in this flame). For the $\phi = 1.77$ flame, which has the same composition as the "nucleation flame" investigated by others [6, 8, 20, 21], no increase in extinction with increasing HAB is observed, despite the sensitivity of the technique. The negative sloping trend with HAB is observed in the less rich and stoichiometric flames is due to the higher thermal losses lower in the flame.

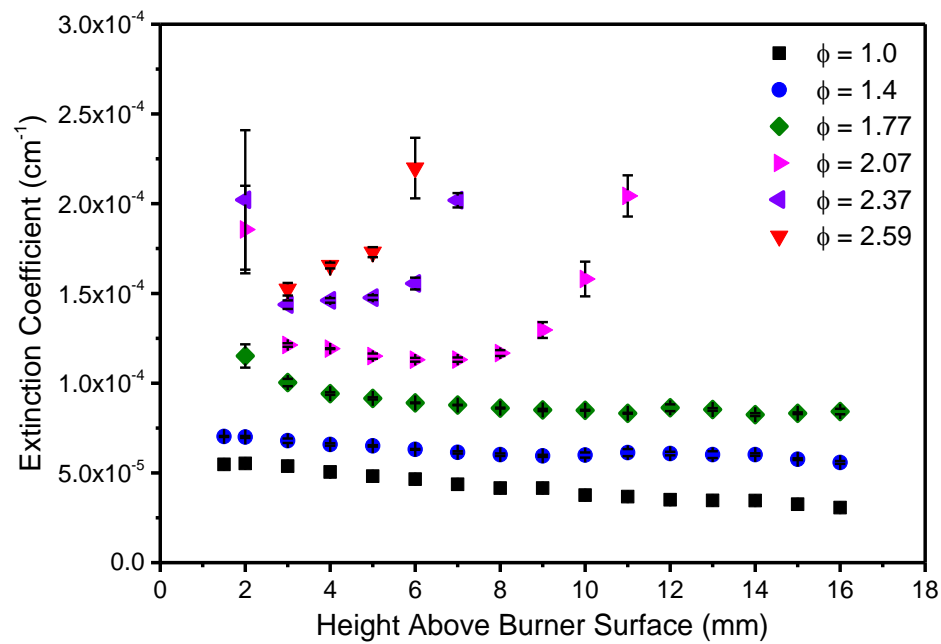


Figure 4.14: Extinction coefficients measured for various equivalence ratio flames at 1 mm increments of height above the burner surface. Error bars show the standard error in 3 measurements.

The apparent increase in extinction for the richer flames, at the lowest vertical positions, can be attributed to the reaction zone being located slightly further above the burner (due to the lower adiabatic flame speed), causing the edge of the steep vertical temperature gradient to perturb the beam in the cavity.

The results presented in this chapter show that reproducible and quantitative measurements of acetylene can be obtained in a flame using the refined cw-CRDS set-up. The measurements with the refined set-up achieved a larger data-set with repetitions than obtained by Humphries [1]. This includes spectra of a stoichiometric flame at various HAB following which acetylene spectra for the rich flames were processed using a different approach. Broad-band optical losses (extinction measurements) in the flame were also obtained using the cw-CRDS technique. This expands the progress made in building on the work of Humphries [1].

4.8 Summary

In this chapter, the results of *in situ* acetylene measurements using cw-CRDS technique have been presented, showing the progress achieved in building on the work of Humphries [1]. A model spectrum of acetylene, as well as that for high-temperature water vapour calculated from HITRAN and HITEMP respectively, were shown to compare with the measured spectra. This helped in the identification of some spectral features due to water vapour. The peak acetylene line is seen to be sufficiently separated from nearby water absorption features to avoid significant interference. The on-resonance ring-down signals were calibrated using ring-down signals recorded at a reference wavelength chosen for normalisation. The recovered absorption spectra recorded over a range of flame compositions showed good agreement in shape for wavelengths where there is no contribution from acetylene.

A methodology for calculating acetylene concentration from the recovered spectra has been established. Spectra due to contribution from acetylene alone were obtained from the recovered spectra by subtracting the stoichiometric spectrum

from the rich spectra. A least-squares fit of a spectral model calculated based on parameters from HITRAN was applied to the subtracted spectra. This fit was limited to the main acetylene feature which is more reliable. The recovered acetylene profiles from the fit show higher acetylene concentrations for increasing equivalence ratio. They also show a trend of decreasing acetylene concentration with increasing height above the burner surface. This would be consistent with the consumption of acetylene, including in reactions forming polycyclic aromatic hydrocarbons and ultimately soot.

The measured extinction coefficients provide a measure of broad-band optical losses in the flame. These measurements show higher losses for richer flames and also with increasing height above the burner surface, including before the onset of soot formation in rich flames. This is partly attributable to broad-band near-infrared absorption by larger aromatic species in the flame.

4.9 References

1. Humphries, G., *Novel diode laser absorption techniques for combustion diagnostics*, in *Department of Electronic and Electrical Engineering*. 2017, University of Strathclyde: Glasgow. p. 144.
2. Humphries, G.S., I.S. Burns, and M. Lengden, *Application of Continuous-Wave Cavity Ring-Down Spectroscopy to Laminar Flames*. *Ieee Photonics Journal*, 2016. **8**(1).
3. Commodo, M., et al., *Physicochemical evolution of nascent soot particles in a laminar premixed flame: from nucleation to early growth*. *Combustion and Flame*, 2015. **162**(10): p. 3854-3863.
4. Schulz, F., et al., *Insights into incipient soot formation by atomic force microscopy*. *Proceedings of the Combustion Institute*, 2019. **37**(1): p. 885-892.
5. Humphries, G.S., et al., *A simple photoacoustic method for the in situ study of soot distribution in flames*. *Applied Physics B*, 2015. **119**(4): p. 709-715.
6. Betrancourt, C., et al., *Investigation of the size of the incandescent incipient soot particles in premixed sooting and nucleation flames of n-butane using LII, HIM, and 1 nm-SMPS*. *Aerosol Science and Technology*, 2017. **51**(8): p. 916-935.

7. Desgroux, P., et al., *Comparative study of the soot formation process in a “nucleation” and a “sooting” low pressure premixed methane flame*. Combustion and Flame, 2017. **184**: p. 153-166.
8. Bladh, H., et al., *Probing the smallest soot particles in low-sooting premixed flames using laser-induced incandescence*. Proceedings of the Combustion Institute, 2015. **35**(2): p. 1843-1850.
9. Gordon, I.E., et al., *The HITRAN2016 molecular spectroscopic database*. Journal of Quantitative Spectroscopy and Radiative Transfer, 2017. **203**: p. 3-69.
10. Bain, J.R.P., *Near infrared tunable diode laser spectroscopy for aero engine related applications*, in Dept. of Electronic and Electrical Engineering. 2012, Thesis [Eng. D] -- University of Strathclyde: Glasgow.
11. Schroeder, P.J., et al., *Speed-dependent Voigt lineshape parameter database from dual frequency comb measurements up to 1305 K. Part I: Pure H₂O absorption, 6801–7188 cm⁻¹*. Journal of Quantitative Spectroscopy and Radiative Transfer, 2018. **210**: p. 240-250.
12. Stolarczyk, N., et al., *Evaluation of different parameterizations of temperature dependences of the line-shape parameters based on ab initio calculations: Case study for the HITRAN database*. Journal of Quantitative Spectroscopy and Radiative Transfer, 2020. **240**: p. 106676.
13. Cybulski, H., et al., *Power-law temperature dependence of collision broadening and shift of atomic and molecular rovibronic lines*. Journal of Quantitative Spectroscopy and Radiative Transfer, 2013. **120**: p. 90-103.
14. Gersen, S., A.V. Mokhov, and H.B. Levinsky, *Extractive probe/TDLAS measurements of acetylene in atmospheric-pressure fuel-rich premixed methane/air flames*. Combustion and Flame, 2005. **143**(3): p. 333-336.
15. Kaiser, E., et al., *Experimental and modeling study of premixed atmospheric-pressure dimethyl ether– air flames*. The Journal of Physical Chemistry A, 2000. **104**(35): p. 8194-8206.
16. Kaiser, E., *Measured and computer-simulated hydrocarbon and hydroxyl radical profiles in fuel-rich atmospheric-pressure flat flames: reactions of methane and acetylene*. Journal of Physical Chemistry, 1990. **94**(11): p. 4493-4499.
17. Roy, S.P. and D.C. Haworth, *A Systematic Comparison of Detailed Soot Models and Gas-Phase Chemical Mechanisms in Laminar Premixed Flames*. Combustion Science and Technology, 2016. **188**(7): p. 1021-1053.
18. Hu, Y., *Radical concentration and temperature measurements in sooting flames by cavity ringdown spectroscopy and laser-induced fluorescence*, in Chemical and Process Engineering. 2015, University of Strathclyde: Glasgow, United Kingdom.

19. El Hachtouki, R. and J. Vander Auwera, *Absolute line intensities in acetylene: the 1.5- μ m region*. Journal of Molecular Spectroscopy, 2002. **216**(2): p. 355-362.
20. Mouton, T., X. Mercier, and P. Desgroux. *Evidence of nucleation flames: A valuable tool for the study of soot particles inception*. in *7th European Combustion Meeting*. 2015.
21. Ergut, A., et al., *The effect of equivalence ratio on the soot onset chemistry in one-dimensional, atmospheric-pressure, premixed ethylbenzene flames*. Combustion and Flame, 2007. **151**(1): p. 173-195.

Chapter 5 : Development of Cavity-Enhanced Absorption Spectroscopy for measurement of Acetylene Concentration in Flames

5.1 Introduction

Concentration measurements of acetylene acquired *in situ* in flames using cw-CRDS have been presented in Chapter 4. The technique has therefore been taken to the point of generating reliable and reproducible data in standard flames of interest in studies of soot formation. A key advantage of the cw-CRDS approach is that it is an absolute method, not requiring calibration. Nevertheless, the slow data acquisition, especially given strong broad-band losses in the richer flames, led to the consideration of alternative approaches. This resulted in work on cavity-enhanced absorption spectroscopy, which forms the bulk of this thesis. As described in Chapter 2, cavity-enhanced absorption spectroscopy (CEAS) is a relatively simpler technique in which species can be monitored rapidly following from the quick acquisition of a CEAS spectrum. This is in contrast to the difficult mode-matching process and the difficulties for triggering in richer flames using cw-CRDS. In this regard, the CEAS technique would be a useful tool to employ for effective monitoring of acetylene in sooting flames.

This chapter presents the first application of cavity-enhanced absorption spectroscopy to acquire *in situ* concentration measurements of acetylene in flames. The results from this technique can be trusted based on the absolute cw-CRDS measurements which are in agreement. The methodology employed has been described in Chapter 3. In this chapter, the advantages of the CEAS technique over the previous measurements of acetylene using cw-CRDS are highlighted, whilst noting the agreement between the two techniques. This allows a comparison to be

made of the advantages and disadvantages of the two approaches. The CEAS measurements were taken in both the porous-plug burner and the McKenna burner.

5.2 Acetylene Absorption Spectra

Like the cw-CRDS measurements of acetylene presented in the previous chapter, the P17e line of acetylene at 1535.39 nm was also interrogated. This will facilitate the comparison of the CEAS and cw-CRDS techniques. A model of the expected flame spectrum simulated from HITRAN has been shown in Figure 4.2. The various changes to the alignment and experimental procedure required to obtain high-quality CEAS data and to achieve quantitative calibration have been described in Chapter 3. During operation, the raw absorption spectrum of acetylene which is shown in Figure 5.1 appears on the oscilloscope directly, which represents an advantage over cw-CRDS in which the spectrum is built up only after acquiring averaged ring-down traces at each spectral location and fitting decay times to each.

A procedure has been developed to measure the ring-down time, τ of the multi-mode cavity without the flame using a nitrogen-purge as part of the calibration. The cavity transmission, I_o recorded in the nitrogen-purged cavity provided a base-line transmission level in the absence of cavity losses. The mode structure effects of the cavity on the cavity transmission, I_o can be seen in Figure 5.2. Generally, a significant contribution to noise in CEAS technique comes from the residual mode structure of the cavity [1, 2]. As described in Chapter 3, measures have been taken to minimise this mode structure by adjusting the cavity length, which had initially been approximately equal to half of the mirror radius of curvature, potentially leading to mode degeneracy. A typical approach to reducing the mode structure would be to apply off-axis alignment [2]. However, this approach will result in reduced transmission power and reduced spatial resolution, the latter of which in particular makes this approach totally unsuitable for *in situ* flame studies. In any case, it is

demonstrated here that the mode-noise is low enough to allow high-fidelity acetylene spectra to be obtained.

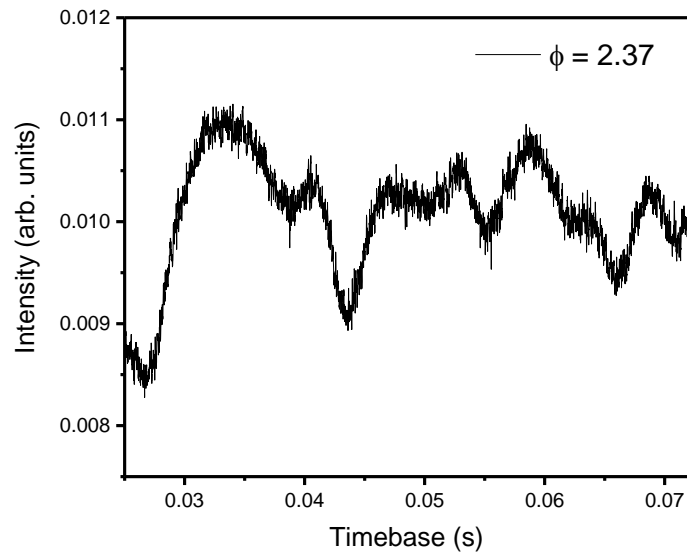


Figure 5.1: 512 averages of a raw CEAS spectrum of acetylene recorded in a $\phi = 2.37$ flame at 4 mm above the burner surface, with an acquisition time of 51.2 s and a scanning frequency of 10 Hz.

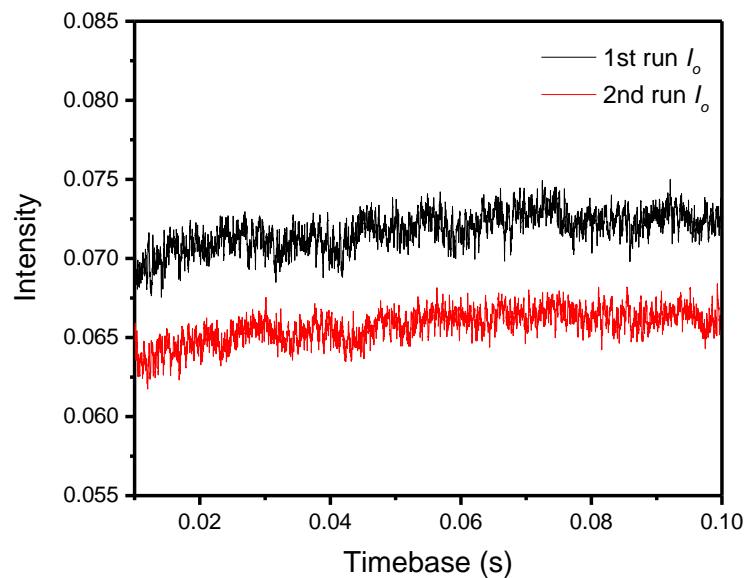


Figure 5.2: 512 averages of the cavity transmission, I_o recorded in the absence of a flame in a nitrogen-flushed cavity with a scanning frequency of 10 Hz.

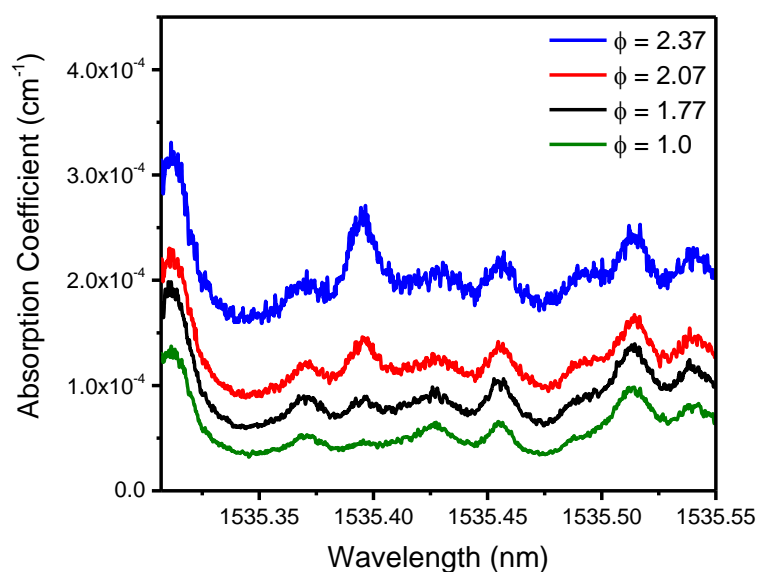


Figure 5.3: 512 averages of the calibrated spectra of acetylene for a range of equivalence ratio flames in the porous-plug burner, recorded at 4 mm above the porous-plug burner surface before shifting the baseline to zero, with an acquisition time of 51.2 s.

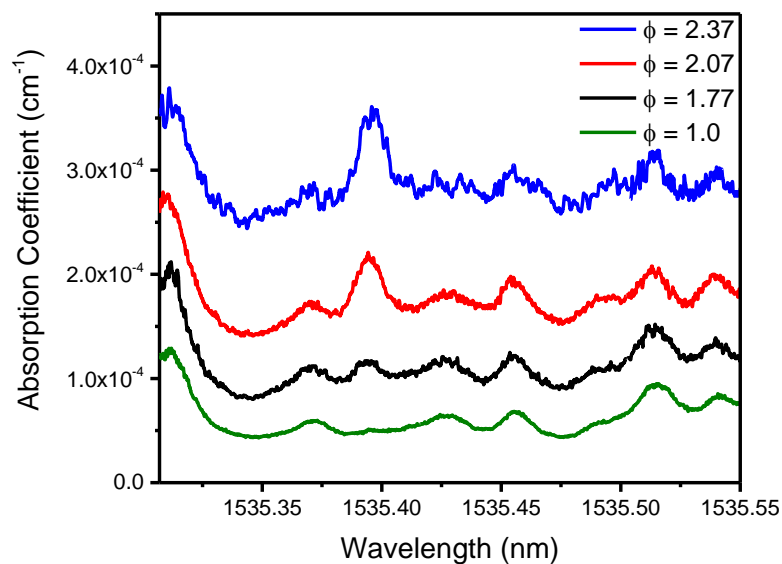


Figure 5.4: 512 averages of the calibrated spectra of acetylene for a range of equivalence ratio flames in the McKenna burner, recorded at 4 mm above the burner surface before shifting the baseline to zero, with an acquisition time of 51.2 s.

$$\alpha = \frac{I_0 - I}{I} \left(\frac{1 - R}{L_c} \right) \quad 5.1$$

The spectrum is calibrated using the effective mirror reflectivity, R and the transmission, I_0 obtained in the nitrogen-purged cavity of length L_c , according to Equation 5.1 [3]. R was typically calculated as ~ 0.99995 which is similar to the theoretical value of the mirror reflectivity given by the manufacturer. The calibration was done using the Matlab algorithm shown in Appendix C, and the calibrated spectra are shown in Figure 5.3 for a range of equivalent ratio flames at 4 mm above the porous-plug burner. The background is seen to be increasing with equivalence ratio, consistent with the increased broad-band absorption that was also observed in the cw-CRDS measurements presented previously. A similar trend is observed for the spectra recorded in the McKenna burner and shown in Figure 5.4. In the analysis of cw-CRDS spectra presented in Chapter 4, the minimum in the spectrum at 1535.34 nm was assumed to be a narrow region of negligible narrow-band absorption and was used in normalising the cw-CRDS spectrum by providing an off-resonance zero-level.

The CEAS spectra of acetylene in Figure 5.3 are vertically shifted by subtracting the value of the absorption coefficient averaged over this narrow region around 1535.34 nm. The shifted spectra are shown in Figure 5.5 for measurements in the porous-plug burner at 4 mm above the burner surface. Corresponding spectra recorded with the McKenna burner are shown in Figure 5.6. The shapes of the spectra are in agreement with the cw-CRDS spectra shown in the previous chapter, and thus also broadly similar to the combined model spectra of acetylene and water simulated from HITRAN and HITEMP respectively and shown in Figure 4.2. As can be seen in Figure 5.5 and Figure 5.6, the spectra recorded for both the porous-plug burner and McKenna burner are almost identical in shape. A comparison of vertical concentration profiles for measurements in each of the burners is presented later. It is also noteworthy that the spectrum recorded in the McKenna burner actually has a

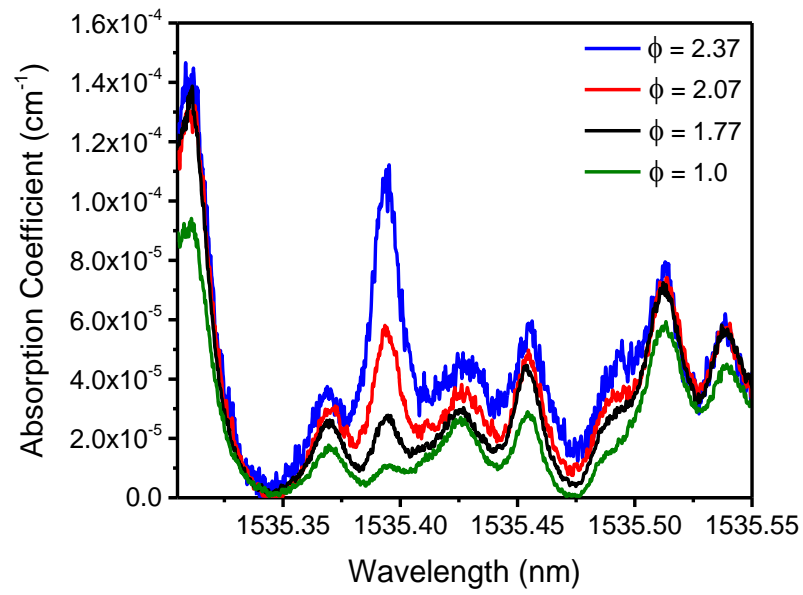


Figure 5.5: CEAS spectra for a range of different equivalence ratio flames recorded at 4 mm above the porous plug burner surface.

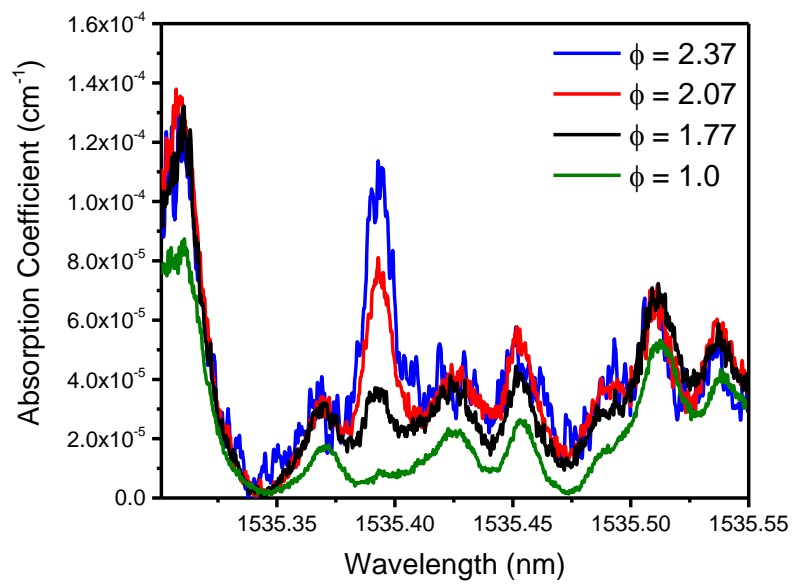


Figure 5.6: CEAS spectra for a range of different equivalence ratio flames recorded at 4 mm above the McKenna burner surface.

less favourable signal-to-noise ratio (SNR) than the one recorded in the porous-plug burner. This is thought to be the result of larger broad-band losses in the McKenna burner due to the longer path-length.

The peak acetylene feature is also similar in magnitude in each of the two burners for each corresponding equivalence ratio. The spectra show the expected trend where higher equivalence ratio flames possess greater absorption peaks for the P17e acetylene feature. The non-acetylene features are seen to converge for spectra of all the equivalence ratio flames with the partial exception of the $\phi = 1.0$ spectrum. This observation is in contrast to what was apparent from the cw-CRDS data in the previous chapter, which were recorded over a narrower spectral range due to the acquisition time. The quality of the CEAS data allows us to observe slight differences from the rich-flame spectra, even in regions of the spectrum with no acetylene absorption. This is presumably due to slight differences in temperature and water mole fraction in these dissimilar flames and leads us to consider the best way of isolating the acetylene spectrum from the interfering water lines.

Comparing the $\phi = 1.0$ spectrum for a number of heights above the burner surface, there is negligible variation of the peak acetylene feature as can be seen in Figure 5.7. This tends to support the previous conclusion that there is negligible concentration of acetylene in the $\phi = 1.0$ flame, even closer to the burner surface. Another conclusion that may be drawn from Figure 5.7 is that the CEAS spectra are very well reproducible since there is close overlap in the data for these experiments repeated under essentially similar conditions. The concentration measurements shown later in this chapter are all the result of three repeated experiments.

From 5 mm above the burner surface, the quality of the signal begins to decrease, especially for the rich flames due to the presence of PAHs. Figure 5.8 shows spectra recorded at 5 mm above the McKenna burner surface. This reduction in signal quality in comparison to the corresponding spectra in Figure 5.6 is in line with the increase in background losses with height above the burner surface, as shown in Figure 5.9.

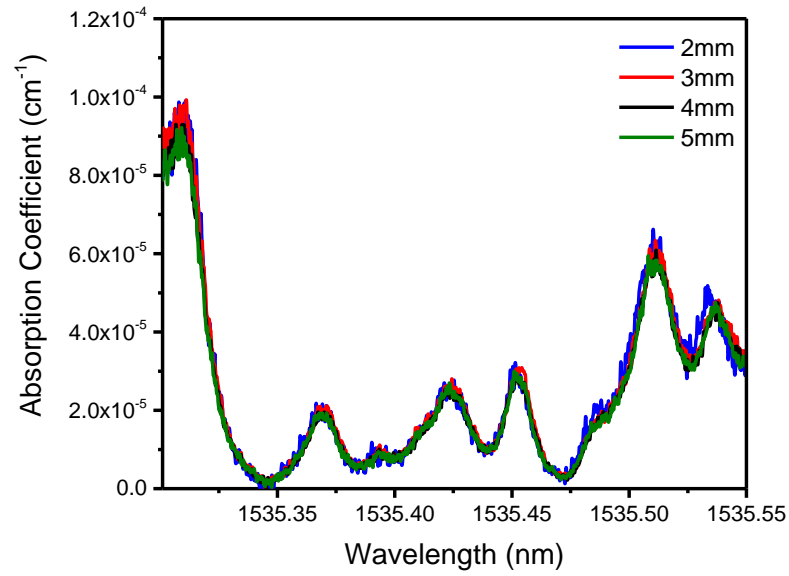


Figure 5.7: CEAS spectra of acetylene for $\phi = 1.0$ flame recorded at different heights above the McKenna burner surface.

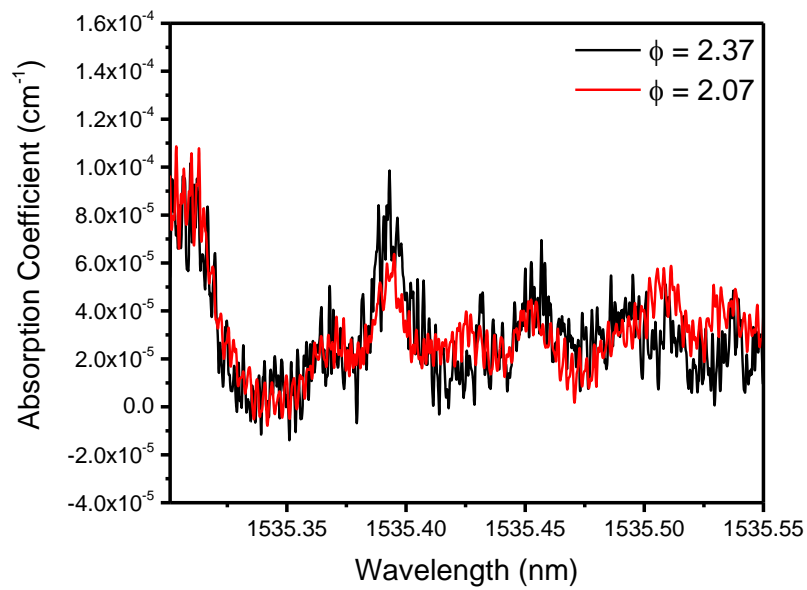


Figure 5.8: CEAS spectra for $\phi = 2.07$ and $\phi = 2.37$ recorded at 5 mm above the McKenna burner surface.

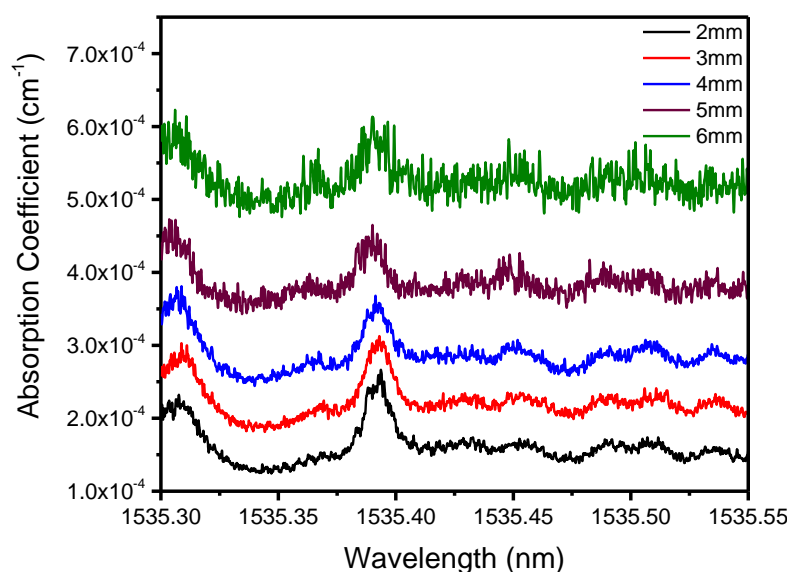


Figure 5.9: CEAS spectra of acetylene for $\phi = 2.37$ flame recorded at different heights above the McKenna burner surface.

5.3 Determination of Acetylene Concentration from CEAS Measured Absorption Spectra

5.3.1 Extraction of Acetylene Spectrum

The aim of the measurements in this work is to determine final concentration profiles of acetylene in the flame. To do this, it is necessary to first extract spectra that are due to acetylene alone from the contribution of water vapour features. The spectrum of the stoichiometric flame ($\phi = 1.0$) is seen to contain negligible contribution from acetylene as stated earlier. Nevertheless, the spectra in Figure 5.5 and Figure 5.6, as well as spectra recorded over a broader wavelength range (shown in Chapter 6) show that the $\phi = 1.0$ trace does not fully converge with the others in the spectral regions where acetylene absorption is absent. This, therefore, leads us to reconsider the approach followed in analysing the cw-CRDS data. Although the ultimate effect on the evaluated acetylene concentration is thought to be minor. In contrast, the spectra

for the rich flames ($\phi = 1.77, 2.07, 2.37$) do converge in those areas where there is no contribution from acetylene. This is also the case for all measurement positions in the flame. Therefore, we propose an alternative approach to determine the acetylene spectrum, which does not require the use of the $\phi = 1,0$ spectrum. This approach is based on the observation that all the rich flame spectra appear to be the sum of a common water vapour spectrum and an acetylene spectrum of differing magnitude. The approach is based on the implicit assumption that the absorption at the centre of the main acetylene feature is entirely due to acetylene. Contingent on these assumptions, the separate water and acetylene spectra can be extracted from the data.

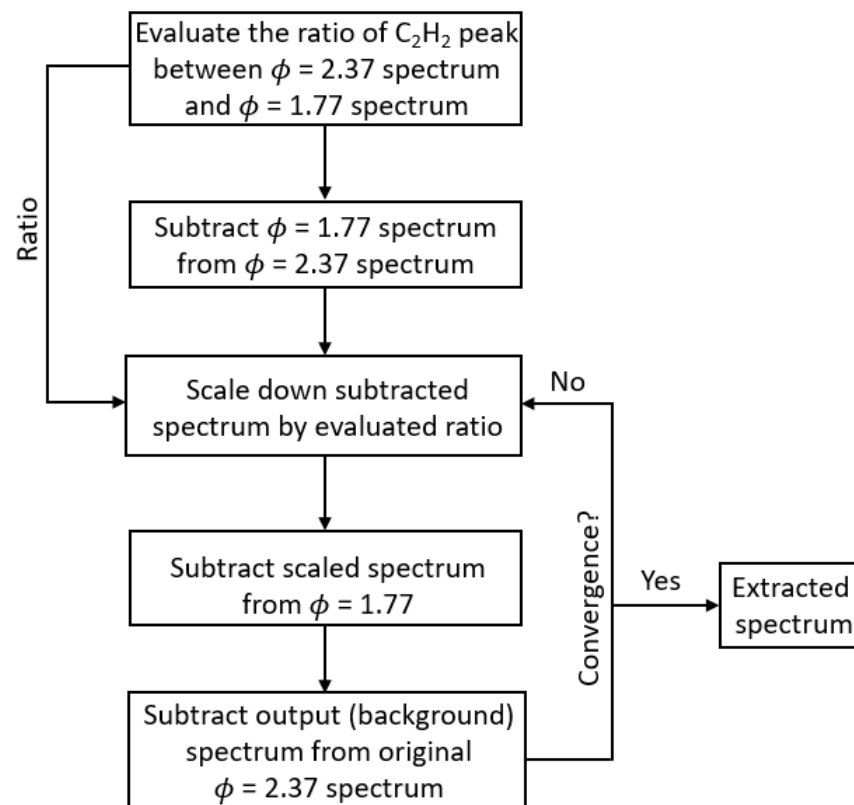


Figure 5.10: Flow diagram for the iterative extraction technique.

The extraction is achieved by subtracting the leaner spectrum from the richer spectrum, using a developed iterative technique summarised in Figure 5.10. For a given pair of spectra ($\phi = 1.77$ and $\phi = 2.37$), the extraction steps are as follows:

1. The leaner spectrum is subtracted from the richer spectrum. This gives an initial estimate of the acetylene spectrum for the rich flame, as shown in Figure 5.11.
2. This initial estimate of the acetylene spectrum is reduced by the intensity ratio of the peak of the strong acetylene feature between the leaner spectrum and the richer spectrum (hence the need to assume that the absorption at the line centre is solely due to acetylene).
3. The resultant spectrum is subtracted from the leaner spectrum resulting in an estimation of the spectrum not due to acetylene. This spectrum is therefore, an estimate of the water background and shown in Figure 5.12.
4. The water background is subtracted from the rich spectrum yielding a second estimate of the acetylene spectrum. The water background is also subtracted from the leaner spectrum.
5. Steps 2, 3, and 4 are repeated until there is convergence for the resulting extracted spectra. Usually, about four iterations are required to achieve convergence.

The estimates of acetylene contribution from iterating steps 2, 3, 4, and 5 are shown in Figure 5.13. The final output from the extraction process for three flame conditions is shown in Figure 5.14. The water features and the unassigned features (also thought to be due to water vapour) have been eliminated from the spectra. This extraction process was executed using the Matlab algorithm shown in Appendix D.

As a summary of the above approach, the acetylene spectra for a pair of flame compositions at a given HAB have been extracted from the raw experimental data with the assumptions that: (i) there is a water background spectrum that is common to both; (ii) the acetylene spectrum has the same shape at both flame conditions,

despite being different in magnitude; (iii) the magnitude of absorption coefficient due to water vapour can be estimated (as zero) at the line-centre of the main acetylene feature, thus allowing the ratio of the acetylene absorption coefficients to be found. This method has the advantage of avoiding the assumption that the water spectrum in these rich flames is identical to that of the $\phi = 1.0$ flame, which turns out not to be accurate, as was shown in Figure 5.5. A comparison of an extracted spectrum to a simulated spectrum from HITRAN is shown in Figure 5.15. This model spectrum is not the result of a least-squares fit to the data but is simulated for the expected flame temperature of 1600 K and an acetylene mole fraction of 0.0122 to approximately match the magnitude of the main feature. It can be seen from the figure that the extracted spectrum bears good resemblance in shape to the model spectrum. This improves the fitting process and makes it easier as there is no need to include the spectrum of water vapour in the fit. Previous authors [4] have analysed direct absorption spectra of acetylene in flames by fitting water spectra from HITEMP. Nevertheless, our own data, recorded with greater sensitivity due to the

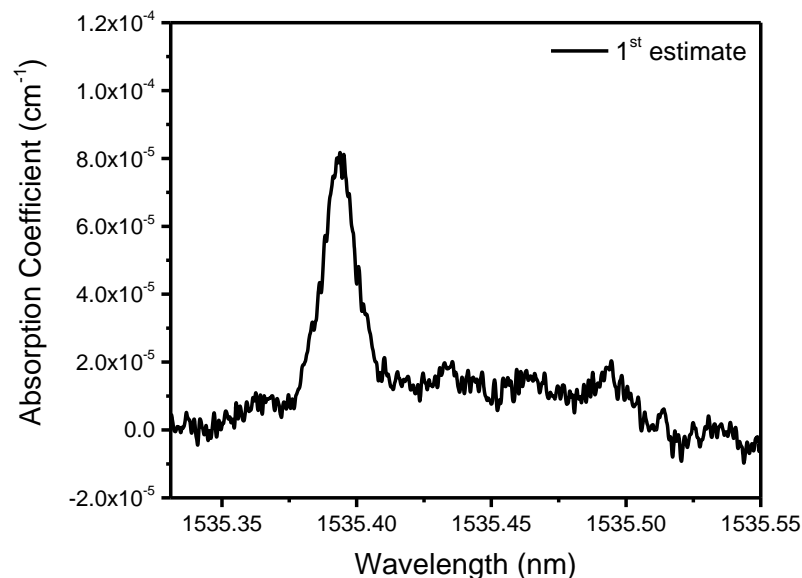


Figure 5.11: Initial estimate of acetylene contribution from the extraction process for $\phi = 2.37$ and 1.77 spectra recorded at 4 mm above the porous-plug burner surface.

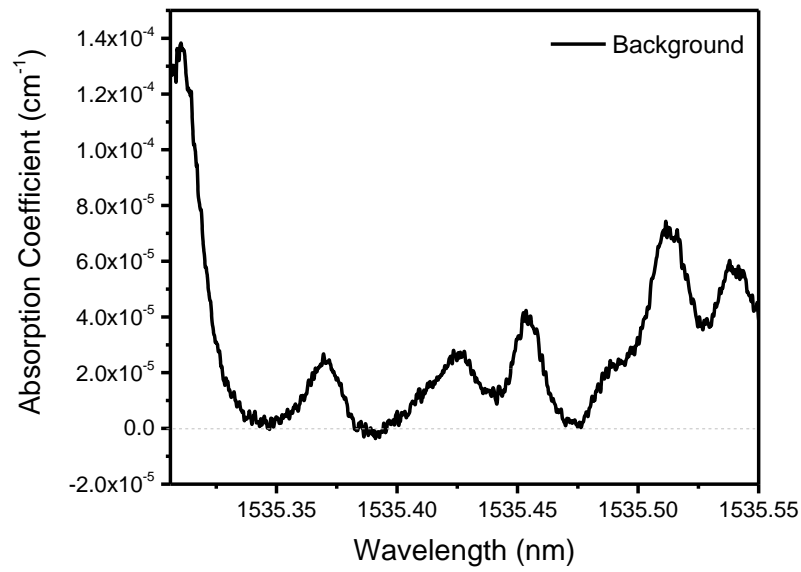


Figure 5.12: Final estimate of water-background spectrum from the extraction process for $\phi = 2.37$ and 1.77 spectra both recorded at 4 mm above the porous-plug burner surface.

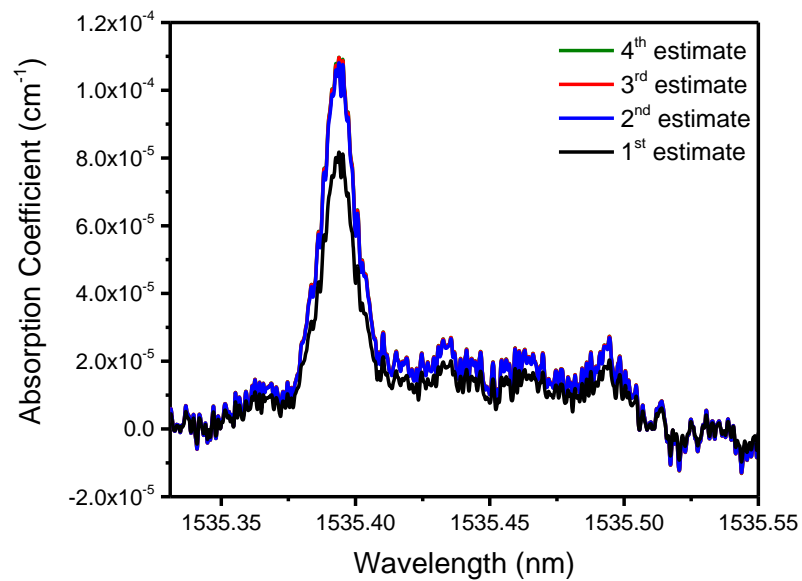


Figure 5.13: Several estimates of acetylene contribution for the richer ($\phi = 2.37$) spectrum from the iterative extraction process using the $\phi = 1.77$ spectra. Both spectra were recorded at 4 mm above the porous-plug burner surface.

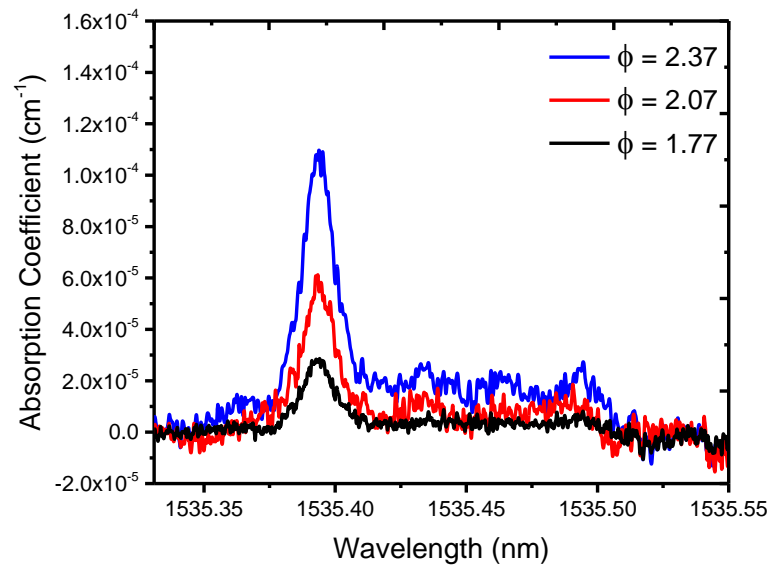


Figure 5.14: Extracted acetylene spectra for a range of different equivalence ratio flames recorded 4 mm above the porous-plug burner surface.

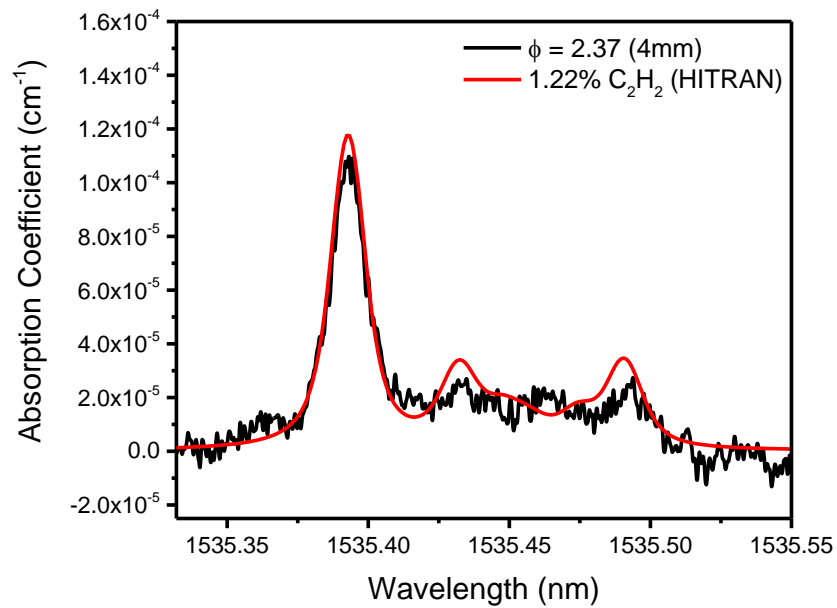


Figure 5.15: Comparison of the extracted $\phi = 2.37$ spectra in Figure 5.14 to a model spectrum using parameters from HITRAN at a temperature and pressure of 1600 K and 1 atm respectively.

CEAS approach, show that the HITEMP water spectrum is not a good match for the experimental spectrum (Figure 5.5 and Figure 5.6).

The resemblance between the extracted spectrum and the model spectrum in Figure 5.15 is not quite perfect. This may be due either to uncertainty in the raw experimental data, in the assumptions used to extract the acetylene spectrum, and/or in the data for acetylene in the HITRAN database. Nevertheless, the discrepancies are small. This leads in turn to uncertainty in parameters extracted from the spectral fitting process described in the subsequent section. One feature of the extraction process that can be seen in Figure 5.12 is that the baseline for some parts of the water-background spectrum goes very slightly below zero. This is not of concern since the chosen reference point for zero absorption is arbitrary. Two possible pairs of spectra are available in the case of each spectrum, which lead to similar extracted spectra and water-background spectra. The spectra shown in Figure 5.14 were obtained using different pairs of spectra. The $\phi = 2.37$ spectrum was extracted using the pair of $\phi = 1.77$ and $\phi = 2.37$ spectra. The $\phi = 2.07$ spectrum was extracted using the pair of $\phi = 1.77$ and $\phi = 2.07$ spectra. For the extracted $\phi = 1.77$ spectrum, the water-background from the latter extraction was subtracted from the $\phi = 1.77$ spectrum.

5.3.2 Fitting of Model Spectrum

The same spectral fitting procedure already applied to the cw-CRDS acetylene spectra is adapted to fit the model spectrum to the measured CEAS acetylene spectra. The fit was achieved using the fitting algorithm shown in Appendix B. The parameters mentioned in Chapter 4, including flame temperature profiles (Table 4.2), atmospheric pressure, as well as line strength and partition function from HITRAN were also employed here. The path-lengths for the McKenna and porous plug burners are 60 mm and 33 mm respectively. However, we later correct the results for edge effects which affect the flame diameter. Figure 5.16 shows the extracted spectra of

acetylene for a range of equivalence ratio alongside fits to the model spectrum calculated from HITRAN database.

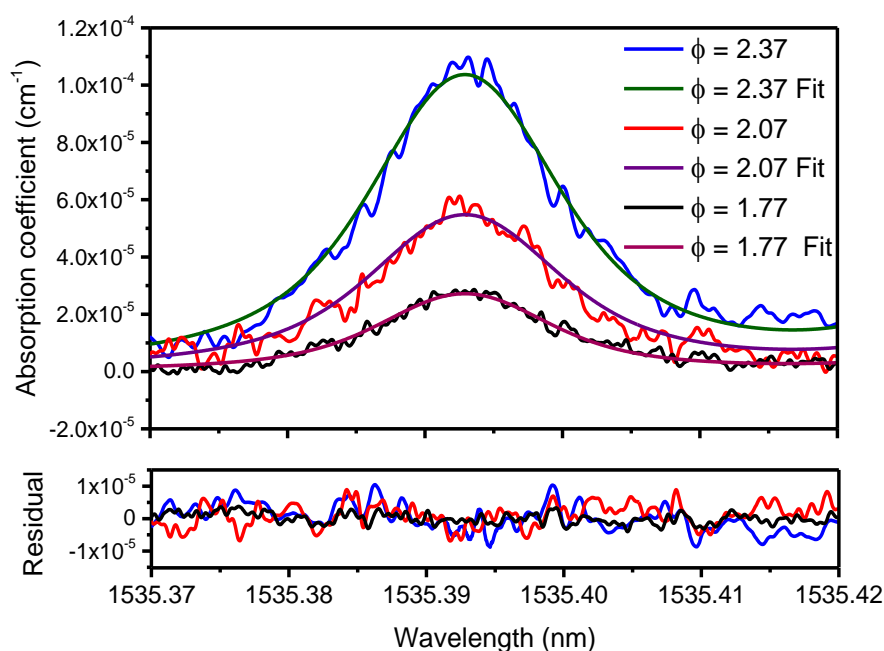


Figure 5.16: Extracted spectra of P17e acetylene line for a range of different flames at 4 mm above the porous-plug burner, shown with a fit to model spectra calculated from HITRAN.

Just as was done for the cw-CRDS spectra, the fits are actually restricted to the region surrounding the main acetylene feature (1535.37 nm – 1535.42 nm). Thus, the fit only includes the 1535.39265 nm acetylene line. Fitting over a broad range of the spectrum for the other features of acetylene resulted in a somewhat poorer fit, especially at the peak acetylene feature. For instance, a broad fit for the $\phi = 2.07$ spectrum recorded at 2 mm above the burner surface, underestimates the concentration of acetylene with an output of 0.97%. When the fit is reduced to the main acetylene feature, the calculated concentration of acetylene is increased to 1.03%. Also, for $\phi = 2.37$ at 2 mm above the burner surface, the calculated concentration of acetylene for the fit to the main acetylene feature is 1.36%. This value is reduced to 1.26% for the fit to a broader range of the spectrum. Although the

discrepancy between the results of these alternative fitting regions is reassuringly small, it is thought that the fit to the narrower region is more reliable, since here we have strong acetylene absorption and low water absorption; elsewhere the extraction of the weak acetylene absorption from stronger water absorption may be imperfect, thus constituting a source of error.

5.4 Acetylene Concentration Profiles

The resulting concentration profiles calculated from the fitting process are shown in Figure 5.17 for the measurements in the porous plug burner and the McKenna burner, respectively. The measurements were obtained at 1 mm height increments above the surface of the burner. The profiles show the reduction of acetylene concentration with height above the burner surface. Also, there is a trend of greater acetylene concentration for higher equivalence ratio flames, in keeping with our expectations and with the CRDS measurements reported in the previous chapter. Generally, the agreement between the concentration profiles with both burners is good but not perfect. The profiles for $\phi = 1.77$ deviate from each other going up the flame. Also, the $\phi = 2.07$ profiles show some discrepancy, whereas the $\phi = 2.37$ profiles show excellent agreement. A possible explanation for the apparent discrepancy observed for both burners could be the non-uniform radial distribution of acetylene concentration following from edge effects in both burners. The non-uniformity of the radial distribution of acetylene concentration at the burner edges are significant in line-of-sight absorption techniques. This leads us to investigate the radial profiles of acetylene concentration recorded in both burners and presented later in this chapter, which helps us correct the concentration profiles.

It was difficult to obtain a useful spectrum for $\phi = 2.37$ at 7 mm in the McKenna burner due to the strong background losses from the flame at that height above the burner surface, which corresponds to the onset of soot formation as discussed in the previous chapter. The concentration profiles of acetylene obtained for the $\phi = 2.37$

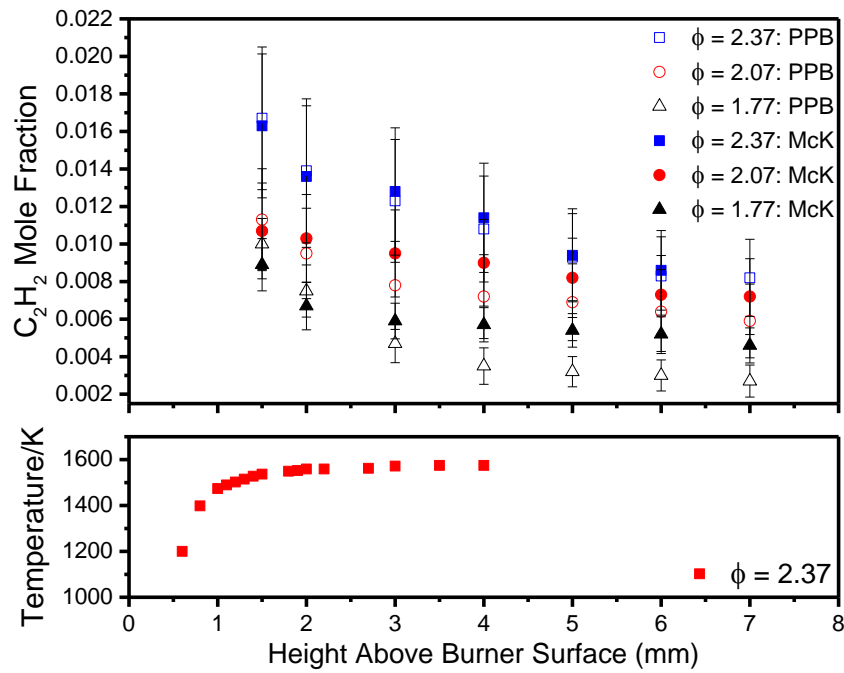


Figure 5.17: (Upper plot) Recovered concentration profiles of acetylene as a function of height above the McKenna and porous-plug burner surfaces. (Lower plot) Previous OH-LIF temperature measurements in the $\phi = 2.37$ flame on the porous-plug burner [5].

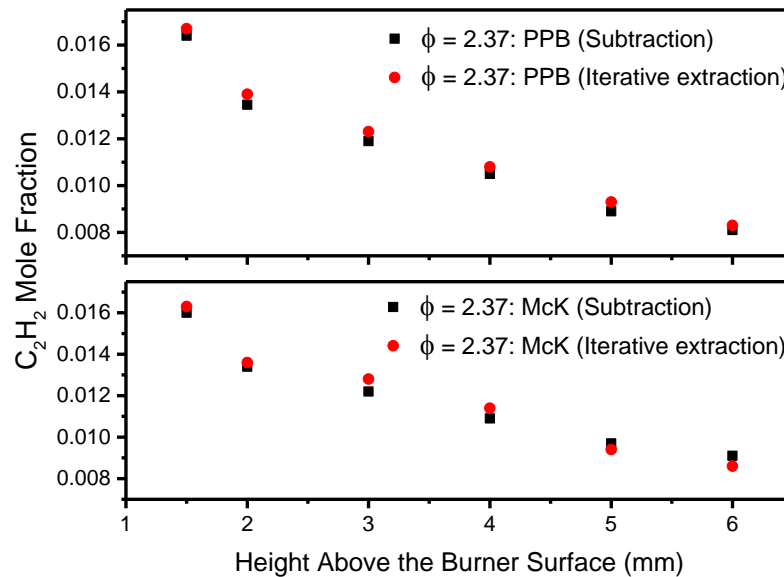


Figure 5.18: Acetylene concentration profiles for the porous-plug burner (upper plot) and the McKenna burner (lower plot) calculated using the iterative extraction technique and by subtracting the $\phi = 1.0$ spectrum.

flame using both burners are shown together with corresponding profiles obtained by subtracting the $\phi = 1.0$ spectrum in Figure 5.18. It can be seen that both methods give similar concentration profiles, whereas the method of iterative extraction provides a better representation of the shape of the acetylene spectrum.

5.4.1 Comparison of Acetylene Concentration Profiles with Model Predictions

The results are compared with profiles of acetylene calculated for the same experimental conditions using ABF [6] and USC [7] kinetic mechanisms with Cantera software. The general concepts of flame kinetic modelling have been described in Chapter 1 of this thesis, and the algorithm used in implementing the calculations is provided in Appendix E. Experimental measurements are useful in testing the accuracy of model predictions. Model predictions of intermediates and important soot precursors are essential in the eventual modelling of soot. To achieve a proper comparison, the flame is considered one-dimensional. There are material and energy balances at each 'slice' of the flame, which take into account convection, diffusion and reactions (of heat and mass). Additional measures are also required to account for the presence of the stabilisation plate above the flame. The input parameters for the calculations which correspond to the experimental flame conditions are listed in Table 5.1.

Parameter	Value
Temperature of the burner surface	373 K
Temperature of the stabilisation plate surface	873 K
Pressure	1 atm
Mass flux of premixed reactants through the burner surface	$0.0654 \text{ kgs}^{-1}\text{m}^{-2}$

Table 5.1: Input parameters for USC and ABF calculations of acetylene concentration.

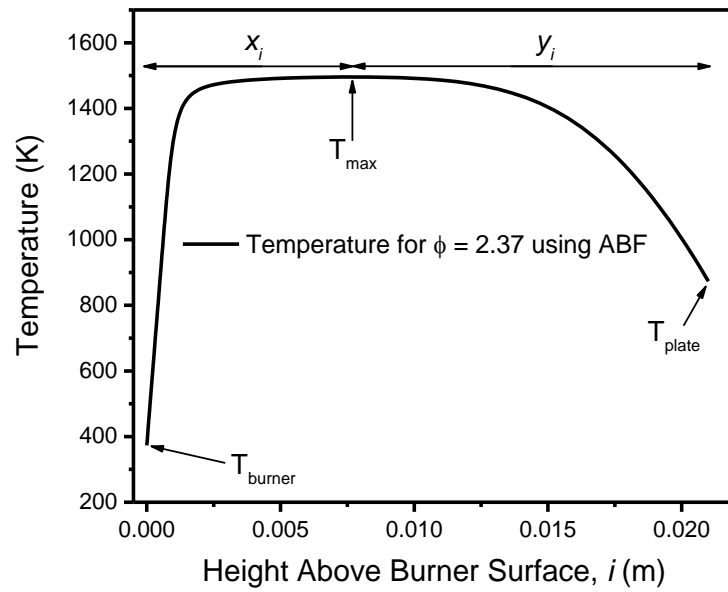


Figure 5.19: ABF temperature profile calculated for $\phi = 2.37$ flame.

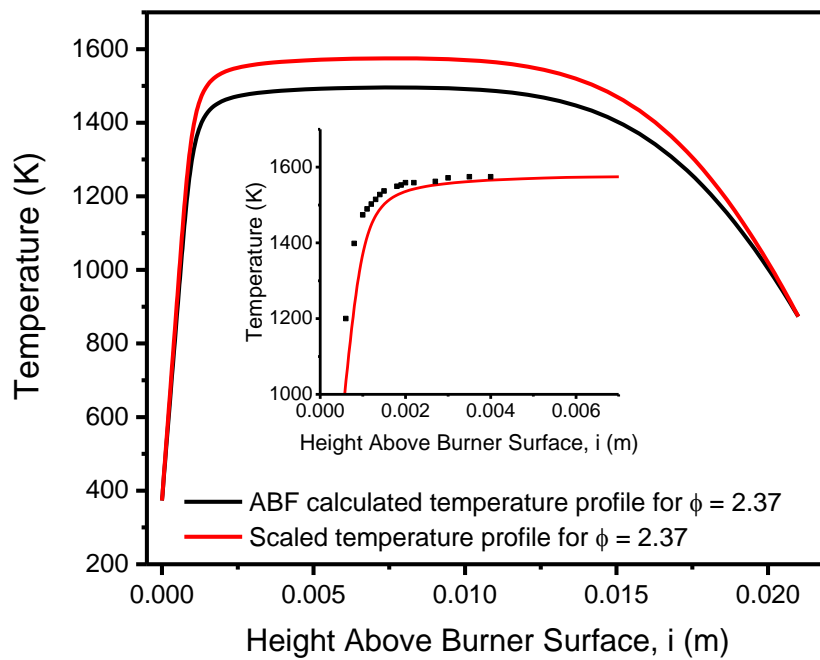


Figure 5.20: ABF calculated temperature profile and scaled temperature profile for $\phi = 2.37$ flame. Inset: scaled temperature profile for $\phi = 2.37$ flame plotted together with OH-LIF temperature measurements in a $\phi = 2.37$ flame.

The mole fractions of O₂, N₂ and C₂H₄ in the premixed gas were adjusted to match each of the flame conditions studied experimentally. For most of the simulations, a fixed temperature profile was imposed on the calculation. However, this requires a smooth temperature profile, whereas only a few discrete data points were available from previous OH-LIF measurements [5], as stated in the previous chapter. Initially, therefore, the full calculation was performed for the $\phi = 2.37$ flame, which output a temperature profile by solving the energy equation. This temperature profile was scaled with reference to the temperature of the various equivalence ratio flames listed in Table 4.2. Figure 5.19 shows the output temperature profile for a $\phi = 2.37$ flame calculated using the ABF mechanism. The temperature, T_{scaled} for each vertical position, i was scaled following Equation 5.2 and 5.3. The parameters in both equations are depicted in Figure 5.19, and $T_{max,expt}$ is the maximum temperature for each of the equivalence ratio flames listed in Table 4.2. The difference between the measured maximum temperature and the maximum calculated temperature is about 80 K.

$$T_{scaled,x_i} = (T_{ABF,i} - T_{burner}) \times \left(\frac{T_{max,expt} - T_{burner}}{T_{max,ABF} - T_{burner}} \right) + T_{burner} \quad 5.2$$

$$T_{scaled,y_i} = (T_{ABF,i} - T_{plate}) \times \left(\frac{T_{max,expt} - T_{plate}}{T_{max,ABF} - T_{plate}} \right) + T_{plate} \quad 5.3$$

The temperature values in the X_i region of the temperature profile in Figure 5.19 are scaled using Equation 5.2. In Equation 5.3, T_{burner} is replaced by T_{plate} to scale the temperature values in the Y_i region. It should be noted that only the maximum temperature measured experimentally is reflected in this scaling: the steep gradient near to the burner surface is not shifted vertically to match the experimental data. The correspondence between the experimental data points and the scaled profile can be seen in Figure 5.20.

The resulting profiles of acetylene concentration for the scaled and ABF calculated temperature profiles are shown in Figure 5.21. The concentration profile of acetylene

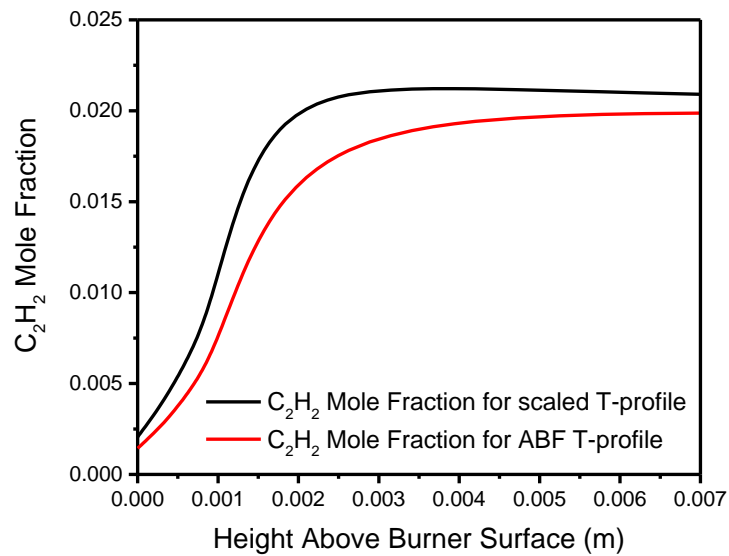


Figure 5.21: ABF concentration profiles of acetylene for $\phi = 2.37$ flame using ABF calculated and scaled temperature profiles.

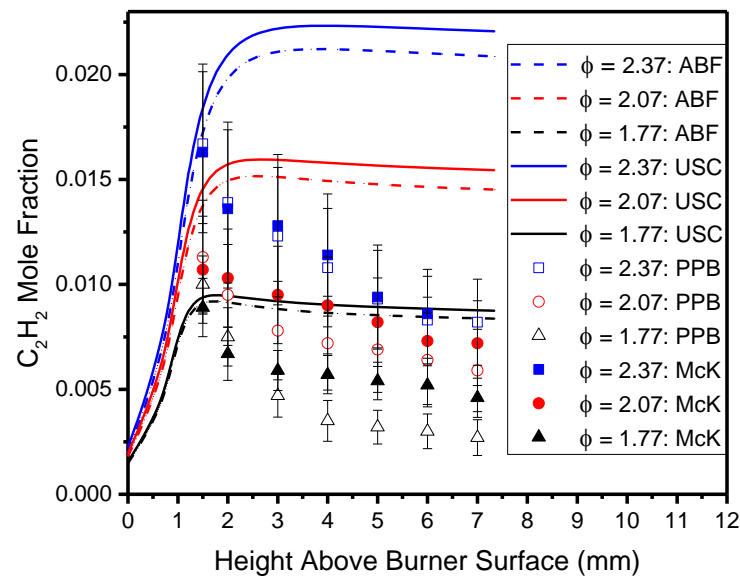


Figure 5.22: Measured and calculated (ABF and USC) concentration of acetylene as a function of height above the burner surface.

for the scaled temperature profile maintains a higher peak and steeper gradient than for the temperature profile resulting from the ABF model (which has lower peak

temperature). This is also the case for the USC model and is due to the higher temperature of the scaled temperature profile, as seen in Figure 5.20. This observation also holds for the different equivalence ratio flames. This analysis, therefore, provides an indication of the sensitivity of the calculated acetylene concentration to uncertainty in the flame temperature profile.

Generally, both the ABF and USC models predict higher acetylene concentration than the measurements, as can be seen in Figure 5.22. However, there is a certain level of agreement in the peak acetylene concentration between the mechanisms and the experimental profiles. The models fail to predict the decline in acetylene concentration observed in the burnt gases for the experimental profiles. This can be seen in Figure 5.22, where the model profiles maintain a plateau as opposed to the experimental profiles that decay with increasing height above the burner surface. The reason for this could be attributed to the fact that the models underestimate the consumption of acetylene in the reactions that produce PAHs. The USC and ABF mechanisms do not account for PAHs growth beyond 4-aromatic rings (pyrene) or indeed for soot formation and growth [6, 7].

Another possible reason could be attributed to what some researchers have claimed to be an inaccurate rate coefficient incorporated in both mechanisms for the $C_2H_2 + OH \rightarrow CH_2CO + H$ reaction as observed and reported by Mokhov et al. [8] and Kaiser et al. [9] for the GRI 3.0 mechanism. This is as some of the chemistry in USC and ABF mechanisms are based on the GRI 3.0 mechanism, and this rate coefficient is given as $2.18 \times 10^{-4} \text{ cm}^3 \text{ mol}^{-1} \text{ s}^{-1}$ in the GRI 3.0 mechanism. Kaiser et al. adopted a much higher rate expression of $3.24 \times 10^{13} \exp(-12000 \text{ cal mol}^{-1} / RT) \text{ cm}^3 \text{ mol}^{-1} \text{ s}^{-1}$ which amounts to $6.54 \times 10^{11} \text{ cm}^3 \text{ mol}^{-1} \text{ s}^{-1}$ at 1600 K (the typical temperature for the flame conditions employed in this work). This rate coefficient still underpredicted the consumption of acetylene. Gersen et al. [10] suggests a rate coefficient of $4.87 \times 10^{13} \text{ cm}^3 \text{ mol}^{-1} \text{ s}^{-1}$ which was used to realise strong agreement between calculated and measured acetylene concentration, which decline with increasing height above the burner surface. Adjusting rate coefficients

of individual reactions to suit the concentration profile of an individual species based on a limited dataset should be treated with some caution as this could influence other reactions and processes occurring in the flame. A rigorous modification of established chemical kinetic mechanisms should be done based on a wide dataset over a range of flame conditions and with multispecies measurements, and this type of activity constitutes a separate field of research in itself [11-13]. Nevertheless, these previous studies may lead us to tentatively consider the possibility of higher rate coefficient for this reaction.

The agreement of measured and simulated acetylene concentration profiles in premixed flames has been discussed by S. Roy and D. Haworth [14] albeit based largely on data obtained by extractive sampling. Here, a trend of decreasing concentration with increasing HAB was observed in a few previous studies [15, 16]. In keeping with our own findings based on the USC and ABF mechanisms, all but one of the mechanisms tested showed a plateau in acetylene concentration downstream of the reaction zone. A Slavinskaya and Frank (SF) mechanism [17] reproduced the decaying trend of acetylene concentration with HAB. The rate coefficient for the $C_2H_2 + OH \rightarrow CH_2CO + H$ reaction is given as $2.19 \times 10^{-4} \text{ cm}^3 \text{ mol}^{-1} \text{ s}^{-1}$ in the SF mechanism. This rate coefficient does not differ meaningfully from that incorporated in the GRI 3.0 mechanism and others [17]. The SF mechanism incorporates additional pathways for pyrene (4-aromatic rings) production and also includes the chemistry of species beyond pyrene up to 5-aromatic rings. As such, it is able to predict the reducing trend of acetylene concentration with HAB [18]. Slavinskaya et al. [19] and Dworkin et al. [18] have reported incomplete PAH growth pathways in USC and ABF mechanisms which result in PAH underprediction for both mechanisms. This together with the limitation of both (USC and ABF) mechanisms to predict PAH growth beyond pyrene contribute to the discrepancy observed with experimental results in Figure 5.22. Adopting the SF mechanism to the software package used in this work was challenging and as such profiles of acetylene could not be obtained using the SF mechanism for comparison with the experimental results.

In this work, standard mechanisms that are widely used have been employed to test for their ability to concur with our experimental results. As already stated, elsewhere, the refinement of chemical kinetic models is beyond the scope of this thesis, whose purpose has instead been to develop methods for measuring acetylene mole fraction in flames contributing to wider efforts to understand its role in soot formation. The comparison has further established the discrepancy between the model predictions and experimental results previously highlighted by others. This presents an opportunity for those who specialise in the development of these models to investigate the reasons for the discrepancy including those already mentioned earlier.

5.4.2 Radial Profiles of Acetylene Concentration

Radial profiles of acetylene concentration were obtained by translating the burner horizontally. This was necessary to understand any possible influence of edge effects on the concentration profiles of acetylene in the flame. It is worth noting that such radial profiles would have been impossible to record using the cw-CRDS technique described in the previous chapter, due to the effect of flame translation on the mode-matching process. As stated in Chapter 3, laminar flat-flames are assumed to be one-dimensional at the centre-line. However, cold gases surrounding the burner influence the radial homogeneity of species at the burner edges. As such, this must be taken into account in measurements that employ line-of-sight absorption techniques [20]. Edge effects arise from mixing with the atmosphere around the burner periphery. This is possible through convective in-flow of the surrounding atmosphere [21]. Edge effects have previously been reported in various studies to have influenced measurements of concentration, temperature and burning velocities [22-24].

Figure 5.23 and Figure 5.24 show the concentration profiles of acetylene along the horizontal axis for both burners at vertical positions of 3 mm and 4 mm. The concentration of acetylene is seen to vary at the edge of both burners due to edge effects. The plot in Figure 5.25 shows the comparison for the radial profiles for both

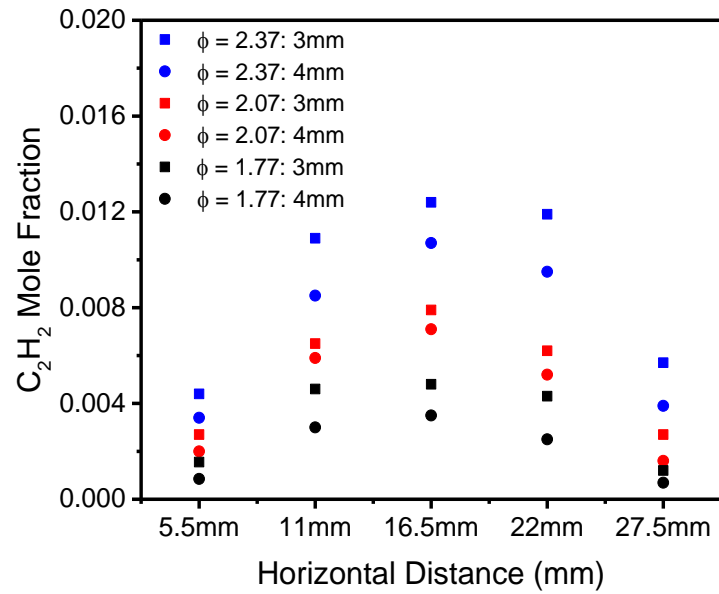


Figure 5.23: Radial distribution of acetylene concentration for a range of equivalence ratio flames at 3 mm and 4 mm above the porous plug burner surface.

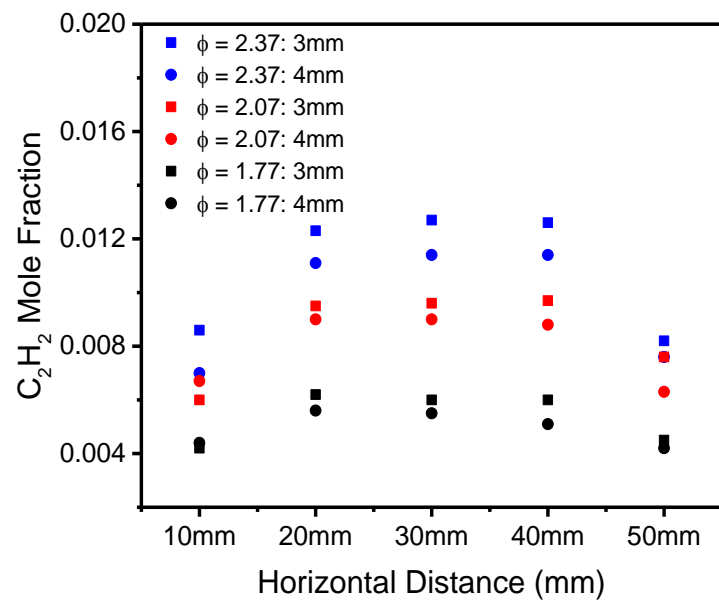


Figure 5.24: Radial distribution of acetylene concentration for a range of equivalence ratio flames at 3 mm and 4 mm above the McKenna burner surface.

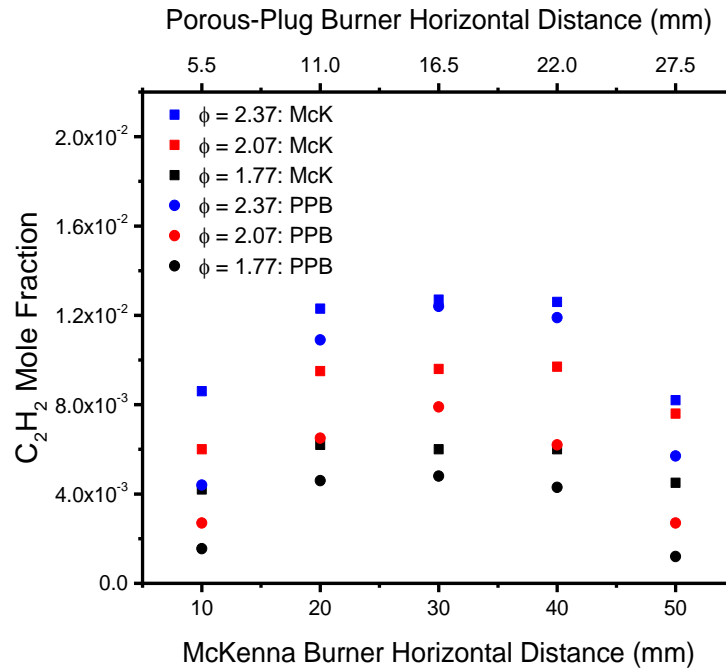


Figure 5.25: Radial distribution of acetylene concentration for a range of equivalence ratio flames at 3 mm above the McKenna burner and porous-plug burner surfaces.

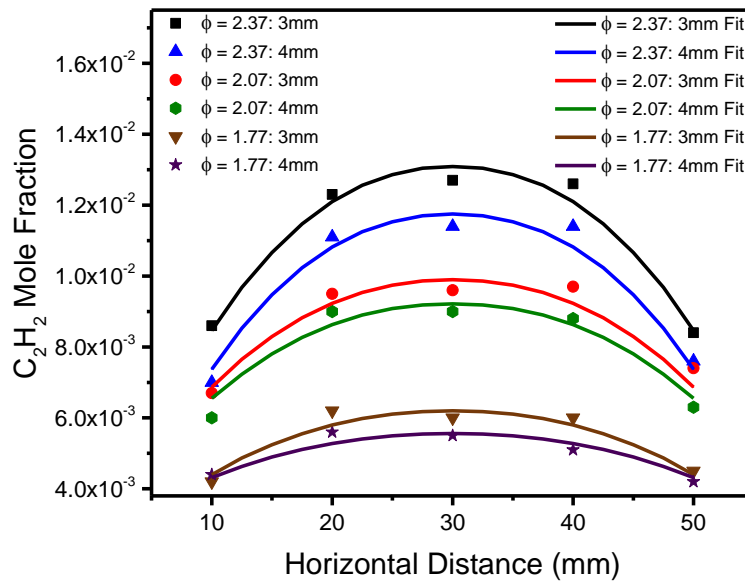


Figure 5.26: Fits of the flat distribution model to the radial concentration of acetylene at 3 mm and 4 mm above the McKenna burner surface.

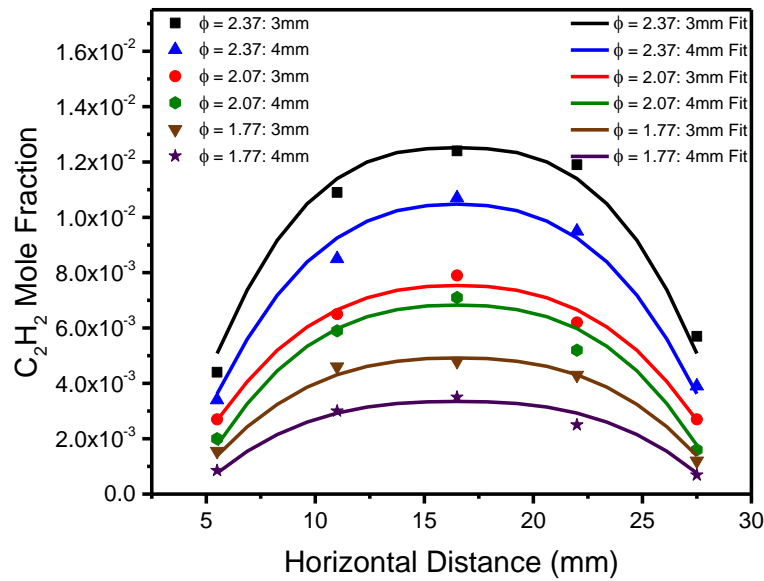


Figure 5.27: Fits of the flat distribution model to the radial concentration of acetylene at 3 mm and 4 mm above the porous-plug burner surface.

Variable	$\phi = 2.37$ 3 mm	$\phi = 2.37$ 4 mm	$\phi = 2.07$ 3 mm	$\phi = 2.07$ 4 mm	$\phi = 1.77$ 3 mm	$\phi = 1.77$ 4 mm
Burner edge	3.78	4.31	2.22	1.57	1.63	-1.73
Effective width	26.22	25.69	27.78	28.43	28.37	31.73

Table 5.2: Values of the burner edges and effective widths extracted from the fit for the McKenna burner.

burners recorded at 4 mm above the burner surface. The reduction in acetylene concentration at the edges is seen to be less significant in the McKenna burner. This will be due to the larger diameter of the McKenna burner.

Variable	$\phi = 2.37$ 3 mm	$\phi = 2.37$ 4 mm	$\phi = 2.07$ 3 mm	$\phi = 2.07$ 4 mm	$\phi = 1.77$ 3 mm	$\phi = 1.77$ 4 mm
Burner edge	4.47	4.78	4.74	5.11	5.04	5.21
Effective width	12.03	11.72	11.76	11.39	11.47	11.29

Table 5.3: Values of the burner edges and effective widths extracted from the fit for the porous-plug burner.

To properly estimate the radial distribution of acetylene concentration in a symmetrical flame configuration like ours, an Abel inversion is typically employed [25, 26]. However, the data we have is too sparse to perform an Abel inversion. Instead, a model calculated based on a flat distribution was fitted to the radial concentration data as can be seen in Figure 5.26 and Figure 5.27 for the McKenna burner and the porous-plug burner respectively. In the model, the local absorption coefficient is constant for radii r less than the predicted effective radii r_0 , and is zero beyond that. Thus, r_0 was a variable parameter in the fit. The equation for the function is given below where α is the absorption coefficient and x is the radial measurement location.

$$\frac{2\alpha r}{\sqrt{|r^2 - x^2|}} \quad 5.4$$

The fit gives an estimate of the shape of the radial distribution and the effective radii (widths) for both burners at the vertical measurement positions of 3 mm and 4 mm. The effective radii extracted from the fit are shown in Table 5.2 and Table 5.3 for the McKenna burner and the porous plug burner respectively. The burner edge is calculated by subtracting the effective radii from the radius of the burner (which is 30 mm for the McKenna burner and 16.5 mm for the porous plug burner). It can be seen from the results in the tables above that the calculated edges (ignoring one anomalous result for the McKenna burner) are larger for the porous-plug burner which corroborates the earlier observation. The anomalous result is considered as an

outlier as all the other values follow a particular trend, hence it was excluded in the analysis.

We go ahead to assume that the differences between the flame compositions and the vertical locations (3 mm and 4 mm) separated by 1 mm cannot be resolved. Performing radial scans at elevated positions in the flame would be more challenging, resulting in lower SNR. Thus, we consider the effective radii extracted from the fit as representative at a mean height of 3.5 mm and of the range of behaviour of the three flame compositions (and consider the entire range of evaluated radii in estimating uncertainty). The reduction in flame diameter appears to lessen with increasing height above the burner surface (including as evidenced by the width of the soot containing region). Thus, we consider a linear decrease up to 3.5 mm, followed by a flat profile to obtain the effective diameters of the flame for the various heights and for both burners employed. By considering the entire range of the evaluated effective radii in evaluating uncertainty (± 1.37 mm for the McKenna burner and ± 0.37 mm for the porous-plug burner), minimum and maximum values of the effective diameter for each height and burner were calculated and the average values are shown in Table 5.4. Calculating the average effective diameter for the vertical positions we obtained acetylene concentration (1.5 mm – 7mm in Table 5.4) in both burners show that the effective diameter is 8% less for the McKenna burner (60 mm diameter) and 27% less for the porous-plug burner (33 mm diameter). Thus, we confirm that the impact of edge effects can be significant in concentration measurements employing cavity-based techniques.

The effective diameters are used to correct the concentration profiles shown in Figure 5.17. This results in a significant uplift of the concentration as shown in Figure 5.28. However, this does not override the general trend of decreasing acetylene concentration with increasing height above the burner surface. The corrected profiles are seen to disagree significantly for the richest flame but show reasonable agreement for the other flames, which possibly suggests that the radial effects are more significant in the richest flame. However, this could also either be due to actual

differences in the concentration profiles or to the assumptions made in the analysis of the radial profiles and/or in calculating concentration. A comparison between the corrected profiles and model predictions are shown in Figure 5.29. There is better agreement between the corrected profiles and the calculated profiles for the peak concentration of acetylene in comparison to that shown in Figure 5.22.

Height Above the Burner (mm)	McKenna Burner (mm)	Porous-plug Burner (mm)
1.0	58.46	30.20
1.5	57.68	28.80
2	56.92	27.42
3	55.38	24.62
4	54.46	22.94
5	54.18	22.36
6	53.88	21.80
7	53.60	21.22

Table 5.4: Effective diameters for the McKenna burner and the porous-plug burner.

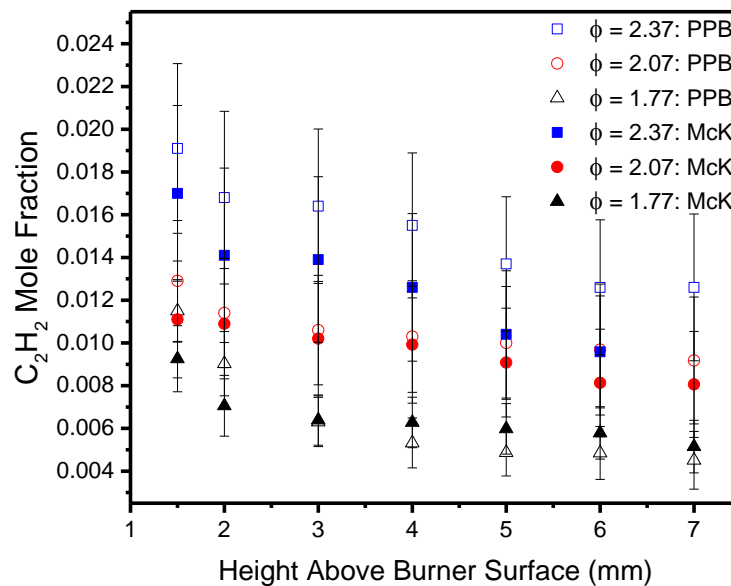


Figure 5.28: Corrected concentration profiles of acetylene as a function of height above the McKenna and porous-plug burner surfaces.

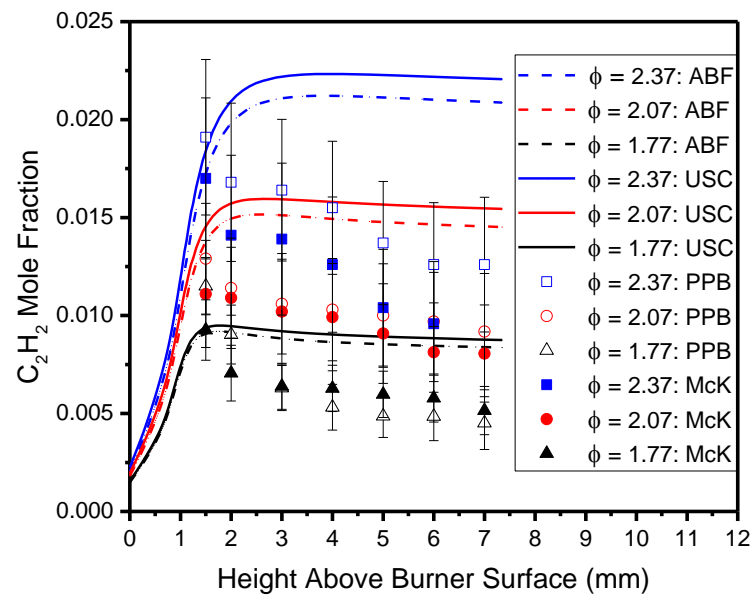


Figure 5.29: Corrected profiles and calculated (ABF and USC) profiles of acetylene as a function of height above the burner surface.

5.5 Extinction Measurements

Let us now look at the extinction measurements obtained in both the McKenna and porous-plug burner. The measurements were obtained at increments of 1 mm for a range of equivalence ratio flames and are shown in Figure 5.30. The figure gives a measure of the optical losses in the flames. These losses are thought to be attributable in part to the presence of large aromatic species as well as soot in the flames, as well as to thermal effects. This is commensurate with the observed trend where richer flames which are expected to contain higher amounts of these aromatic species possess higher losses [27, 28]. Flames with low sooting potential do not exhibit any considerable change in optical losses with height above the burner surface. However, the richer flames show a significant increase in optical loss beyond a certain point in the flame.

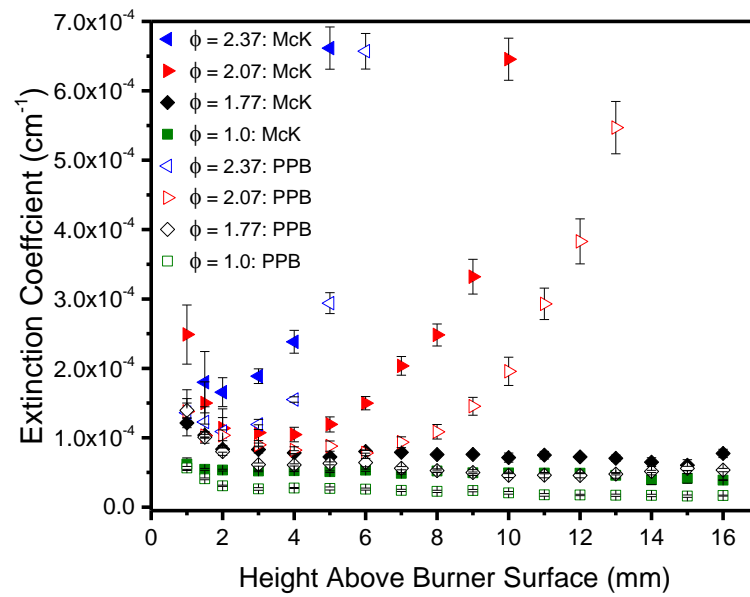


Figure 5.30: Extinction coefficients measured for various equivalence ratio flames at 1 mm increments of height above the porous plug burner and McKenna burner surfaces.

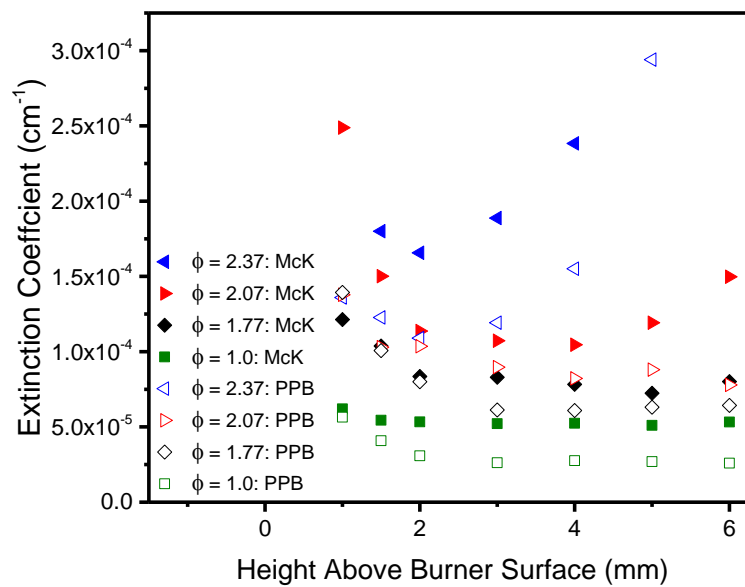


Figure 5.31: Extinction measurements in Figure 5.30 shown on an expanded scale for 1 mm – 6 mm heights above the porous plug burner and McKenna burner surfaces.

The agreement between the extinction measurements obtained with both burners is reasonable, although not perfect. The losses in the porous-plug burner are relatively lower than those obtained with the McKenna burner. The agreement is relatively better in the less rich flames where optical losses are minimal. Lower down in the flame, the extinction coefficients for both burners are closely matched (except for the richest flame) but begin to deviate as the measurements go downstream the flame. This may be explained through a path-length effect related to edge-effects, as has already been discussed for acetylene.

5.6 CEAS vs cw-CRDS

Similar measurements of acetylene have been obtained in the same combustion system (ethylene-air flames supported on the porous plug burner) for both CEAS and cw-CRDS techniques, the latter of which were reported in the previous chapter. The sensitive measurements obtained using both techniques are mutually comparable, and this, therefore, allows cross-validation of the resulting measurements. It also permits an assessment of the relative merits of these approaches for measurements of trace species in laminar flames. CEAS and cw-CRDS are related techniques that have been employed in measurements outside of combustion systems. Previous CEAS and cw-CRDS studies in non-combustion systems have compared the sensitivities of both techniques with cw-CRDS being the more sensitive technique [29, 30]. Another important feature of cw-CRDS is that it is an absolute measurement technique. On the other hand, CEAS is associated with shorter measurement time (as explained below) and thus can be used to obtain spectra with better spectral resolution and covering a broader spectral range within a convenient timescale. The reason for the shorter measurement time of CEAS is that a complete spectrum is acquired by scanning the laser rather than the step-wise acquisition sequence of ring-down events for CRDS. CEAS is a simpler and related technique that incorporates much of the desired features of cw-CRDS. Phase-sensitive detection can be applied to increase the sensitivity of CEAS technique [2, 31]. However, this would diminish

the advantages of simplicity provided by the CEAS technique and the relatively lower cost of the CEAS set-up.

Figure 5.32 shows spectra recorded with both techniques at the same position in the flame for a range of equivalence ratio flames. Overall, the spectra from both techniques are identical in shape. The CEAS measurement agrees very well with that of cw-CRDS for $\phi = 1.0$ flame. The agreement for the richer flames is also very good with only slight deviations. This agreement is also observed for the $\phi = 1.77$ spectra which is not included in Figure 5.32 so as not to overcrowd the plot. The slight deviations would be partly because of the poorer spectral resolution of the cw-CRDS measurements for the rich flames. In the previous chapter, it was seen that the cw-CRDS spectra for the various equivalence ratio flames appeared to converge in areas where there is no contribution from acetylene. Therefore, a simple subtraction of the $\phi = 1.0$ spectrum from the rich spectrum would yield a spectrum due to acetylene. For the CEAS spectra shown in Figure 5.5, which were recorded over a broader spectral range and with better spectral resolution, it became apparent that the $\phi = 1.0$ spectrum did not quite converge with the spectra of the rich flames. These slight differences are perhaps more apparent in the CEAS spectra due to the broader spectral coverage and better spectral resolution. It was also noted that the spectra for the three rich flame conditions do overlap with each other for regions of the spectrum where acetylene absorption is negligible (presumably due to similar profiles of flame temperature and water vapour mole fraction). Hence, an “iterative extraction” technique was developed as described earlier in this chapter. As shown previously in Figure 5.18, these two approaches result in very similar concentration profiles, whereas we believe the iterative approach should provide a better representation of the overall shape of the acetylene spectrum.

The procedure for aligning the CEAS cavity is relatively simpler than that of cw-CRDS which involves mode-matching to a single cavity mode. As mentioned earlier, CEAS also has the advantage that a spectrum can be obtained in shorter measurement time (in seconds); hence, it is easier to acquire a spectrum over a broad wavelength range.

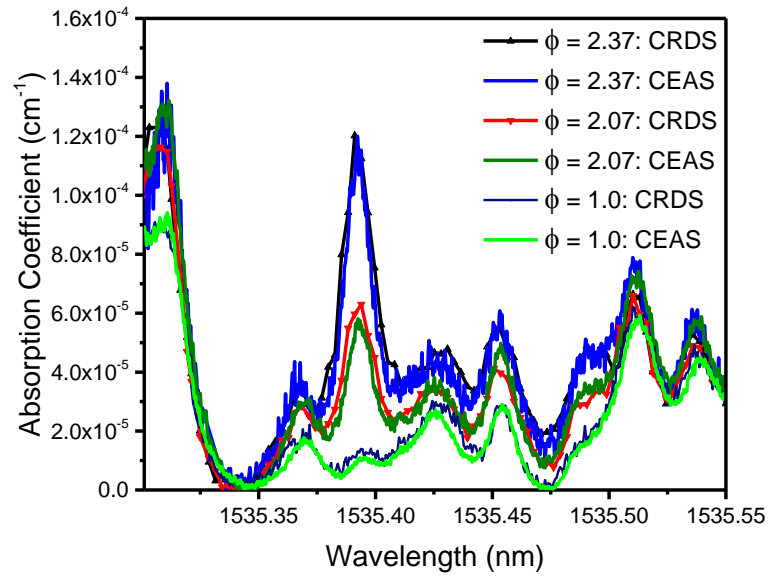


Figure 5.32: CEAS and cw-CRDS spectra for a range of equivalence ratio flames recorded at 4 mm above the porous plug burner surface.

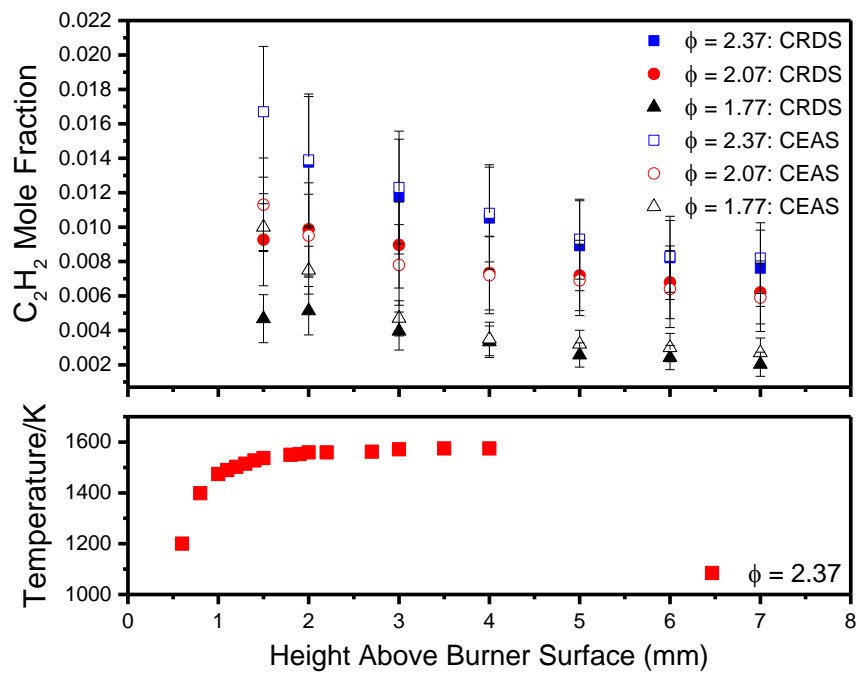


Figure 5.33: (Upper plot) CEAS and cw-CRDS recovered concentration profiles of acetylene as a function of height above the porous plug burner surface. (Lower plot) Previous OH-LIF temperature measurements in the $\phi = 2.37$ flame on the porous-plug burner.

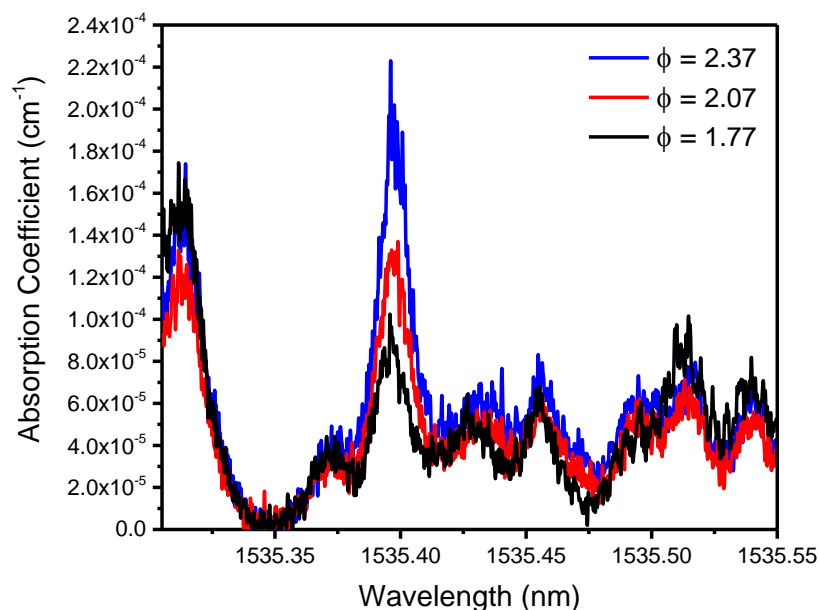


Figure 5.34: CEAS spectra recorded for a range of equivalence ratio flames recorded at 1 mm above the porous-plug burner surface.

The CEAS advantage of acquiring a broad spectrum provides a further advantage that multiple species could, in principle, be detected simultaneously. The cw-CRDS measurement was recorded over a narrower range, and the spectral resolution was less good due to the time taken to record each single spectral data-point by averaging multiple ring-down traces. It took an average time of about 30 minutes to record a cw-CRDS spectrum over the narrower range. As was explained in Chapter 4, data acquisition is particularly slow with cw-CRDS for the richer flames, in which transmission is low. The CEAS spectra recorded at the different flame conditions have a common wavelength scale and better resolution.

The cw-CRDS technique has the advantage that it is self-calibrating. This advantage lends credence to the results obtained using CEAS in this work due to the close correspondence between the two methods. Figure 5.33 shows the concentration profiles of acetylene obtained using both techniques. The agreement for both techniques is good beyond 2 mm above the burner surface. There is less good

agreement low down in the flame, specifically at 1.5 mm and 2 mm heights above the burner for $\phi = 1.77$ and at 1.5 mm HAB for $\phi = 2.07$. It is thought that this can be attributed to the strong temperature gradient in this region of the flame, as can be seen in Figure 5.33 (lower plot) for the temperature of the $\phi = 2.37$ flame, when considered together with the larger beam waist of the light circulating in the cavity for the CEAS technique. This larger beam waist is the result of deliberately exciting multiple longitudinal modes of the cavity which was not measured. With the CEAS technique, measurements can be obtained even lower down in the flame than can be achieved with cw-CRDS technique (as the strong temperature gradient low down in the flame significantly affects the delicate mode-matching process).

Characteristics	cw-CRDS	CEAS
Spatial resolution	✓	
Spectral resolution		✓
Ease of alignment		✓
Record a broad spectrum in real-time		✓
Calibration-free	✓	
Less susceptible to vertical temperature gradients		✓
Speed of data acquisition		✓

Table 5.5: Comparison of the characteristics of CEAS and cw-CRDS techniques.

Figure 5.34 shows CEAS spectra of acetylene obtained at 1 mm in the flame supported on the porous plug burner. This helps us put an upper bound on the beam waist as 1 mm. The spectra in Figure 5.34 are relatively noisier than those obtained

at other measurement positions in the flame before the onset of significant broadband absorption. Also, there is a certain amount of variation among the spectra in areas where there is no contribution from acetylene, which is likely to be the results of strong gradients in temperature and water vapour mole fraction in this region of the flame, in addition to the lower signal levels. However, it was impossible to obtain a useful spectrum at this position in the flame using cw-CRDS, presumably due to the effect of thermal gradients on the stability of the cavity. As can be seen in Figure 5.33, an acetylene spectrum could not be obtained using cw-CRDS at 1.5 mm for the richest flame, hence, no value for the concentration of acetylene at that height above the burner surface. This makes sense since the reaction zone shifts slightly away from the burner surface as the equivalence ratio is increased. Table 5.5 simply summarises the comparison of the essential characteristics of both techniques.

5.6.1 Comparison of Extinction Measurements for cw-CRDS and CEAS

The extinction measurements for both techniques are shown at 1 mm increments in

Figure 5.35. An identical trend where higher equivalence ratio flames exhibit higher losses can be seen for the extinction profiles from both techniques. Also, the losses increase significantly above a certain point in the very rich flames. Generally, similar trends are observed for both techniques. However, CEAS records relatively lower optical losses than cw-CRDS. This is thought to be due to the different effects of thermal gradients on the two methods, with the single-mode cw-CRDS method suffering greater round-trip thermal losses. As a consequence, it is only relative broad-band absorption that can be measured by this approach. At some point in the very rich flames, the CEAS optical losses become higher than those of cw-CRDS, which is attributable to the sharply rising extinction (due to PAH and soot) together with the slightly poorer spatial resolution of CEAS. The leaner flames maintain a flat profile for both techniques.

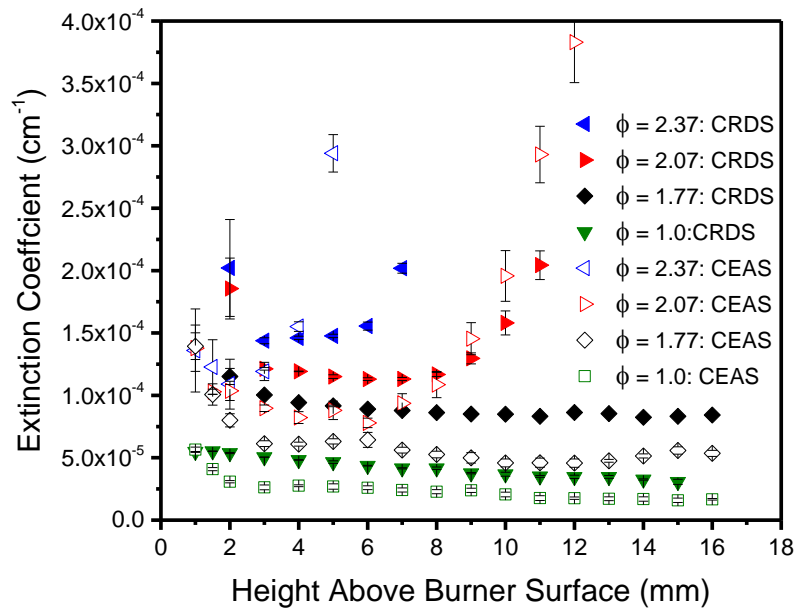


Figure 5.35: Extinction coefficients measured using CEAS and cw-CRDS techniques for various equivalence ratio flames at 1 mm increments of height above the burner surface.

5.7 Uncertainty Analysis

Some of the sources of uncertainty in the recovery of acetylene concentration from the cw-CRDS measurements present the same impact on the CEAS measurements. They include uncertainties resulting from temperature, mass flow controllers, line strength and collisional broadening parameter. These sources similarly influence the CEAS measurements with temperature being the major source of uncertainty. Varying the temperature by 80 K for the $\phi = 2.37$ spectrum recorded at 2 mm gives an uncertainty of +29% and -24%. The uncertainty for the line strength $S(T_0)$ of the P17e acetylene feature and that obtained in fitting for the collisional broadening parameter are given as $\pm 2\%$ and $\pm 0.8\%$ respectively (refer to Chapter 4). The uncertainty introduced by the mass flow controllers is $\pm(0.8\% \text{ of reading} + 0.2\%)$ which translates to slightly different uncertainty values for the various flows

corresponding to different equivalence ratios (mass flow controller readings and corresponding equivalence ratios are shown in Table 3.1 and Table 3.2 for the McKenna burner and porous-plug burner respectively). For $\phi = 2.07$, the uncertainty values for the mass flow controllers are calculated as 0.5% and 1.2% for the flow of ethylene in the porous-plug burner and McKenna burner, respectively. Like the cw-CRDS measurements presented earlier, the standard errors of the measurements average about 10% and differ based on the measurement location in the flame. It is important to note that the CEAS spectra was processed using the iterative extraction technique which is based on some assumptions and results in spectra that give a better representation of the spectrum due to acetylene alone. It is thought that this should greatly affect the recovered concentration of acetylene. However, since the fit is limited to the main acetylene feature, this should be less significant to the final concentration of acetylene as evidenced by the results in Figure 5.18 and Figure 5.33. The uncertainty values calculated based on the concentration values resulting from both methods of processing the spectra for all HAB in both burners averaged less than $\pm 3\%$. The results from the radial measurements of acetylene using the CEAS technique highlight the impact of edge effects on the measurements. The uncertainty in calculating the effective diameter for each vertical measurement position was estimated utilising the maximum and minimum values. The maximum and minimum values were obtained using the uncertainty calculated for the entire range of the evaluated effective widths (± 1.37 mm for the McKenna burner and ± 0.37 mm for the porous-plug burner).

The overall measurement uncertainty is obtained (as previously stated in Chapter 4) as the square root of the sum of the squares of the individual uncertainties leading to an overall measurement uncertainty of +31% and -26%. Like in the cw-CRDS measurements presented in the previous chapter, the uncertainty (+29% and -24%) from the temperature values used is the most significant uncertainty followed by the standard error in the measurements. All other uncertainties pale in comparison to the overall measurement error.

5.8 Summary

Cavity-enhanced absorption spectroscopy has been applied to measure acetylene concentration *in situ* in flames for the first time using a near-infrared diode laser. The advantages of this technique over the work on continuous-wave cavity ring-down spectroscopy reported in the previous chapter have been highlighted, whilst noting the agreement between the two techniques. The CEAS approach allows spectra to be acquired much more rapidly and with better spectral resolution, as well as having a somewhat simpler experimental set-up. This, therefore, provides a convenient approach for sensitive detection of trace species in laminar flames.

Acetylene concentrations have been measured in a laminar premixed ethylene-air flat-flame at atmospheric pressure. This was achieved by recording CEAS spectra of the P17e feature of acetylene at 1535 nm for a range of equivalence ratios. The resulting CEAS acetylene profiles show higher acetylene concentrations for higher equivalence ratio flames. They also show a trend of decreasing acetylene concentration with increasing height above the burner surface (HAB). This would be consistent with the consumption of acetylene, including in reactions forming polycyclic aromatic hydrocarbons (PAHs) and ultimately soot. The profiles obtained using both burners show good agreement for the richest flame. This is not the case for the other flame compositions. A possible explanation for the discrepancy could be radial effects, and efforts were made to compensate for the effects by investigating the radial profiles of acetylene obtained for both burners. The corrected profiles show greater radial effects in the richest flame, but the effects are not sufficient to override the decreasing trend of acetylene in all the flame compositions.

The concentration profiles of acetylene are compared with those obtained using cw-CRDS technique in Chapter 4. The results show that both techniques are sensitive with CEAS being more advantageous owing to its faster data acquisition, which allows broader spectra to be acquired with favourable spectral resolution. The recovered

profiles of acetylene are compared with predicted profiles from USC and ABF kinetic mechanisms. The mechanisms are seen to underestimate the consumption of acetylene downstream in the flame. This is perhaps simply because the occurrence of neither larger PAHs nor soot is accounted for by these models, or possibly due to an underestimation of the rate of reaction of acetylene with the hydroxyl radical. Extinction data which provide a measure of broad-band optical losses in the flame were also obtained. These measurements show higher losses for richer flames and with increasing HAB, including prior to the onset of soot formation in rich flames. The losses are thought to be partly attributable to broad-band near-infrared absorption by larger aromatic species and soot in the flame.

5.9 References

1. Drake, G.W., *Springer handbook of atomic, molecular, and optical physics*. 2006: Springer Science & Business Media.
2. Mazurenka, M., et al., *Cavity ring-down and cavity enhanced spectroscopy using diode lasers*. Annual Reports Section "C" (Physical Chemistry), 2005. **101**: p. 100.
3. Peeters, R., G. Berden, and G. Meijer, *Near-Infrared Cavity Enhanced Absorption Spectroscopy of Hot Water and OH in an Oven and in Flames*. Applied Physics B-Lasers and Optics, 2001. **73**: p. 65-70.
4. Wagner, S., et al., *In situ TDLAS measurement of absolute acetylene concentration profiles in a non-premixed laminar counter-flow flame*. Applied Physics B, 2012. **107**(3): p. 585-589.
5. Hu, Y., *Radical concentration and temperature measurements in sooting flames by cavity ringdown spectroscopy and laser-induced fluorescence*, in *Chemical and Process Engineering*. 2015, University of Strathclyde: Glasgow, United Kingdom.
6. Appel, J., H. Bockhorn, and M. Frenklach, *Kinetic Modeling of Soot Formation with Detailed Chemistry and Physics: Laminar Premixed Flames of C₂ Hydrocarbons*. Combustion and Flame, 2000. **121**(122).
7. Wang, H. and M. Frenklach, *A Detailed Kinetic Modeling Study of Aromatics Formation in Laminar Premixed Acetylene and Ethylene Flames*. Combustion and Flame, 1997. **110**: p. 173-221.

8. Mokhov, A.V., et al., *Experimental and computational study of C₂H₂ and CO in a laminar axisymmetric methane–air diffusion flame*. Proceedings of the Combustion Institute, 2007. **31**(1): p. 997-1004.
9. Kaiser, E., et al., *Experimental and modeling study of premixed atmospheric-pressure dimethyl ether– air flames*. The Journal of Physical Chemistry A, 2000. **104**(35): p. 8194-8206.
10. Gersen, S., A.V. Mokhov, and H.B. Levinsky, *Extractive probe/TDLAS measurements of acetylene in atmospheric-pressure fuel-rich premixed methane/air flames*. Combustion and Flame, 2005. **143**(3): p. 333-336.
11. Aubagnac-Karkar, D., A. El Bakali, and P. Desgroux, *Soot particles inception and PAH condensation modelling applied in a soot model utilizing a sectional method*. Combustion and Flame, 2018. **189**: p. 190-206.
12. Marchal, C., et al., *Modelling of aromatics and soot formation from large fuel molecules*. Proceedings of the Combustion Institute, 2009. **32**(1): p. 753-759.
13. Blanquart, G., P. Pepiot-Desjardins, and H. Pitsch, *Chemical mechanism for high temperature combustion of engine relevant fuels with emphasis on soot precursors*. Combustion and Flame, 2009. **156**(3): p. 588-607.
14. Roy, S.P. and D.C. Haworth, *A Systematic Comparison of Detailed Soot Models and Gas-Phase Chemical Mechanisms in Laminar Premixed Flames*. Combustion Science and Technology, 2016. **188**(7): p. 1021-1053.
15. Menon, A.V., et al., *Addition of NO₂ to a laminar premixed ethylene–air flame: effect on soot formation*. Proceedings of the Combustion Institute, 2007. **31**(1): p. 593-601.
16. Kazakov, A., H. Wang, and M. Frenklach, *Detailed modeling of soot formation in laminar premixed ethylene flames at a pressure of 10 bar*. Combustion and Flame, 1995. **100**(1-2): p. 111-120.
17. Slavinskaya, N.A. and P. Frank, *A modelling study of aromatic soot precursors formation in laminar methane and ethene flames*. Combustion and Flame, 2009. **156**(9): p. 1705-1722.
18. Dworkin, S.B., et al., *Application of an enhanced PAH growth model to soot formation in a laminar coflow ethylene/air diffusion flame*. Combustion and Flame, 2011. **158**(9): p. 1682-1695.
19. Slavinskaya, N.A., et al., *Detailed numerical modeling of PAH formation and growth in non-premixed ethylene and ethane flames*. Combustion and Flame, 2012. **159**(3): p. 979-995.
20. Nau, P., et al., *Quantum cascade laser-based MIR spectrometer for the determination of CO and CO₂ concentrations and temperature in flames*. Applied Physics B, 2015. **118**(3): p. 361-368.
21. Pritchard, R., H. Edmondson, and M.P. Heap, *Diameter effects in cooled-flat-flame burners*. Combustion and Flame, 1972. **18**(1): p. 13-18.

22. Jenkins, J.W., *The flat flame burner and its characteristics as applied to theoretical studies*. 1955, James Forrestal Research Centre, Princeton University.
23. Edmondson, H., M.P. Heap, and R. Pritchard, *Ambient atmosphere effects in flat-flame measurements of burning velocity*. *Combustion and Flame*, 1970. **14**(2): p. 195-201.
24. Kihara D. H., F., J. S., Kinoshita, C. M., *Temperature and Velocity Non-Uniformity in Edge Cooled Flat Flame Burners*. *COMBUST SCI TECHNOL*, 1975. **11**(5-6): p. 239-246.
25. Simons, S.N. and Z.-G. Yuan, *The filtered Abel transform and its application in combustion diagnostics*. 2003.
26. Villarreal, R. and P.L. Varghese, *Frequency-resolved absorption tomography with tunable diode lasers*. *Applied optics*, 2005. **44**(31): p. 6786-6795.
27. Melton, T.R., F. Inal, and S.M. Senkan, *The effects of equivalence ratio on the formation of polycyclic aromatic hydrocarbons and soot in premixed ethane flames*. *Combustion and Flame*, 2000. **121**(4): p. 671-678.
28. Goldman, A. and S. Cheskis, *Intracavity laser absorption spectroscopy of sooting acetylene/air flames*. *Applied Physics B*, 2008. **92**(2): p. 281.
29. Peeters, R., et al., *Cavity enhanced absorption spectroscopy in the 10 μm region using a waveguide CO₂ laser*. *Chemical Physics Letters*, 2001. **337**(4): p. 231-236.
30. Mürztz, M., B. Frech, and W. Urban, *High-resolution cavity leak-out absorption spectroscopy in the 10- μm region*. *Applied Physics B*, 1999. **68**(2): p. 243-249.
31. Chan, M.-C. and S.-H. Yeung, *High-resolution cavity enhanced absorption spectroscopy using phase-sensitive detection*. *Chemical Physics Letters*, 2003. **373**(1): p. 100-108.

Chapter 6 : Cavity-Enhanced Absorption Spectroscopy of OH Radical in Flames.

6.1 Introduction

Owing to the importance of acetylene's role in the formation of soot as presented in Chapter 1, the measurement of acetylene has been the main focus of this project up to this point. The measurements of acetylene using both cw-CRDS and CEAS techniques were presented in Chapter 4 and Chapter 5. The CEAS results presented in Chapter 5 highlight the practicality of the CEAS set-up in obtaining sensitive concentration measurements in a flame. The CEAS set-up has the advantage of shorter measurement time, with favourable spatial resolution and over a useful wavelength range. Having successfully obtained concentration measurements of acetylene, it is useful to explore the possibility of extending this technique to other important species in flames. Species such as HCO, OH, CH, $^1\text{CH}_2$, and HCN (amongst others) could be considered as there is existing literature on flame measurements of these species using cavity-based techniques [1-7], albeit that some of these were at much shorter wavelengths in the visible or UV ranges and mostly involved pulsed lasers. Some of these measurements for HCN and OH species [1, 2, 7] have been performed in the near-infrared (NIR) spectrum, which is the region of interest in this project. The HCN measurements have only been performed by extractive sampling. Peeters et al. performed OH radical measurements *in situ* using CEAS technique at about 1515 nm. This OH line is overlapping a water line, and as mentioned in Chapter 2, the authors assume temperature from simulations and oven measurements. They also assume an effective reflectivity value from the measurement of ambient water vapour. Hence, they show semi-quantitative OH radical measurements. The choice of species to which the CEAS technique would be extended to will be determined by the availability of a laser (as well as cavity mirrors) of the right wavelength and the concentration of the species in the flame.

An advantage of the CEAS technique is that an absorption spectrum can be obtained quickly. With this advantage, broad absorption spectra were obtained using the 1535 nm laser and the 1547 nm laser to identify any spectral features whose intensity depends strongly on flame composition and could thus be utilised for concentration measurement. The broad scans which were repeated and are reproducible reveal numerous acetylene lines, some of which look promising. OH spectra were also obtained using an available 1573 nm laser. Water lines overlap the OH lines within the spectral region of the laser; as previously discussed, the avoidance of strong water vapour absorption lines is of central importance.

This chapter begins with a discussion of the broad spectral scans and goes on to show some OH absorption lines identified using HITEMP. Measured spectra of some of the identified OH lines using the CEAS technique in the porous-plug burner are shown, and the challenge in analysing the spectra due to overlapping water lines are discussed next. The chapter ends with a discussion of the future potential of relative OH concentration measurements in lean and stoichiometric flames, despite interference from overlapping water lines.

6.2 Broad Spectral Scans

Owing to the availability of lasers with centre wavelengths at 1535 nm and 1547 nm, it was of interest to practically look out for any other species with an absorption line within the tuneable range of these lasers. Figure 6.1 to Figure 6.10 show the broad scans obtained at 4 mm height above the porous-plug burner using both lasers. The spectra are an average of two repetitions. The broad scans were performed for a range of equivalence ratio flames ranging from the stoichiometric flame to the rich flames. The tuning range for the 1535 nm and 1547 nm lasers are 1533.3 nm - 1538.2 nm and 1546.3 nm - 1549.8 nm respectively. The entire wavelength range of the lasers could not be assessed in one broad scan as this would require supplying too much current (above the maximum current of 150 mA and typical threshold

current of 10 mA) through the laser diode controller which could damage the lasers. The entire spectral range for each laser was assessed in five separate scans. The separate scans were obtained by coarse wavelength tuning via the diode laser temperature, and the limit on the tuning ranges stems from the allowable temperature range. The scans were done in a way that some parts of successive spectra could overlap on the previous spectrum. This made it easy to assign wavelength scales to the spectra. With the help of simulations from HITRAN and HITEMP databases, several acetylene and high-temperature water lines were identified. This, together with resonator traces, were used to assign absolute wavelength scales to the spectra.

The concentration of many species in flames varies significantly from rich to lean conditions. In the event of absorption by any other species other than water vapour, it is expected that there would be significant variation in the peak absorption among the spectra for the different flame conditions. In this region of the electromagnetic spectrum, high-temperature water vapour is known to possess many absorption lines, and as such, it overlaps many absorption lines of other species. The water peak absorption features are also expected to vary (based on our observation of acetylene spectra in Chapter 5 where some parts of the spectrum were different for the $\phi = 1.0$ spectrum, whereas the rich flames overlapped) due to the difference in temperature. This can be seen in Figure 6.1 to Figure 6.10, where the peak for most water features agrees for the rich flames and reduces for the stoichiometric flame. This could possibly be explained by a greater difference in temperature between the rich flames and the stoichiometric flame than between the rich flames. This difference in temperature arises from the fact that the rich flames contain some unburned fuel which absorbs some of the heat released during combustion, resulting in lower temperatures for the rich flames. The presence of the excess fuel gives rise to incomplete combustion, resulting in the formation of soot. Soot particles emit radiation as they absorb some of the heat from the flame. This contrasts with the stoichiometric flame which burns at a higher temperature [8].

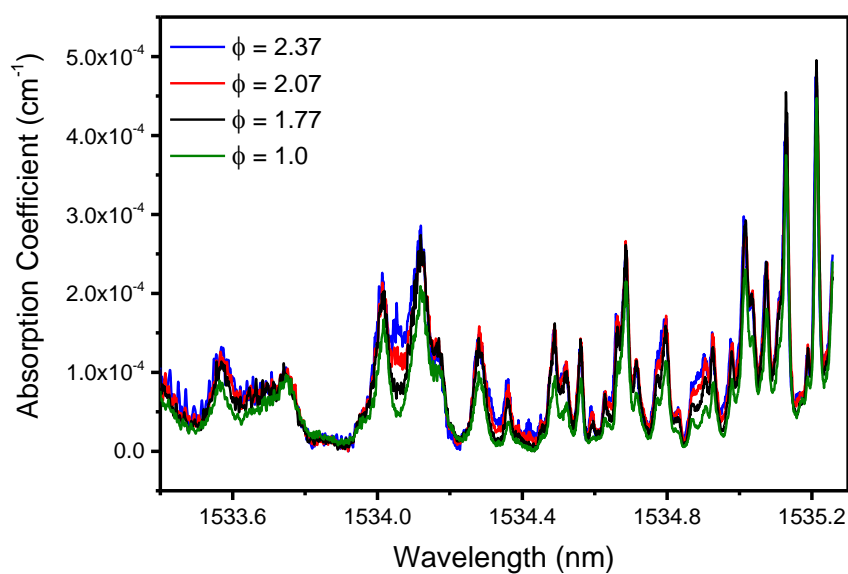


Figure 6.1: Broad CEAS spectra for a range of different equivalence ratio flames recorded at 4 mm above the burner surface.

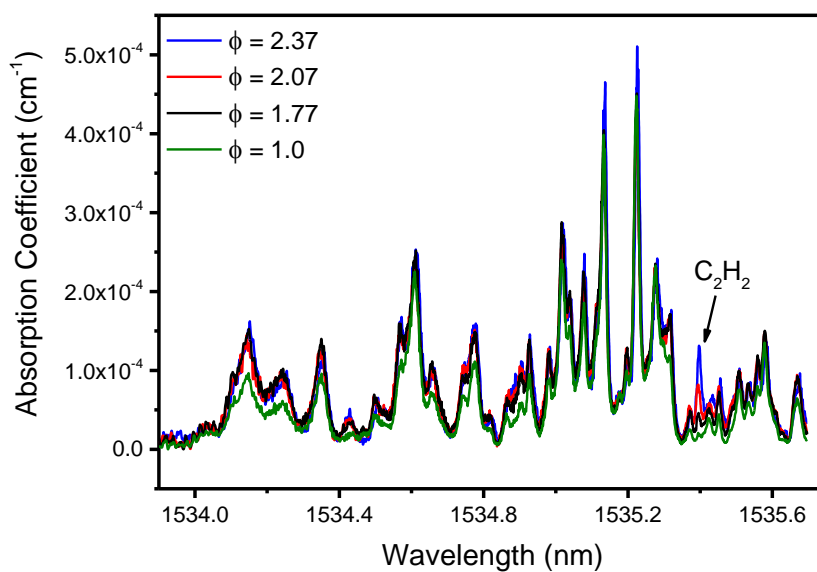


Figure 6.2: Broad CEAS spectra for a range of different equivalence ratio flames recorded at 4 mm above the burner surface.

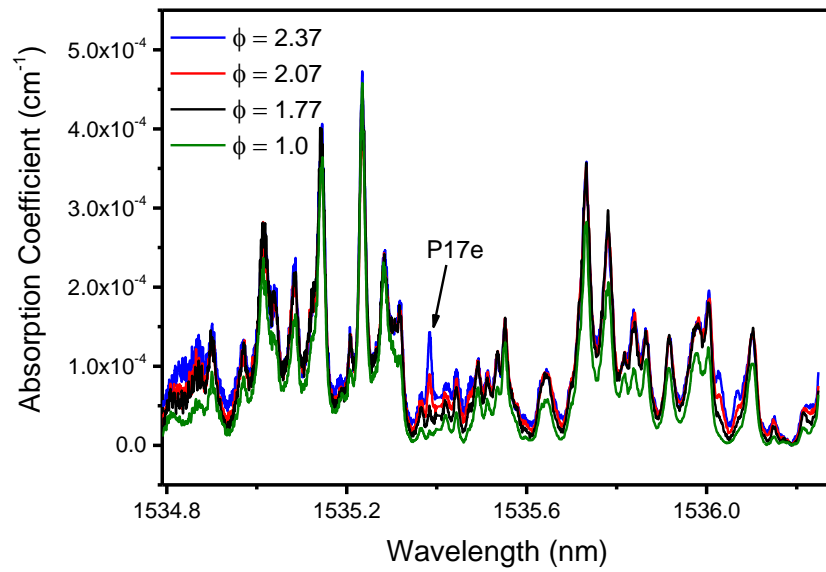


Figure 6.3: Broad CEAS spectra for a range of different equivalence ratio flames recorded at 4 mm above the burner surface.

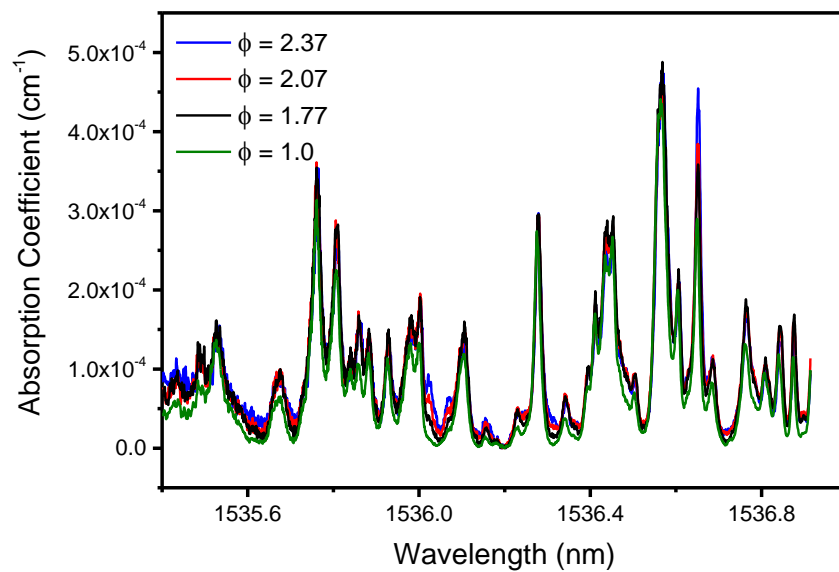


Figure 6.4: Broad CEAS spectra for a range of different equivalence ratio flames recorded at 4 mm above the burner surface.

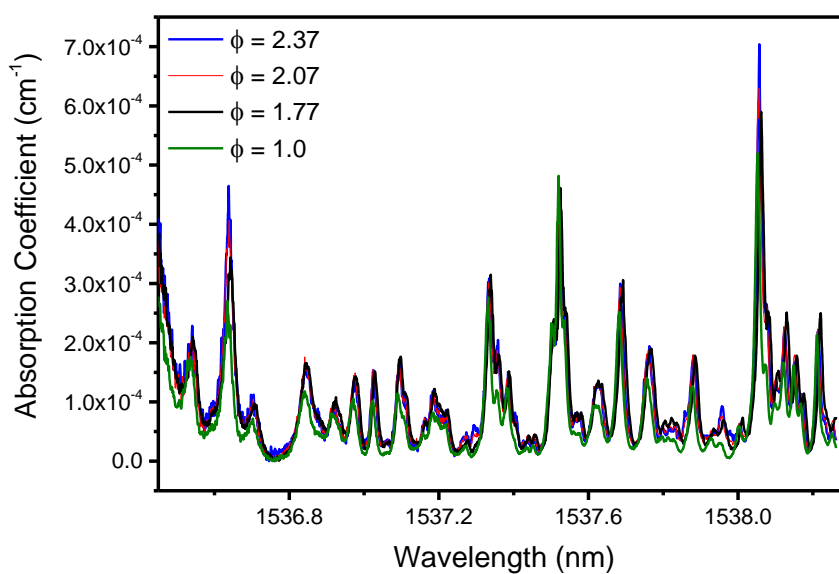


Figure 6.5: Broad CEAS spectra for a range of different equivalence ratio flames recorded at 4 mm above the burner surface.

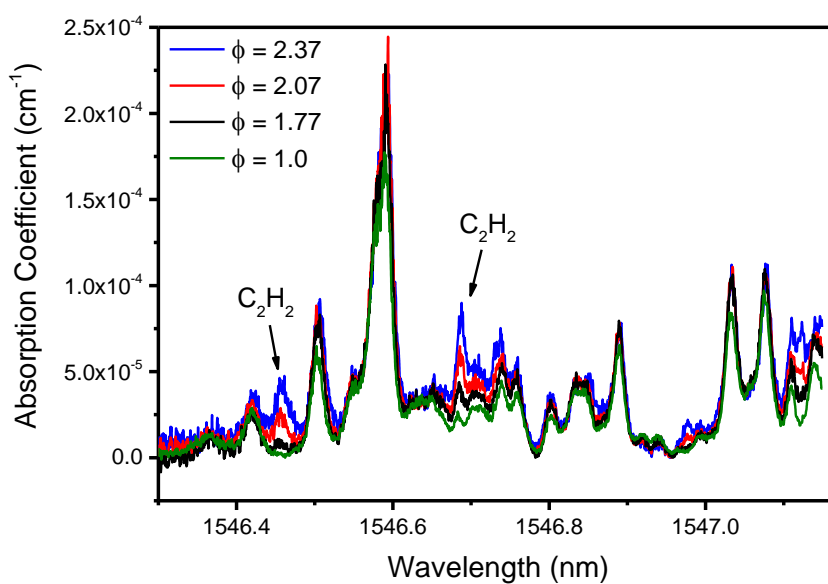


Figure 6.6: Broad CEAS spectra for a range of different equivalence ratio flames recorded at 4 mm above the burner surface.

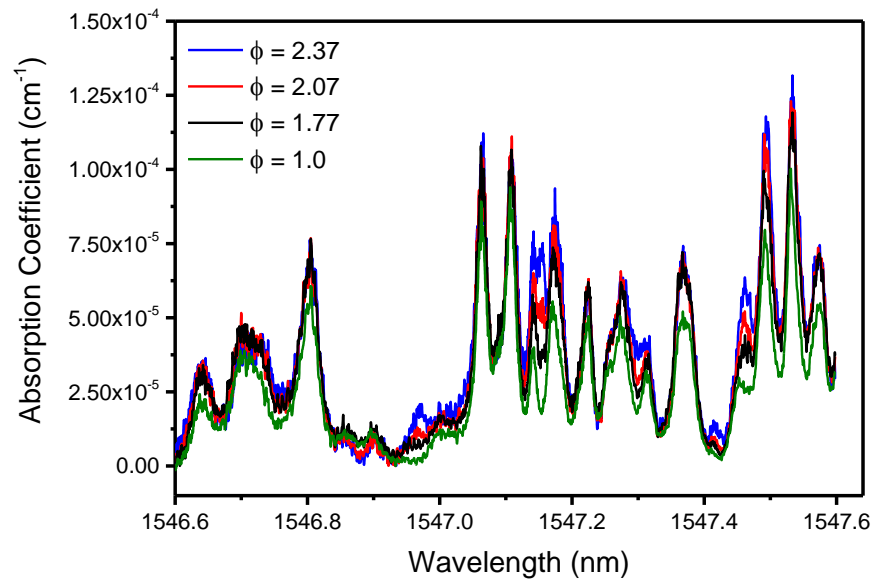


Figure 6.7: Broad CEAS spectra for a range of different equivalence ratio flames recorded at 4 mm above the burner surface.

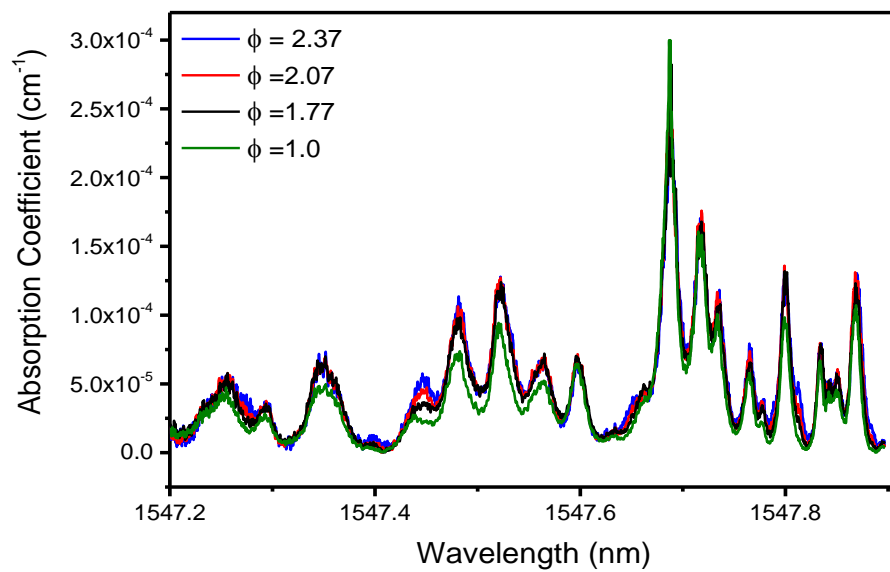


Figure 6.8: Broad CEAS spectra for a range of different equivalence ratio flames recorded at 4 mm above the burner surface.

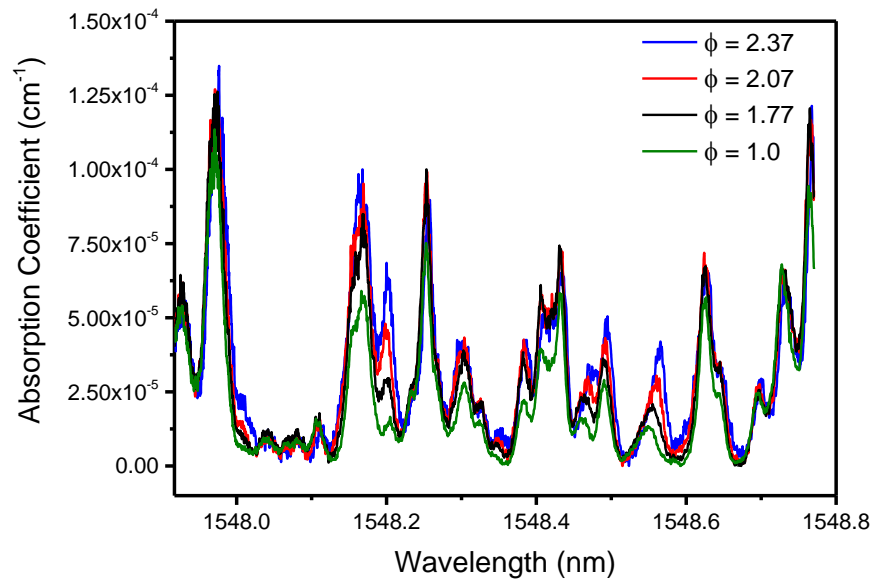


Figure 6.9: Broad CEAS spectra for a range of different equivalence ratio flames recorded at 4 mm above the burner surface.

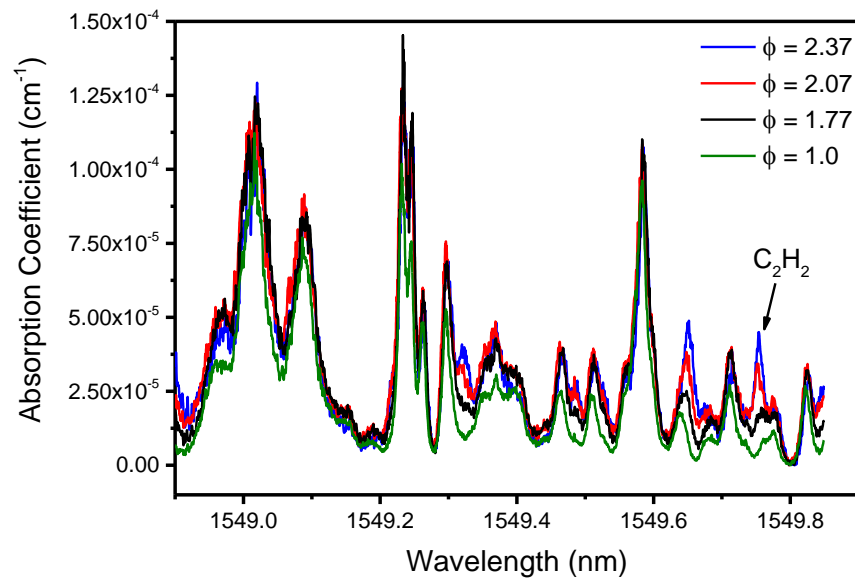


Figure 6.10: Broad CEAS spectra for a range of different equivalence ratio flames recorded at 4 mm above the burner surface.

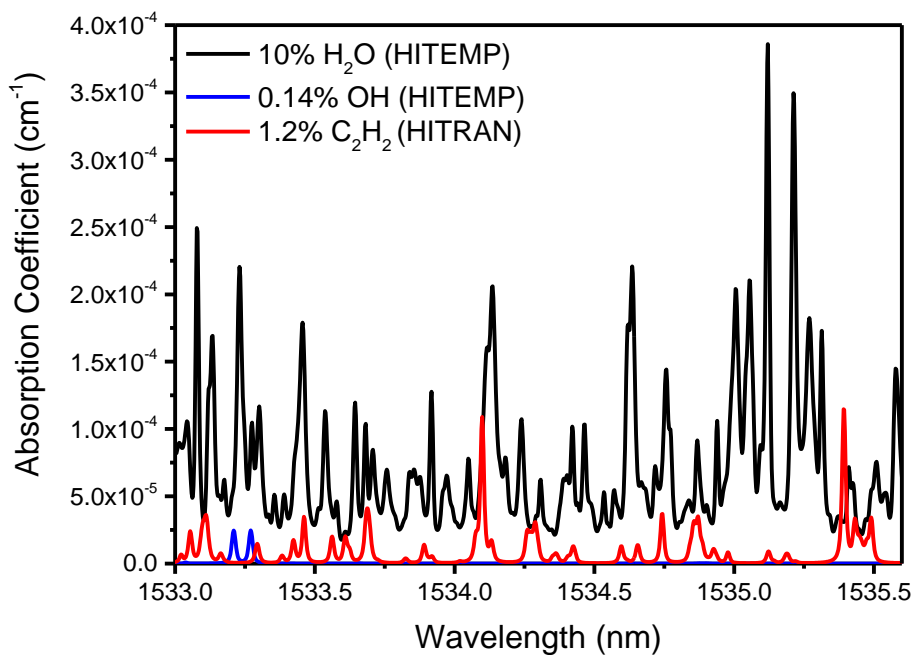


Figure 6.11: HITRAN and HITEMP simulations of water vapour, OH and acetylene at 1600 K.

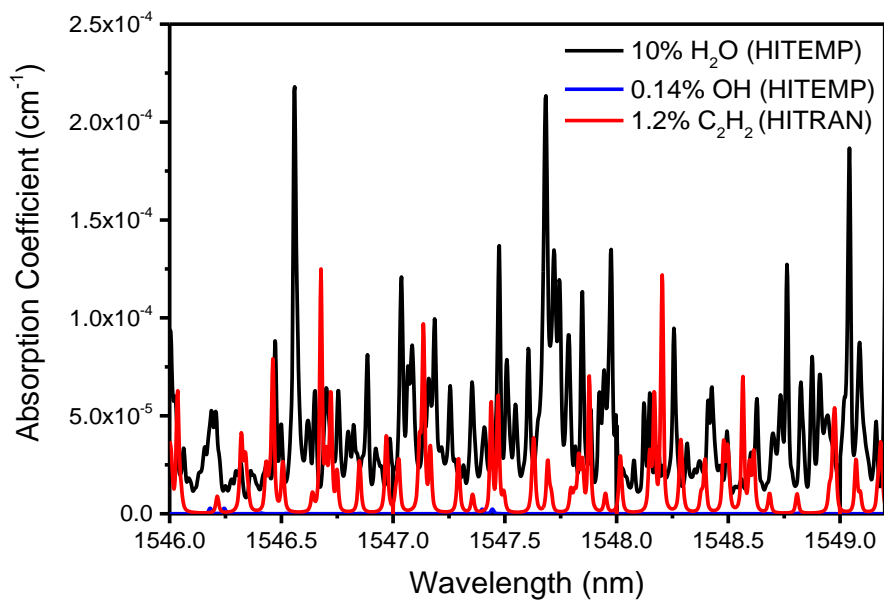


Figure 6.12: HITRAN and HITEMP simulations of water vapour, OH and acetylene at 1600 K.

The P17e acetylene feature at 1535.39 nm interrogated in Chapter 4 and Chapter 5 can be seen in Figure 6.3, and the peak of this feature is similar to that in the measurements in Chapter 5. The portion of the spectrum in Figure 6.3 that corresponds to that in the measurements in Chapter 5 agrees very well with the measured spectrum in Chapter 5. In some areas of the spectra, some differences in absorption can be seen for the various equivalence ratios. This is due to absorption from many non-isolated acetylene lines. From the simulation shown in Figure 6.11 and Figure 6.12, acetylene can be seen to possess many absorption lines in this region. The observation is the case for the entire wavelength tuning range for the 1535 nm and 1547 nm lasers, albeit most of these absorption lines overlap with water lines. From the measurements, some acetylene lines, including the lines at 1546.46 nm, 1546.68 nm and 1549.76 nm look promising for measurements as they can be seen to be sufficiently isolated from neighbouring water lines. However, the 1535.39 nm acetylene line probed in Chapter 4 and Chapter 5 is preferable as it is seen to possess stronger absorption peak. Generally, the spectra from the simulations agree with the measured spectra, although not perfectly as the water spectrum show some disagreement in a few areas.

In Figure 6.11, two weak OH absorption lines can be seen at 1533.21 nm and 1533.27 nm. This is just outside the lower limit of the tuning range of the 1535 nm laser. Even in the event of the availability of a suitable laser, it would, however, be impossible to obtain OH absorption spectra at 1533.21 nm and 1533.27 nm as both OH lines are completely overshadowed by water absorption. The mole fractions of OH used in the simulation were obtained from Cantera simulations with ABF mechanism.

Owing to the availability of a 1573 nm laser, HITRAN and HITEMP simulations were performed around this wavelength region and a few OH lines were identified. The input values for the concentration of OH in the simulations were also obtained from Cantera simulations with ABF mechanism. This was done to give a preliminary idea of what to expect in terms of identifying suitable and isolated OH lines. The identified

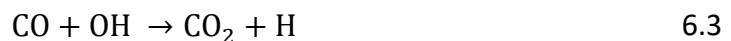
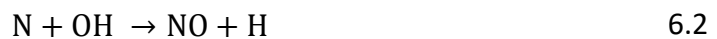
OH absorption lines present an opportunity for exploring the CEAS technique to detect OH. This is also as OH is present in substantial concentration in flames. The importance of OH in flames and the identified absorption lines are discussed in the following section.

6.3 OH Species in Combustion

Several species in flames play important roles in pollutant formation. OH radical is one of those species and it is also generally an important species in combustion. This is owing to its abundance in flames, especially hydrocarbon flames, and much of it usually exists in the flame reaction zone [9]. OH radical is used as a flame marker to identify the flame front and hot zones in flames (specifically the steep gradient of OH mole fraction) [10]; hence, the ratio of OH hot bands is used in flame temperature measurements [11-13]. An important reaction that is commonly used for studies of heat release rates in combustion processes is that of OH and CH₂O shown below, where the reaction rate is proportional to the heat release rate [14-17]



It is also involved in several important reaction pathways including in the formation of pollutants. The oxides of nitrogen and carbon are mentioned in Chapter 1 as some of the pollutants released from combustion process. OH species is very much involved in NO formation as well as the oxidation of CO during combustion as shown in the elementary reactions below [18-20].



Since much of the work in this project is directed towards soot, it is important to also discuss OH with respect to soot. The oxidation of soot is one of the processes that has been studied and shown to involve OH [20-26]. Although O₂ molecules are also involved in soot oxidation, studies have shown OH to be primarily responsible for

soot oxidation, even more so in rich flames where the concentration of O_2 is low [22-24]. The soot oxidation process competes with CO oxidation for OH species [20]. All these highlight the importance of OH species in combustion. While this provides useful context, it should be noted that OH concentration is particularly low in sooting flames so our efforts will at this stage be focussed on lean and stoichiometric flames in which OH is far more abundant.

Flame measurements of OH have previously been done using a variety of techniques including LIF/PLIF [27-30], CRDS [31, 32], intra-cavity laser absorption spectroscopy [33], continuous-filtering vernier spectroscopy [34] and optical frequency comb spectroscopy [7]. Some of these techniques involve the use of relatively bulky laser systems (such as dye lasers or optical parametric oscillators) which are also relatively expensive. As mentioned previously in Chapter 2, these lasers require frequency conversion to the required wavelength, which typically results in pulses with large line-widths. The continuous-filtering vernier spectroscopy and optical frequency comb spectroscopy techniques are relatively complex, and the OH measurements using both techniques utilised an Er:fibre femtosecond laser, which is relatively expensive in comparison to diode lasers. The nature of the CEAS technique which was performed by Peeters et al. allows for OH spectra to be obtained in a relatively simple and quick approach with the use of a diode laser, although their measurements were limited by lack of proper calibration. Using a similar approach, we obtain properly calibrated spectra of OH, which is presented in the next section.

6.4 OH Spectra

Having established the importance of OH in flames and combustion processes in general, it was necessary to identify a suitable OH absorption line within the tuning

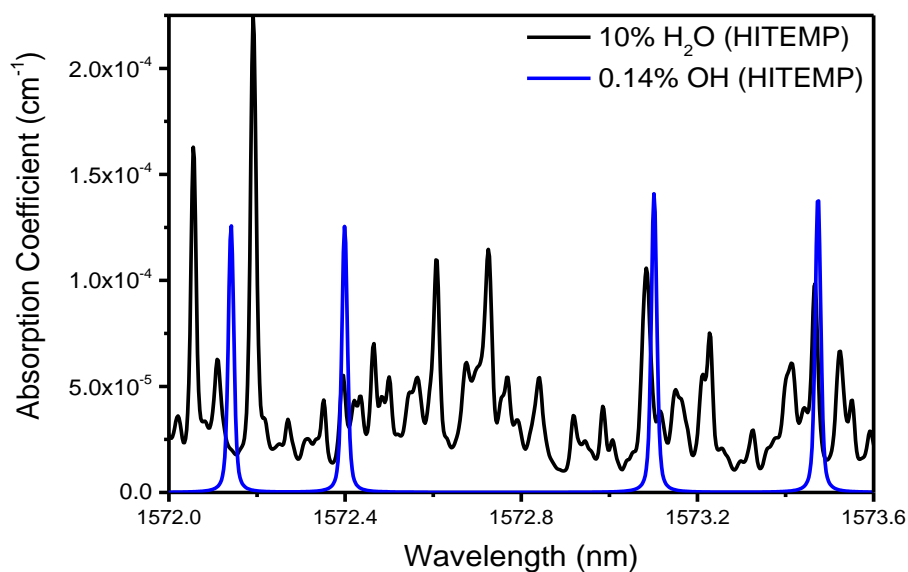


Figure 6.13: HITEMP simulations of OH and water vapour spectra at 1600 K.

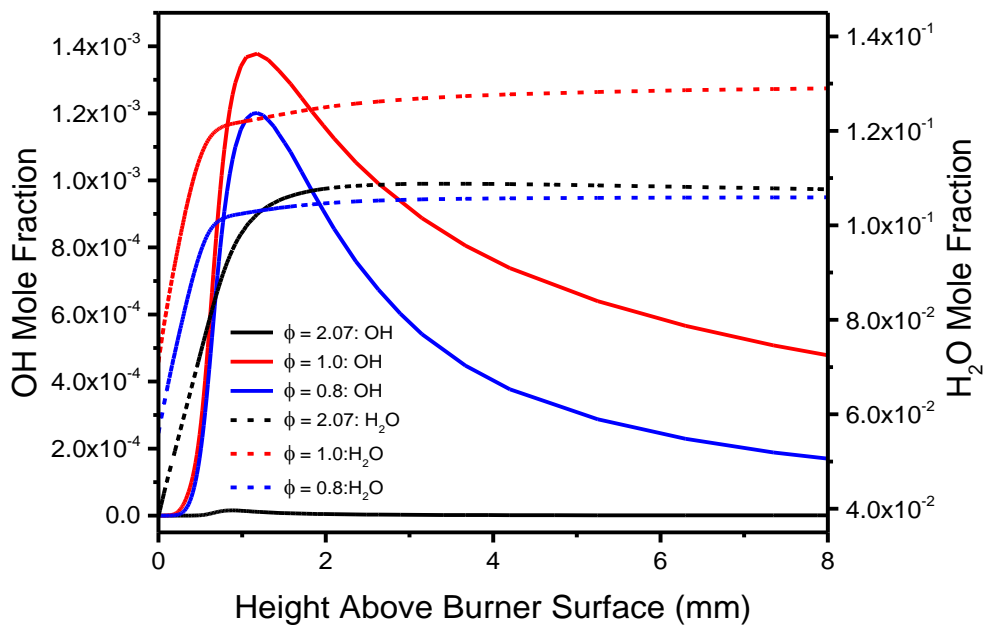


Figure 6.14: Cantera simulations of OH and water mole fractions at expected flame conditions using ABF mechanism.

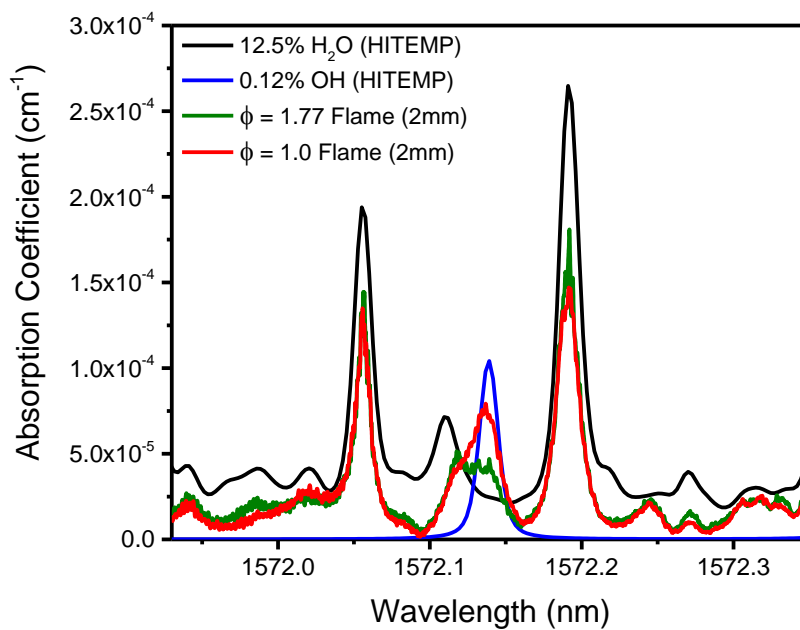


Figure 6.15: Measured OH spectrum plotted with HITEMP simulations of OH and water vapour spectra.

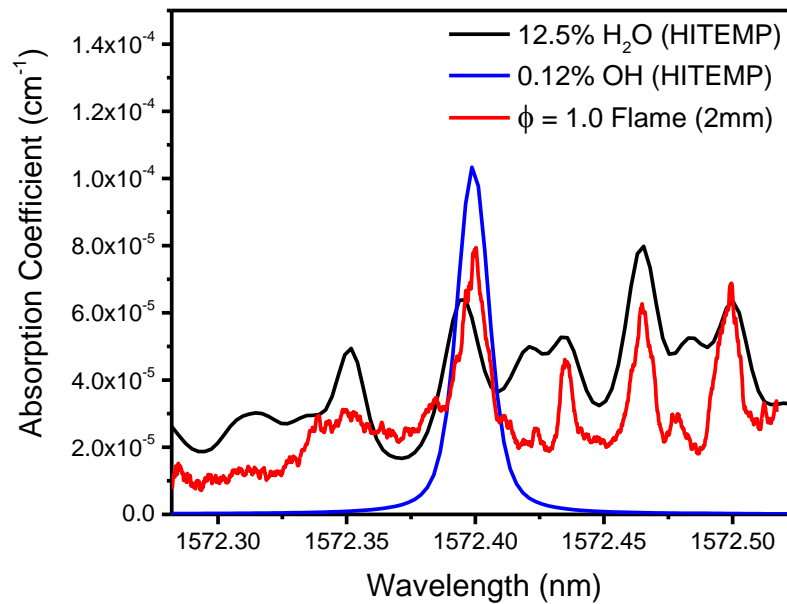


Figure 6.16: Measured OH spectrum plotted with HITEMP simulations of OH and water vapour spectra.

range of the available 1573 nm laser. The several OH absorption lines identified from simulations using HITRAN and HITEMP databases include 1573.47 nm, 1573.10 nm, 1572.40 nm, and 1572.14 nm as can be seen in Figure 6.13. This clearly seems to show that we have a better chance of detecting OH than would have been the case at about 1533.2 nm. One-dimensional flame model calculations of OH and water have been performed using ABF mechanism with Cantera at the expected flame conditions and shown in Figure 6.14. The stoichiometric flame is seen to possess the highest mole fraction [although the concentration (mol/m^3) is probably also higher; it depends on the temperatures of the respective flames] of OH and water.

Measured CEAS spectra for this spectral range are shown in Figure 6.15 and Figure 6.16, together with the simulated OH and water spectra. Approximate wavelength scales were assigned (based on a resonator trace from a different diode laser) to the measured OH spectra as the resonator trace for the laser could not be obtained. A major concern in flame measurements in this spectral region is the strong interference from neighbouring high-temperature water lines. The 1572.14 nm OH absorption line is the only line that appears from the model to be sufficiently isolated from high-temperature water vapour absorption. This looks promising. However, the spectrum obtained at this wavelength which can be seen in Figure 6.15 is not quite so encouraging. The OH feature has a shoulder on its left side due to water absorption. Hence, the OH feature is not as isolated from the neighbouring water vapour absorption as predicted by HITRAN and HITEMP. Whilst the overlap doesn't completely rule out the possibility of at least relative concentration measurements being made [7]; this leads to the exploration of the OH line at 1572.40 nm as a comparison.

The measured spectrum of OH at 1572.40 nm is presented in Figure 6.16 alongside HITEMP simulated spectra and in Figure 6.17. The OH line is accompanied by an underlying water feature, as clearly shown in Figure 6.16. The 1572.40 nm, and 1572.14 nm OH lines have previously been measured by Rutkowski et al. and Chuang et al. [7, 34]. The measurements corroborate the point that both OH lines spectrally

overlap high-temperature water vapour lines. This presents a challenge in processing the spectrum as it is impossible to accurately quantify the water contribution at the OH line centre with the limited information available from the measurements. Hence, the background at the centre of the OH line remains unknown.

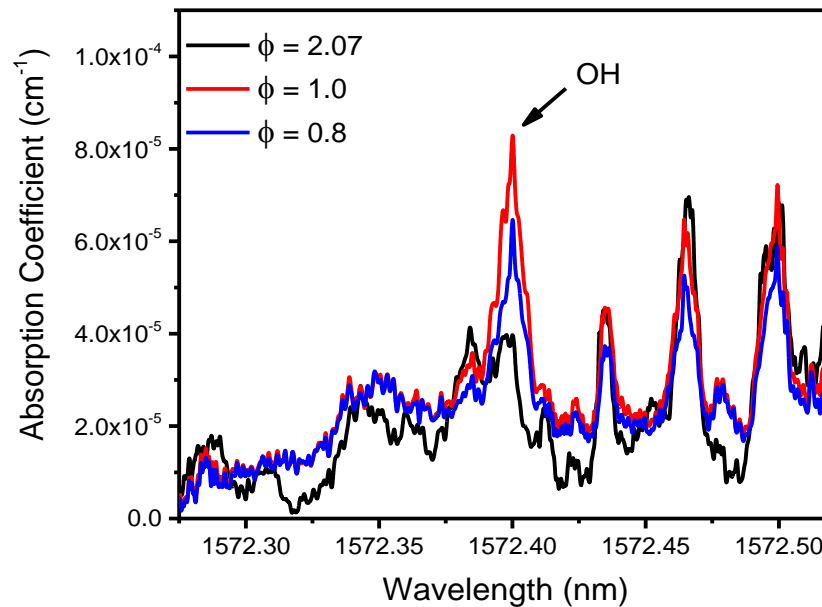


Figure 6.17: CEAS spectra of OH recorded for a range of equivalence ratio flames at 2 mm above the burner surface.

The spectrum of the $\phi = 2.07$ flame should contain an insignificant amount of OH as seen in Figure 6.14, which should lead to the assumption that the peak at the OH line of the $\phi = 2.07$ spectrum is solely due to water absorption. Following from this, a simple subtraction of the $\phi = 2.07$ spectrum from the stoichiometric spectrum should yield a stoichiometric spectrum that is due to OH alone. However, the difference would not be an accurate representative of the water contribution to the stoichiometric spectrum because of the difference in water absorption for both spectra as seen in Figure 6.17, where the $\phi = 2.07$ spectrum does not overlap very well with the other spectra. As previously, we can only suggest that the difference in the water spectrum may be due to the difference in flame temperature. The temperature of the rich flame is lower for reasons stated earlier. The difference in

water mole fraction can also be seen in Figure 6.14. Hence, no further processing of the spectra can be done in the absence of some additional information. This situation is in contrast to the case for acetylene in Chapter 5, where the iterative extraction technique was applied to obtain a spectrum that is due to acetylene alone. This is because the acetylene line is sufficiently isolated and the background at the line centre is known, which is common for all the measured acetylene spectra.

Some extra information about the underlying water feature is required to further process the OH spectra and obtain accurate concentration of OH. One way to obtain this information is to measure the spectrum of hot water at the different flame temperatures [13]. This water spectrum can then be subtracted from the corresponding spectra recorded for the various flames (as long as the flame temperature is known). In a study of OH measurements near $1.55\ \mu\text{m}$, Aizawa [13] was able to estimate the magnitude of hot water interference by comparing the measured OH spectra to spectra of heated pure water vapour. Aizawa also accounted for the interfering water lines in a fit to the OH spectra to determine OH concentration. However, this approach was plagued by the lack of reliable information on these hot water lines from spectroscopic databases (such as HITEMP and HITRAN as discussed in Section 2.3.3).

Given that water is an end product of combustion, then above the production zone in the flame, the concentration of water should remain relatively constant as seen in Figure 6.14 (as indeed the flame temperature). This can also be seen in Figure 5.7 for $\phi = 1.0$ spectrum, where the spectra recorded above 2 mm do not vary significantly with increasing height above the burner surface. Here we suggest a possible way forward based on a study by Rutkowski et al., which suggests that above 2.5 mm, the concentration of water remains essentially constant [7]. As a result, a spectrum obtained at a reference position much higher in the flame ($\sim 16\ \text{mm}$), for which models predict almost negligible OH concentration can be assumed to represent the contribution of water alone and to be valid at all vertical locations upstream of the reaction zone. The peak at the wavelength corresponding to the OH line of the

spectrum can then be assumed to be solely due to water absorption. This spectrum could be taken as a reference which can be subtracted from other spectra obtained at heights below the reference height. This will yield a proper estimate of the peak OH contribution for the spectra recorded below the reference height. Since the data recorded during this project were of a preliminary nature and concentrated on locations near to the reaction zone (Figure 6.18) where OH is expected to be abundant, we are not in a position to implement this approach, but it holds promise as a way to gain quantitative OH measurements in flat flames. In the study by Rutkowski et al., the authors match model simulations at a reference height and as such, are able to obtain relative OH concentration measurements. Whereas the approach described above would allow absolute concentrations if properly implemented. Also, the CEAS technique presents a simpler measurement approach than the frequency comb approach employed by the authors.

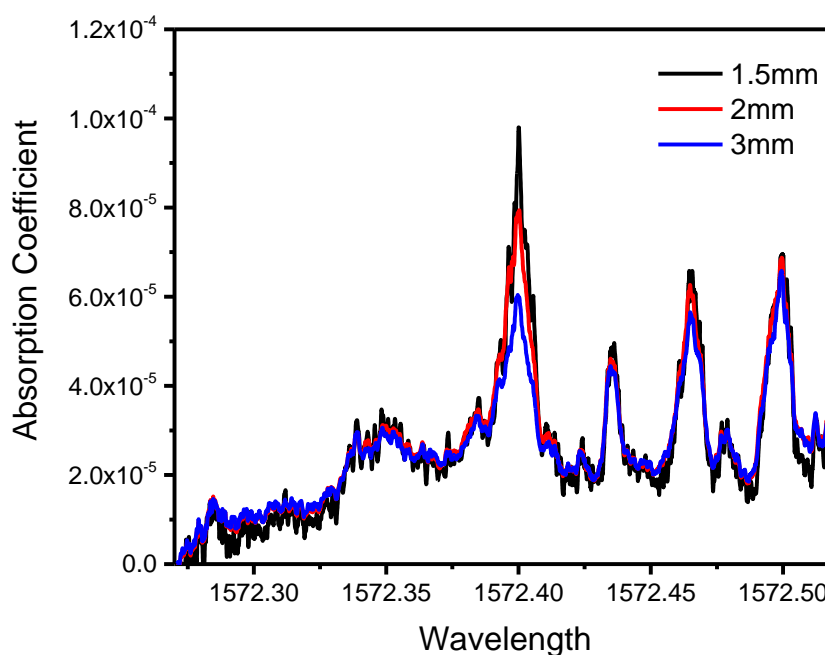


Figure 6.18: CEAS spectra of OH recorded in the stoichiometric flame at different heights above the burner surface.

6.5 Uncertainty Analysis

As mentioned previously, the CEAS spectra of OH radical could not be processed to yield OH concentration because of the lack of key data to aid in quantifying the overlapping water features. Therefore, no quantitative analysis of the resulting OH spectra was done. As such, the sources of uncertainties in obtaining the spectra which include uncertainties from the mass flow controllers (stated previously) and edge effects have not been considered in any analysis of the spectra. To properly quantify the edge effects (and its uncertainty), a radial study of OH radical needs to be performed as the radial distribution of OH radical and the sensitivity of OH radical to the edge effects may differ from that of acetylene. These uncertainties should be considered in analysing the measured OH spectra to obtain OH concentration. In addition to the above uncertainty sources, other potential sources of uncertainty that should be considered in the analysis include the overlapping water features, temperature and HITRAN parameters such as line strength and collisional broadening parameter.

6.6 Summary

As part of the objectives of this project described in Chapter 1, it is useful to explore the possibility of the CEAS technique to detect other important flame species. This comes after successfully applying the CEAS technique to obtain sensitive measurements of acetylene in the previous chapter. The advantage that CEAS spectra can be obtained quickly was utilised in obtaining broad spectra using available 1535 nm and 1547 nm lasers. This was done anticipating absorption by flame species other than high-temperature water vapour and acetylene which has been measured. Acetylene is seen to possess many absorption lines in this NIR region. Although many of the lines are overlapping water lines, a few of the lines show potential as alternatives for quantitative measurement. No other species were found to absorb within the wavelength range of the broad scans.

OH lines were identified within the tuneable range of an available 1573 nm laser. OH is an important flame species, and its importance in flames has been presented. The OH line measured at 1572.14 nm largely overlaps a neighbouring water line even though HITEMP predicts that this OH line is sufficiently isolated. This highlights the shortcomings of the HITEMP database in predicting high-temperature water absorption. The OH spectra were recorded at 1572.40 nm for a range of flame conditions and here too an overlapping water line prevented direct measurement of OH mole fraction. Due to the challenge in accurately quantifying the underlying water feature, we are not able to calculate OH concentration from the measured OH spectra. Strategies to obtain quantitative OH concentration profiles based on a complete data-set for one of these absorption features have been discussed.

6.7 References

1. Miller, J.H., et al., *Measurements of Hydrogen Cyanide and its Chemical Production Rate in a Laminar Methane/Air, Non-Premixed Flame Using cw Cavity Ringdown Spectroscopy*. Proceedings of the Combustion Institute, 2002. **29**: p. 2203-2209.
2. Peeters, R., G. Berden, and G. Meijer, *Near-Infrared Cavity Enhanced Absorption Spectroscopy of Hot Water and OH in an Oven and in Flames*. Applied Physics B-Lasers and Optics, 2001. **73**: p. 65-70.
3. Lozovsky, V.A., et al., *Absolute HCO concentration measurements in methane/air flame using intracavity laser spectroscopy*. The Journal of Chemical Physics, 1997. **106**(20): p. 8384-8391.
4. Evertsen, R., et al., *Measurements of absolute concentrations of CH in a premixed atmospheric flat flame by cavity ring-down spectroscopy*. Combustion and Flame, 2003. **132**(1–2): p. 34-42.
5. Evertsen, R., et al., *Measurements of the absolute concentrations of HCO and $^1\text{CH}_2$ in a premixed atmospheric flat flame by cavity ring-down spectroscopy*. Combustion and Flame, 2003. **135**(1–2): p. 57-64.
6. Bernstein, J.S., et al., *Laser-based flame species profile measurements: A comparison with flame model predictions*. Combustion and Flame, 1993. **92**(1): p. 85-105.
7. Rutkowski, L., et al., *Detection of OH in an atmospheric flame at 1.5 μm using optical frequency comb spectroscopy*. Photonics letters of Poland, 2016. **8**(4): p. 110-112.

8. Akbar, M. and S. Ghiaasiaan, *Radiation heat transfer and soot thermophoresis in laminar tube flow*. Numerical Heat Transfer, Part A: Applications, 2005. **47**(7): p. 653-670.
9. Telle, H.H., A.G. Ureña, and R.J. Donovan, *Laser chemistry: spectroscopy, dynamics and applications*. 2007: John Wiley & Sons.
10. Pfadler, S., F. Beyrau, and A. Leipertz, *Flame front detection and characterization using conditioned particle image velocimetry (CPIV)*. Optics Express, 2007. **15**(23): p. 15444-15456.
11. Brown, D.M., et al., *Determination of Lean Burn Combustion Temperature Using Ultraviolet Emission*. IEEE Sensors Journal, 2008. **8**(3): p. 255-260.
12. Yip, B., P. Danehy, and R. Hanson, *Degenerate four-wave mixing temperature measurements in a flame*. Optics letters, 1992. **17**(10): p. 751-753.
13. Aizawa, T., *Diode-laser wavelength-modulation absorption spectroscopy for quantitative in situ measurements of temperature and OH radical concentration in combustion gases*. Applied optics, 2001. **40**(27): p. 4894-4903.
14. Fayoux, A., et al., *Experimental and numerical determination of heat release in counterflow premixed laminar flames*. Proceedings of the Combustion Institute, 2005. **30**(1): p. 251-257.
15. Gordon, R.L., A.R. Masri, and E. Mastorakos, *Heat release rate as represented by $[OH] \times [CH_2O]$ and its role in autoignition*. Combustion Theory and Modelling, 2009. **13**(4): p. 645-670.
16. Mulla, I.A., et al., *Heat release rate estimation in laminar premixed flames using laser-induced fluorescence of CH_2O and H-atom*. Combustion and Flame, 2016. **165**: p. 373-383.
17. Nikolaou, Z.M. and N. Swaminathan, *Heat release rate markers for premixed combustion*. Combustion and flame, 2014. **161**(12): p. 3073-3084.
18. Heard, D.E., et al., *LIF measurements in methane/air flames of radicals important in prompt-NO formation*. Combustion and Flame, 1992. **88**(2): p. 137-148.
19. Warnatz, J., U. Maas, and R.W. Dibble, *Combustion*. 4th ed. 2006, Berlin: Springer. 367.
20. Puri, R., R.J. Santoro, and K.C. Smyth, *The oxidation of soot and carbon monoxide in hydrocarbon diffusion flames*. Combustion and Flame, 1994. **97**(2): p. 125-144.
21. Lu, J., X. Ren, and L. Cao, *Studies on Characteristics and Formation of Soot Nanoparticles in an Ethylene/Air Inverse Diffusion Flame*. Journal of Energy Engineering, 2016. **142**(3): p. 04015041.
22. Cavaliere, A., et al., *Fuel and soot oxidation in diesel-like conditions*. Symposium (International) on Combustion, 1994. **25**(1): p. 167-174.

23. Neoh, K.G., J.B. Howard, and A.F. Sarofim, *Effect of oxidation on the physical structure of soot*. Symposium (International) on Combustion, 1985. **20**(1): p. 951-957.
24. Roth, P., O. Brandt, and S. Von Gersum. *High temperature oxidation of suspended soot particles verified by CO and CO₂ measurements*. in *Symposium (international) on Combustion*. 1991. Elsevier.
25. Stanmore, B.R., J.F. Brillhac, and P. Gilot, *The oxidation of soot: a review of experiments, mechanisms and models*. Carbon, 2001. **39**(15): p. 2247-2268.
26. Haudiquert, M., et al., *OH and soot concentration measurements in a high-temperature laminar diffusion flame*. Combustion and Flame, 1997. **111**(4): p. 338-349.
27. Lee, S.-Y., S.R. Turns, and R.J. Santoro, *Measurements of soot, OH, and PAH concentrations in turbulent ethylene/air jet flames*. Combustion and Flame, 2009. **156**(12): p. 2264-2275.
28. Chen, S., et al., *Quantitative measurement of hydroxyl radical (OH) concentration in premixed flat flame by combining laser-induced fluorescence and direct absorption spectroscopy*. Chinese Physics B, 2016. **25**(10).
29. Azzazy, M. and J.W. Daily, *Fluorescence measurements of OH in a turbulent flame*. AIAA Journal, 1983. **21**(8): p. 1100-1106.
30. Chen, S., et al., *Calibration method for 2D instantaneous OH-PLIF temperature measurements in flame*. Chinese Optics Letters, 2013. **11**(5): p. 053001.
31. Cheskis, S., et al., *Cavity ring-down spectroscopy of OH radicals in low pressure flame*. Applied Physics B, 1998. **66**(3): p. 377-381.
32. Scherer, J.J., D. Voelkel, and D.J. Rakestraw, *Infrared cavity ringdown laser absorption spectroscopy (IR-CRLAS) in low pressure flames*. Applied Physics B, 1997. **64**(6): p. 699-705.
33. Löhden, B., et al., *Fiber laser intracavity absorption spectroscopy for in situ multicomponent gas analysis in the atmosphere and combustion environments*. Applied Physics B, 2011. **102**(2): p. 331-344.
34. Lu, C., et al., *Time-resolved continuous-filtering Vernier spectroscopy of H₂O and OH radical in a flame*. Optics express, 2019. **27**(21): p. 29521-29533.

Chapter 7 : Conclusions and Further Work

7.1 Conclusions

This thesis has described the measurement of the P17e feature of acetylene using two cavity-based techniques, namely: continuous-wave cavity ring-down spectroscopy (cw-CRDS) and cavity-enhanced absorption spectroscopy (CEAS). As described in Chapter 1, The objectives of this project were to develop a CEAS system capable of *in situ* measurements of acetylene in a premixed laminar flame and to explore the possibility of extending the system to the measurement of other species in flames. Following the measurements of acetylene, the CEAS system was extended to detect OH species in flames.

Much of the work in this project has been directed towards sooting flames owing to the polluting effects of soot on the environment and its effect on human health. The importance of acetylene in soot formation through the HACA mechanism for soot growth and its role in the formation of the first aromatic ring has been described in this thesis and various literature. Owing to this importance, the data-set of acetylene mole fraction profiles in laminar ethylene-air premixed flat flames will be a useful step in studies aimed at soot reduction. The measurements were performed in a range of laminar premixed flames of ethylene and air at atmospheric pressure. The flames which range from lean to highly sooting were supported on a McKenna burner and a porous-plug burner. These burners have been characterised as flat-flame burners and are assumed to be one-dimensional; as such, species concentration in the flame change only with height above the burner surface.

7.1.1 Continuous-wave Cavity Ring-down Measurements of Acetylene

This work builds on the first demonstration of *in situ* diode laser cavity ring-down measurements of acetylene in a laminar flame. A limited data-set was obtained previously [1], which demonstrated the proof of concept and opportunities that exist with diode lasers. In this thesis, the initial design was made simpler by excluding some optical components, including a second laser and an optical switch used in normalising the cw-CRDS acetylene spectra. A region of negligible (narrow-band) absorption was chosen as a reference for which the non-resonant losses were obtained for use in calibrating the spectra. During the cw-CRDS operation, the laser wavelength switches to the reference point for each measurement. This compensates for the drift in alignment and fouling of the mirrors over the course of the measurements. The cw-CRDS measurements were performed using the porous-plug burner.

The spectra obtained from the cw-CRDS measurements for a range of flame conditions show good agreement in shape for wavelengths where there is no contribution from acetylene. This is also the case for spectra recorded across other measurement positions in the flame. The peak acetylene absorption increases with equivalence ratio, and this peak for a spectrum recorded in the stoichiometric flame is seen to be negligible. Following this, the stoichiometric spectrum is subtracted from each of the spectra to yield a spectrum due to acetylene alone. The subtracted spectrum was fitted to a model spectrum calculated from HITRAN. The fit was limited to the main acetylene feature to improve the fit and yield accurate acetylene concentration. The resulting concentration profiles of acetylene from the cw-CRDS measurements show good reproducibility. The profiles show higher acetylene concentrations for higher equivalence ratio flames, as expected. The concentration is seen to decrease with height above the burner surface. This suggests that acetylene is being used up in the formation of PAHs and soot downstream the flame. Extinction measurements obtained using the technique showed higher losses for higher

equivalence ratio flames, which could partly be attributed to broad-band absorption by larger aromatic species in the flame.

7.1.2 Cavity-enhanced Absorption Measurements of Acetylene

The CEAS technique is a variant technique that has the advantages of better resolution and faster acquisition with which broader spectra can be obtained. These advantages are all linked to the fact that the spectrum is not built up by acquiring ring-down events at discrete wavelengths. Despite requiring calibration, the results obtained using this technique are corroborated by results from cw-CRDS which is an absolute technique. A key consideration in the development of the CEAS technique is the length of the cavity. CEAS involves simultaneously exciting several higher-order modes of the cavity. The initial length of 500 mm, which is half the length for the confocal configuration supports the degeneracy of certain higher-order modes of the cavity which is not good for CEAS. This initial length was adjusted to a length of 750 mm to prevent the degeneracy of higher-order cavity modes. A procedure was established to obtain the base-line transmission in the absence of a flame as well as the effective mirror reflectivity by passing an inert purge through the cavity. With these parameters, the CEAS spectrum could be properly calibrated. The calibrated spectrum was shifted to zero based on the reference point of negligible absorption identified in the cw-CRDS operation. CEAS spectra were recorded in flames supported on McKenna burner and the porous-plug burner. The spectra show good agreement in shape with higher equivalence ratio flames possessing greater peaks for the main acetylene feature. This is similar to the observations from the cw-CRDS spectra.

The CEAS technique allows us to obtain a broader spectrum more quickly with better resolution. With this, it is observed that the stoichiometric spectrum does not fully converge with the rich spectra in spectral regions where acetylene absorption is absent. This, therefore, leads us to apply an iterative extraction technique to extract the acetylene contribution to the rich CEAS spectrum. The extracted spectrum was

fitted according to the fitting process used for cw-CRDS spectra to yield acetylene concentration. The recovered concentration profiles for both burners exhibit the decaying trend with height above the burner surface. The profiles for both burners are in agreement for the richest flame but disagree for the two leaner flame compositions. This possibly could be due to radial effects, and efforts were made to correct for the radial effects, resulting in good agreement for the two leaner flames and disagreement for the richest flame.

The CEAS and cw-CRDS concentration profiles for the porous-plug burner show good agreement except low down in the flame, which could be attributed to the strong temperature gradient low down in the flame. The profiles were compared with Cantera simulations using ABF and USC mechanisms. These mechanisms underestimate the consumption of acetylene for PAHs formation.

7.1.3 Cavity-enhanced Absorption Measurements of OH

In order to extend this technique to other important flame species, due diligence was done to carefully observe the wavelength range of the available lasers for absorption by any species. The spectra from the tuneable range of the 1535 nm and 1547 nm lasers show a lot of absorption for only high-temperature water and acetylene. Although a few acetylene lines other than the P17e acetylene feature at 1535.39 nm look promising, majority of the acetylene lines are seen to overlap the water lines.

The OH transition identified at 1572.14 nm has been probed, and the resulting spectrum reveals that this line is strongly interfered with by neighbouring water lines. However, the simulations from HITEMP suggest otherwise, and this highlights the shortcomings of the HITEMP database in correctly predicting the high-temperature water vapour lines in this wavelength region. The spectrum obtained for the OH transition line at 1572.40 nm is seen to possess a water line underlying the OH transition line as predicted by HITEMP. The spectra obtained for a range of flame conditions do not provide sufficient information on the water background at the line

centre of the OH feature. This would mean that the OH spectrum could not be further processed to acquire absolute concentration of OH in the flame with the data currently available.

7.2 Further Work

The CEAS concentration profiles of acetylene obtained using both burners show some discrepancy which is believed to be due to radial effects. We correct for the radial effects using a limited data-set of radial profiles obtained at two close heights above the burner surfaces. To properly understand the reason for the discrepancy in the concentration profiles, an extensive study of radial profiles would need to be performed.

Having obtained measurements of acetylene using the CEAS approach, a major avenue for furthering this work would be by extending the technique to other important flame species such as OH radical. The OH measurements in this work could not be quantified due to interference by neighbouring high-temperature water absorption lines. Given the challenge in accurately processing the OH spectra to acquire absolute concentration values of OH, some suggestions for further work are next prescribed for overcoming this challenge.

Following the interference of water lines in this wavelength region, a possible approach to improve the spectral selectivity of OH would be lowering the pressure of the flame, so that the absorption lines become narrower [2]. To quantify the contribution of water to the CEAS measured OH spectra, the spectrum of pure hot water vapour can be measured and subtracted from the OH spectra. This will require that the pure water vapour spectrum is obtained at the various temperatures for each flame height. One way to get around this is to scale the spectrum of water vapour based on the temperature for each flame height, albeit this might introduce some uncertainties in the subtracted OH spectrum [3]. The water spectra recorded for acetylene in Figure 5.7 show good agreement, especially beyond the region of the

temperature gradient (~ 2.5 mm) in the flame. Therefore, a spectrum recorded at a height where OH concentration is assumed to be negligible can be estimated to be the contribution of water. Subtracting this water spectrum from the spectrum recorded in a position of significant OH concentration will yield a spectrum due to OH contribution alone. This spectrum can be further processed to yield absolute concentration values of OH in the flame.

Temperature measurements are essential in characterising flames and calculating concentration from measured spectra. OH is commonly used as a temperature probe in flames and as such, the OH transitions in this wavelength can be used to characterise the temperature of our flames using OH two-line thermometry. The temperature sensitivity of the various OH lines in this wavelength region can be properly surveyed to identify a suitable pair of OH lines for OH-temperature measurements.

The CEAS approach can be combined with other techniques to calibrate the measurements. CEAS is not a self-calibrating technique, and the CEAS measurements in this work have relied on ring-down time measurements of the multi-mode cavity for calibration. Some studies on CEAS, albeit not in flames, have employed Phase-shift cavity ring-down and WMS techniques to calibrate CEAS measurements [4-6]. These techniques rely on phase-sensitive detection, as described earlier in this thesis for the individual techniques

7.3 References

1. Humphries, G., *Novel diode laser absorption techniques for combustion diagnostics*, in the *Department of Electronic and Electrical Engineering*. 2017, University of Strathclyde: Glasgow. p. 144.
2. Löhden, B., et al., *Fiber laser intracavity absorption spectroscopy for in situ multicomponent gas analysis in the atmosphere and combustion environments*. *Applied Physics B*, 2011. **102**(2): p. 331-344.

3. Rutkowski, L., et al., *Detection of OH in an atmospheric flame at 1.5 μm using optical frequency comb spectroscopy*. Photonics letters of Poland, 2016. **8**(4): p. 110-112.
4. Laurila, T., et al., *A calibration method for broad-bandwidth cavity enhanced absorption spectroscopy performed with supercontinuum radiation*. Applied Physics B, 2011. **102**(2): p. 271-278.
5. Vasudev, R., *Wavelength Modulated Cavity Enhanced Absorption Spectroscopy of Water in the 1.37 μm Region*. Applied Spectroscopy, 2006. **60**(8): p. 926-930.
6. Hamilton, M., et al., *Wavelength modulation and cavity enhanced absorption spectroscopy using $\sim 1.9 \mu\text{m}$ radiation produced by difference frequency generation with a MgO doped PPLN crystal*. Applied Physics B, 2009. **97**(3): p. 715.

Appendices

Appendix A: Conferences/meetings attended

Oral presentation at the Institute of Physics' One-day meeting on Current Research in Combustion – University of Sheffield (19th September, 2019).

Oral presentation at Chemical and Process Engineering Department Research Celebration Event – University of Strathclyde (18th September, 2019).

Poster presentations at Gordon Research Conference and Gordon Research Seminar on Laser Diagnostics in Combustion Energy - Switzerland (23rd -28th June, 2019).

Poster presentations at Chemical and Process Engineering Department Research Celebration Event – University of Strathclyde (12th September, 2018 and 5th December, 2016).

Poster presentation at the Combustion Institute (British Section) Spring Meeting on Advanced Combustion Methods – University of Manchester (5th April, 2018).

Oral presentation at 2nd SIG combustion meeting – University of Newcastle (26th March, 2018).

Oral presentation at CIDER meeting at the University of Edinburgh (29th January, 2018).

Appendix B: Matlab code for calculating acetylene concentration

```

clear all
format long

% 1.0 INPUT DATA
global T_0 S_T gas L A B YYYY_wavelength amps2 YYYY_wave
global C D X gammag z lambda v pressure partition gammal
global h c M k acetylenelines Q_T0

for i = 1:1

% 1.1 Reading in Data
%=====
====
% 1.2 Input of gas signal and trimming ends of data

str1 = strcat('xxxx.csv');
gas_in = csvread('xxxx.csv');
gas = gas_in(3500:5000,2);%
YYYY_wave = csvread('xxxx.csv');

partition = csvread('xxxx.csv');
acetylenelines = csvread('xxxx.csv');

% Parameters for Voigt Profiling
%
%=====

gases = {'C2H2'};% gases to be included in simulation (max 4)(must match data file
name)

wavelength_range=[ 1535.5 1535.3 ]; %spectral region to plot [upper lower] (nm)
% Constants
k = 1.3806503e-23; % Boltzmann's constant
M = 26; % Methane molecular mass
c = 299792458e2; % Speed of light (cm^-1)
h = 6.626e-34; % Planck's constant
L = 1; % Path length of cell

% Defining temperature
T_0 = 296; % Reference Temperature in Kelvin
T_K = 273.15; %0 degrees celcius in Kelvin

```

```

range = [1559];
T = range(i); %Converting to Kelvin

% Defining pressure and converting from bar to atm
pressure = 1; %bar
pressure = pressure*0.986926; %atm

%===== Defining Frequency steps =====

vsteps = 3000;
Start = wavelength_range(1);
End = wavelength_range(end);

lambda = linspace(Start,End,vsteps);
v = 1./lambda.*1e7;

lower_trunc = (abs(v(1)-acetylenelines(:,1)));
lower_trunc = find(lower_trunc == min(abs(v(1)-acetylenelines(:,1))) );

higher_trunc = (abs(v(end)-acetylenelines(:,1)));
higher_trunc = find(higher_trunc == min(abs(v(end)-acetylenelines(:,1))) );

acetylenelines = acetylenelines(lower_trunc:higher_trunc,:);

z = length(acetylenelines);

index1 = find(partition(:,1) == T_0);
Q_T0 = partition(index1,2);

deltaT = abs(partition(:,1)-T);

minT = min(deltaT);

index2 = find(deltaT == minT);

Q_T = partition(index2(1),2);

% Calculate line-strength

S1 = (1-exp(-(h*c.*acetylenelines(:,1))/(k*T)))/(1-exp(-
(h*c.*acetylenelines(:,1))/(k*T_0)));
S4 = (Q_T0./Q_T).*(T_0/T).*(exp((-h*c*acetylenelines(:,5)/k)*((1/T)-(1/T_0))));

```

```

S7 = S1.*S4;

S_T = S7.*acetylenelines(:,2);

% Gaussian Broadening
gammag = 7.1625e-7.*acetylenelines(:,1).*(T/M)^0.5;
gammag = gammag';

for j = 1:z
X(:,j) = 2*sqrt(log(2))*(v-acetylenelines(j,1)-acetylenelines(j,7))./gammag(j);
end

A = [-1.2150 -1.3509 -1.2150 -1.3509];
B = [1.2359 0.3786 -1.2359 -0.3786];
C = [-0.3085 0.5906 -0.3085 0.5906];
D = [0.0210 -1.1858 -0.0210 1.1858];

%
=====
% VOIGT FITTING (MCLEAN METHOD)
%
=====

lsq_low_limits = [ 0.0001 ]; % Limits of concentration and temperature in fitting
algorithm
lsq_high_limits = [ 0.1 ];

clc%%%%%%%%%%%%%%

fit_variables = [ 0.1 1.535393316684490e+03];

options=optimset('MaxFunEvals',50000,'TolFun',1e-
15,'MaxIter',10000,'ToIX',0.000001);

[Z1 ,RESNORM1,RESIDUAL1,EXITFLAG1,OUTPUT1] =
lsqnonlin(@myacetyleneconconlynlsql,fit_variables,lsq_low_limits,lsq_high_limits,o
ptions);

conc(i) = Z1(1);

figure
hold on
plot(YYY_wavelength,gas)
plot(YYY_wavelength,amps2,'r')

```

```

end

height = linspace(2,7,6);
conc=conc';
figure
plot(height,conc*100,'ro')

function SSE = myacetyleneconconlynlsql(Z1)

global YYY_wavelength T_0 S_T gas L A B YYY_wave
global C D X gammag z lambda pressure amps2 gammal cut_waves

YYY_wavelength = YYY_wave(3500:5000,1);
YYY_wavelength = YYY_wavelength';
gammal=0.055156007;

Y = (gammal./gammag)*sqrt(log(2));

for j = 1:z
    for i = 1:4
        V_top(i,:)= (C(i)*(Y(j)-A(i)))+(D(i)*(X(:,j)-B(i)));
        V_bottom(i,:) = (Y(j)-A(i))^2+(X(:,j)-B(i)).^2;
    end
    V = V_top./V_bottom;
    Vffinal(:,j) = (2/gammag(j))*(log(2)/pi)^0.5*Z1(1)*(7.339e21/T_0)*S_T(j)*sum(V);
end

voigt = pressure*sum(Vffinal').*L;

IND1 = find(lambda <= YYY_wavelength(1));
IND1 = IND1(1);
IND2 = find(lambda <= YYY_wavelength(length(gas)));
IND2 = IND2(1);

%Calculate the wavelengths and amplitudes of the theory data in range
%of experimental data
cut_waves = linspace(lambda(IND2),lambda(IND1),IND1-IND2+1);
cut_amps = voigt(IND2:IND1);

% Interpolating theory data over length of experimental
% data, making sets of data over equal range and equal length

```

```
amps2 = interp1(cut_waves, cut_amps, YYY_wavelength, 'linear', 'extrap');  
SSE = amps2(100:800) - gas(100:800);  
% SSE = amps2 - gas;  
end
```

Appendix C: Matlab code for CEAS spectra calibration

```

close all
clear all

%Read in the files
flame = csvread('xxx.csv');
Background = csvread('xxx.csv');
Bkgd_purge = csvread('xxx.csv');
Detector_bkgd = csvread('xxx.csv');

%Extract data from the files
flamex = flame(:,1);
flamey = flame(:,2);
Backgroundy = Background(:,2);
Backgroundpurge = Bkgd_purge(:,2);
Detctrbkgd = Detector_bkgd(:,2);

%subtract detector background
Io = Backgroundpurge - Detctrbkgd;

%subtract flame background
I = flamey - Backgroundy;

%state other parameters
R = 0.999951236862770;%effective mirror reflectivity
d = 6; %McKenna burner diameter in cm
%d = 3.3; % porous plug burner diameter in cm

%calculate absorption coefficient
Absorption_coeff = 1/d.*((Io - I)./I).*(1-R);
figure
plot(flamex,Absorption_coeff,'r')

%%%%%%%%%%%%%%%%%%%%%%%%%%%%%%%%%%%%%%%%%%%%%%%%%%%%%%%%%%%%%%%%%%%%%%%%wavelength_reference%%%%%%%%%%%%%%%%%%%%%%%%%%%%%%%%%%%%%%%%%%%%%%%%%%%%%%%%%%%%%%%%%%%%%%%%
%

c=299792458; %speed of light
signal=Absorption_coeff;

%read in resonator trace file
trace=csvread('xxx.csv');
time=trace(:,1);

```

```

resonator=trace(:,2);

%filter peaks
[b1 a1] = ellip(3,0.00001,60,0.02);
res = filtfilt(b1,a1,resonator);
g = 500;
res=res(g:end);

% 2.2 Find Peaks
diff_res = diff(res);
JJ = [];

for n = 1:length(diff_res)-1
    if ( ne(sign(diff_res(n)),sign(diff_res(n+1))) && (diff_res(n) > diff_res(n+1)) )
        JJ = [JJ n+1];
    end
end
% 2.3 Define x and y values of peaks

resonator_peak(:,:)=res(JJ(:,:));
int = find(resonator_peak > 0.1);
JJ = JJ(int);
resonator_peak = resonator_peak(int);

%filter results
results = signal;
results = smooth(results,5);

%Assign wavelength
Line_cent_wave=1.535393316684490e+03; %For Acetylene
Line_Cent_Freq = 299792458./(Line_cent_wave);

Q = max(results(3000:4000));
Q_Index = find(results == Q);
Line_Cent_Index = Q_Index(1);

[error1, closest_peak]=min(abs(JJ-Line_Cent_Index));
delta_f= 0.4276;

% 2.7.2 Declare vector for storing frquencies
Res_Peak_Wave = [];
Res_Peak_Wave(closest_peak)=150000;

```

```
FF=length(JJ)+1;
nn=1;
while nn < FF
    if nn<closest_peak
        Res_Peak_Wave(nn)=[150000+((closest_peak-nn)*delta_f)];
    end;

    if nn>closest_peak
        Res_Peak_Wave(nn)=[150000-((nn-closest_peak)*delta_f)];
    end;
nn=nn+1;
end;
% resonator frequencies
data_time = flamex;
data_time = data_time';

P=polyfit(data_time(JJ),Res_Peak_Wave,5);
xx = length(results);
x=[1:1:xx];

YYY=polyval(P, data_time);

shift=Line_Cent_Freq-YYY(Line_Cent_Index);
YYY=YYY+shift;
YYY_wavelength=c./YYY;
YYY_wavelength=YYY_wavelength';
figure
plot(YYY_wavelength,results)

%adjust baseline/background
Base = mean(results(3480:3530));
zero = Base;
Resulty = results-zero;
figure
plot(YYY_wavelength,Resulty,'g')
```

Appendix D: Matlab code for the iterative extraction technique

```
close all
clear all
format long
clc

%Read in files(CEAS spectra)
Rich_flame = csvread('xxxx.csv');
Lean_flame = csvread('lxxxx.csv');

Rich_flamex = Rich_flame(1:9500,1);
Rich_flamey = Rich_flame(1:9500,2);
Lean_flamex = Lean_flame(1:9500,1);
Lean_flamey = Lean_flame(1:9500,2);

figure(1)
set(gcf,'WindowStyle','docked')
hold on
plot(Rich_flamey)
plot(Lean_flamey,'k')
hold off

%find the peak of the strong acetylene feature for the rich flame and the leanflame

Rich_peak = max(Rich_flamey(4000:4400));
Rich_Index = find(Rich_flamey == Rich_peak);
Rich_Index_2 = Rich_Index(1);
Lean_peak = max(Lean_flamey(4000:4400));
Lean_Index = find(Lean_flamey == Lean_peak);
Lean_Index_2 = Lean_Index(1);

%Ratio of the rich/lean peak
I_Ratio = Rich_peak/Lean_peak;

%Subtract lean spectrum from rich spectrum. Consider the result as a first estimate
of the acetylene spectrum.

Acet_estimate = Rich_flamey-Lean_flamey;

%Get an improved estimate of the water spectrum
Water_estimate = (Lean_flamey)-((Rich_flamey-Lean_flamey)./I_Ratio);
```

```
%subtract water background estimate from lean flame and rich flame
```

```
rich = Rich_flamey-Water_estimate;  
lean = Lean_flamey-Water_estimate;
```

```
for i = 1:4
```

```
l_Ratio_2 = max(rich(4000:4400))/max(lean(4000:4400));
```

```
rich = rich./l_Ratio;
```

```
Water_estimate = Lean_flamey - rich;
```

```
rich = Rich_flamey - Water_estimate;  
lean = Lean_flamey - Water_estimate;
```

```
figure(2)  
set(gcf,'WindowStyle','docked')  
hold on  
plot(rich)  
plot(Water_estimate)  
pause(0.5)
```

```
end
```

```
figure(3)  
set(gcf,'WindowStyle','docked')  
%set (gca,'YDir','reverse')  
hold on  
plot(rich,'r')  
plot(Water_estimate)  
plot(Rich_flamey,'g')
```

```
pause(0.5)
```

Appendix E: Cantera code for a stagnation flame with a fixed temperature profile

```

"""
A burner-stabilized, premixed methane/air flat flame with multicomponent
transport properties and a specified temperature profile.
"""

import cantera as ct
import numpy as np

#####
# parameter values
p = ct.one_atm # pressure
tburner = 373.7 # burner temperature
mdot = 0.065 # kg/m^2/s
comp = 'CH4:0.467, O2:1, N2:3.76' # premixed gas composition

# The solution domain is chosen to be 1 cm
width = 0.01 # m

loglevel = 1 # amount of diagnostic output (0 to 5)
refine_grid = True # 'True' to enable refinement

##### create the gas object #####
#
# This object will be used to evaluate all thermodynamic, kinetic, and
# transport properties. It is created with two transport managers, to enable
# switching from mixture-averaged to multicomponent transport on the last
# solution.
gas = ct.Solution('gri30.xml', 'gri30_mix')

# set its state to that of the unburned gas at the burner
gas.TPX = tburner, p, comp

# create the BurnerFlame object.
f = ct.BurnerFlame(gas=gas, width=width)

# set the mass flow rate at the burner
f.burner.mdot = mdot

# read temperature vs. position data from a file.
# The file is assumed to have one z, T pair per line, separated by a comma.

```

```
zloc, tvalues = np.genfromtxt('tmp.txt', delimiter=',', comments='#').T
zloc /= max(zloc)

# set the temperature profile to the values read in
f.flame.set_fixed_temp_profile(zloc, tvalues)

# show the initial estimate for the solution
f.show_solution()

# don't solve the energy equation
f.energy_enabled = False

# first solve the flame with mixture-averaged transport properties
f.transport_model = 'Mix'
f.set_refine_criteria(ratio=3.0, slope=0.3, curve=1)

f.solve(loglevel, refine_grid)
f.save('ch4_flame_fixed_T.xml', 'mixav',
      'solution with mixture-averaged transport')

print('\n\n switching to multicomponent transport...\n\n')
f.transport_model = 'Multi'

f.set_refine_criteria(ratio=3.0, slope=0.1, curve=0.2)
f.solve(loglevel, refine_grid)
f.save('ch4_flame_fixed_T.xml', 'multi',
      'solution with multicomponent transport')

# write the velocity, temperature, density, and mole fractions to a CSV file
f.write_csv('flame_fixed_T.csv', quiet=False)
f.show_stats()
```